Investigating Plasma Interactions with Multiphase Surfaces using Computational Models

by

Mackenzie E. Meyer

A dissertation submitted in partial fulfillment
of the requirements for the degree of
Doctor of Philosophy
(Applied Physics)
in the University of Michigan
2022

Doctoral Committee:

Professor Mark J. Kushner, Chair
Associate Professor Herek Clack
Professor John Foster
Associate Professor Benjamin Jorns
Associate Professor Carolyn Kuranz

Mackenzie E. Meyer

maemeyer@umich.edu

ORCID iD: 0000-0002-2105-6690

Dedication

To Greg

Acknowledgements

I am grateful for my experience at University of Michigan. Many wonderful people helped me along the way, only some of whom I have space to thank below. First, I would like to thank my advisor, Professor Mark Kushner. I appreciate you welcoming me into your group as a third year Ph.D. student, and your encouragement and support over the past few years has meant a lot to me. Thank you for sharing your immense knowledge base in low-temperature plasmas with me and the rest of the group. I would also like to thank my first advisor in graduate school, Professor Iain Boyd, for introducing me to the world of low-temperature plasmas and electric propulsion. I am grateful for my committee members as well: Professors Ben Jorns, John Foster, Herek Clack, and Carolyn Kuranz. Your insight into plasma physics has been valuable throughout my Ph.D. I would like to extend a special thank you to Professor Ben Jorns, whose encouragement in the work on uncertainty in erosion profiles was invaluable.

I have also worked with many lab mates, past and present, who I would like to thank: Juliusz Kurszelnicki, Chenhui Qu, Steven Lanham, Jordyn Polito, Florian Krueger, Kseniia Konina, Evan Litch, Yifan Gui, Xifeng Wang, Astrid Raisanen, Sanjana Kerketta, Tugba Piskin, Scott Doyle, Horatiu Dragnea, Lauren Mackey, Candice Martin, Sam Chen, Kaelan Hansson, Mike Holloway, Alex Vazsonyi, Thomas Marks, and Austin Brenner. Your friendship inside and outside of the lab has helped make my career at Michigan very enjoyable. I would also like to thank Julia Falkovitch-Khan for all her work, both for me and for the plasma community.

There are other collaborators I would like to mention: Matt Byrne, Gaurav Nayak, Professor Peter Bruggeman, Zimu Yang, Xiaheng Huang, Anjali Devi Sivakumar, and Professor

Xudong Fan. Thank you for providing interesting ideas and an insight into how measurements of plasmas are conducted. I would also like to thank the sponsors that funded my work, including the Applied Physics Program, Aqua-Aerobic Systems, US Department of Energy Office of Fusion Energy Science (DE-SC000319, DE-SC0020232), the National Science Foundation (IIP-1747739, PHY-1902878), and the Army Research Office (W911NF-20-1-0105).

To my friends who have encouraged me along the way, including Jessie Paulson, Natalie Gaughan, Katherine Kokkinias, and Christine Morris – thank you. I could not ask for a better and more supportive group of friends. I would also like to thank my cats throughout grad school (Cinnamon, Charlotte, and Margaret) for being adorable and cute, and for letting me pet them when I'm feeling down. My parents, Al and Tina Meyer, have constantly supported me for my entire life – thank you for continuing to support me throughout grad school. Thank you for instilling in me a love of learning that persists to this day.

Last but certainly not least, I would like to thank my fiancé Greg. Thank you for coming to Michigan with me. I'm not sure how I would have gotten through graduate school without your constant support and encouragement, particularly on the tough days. I can't wait to marry you and spend the rest of our lives together.

Table of Contents

List of Tables

List of Figures

Abstract

Low-temperature plasmas affect multiphase surfaces in contact with the plasma, and the surfaces can in turn affect the plasma. These effects can be destructive (i.e., erosion) or productive (i.e., increased reactive species generation). However, many of these effects are not well understood. In this dissertation, computational modeling of low-temperature plasmas and their interactions with multiphase surfaces is performed to increase understanding and improve systems.

One such model, *MEOWS*, was developed by the author to model erosion of a wire by ion-impact sputtering in the plasma plume of a Hall thruster. The eroded wire profiles from *MEOWS* were validated against experimental measurements of wire erosion. The sputtering yield models that best fit the measurements were identified. Following validation, distributions of model parameters were generated using a Bayesian approach due to the variation in sputtering yield measurements. *MEOWS* sampled from the distribution to generate median predictions with credible intervals for the eroded wire profiles. The over-erosion uncertainty in the maximum predicted erosion was demonstrated to be up to 190% of the median maximum predicted erosion, showing the necessity for uncertainty consideration in lifetime estimates.

Liquid droplets immersed in the plasma form another multiphase surface examined in this dissertation. The interactions between the atmospheric pressure plasma and the droplet were examined using *nonPDPSIM*, a 2D plasma dynamics model, and *GlobalKin*, a 0D plasma chemistry model. Using the results of *nonPDPSIM*, the sheath that forms around a dielectric droplet immersed in the radio frequency plasma was shown to be asymmetric. The effect of the polarization of the droplet, the sheath electric field, and the bulk electric field led to increased

electric field on one equator of the droplet and a decreased electric field on the opposing equator. The charge on the droplet was positive on the poles and negative on the equator. The degradation of the organic compound $HCOO^-_{aq}$ was examined using *GlobalKin*. When $HCOO^-_{aq}$ was abundant, OH_{aq} was consumed in reaction with $HCOO^-_{aq}$. If $HCOO^-_{aq}$ was substantially reduced before the power turned off, OH_{aq} could decrease due to reactions with $HO_2{}^-_{aq}$ and OH^-_{aq}, formed as byproducts from $HCOO^-_{aq}$ consumption.

Pulsed dielectric barrier discharges at atmospheric pressure can generate large quantities of reactive species. O_3 production is a common use of these systems. The results of *nonPDPSIM* showed the maximum in O and O_3 followed the electron density maximums. Roughness of the dielectric surface locally enhanced O and O_3 density without significant changes in O_3 production efficiency. A general surface mechanism was developed and implemented in *GlobalKin*. The O_3 production was maximized at 0.05% N_2 in O_2 due to adsorbed N occupying surface sites otherwise contributing to O_3 destruction. Another application of pulsed dielectric barrier discharges is discharge photoionization detectors, relying on the VUV photons produced by a He discharge. The results of *nonPDPSIM* showed the lifetime of radiating state He(3P) was shorter than He(2^1P). He_2^* was long-lived relative to the pulse length. Different approaches to increase the photon flux to the analyte gas include increasing the capacitance of the surrounding dielectric, moving the electrodes closer to the analyte gas inlet, and adding points to electrodes and additional electrodes.

The studies in this dissertation examined low-temperature plasma interactions with a variety of multiphase surfaces using computational models. Better understanding of these interactions was demonstrated and will lead to improvements in real-world systems.

Chapter 1 Introduction

Plasmas are often called the fourth state of matter, differing from neutral gases by containing charged species. Since plasmas contain charged species, they can respond to electromagnetic fields and exhibit collective motion. One category of plasmas is low-temperature plasmas (LTPs). The current uses of LTPs in industry are numerous, including microelectronics processing [1], functionalization of polymers [2,3], electric propulsion [4], and ozone production for water treatment [5]. Areas of opportunity for LTPs include pollution remediation [6], plasma medicine [7], plasma catalysis [8], and nanoparticle synthesis [9]. Improving the understanding of LTPs in these systems will lead to further development and optimization of these systems.

To that end, computational modeling of LTPs and their interactions with multiphase surfaces are studied in this dissertation. These surface interactions include erosion of a wire in the plume of a Hall thruster, electrical and chemical characteristics of a liquid droplet immersed in the plasma, destruction of plasma-produced species on the walls of the reactor, and production of photons. The results of the computational models reveal the underlying processes in each system and point to strategies for improvement.

In Section 1.1, an overview of LTPs is presented. Specific applications examined in this dissertation are discussed in Sections 1.2, 1.3, and 1.4. Different approaches for modeling LTPs are discussed in Section 1.5. Motivation for the work performed in this dissertation is presented in Section 1.6. An overview of the following chapters in this dissertation is given in Section 1.7.

1.1 Low-Temperature Plasmas

Plasmas are believed to encompass most of the matter in the universe [10], though the issue of dark matter still remains to be resolved. The range of number density and temperature of these plasmas is quite large, as shown in Figure 1.1. This range includes space plasmas with low densities (1 cm^{-3}) and low temperatures (1 - 100 eV) and fusion plasmas with high densities (10^{15} cm^{-3}) and high temperatures (> 10 keV) [11].

Despite the wide range of plasma properties, some characteristics apply to all plasmas. Plasmas are typically quasineutral, where the positive charge is equal in magnitude to the negative charge. Quasineutrality can be broken over small time or length scales [10]. The time scale is defined by the plasma frequency, derived by determining the frequency of electrostatic oscillation of charged species displaced from neutral. In LTPs, the plasma frequency is the electron plasma frequency ω_{pe}, given by

$$\omega_{pe} = \sqrt{\frac{e^2 n_e}{\varepsilon_0 m_e}}, \tag{1.1}$$

where e is the fundamental charge, n_e is the electron density, ε_0 is the permittivity of free space, and m_e is the electron mass. The length scale over which quasineutrality can be broken is the Debye length λ_D, given by

$$\lambda_D = \sqrt{\frac{\varepsilon_0 k_B T_e}{e^2 n_e}}, \tag{1.2}$$

where k_B is Boltzmann’s constant and T_e is electron temperature. The convention in plasma physics is to refer to the electron temperature as $k_B T_e$ in units of eV.

Quasineutrality is broken in the sheath that forms around material in contact with the plasma, as shown in Figure 1.2. Electrons diffuse more rapidly due to their lower mass (m_e/m_i <

5×10^{-4}) and higher temperature in non-equilibrium systems. Therefore, electrons diffuse more rapidly to surfaces in the plasma, charging the surface negatively. The negative surface charge creates an electric field that draws positive ions towards the surface but repels electrons, creating a region of positive space charge surrounding the material called the sheath. In general, sheaths have dimensions on the order of λ_D.

In plasmas with applied magnetic fields, the charged species will orbit the magnetic field lines, as shown in Figure 1.3. The frequency of the circular motion is called the cyclotron frequency ω_c, and is given by

$$\omega_c = \frac{qB}{m}, \tag{1.3}$$

where q is the species charge, B is the magnetic field, and m is the species mass. Each species orbits at its own ω_c. The radius of this circular motion is the Larmor radius r_L, given by

$$r_L = \frac{mv_\perp}{|q|B}, \tag{1.4}$$

where $v_\perp$ is the velocity perpendicular to the magnetic field. In general, due to the lower mass of electrons compared to ions, the electrons have a higher ω_c and smaller r_L than ions.

While the parameters discussed above are common to all plasmas, LTPs occupy only a small regime of plasmas, near the neon sign in Figure 1.1. LTPs can be formed in a range of pressures from mTorr to atmospheric pressure. LTPs have low ionization fractions of 10^{-6} to 10^{-1} [11]. Therefore, charged species will interact with neutral species more frequently than with other charged species. In LTPs, the neutral gas temperature is near room temperature, while the ion temperature can be higher depending upon the application. The electron temperature is a few eV. Since the neutral gas temperature, ion temperature, and electron temperature are different, LTPs are nonequilibrium plasmas.

Electron-impact collisions in LTPs ionize and excite the neutral gas. Electron-impact collisions occur as the electrons gain energy from the external electric field. Once the electron gains energy larger than the threshold energy for excitation or ionization, that process can occur, and the electron will lose the requisite energy. This process cuts off the electron energy distribution, as electrons with energies larger than the threshold energy will undergo the collision. Therefore, the energy distribution is not well represented by a Maxwell-Boltzmann distribution, and LTPs are nonthermal plasmas [12].

Much of the reactive chemistry in LTPs is driven by electron-impact collisions, like dissociation (i.e., $e + H_2O \rightarrow e + OH + H$). Heavy species reactions can also be responsible for forming reactive species (i.e., $OH + OH + M \rightarrow H_2O_2 + M$). Reactive species common in plasmas generally include excited states of noble gases and reactive oxygen and nitrogen species (RONS) like OH, O, O_3, NO, NO_2, and NO_3. Excited noble gas atoms can emit VUV photons or can Penning ionize molecular gases (i.e., $Ar^* + N_2 \rightarrow Ar + N_2^+$), as the threshold for excitation of noble gases is higher than the ionization potential of molecular gases. Reactive chemistry can be tuned by forming the plasma in different gas mixtures [13].

While LTPs are one regime of plasmas, differences exist between LTPs formed at low pressure and atmospheric pressure. These differences stem from the mean free path λ_{mfp}, expressed as

$$\lambda_{mfp} = \frac{1}{n\sigma}, \tag{1.5}$$

where n is the number density and σ is the cross-section for collisions. As the pressure decreases, the gas number density decreases; therefore, λ_{mfp} increases. The increase in λ_{mfp} can lead to increases in ion energies. At low pressures, ions can gain energy from the external electric field and not lose the energy in collisions. However, at atmospheric pressure, λ_{mfp} is small due to the high gas density, and ions undergo collisions more rapidly than at low pressure, leading to less acceleration from the external electric field. The larger λ_{mfp} at low pressure also allows charged species to be magnetized at a lower magnetic field strength. Species are magnetized when their motion is dominated by circular motion around magnetic field lines due to the Lorentz force. Magnetization of species occurs when particles will complete many rotations around the magnetic field before being knocked away from the magnetic field line by a collision ($\lambda_{mfp} > r_L$).

1.2 Electric Propulsion

One application of LTPs is electric propulsion (EP). In EP, ions are produced and accelerated by electromagnetic fields to provide thrust to a spacecraft. The advantage of EP over traditional chemical propulsion lies in its high specific impulse I_{sp}, given by

$$I_{sp} = \frac{v_{ex}}{g}, \tag{1.6}$$

where v_{ex} is the exhaust velocity of the propellant and $g = 9.8$ m s^{-2}. More efficient usage of mass flow in the thruster gives a higher I_{sp}. EP systems typically have $I_{sp} > 1000$ s, compared to 100 s – 500 s typical of chemical rockets [14]. Despite its high I_{sp}, the thrust produced by EP systems is low, ranging from 2 mN [15] to over 5 N [16]. Given this relatively low value of thrust, EP is used primarily for space-based propulsion, including orbit raising and station-keeping applications [14]. EP has also been used for deep-space missions, where the thruster continually operates to provide thrust over a long time period [17]. There are many different EP systems, including electrothermal, electrostatic, and electromagnetic approaches [14]. The EP system examined in this dissertation is the Hall thruster.

A schematic of a Hall thruster is shown in Figure 1.4. Hall thrusters are azimuthally symmetric devices, with electrons emitted by an externally or centrally mounted cathode. The discharge voltage is the applied potential difference between the cathode and anode. The electrons are drawn into the discharge channel by the axial electric field from the discharge voltage. A strong, radial magnetic field confines the electrons near the exit of the discharge channel, as their r_L is small compared to the discharge channel size. The neutral propellant is injected through the anode at the back of the discharge channel and is ionized through collisions with the magnetized electrons. The neutral propellant is typically xenon, though other noble gases like Krypton are under investigation [18]. The r_L of the ions is much larger than the discharge channel, so the ions are not magnetized. The ions are therefore accelerated out of the discharge channel by the axial electric field, producing thrust. The ions typically have an energy near the discharge voltage, which is often around 300 V [19]. Electrons from the cathode neutralize the ions in the plume after they leave the discharge channel. The mass utilization efficiency, or the ratio of the mass flux of the ions to the mass flux of the incoming propellant, is high, typically above 80% [14].

1.2.1 Erosion of Spacecraft Components

Since the energetic ions in the plume of EP devices possess enough energy to erode surfaces by ion-impact sputtering [20,21], the integration of EP systems onto spacecraft requires special attention. The distribution of ions in the plume of a Hall thruster is shown in Figure 1.5. While the most obvious threat to components is the energetic beam of ions emitted by the thruster (typical divergence angle of 30° from the thruster centerline), ions formed by charge-exchange collisions can also be energetic enough to sputter components. These ions are often found at large angles from the thruster centerline, as their trajectory is influenced by the local electric field as opposed to the electric field inside the thruster.

To predict erosion of spacecraft components, the sputtering yield (number of atoms sputtered per incident ion) for materials typically used in spacecraft components has been experimentally measured [22–33], and semi-empirical models for the sputtering yield have been developed [25,30–32,34–38]. These semi-empirical sputtering yield models are based on physical understanding but require experimental data to tune model parameters to predict the sputtering yield for different materials. These models can predict the sputtering yield of flat surfaces at different angles of incidence of the ions θ due to a mono-energetic ion beam, as shown in Figure 1.6.

Due to the threat to spacecraft components, many studies have assessed the erosion of spacecraft components due to ion-impact sputtering. Several studies have computationally examined the erosion of solar panel components, like glass and silver [39–45], while other studies have performed experimental tests to measure the erosion of solar panel components [46–50]. Most of these studies have examined the sputtering or erosion of flat spacecraft components due to a mono-energetic ion beam.

While many studies have examined the erosion of flat surfaces, spacecraft components are not necessarily flat surfaces. One such component is the meshed reflector, used as an antenna on communication satellites. This reflector is typically composed of a mesh of small molybdenum wires coated with gold. Accurately predicting the erosion of the meshed reflector requires predicting the erosion of a single wire exposed to the plume of a Hall thruster. However, analytically determining the erosion of wires is difficult, as the angle of incidence changes from grazing incidence to normal incidence around the circumference of the wire. Predicting wire erosion is difficult not only due to the changes in angle of incidence; in parts of the Hall thruster plume, the ion energy distribution also strays quite drastically from a mono-energetic beam. Since the sputtering yield can vary non-linearly with energy, capturing the distribution of ion energies is necessary for an accurate prediction of erosion. To incorporate the change in angle of incidence and distribution of ion energies, predictions of erosion of a wire exposed to a Hall thruster plume must be numerically modeled.

1.3 Plasma-Liquid Interactions

Atmospheric pressure LTPs interacting with liquids is an active area of research [51]. These interactions are important in plasma medicine [7] and water treatment [52]. In these applications, reactive species like RONS formed in the gas phase solvate into the liquid and chemically activate the liquid. Once solvated, RONS can either react quickly (OH, O) or can persist for minutes (H_2O_2, NO_3^-/HNO_3). Many different geometries exist for exposing liquids to plasmas, as shown in Figure 1.7. These include forming plasmas directly in the liquid [53], forming plasmas in bubbles in the liquid [54–56], forming plasmas in the gas phase with the liquid as an electrode [57,58], forming plasmas in the gas phase with the liquid in the effluent [59,60], and forming plasmas in the gas phase with droplets flowing through them [61,62].

Many studies have been conducted to determine the reactive chemistry in the liquid. Modeling studies, including one by Heirman et al., have shown that H_2O_{2aq}, $NO_2^-{}_{aq}/HNO_{2aq}$, and $NO_3^-{}_{aq}/HNO_{3aq}$ are the long-lived RONS that persist in the liquid after plasma exposure [63]. NO_3 synthesis can depend upon NO_2 synthesis and increases as O_2 fraction increases [64]. Ganesh et al. showed that plasmas can produce $NO_3^-{}_{aq}$, a desired fertilizer for agriculture, at a low specific energy [65]. Conductivity increases and pH decreases when water is exposed to plasma [59,66]. Production of certain RONS can be tuned by using different gas mixtures [13]. While water is the most common liquid under investigation, other liquids including oil-water mixtures have also been investigated [67].

LTPs have been used to treat water that contains organic compounds. Volatile organic compounds present in water, including toluene and benzene, have been showed to be degraded by exposure to plasmas [68,69]. Studies have shown that methylene blue dye, a model organic compound, can be degraded [70,71]. Yang et al. showed that pharmaceutical chemicals like amoxicillin can be oxidized by LTPs [72]. Emerging areas of research include using plasma to treat so-called “forever chemicals” like PFAS [73].

LTPs have also been shown to kill cancer cells in a liquid and inactivate bacteria and viruses found in water [74]. Many studies, including Liu et al., expose liquid to plasma and treat cancer cells with the activated liquid [75]. Sklias et al. showed that while direct plasma exposure can damage cancer cells as well as normal cells, only cancer cells are damaged when liquid is exposed to plasma and then used to treat cells [76]. Jiang et al. showed that different cancer cells respond differently to plasma treatment; after 60 s, breast cancer cells were less viable than pancreatic cancer cells [77]. However, using plasmas in the human body, as opposed to looking solely at cell cultures, may be more difficult, as Lin et al. showed that RONS can be scavenged by components of blood [78].

While many studies have examined plasma-liquid interactions, increasing RONS concentrations in the liquid remains a challenge. The transport of RONS at the interface between the liquid and the plasma is complex, due to Henry’s law equilibrium, sheath formation, and a high density of vapor surrounding the liquid, as shown in Figure 1.8. Silsby et al. showed that using a two-film transport theory more accurately predicted transport across the interface [79]. Another complicating factor is interfacial chemistry, as short-lived reactive species, including OH_{aq}, will react quickly in the liquid and not reach the bulk liquid. For example, the penetration depth of solvated electrons is low, about 17 nm from the interface of the gas and liquid [80]. Using aerosols immersed in the plasma can increase the transport of RONS to the bulk liquid.

1.3.1 Plasma-Aerosol Interactions

Aerosols interacting with plasmas can enhance the transfer of reactive species to the liquid [81]. The increase in RONS in aerosols compared to bulk liquid is due to the mitigation of transport limits. The transport limits can be divided into two parts: solvation of RONS into the liquid at the interface and diffusion of RONS from the interface to the bulk liquid. The first transport limit can be mitigated by placing the liquid as close as possible to the plasma itself. This decreases the distance the RONS are required to travel to reach the liquid and can increase the short-lived reactive species densities in the liquid. In aerosol applications, the aerosols are immersed in the plasma. The second transport limit is mitigated by using a liquid with a high surface area to volume ratio (SVR). The RONS take less time to reach the bulk liquid with a high SVR. A high SVR is often associated with aerosols with diameters < 100 μm, but other geometries like thin sheets of liquid also have high SVRs [13].

Aerosols immersed in a plasma have been studied previously. Densities of the RONS in the droplet depend on their Henry's law constants. Liquid phase densities of species with high Henry's law constants have been shown to be limited by depletion of the gas phase surrounding the droplet; however, liquid phase densities of species with low Henry's law constants can saturate before the gas phase is depleted [82,83]. Viruses in aerosol droplets have been inactivated by plasma exposure [84,85].

A series of studies aim to measure the amount of OH_{aq} in an aerosol droplet immersed in a radio frequency (RF) glow discharge shown in Figure 1.9 [61,62,86,87]. To do this, $HCOO^-_{aq}$ is dissolved in the droplet that is then flowed through the plasma. The droplets are frozen after exposure to the plasma to enable chemical analysis at a later time. As OH_{aq} reacts quickly with $HCOO^-_{aq}$ in the droplet, the change in $HCOO^-_{aq}$ concentration after exposure to the plasma measures the accumulated OH_{aq}. Since short-lived reactive species like OH_{aq} play large roles in activating the liquid, understanding how OH_{aq} reacts at the surface of the liquid will improve the understanding of plasma-liquid interactions more generally.

1.4 Pulsed Dielectric Barrier Discharges

LTPs can be formed in pulsed, high voltage systems like plasma jets [88–91] or dielectric barrier discharges (DBDs) [92,93]. In these systems, the plasma propagates as an ionization wave, often called a streamer, marked by the increase in electron density caused by electron-impact ionization of neutral gas. An ionization wave is shown in Figure 1.10. Typically, the electron temperature is maximized just ahead of the increase in electron density, continuing plasma propagation [88]. Another feature of these systems is the spreading of the electrons along the surfaces of dielectrics, called a surface ionization wave. Surface ionization waves occur because charge accumulates on the dielectric surface. The accumulated charge produces a parallel component of the electric field at the surface, ensuring further propagation of the surface ionization wave [94].

In this dissertation, two DBD systems are modeled. Generally, DBDs have two parallel electrodes, as shown in Figure 1.11. One or both of the electrodes are separated from the plasma by a dielectric barrier. The dielectric protects the electrodes from sputtering induced by the plasma. The gap the plasma is formed in is typically 100 – 500 µm. The following section discusses the applications of the DBDs modeled in this dissertation.

1.4.1 Applications of Pulsed Dielectric Barrier Discharges

The first application of pulsed DBDs is in forming O_3, commonly used to oxidize molecules found in water [52]. O_3 is formed from O_2 in a two-step process:

$$e + O_2 \rightarrow O + O + e \tag{1.7}$$

$$O + O_2 + M \rightarrow O_3 + M. \tag{1.8}$$

The third body M is required in the second reaction to ensure momentum conservation after the collision. To form O_3, the plasma is formed in a feed gas with a high admixture of O_2, often pure O_2 [95,96]. Including N_2 in the feed gas at high admixtures can increase the formation of nitrous oxides like NO, NO_2, NO_3, N_2O, and N_2O_5. When a high admixture of N_2 is present in O_2, O is consumed in the formation of nitrous oxides instead of formation of O_3, and O_3 concentration decreases.

Studies have shown that O_3 production decreases after several hours, called the ozone zero phenomenon [95–101]. Additional work has shown that including N_2 in small admixtures into otherwise pure O_2 can actually increase the O_3 concentration, and the effect persists even when the N_2 flow is turned off [96,98–100]. This increase in O_3 concentration seems counterintuitive, as N_2 should increase nitrous oxides concentrations and therefore decrease O_3 concentration. One hypothesis is that N occupies surface sites that otherwise destroy O_3 [100,102].

The second application of pulsed DBDs is in photoionization detectors (PIDs). PIDs are used in gas chromatography to detect volatile organic compounds in the analyte gas [103–105]. One PID design is a discharge PID, where a plasma is formed without being physically separated from the analyte gas [106–108]. These plasmas are typically formed in noble gases like He and Ar, as excited states of noble gases can emit VUV photons. The VUV photons from the plasma ionize the analyte gas, and the ions are collected by biased collection electrodes. The performance of a discharge PID can be improved by increasing the photon flux to the analyte gas, increasing the ions produced by photoionization.

1.5 LTP Modeling Approaches

This section reviews the current modeling methods for LTPs and discusses the differences between them. These methods can be sorted into three approaches: kinetic approaches, including direct kinetic and statistical methods [40,43,80,109–117], fluid approaches [88,118–126], and global approaches [13,60,82,127–130].

The kinetic approaches do not require assumptions about the energy distribution of each species. Direct-kinetic models directly solve Boltzmann's equation for each species in spatial and velocity dimensions [112]. Statistical models use macroparticles to simulate thousands of real particles. Statistical models often couple the particle-in-cell method for moving particles in response to electric fields, as well as a Monte Carlo approach to perform collisions between the macroparticles [113,114]. To mitigate statistical noise, many macroparticles need to be tracked. While the kinetic approaches do not assume a form of the energy distributions of each species, these approaches are computationally expensive, often limiting the time or number of species that can be resolved. This computational cost continues increasing as more dimensions are modeled. Kinetic methods are often used in modeling Hall thrusters, where the ions cannot be assumed to have a Maxwell-Boltzmann energy distribution. However, the electrons are often modeled as a fluid in Hall thrusters to lower computational cost, leading to a hybrid approach [113,114].

The fluid approaches assume the energy distribution of each species follows a Maxwell-Boltzmann energy distribution. The fluid models solve for species densities at each spatial location instead of relying on macroparticles. In LTPs, the fluid models also solve Poisson's equation for potential, as the electric field is required to correctly compute charged species dynamics [120]. Typically, 2D fluid models are used with either cylindrical or Cartesian symmetry. Since the fluid models assume a Maxwell-Boltzmann energy distribution, the fluid models are particularly useful for modeling systems where this assumption is appropriate. In LTPs, this assumption is typically valid for ions and neutral species, but not for electrons. Therefore, Boltzmann's equation is solved for the electrons only, giving a look-up table of electron-impact rate coefficients for various E/N (electric field/gas number density) [120]. The fluid approaches are less computationally expensive than the kinetic approaches, making them the preferred choice for many applications.

The global approaches assume the plasma can be modeled as a well-stirred reactor. These models solve for species densities as a function of time and provide no spatial information as they are 0D [129]. Some 0D models can become quasi-1D models and provide some spatial information by a plug flow assumption, where the densities in a plug of gas are tracked as the gas flows through the reactor. While the global approaches require the most assumptions, they are the least computationally expensive of the three approaches summarized in this section. Global models typically give results in minutes, instead of days or weeks required for fluid and kinetic approaches. Therefore, global models are preferred for detailed studies of plasma chemistry or when long times need to be modeled.

1.6 Motivation

Plasmas are complex systems, making measurements of the plasmas difficult. While some measurement techniques like optical emission spectroscopy are non-invasive [86,90–92,127,131,132], some measurement techniques require disrupting the plasma [133,134]. Additionally, many plasma phenomena like ionization waves and sheaths occur over small length scales (100s µm) and fast time scales (ns). Making measurements that capture these dynamics can be very challenging.

Modeling LTPs can expand the understanding of how LTPs function. In these validated models, timescales of ps and length scales of µm can be resolved. Therefore, the details of ionization wave propagation, sheaths, and short timescale chemistry can be resolved. The importance of different processes can be examined separately, and steps in the production of different RONS can be identified. With validated models, the design of systems can be tested in the model before being implemented. For example, modeling can inform the locations to place spacecraft components in the plasma plume to avoid sputtering and strategies to produce more reactive species and solvate the reactive species into the liquid.

This dissertation focuses on modeling LTPs, with a focus on modeling interactions between the plasma and multiphase surfaces. Strategies will be identified to improve real-world systems.

1.7 Scope of This Dissertation

The studies in this dissertation focus on modeling the interactions between LTPs and multiphase surfaces, with the results suggesting improvements to these systems. A summary of each chapter is presented in this section.

In Chapter 2, the three models used in this dissertation are described. The erosion model *MEOWS*, developed by the author, models the erosion of a wire in the plume of a Hall thruster due to ion-impact sputtering. *nonPDPSIM* is a 2D plasma dynamics model, solving Poisson's equation on an unstructured mesh. Updates to *nonPDPSIM* were made by this author, as well as numerous post-processing scripts to convert the output of *nonPDPSIM*. The final model described is the 0D model *GlobalKin*, modeling the plasma as a well-stirred reactor.

In Chapter 3, the validation of *MEOWS* is described. The modeled wire profiles are compared to experimental measurements of the wire erosion and are found to agree well. Trends in the erosion experienced at different locations in the Hall thruster plume are identified and explained.

In Chapter 4, *MEOWS* was used to generate median predictions of eroded wire profiles, as well as credible intervals on the eroded wire profiles. The uncertainty is based on the variation of sputtering yield measurements and therefore model parameters of the semi-empirical sputtering yield models. These median wire profiles with uncertainty are compared to experimental measurements and found to agree well. The high uncertainty in the eroded wire profiles is discussed in the context of lifetime estimates of components.

In Chapter 5, the sheath that forms around an embedded dielectric droplet in a He RF glow discharge at atmospheric pressure is examined using the results of *nonPDPSIM*. The dielectric droplet serves as a proxy for a water droplet, while isolating the electrical properties from the chemical properties of the droplet. First, a validation of the model and experiments is shown by comparing the emissivity of the plasma and He metastable states. Following that, variation of electron density, E/N, electron temperature, and charge on the droplet are discussed as they vary over the RF cycle. How these plasma properties vary with droplet properties (permittivity, diameter, and conductivity) and plasma properties (frequency, power) are also presented.

In Chapter 6, the long timescale chemistry of $HCOO^-_{aq}$ in a small water droplet embedded in a He/H_2O RF glow discharge at atmospheric pressure is discussed using the results of *GlobalKin*. The model reproduces experimental measurements of $HCOO^-_{aq}$ remaining after plasma exposure well, and variation of OH, OH_{aq}, and $HCOO^-_{aq}$ concentration is discussed with variation of droplet properties (diameter, initial $HCOO^-_{aq}$ concentration) and plasma properties (gas flow rate, power deposition, gas mixtures, and H_2O percentage in the inlet gas).

In Chapter 7, a DBD used for O_3 production is examined using both *nonPDPSIM* and *GlobalKin*. The ionization wave propagation is discussed using the results of *nonPDPSIM*. In *GlobalKin*, a surface reaction mechanism is proposed and implemented. This surface mechanism can explain the increase in O_3 production with N_2 percentage, as N occupies otherwise empty surface sites used for O_3 destruction.

In Chapter 8, a discharge PID in a DBD configuration used to produce VUV photons from the He plasma is examined using *nonPDPSIM*. The streamer propagation is discussed. Strategies to increase the VUV photon flux to the analyte gas include increasing the capacitance of the surrounding dielectric and changing the electrode geometry.

A summary of the findings of the studies in this dissertation, as well as the implications of these findings, is presented in Chapter 9. Improvements to the models and potential future studies to expand upon the work in this dissertation are also discussed.

1.8 Figures

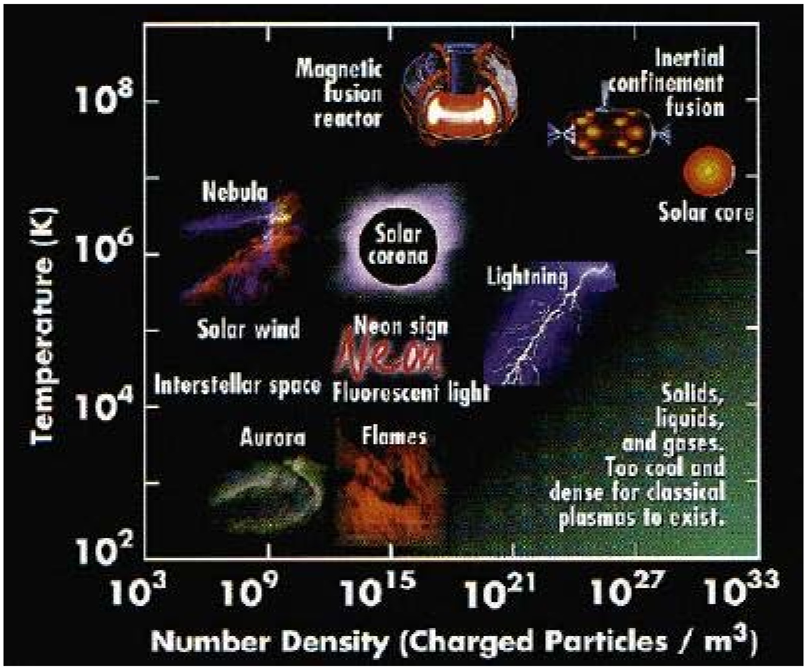

Figure 1.1. Plasma parameter space. Reproduced from University of Rochester [135].

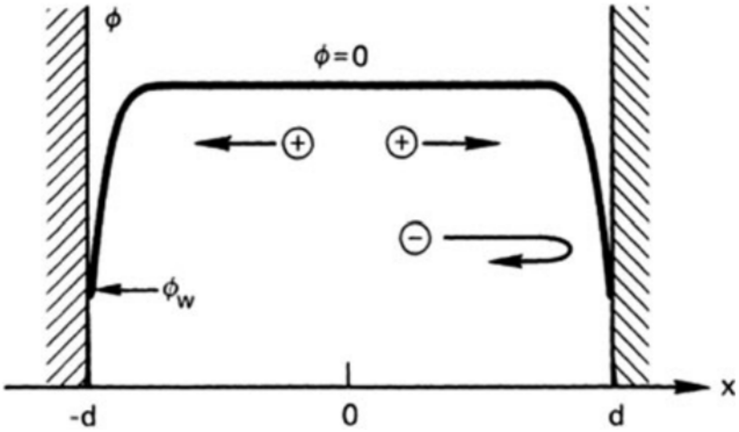

Figure 1.2. Schematic of a plasma sheath. Reproduced from Chen [10].

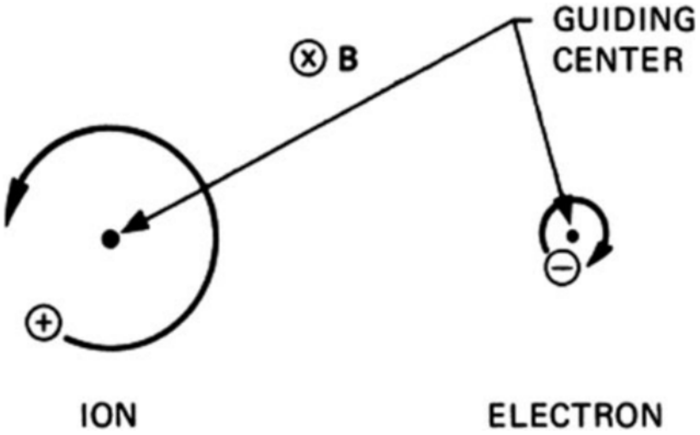

Figure 1.3. Cyclotron motion around the magnetic field B. Reproduced from Chen [10].

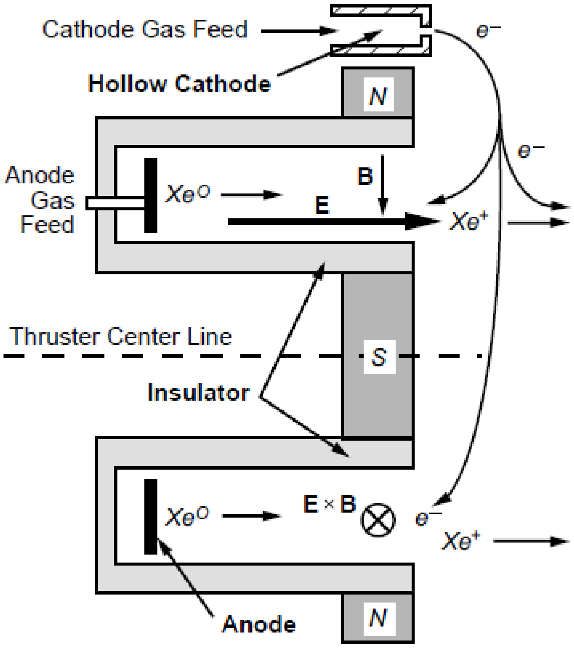

Figure 1.4. Hall thruster diagram. Reproduced from Goebel and Katz [14].

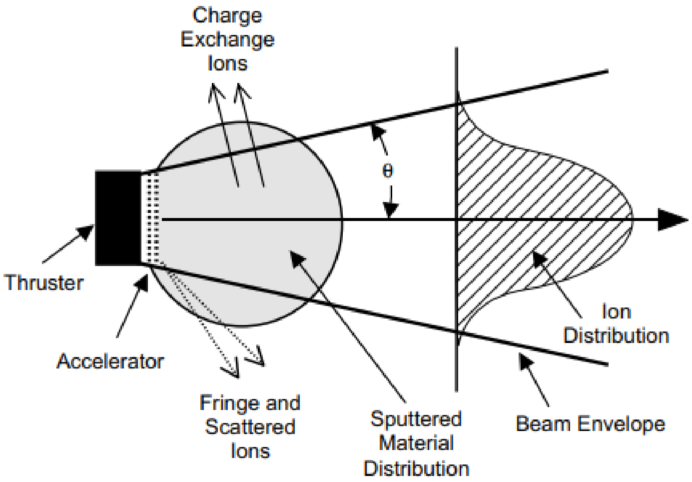

Figure 1.5. Diagram of a thruster plume. Reproduced from Goebel and Katz [14].

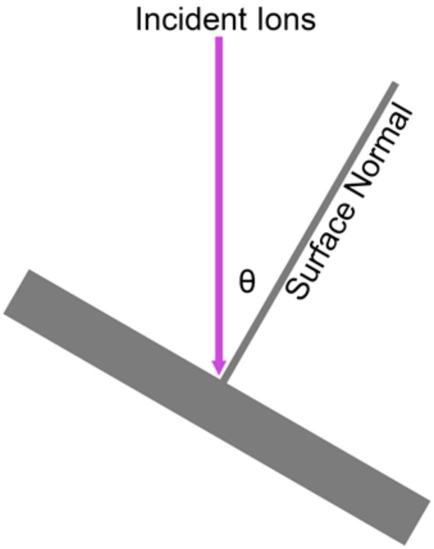

Figure 1.6. Ion-impact sputtering schematic.

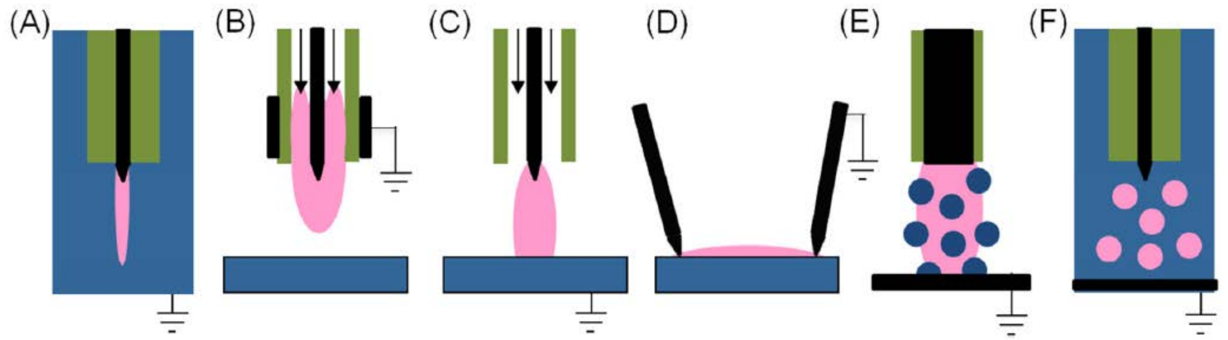

Figure 1.7. Different geometries for forming plasmas near liquids. Pink represents plasma, blue represents liquid, black represents metal electrodes, and green represents other dielectrics. (a) Plasma formation directly in liquid, (b) remote plasma above a liquid, (c) liquid as an electrode, (d) plasma formation on a liquid surface, (e) plasma with interspersed droplets, and (f) plasma in bubbles in liquid. Reproduced from Bruggeman et al. [51].

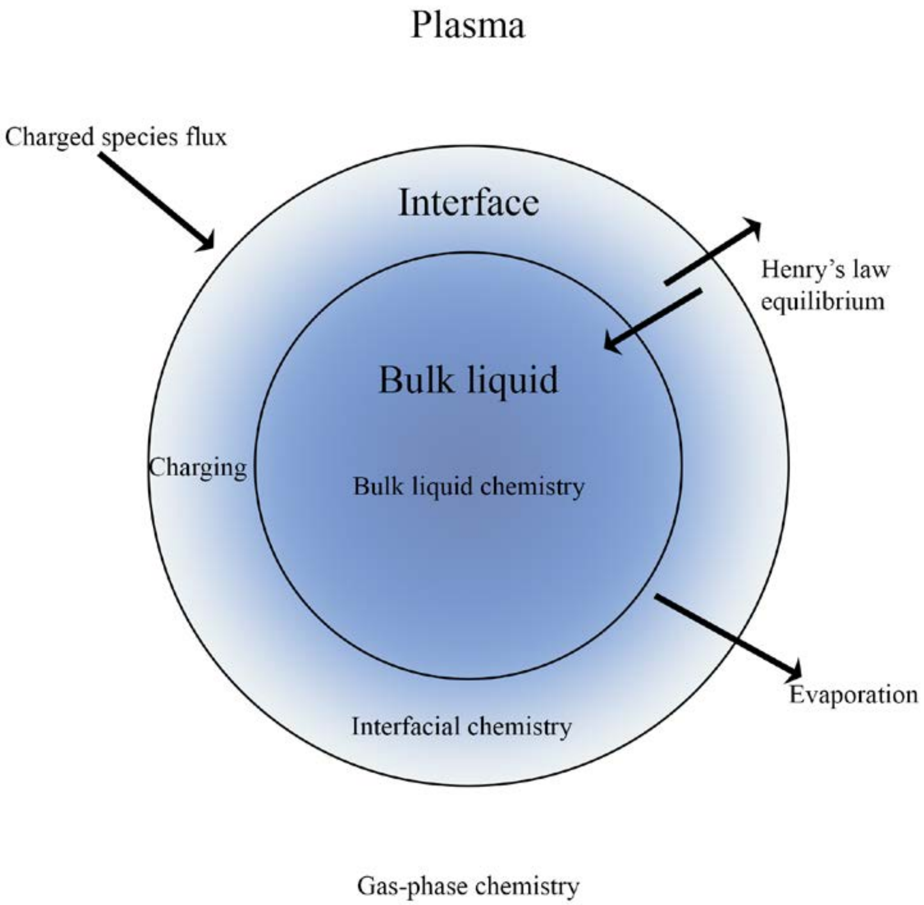

Figure 1.8. Processes at the interface between the plasma and a liquid.

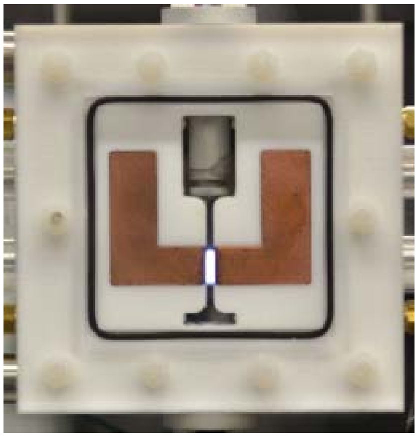

Figure 1.9. RF glow discharge for studying plasma-aerosol interactions. Reproduced from Oinuma et al. [62].

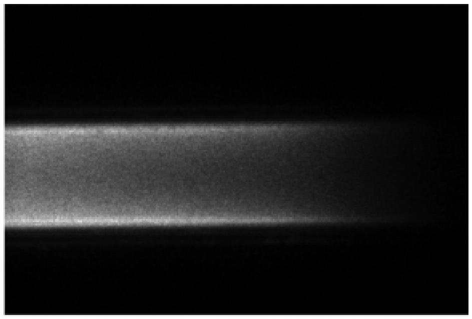

Figure 1.10. Image of a negative ionization wave. Reproduced from Takashima et al. [136].

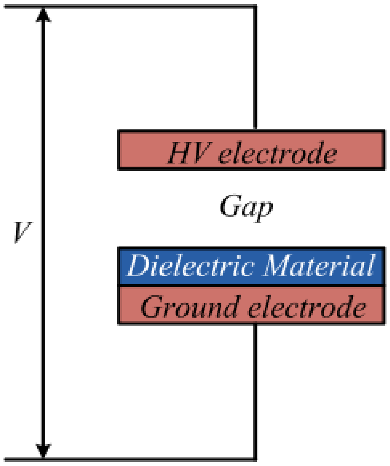

Figure 1.11. Geometry for a dielectric barrier discharge. Reproduced from El-Zein et al. [137].

1.9 References

[1] I. Adamovich, S. D. Baalrud, A. Bogaerts, P. J. Bruggeman, M. Cappelli, V. Colombo, U. Czarnetzki, U. Ebert, J. G. Eden, P. Favia, D. B. Graves, S. Hamaguchi, G. Hieftje, M. Hori, I. D. Kaganovich, U. Kortshagen, M. J. Kushner, N. J. Mason, S. Mazouffre, S. M. Thagard, H. R. Metelmann, A. Mizuno, E. Moreau, A. B. Murphy, B. A. Niemira, G. S. Oehrlein, Z. L. Petrovic, L. C. Pitchford, Y. K. Pu, S. Rauf, O. Sakai, S. Samukawa, S. Starikovskaia, J. Tennyson, K. Terashima, M. M. Turner, M. C. M. Van De Sanden and A. Vardelle, J. Phys. D. Appl. Phys. **50,** 323001 (2017).

[2] J. Polito, M. Denning, R. Stewart, D. Frost and M. J. Kushner, J. Vac. Sci. Technol. A **40,** 043001 (2022).

[3] A. N. Bhoj and M. J. Kushner, J. Phys. D. Appl. Phys. **39,** 1594 (2006).

[4] I. Levchenko, S. Xu, S. Mazouffre, D. Lev, D. Pedrini, D. Goebel, L. Garrigues, F. Taccogna and K. Bazaka, Phys. Plasmas **27,** 020601 (2020).

[5] B. Eliasson and U. Kogelschatz, IEEE Trans. Plasma Sci. **19,** 1063 (1991).

[6] I. Adamovich, S. Agarwal, E. Ahedo, L. L. Alves, S. Baalrud, N. Babaeva, A. Bogaerts, A. Bourdon, P. J. Bruggeman, C. Canal, E. H. Choi, S. Coulombe, Z. Donko, D. B. Graves, S. Hamaguchi, D. Hegemann, M. Hori, H.-H. Kim, G. M. W. Kroesen, M. J. Kushner, A. Laricchiuta, X. Li, T. E. Magin, S. Mededovic Thagard, V. Miller, A. B. Murphy, G. S. Oehrlein, N. Puac, R. M. Sankaran, S. Samukawa, M. Shiratani, M. Simek, N. Tarasenko, K. Terashima, E. Thomas Jr, J. Trieschmann, S. Tsikata, M. M. Turner, I. J. van der Walt, M. C. M. van de Sanden and T. von Woedtke, J. Phys. D. Appl. Phys. **55,** 373001 (2022).

[7] T. Von Woedtke, D. Weltmann, S. Emmert, H. Metelmann, S. Rupf and K.-D. Weltmann, Phys. Plasmas **27,** 070601 (2020).

[8] A. Bogaerts, X. Tu, J. C. Whitehead, G. Centi, L. Lefferts, O. Guaitella, F. Azzolina-jury, H. Kim, A. B. Murphy, W. F. Schneider, T. Nozaki, J. C. Hicks, A. Rousseau, F. Thevenet, A. Khacef and M. Carreon, J. Phys. D. Appl. Phys. **53,** 443001 (2020).

[9] Y. Zheng, L. Wang and P. Bruggeman, J. Vac. Sci. Technol. A **38,** 063005 (2020).

[10] F. F. Chen, *Introduction to Plasma Physics and Controlled Fusion*, Springer (2006).

[11] P. M. Bellan, *Fundamentals of Plasma Physics*, Cambridge University Press (2006).

[12] G. J. M. Hagelaar and L. C. Pitchford, Plasma Sources Sci. Technol. **14,** 722 (2005).

[13] S. Mohades, A. M. Lietz and M. J. Kushner, J. Phys. D. Appl. Phys. **53,** 435206 (2020).

[14] D. M. Goebel and I. Katz, *Fundamentals of Electric Propulsion: Ion and Hall Thrusters*, John Wiley & Sons, Incorporated (2008).

[15] A. Gurciullo, J. Jarrige, P. Lascombes and D. Packan, 36th International Electric Propulsion Conference, IEPC-2019-142 (2019).

[16] S. J. Hall, B. A. Jorns, S. E. Cusson, A. D. Gallimore, H. Kamhawi, P. Y. Peterson, T. W. Haag, J. A. Mackey, M. J. Baird and J. H. Gilland, J. Propuls. Power **38,** 40 (2022).

[17] G. Cardell, A. Ulloa-Severino and M. Gross, 10th Annual International Energy Conversion Engineering Conference, IECEC 2012, AIAA Paper 2012-3898 (2012).

[18] L. L. Su, A. R. Vazsonyi and B. A. Jorns, AIAA Propulsion and Energy Forum 2020, AIAA Paper 2020-3617 (2020).

[19] M. P. Byrne, M. E. Meyer, I. D. Boyd and B. A. Jorns, AIAA Propulsion and Energy 2019 Forum, AIAA Paper 2019-3988 (2019).

[20] I. D. Boyd and M. L. Falk, AIAA 37th Joint Propulsion Conference, AIAA Paper 2001-3353 (2001).

[21] I. D. Boyd and A. Ketsdever, J. Spacecr. Rockets **38,** 380 (2001).

[22] D. Rosenberg and G. K. Wehner, J. Appl. Phys. **33,** 1842 (1962).

[23] R. P. Doerner, D. G. Whyte and D. M. Goebel, J. Appl. Phys. **93,** 5816 (2003).

[24] O. B. Duchemin and J. E. Polk, 35th Joint Propulsion Conference and Exhibit, AIAA Paper 1999-2858 (1999).

[25] K. Kannenberg, V. Khayms, B. Emgushov, L. Werthman and J. E. Pollard, 37th Joint Propulsion Conference and Exhibit, AIAA Paper 2001-3986 (2001).

[26] N. Noushkam, D. Basak, M. Glogowski, M. Crofton, J. Young and B. Plecque, AIAA SPACE 2015 Conference and Exposition, AIAA Paper 2015-4642 (2015).

[27] R. D. Kolasinski, 41st AIAA/ASME/SAE/ASEE Joint Propulsion Conference and Exhibit, AIAA Paper 2005-3526 (2005).

[28] E. Oyarzabal, J. H. Yu, R. P. Doerner, G. R. Tynan and K. Schmid, J. Appl. Phys. **100,** 063301 (2006).

[29] P. C. Zalm, J. Appl. Phys. **54,** 2660 (1983).

[30] K. Ikuse, S. Yoshimura, K. Hine, M. Kiuchi and S. Hamaguchi, J. Phys. D. Appl. Phys. **42,** 135203 (2009).

[31] B. Rubin, Topper J L, C. C. Farnell and A. P. Yalin, Rev. Sci. Instrum. **80,** 103506 (2009).

[32] M. Tartz, T. Heyn, C. Bundesmann, C. Zimmermann and H. Neumann, Eur. Phys. J. D **61,** 587 (2011).

[33] T. Tondu, V. Inguimbert, F. Darnon and J. F. Roussel, 4th International Spacecraft Propulsion Conference, Paper 2004ESASP.55E.105T (2004).

[34] W. Eckstein and R. Preuss, J. Nucl. Mater. **320,** 209 (2003).

[35] Q. Wei, K.-D. Li, J. Lian and L. Wang, J. Phys. D. Appl. Phys. **41,** 172002 (2008).

[36] Y. Yamamura and S. Shindo, Radiat. Eff. **80,** 57 (1984).

[37] J. Bohdansky, Nucl. Instruments Methods Phys. Res. B **2,** 587 (1984).

[38] C. García-Rosales, W. Eckstein and J. Roth, J. Nucl. Mater. **218,** 8 (1995).

[39] D. Y. Oh, D. E. Hastings, C. M. Marrese, J. M. Haas and A. D. Gallimore, J. Propuls. Power **15,** 345 (1999).

[40] A. Tekinalp and D. A. Levin, AIAA Propulsion and Energy Forum and Exposition, 2019, AIAA Paper 2019-3989 (2019).

[41] Y. Inanaga and T. Muranaka, 36th International Electric Propulsion Conference, Paper IEPC-2019-858 (2019).

[42] J. M. Fife, M. R. Gibbons, D. B. VanGilder and D. E. Kirtley, 33rd Plasmadynamics and Lasers Conference, AIAA 2002-2125 (2002).

[43] N. Nuwal, R. Jambunathan and D. A. Levin, IEEE Trans. Plasma Sci. **48,** 4305 (2020).

[44] P. Sarrailh, S. L. G. G. Hess, J. C. Mateo-Velez, T. Gineste and M. Belhaj, AIAA SPACE 2015 Conference and Exposition, AIAA Paper 2015-4640 (2015).

[45] L. M. Bermúdez, K. J. Barnhart, C. A. Agathon-Burton, D. Basak and M. J. Glogowski, 35th International Electric Propulsion Conference, Paper IEPC-2017-238 (2017).

[46] J. M. Fife, W. A. Hargus Jr., D. A. Jaworske, C. Sarmiento, L. Mason, R. Jankovsky, J. S. Snyder, S. Malone, J. Haas and A. Gallimore, 36th AIAA/ASME/SAE/ASEE Joint Propulsion Conference & Exhibit, AIAA Paper 2000-3521 (2000).

[47] T. Randolph, E. Pencil and D. Manzella, AIAA 30th Joint Propulsion Conference, AIAA Paper 1994-2855 (1994).

[48] E. J. Pencil, T. Randolph and D. Manzella, AIAA 32nd Joint Propulsion Conference, AIAA Paper 1996-2709 (1996).

[49] J. A. Young, R. J. Sedwick, S. Dumpala and K. Rajan, 52nd Aerospace Sciences Meeting,

AIAA Paper 2014-1032 (2014).

[50] S. H. Hu, A. Joshi, V. Khayms, B. Emgushov, L. Werthman and V. S. Smentkowski, 37th Joint Propulsion Conference and Exhibit, AIAA Paper 2001-3356 (2001).

[51] P. J. Bruggeman, M. J. Kushner, B. R. Locke, J. G. E. Gardeniers, W. G. Graham, D. B. Graves, R. C. H. M. Hofman-Caris, D. Maric, J. P. Reid, E. Ceriani, D. Fernandez Rivas, J. E. Foster, S. C. Garrick, Y. Gorbanev, S. Hamaguchi, F. Iza, H. Jablonowski, E. Klimova, J. Kolb, F. Krcma, P. Lukes, Z. MacHala, I. Marinov, D. Mariotti, S. Mededovic Thagard, D. Minakata, E. C. Neyts, J. Pawlat, Z. L. Petrovic, R. Pflieger, S. Reuter, D. C. Schram, S. Schröter, M. Shiraiwa, B. Tarabová, P. A. Tsai, J. R. R. Verlet, T. Von Woedtke, K. R. Wilson, K. Yasui and G. Zvereva, Plasma Sources Sci. Technol. **25,** 053002 (2016).

[52] J. E. Foster, Phys. Plasmas **24,** 055501 (2017).

[53] A. Starikovskiy, Y. Yang, Y. I. Cho and A. Fridman, Plasma Sources Sci. Technol. **20,** 024003 (2011).

[54] W. Tian, K. Tachibana and M. J. Kushner, J. Phys. D. Appl. Phys. **47,** 055202 (2014).

[55] S. M. Korobeinikov, A. V. Melekhov and A. S. Besov, High Temp. **40,** 652 (2002).

[56] J. E. Foster, B. Sommers and S. Gucker, Jpn. J. Appl. Phys. **54,** 01AF05 (2015).

[57] P. Rumbach, A. E. Lindsay and D. B. Go, Plasma Sources Sci. Technol. **28,** 105014 (2019).

[58] P. Bruggeman, J. Liu, J. Degroote, M. G. Kong, J. Vierendeels and C. Leys, J. Phys. D. Appl. Phys. **41,** 215201 (2008).

[59] P. Y. Tan, O. H. Chin, R. Anpalagan, Y. T. Lau and H. C. Lee, AIP Conf. Proc. **2319,** 5 (2021).

[60] Y. Gorbanev, C. C. W. Verlackt, S. Tinck, E. Tuenter, K. Foubert, P. Cos and A. Bogaerts, Phys. Chem. Chem. Phys. **20,** 2797 (2018).

[61] G. Nayak, G. Oinuma, Y. Yue, J. S. Sousa and P. Bruggeman, Plasma Sources Sci. Technol. **30,** 115003 (2021).

[62] G. Oinuma, G. Nayak, Y. Du and P. J. Bruggeman, Plasma Sci. Technol. **29,** 095002 (2020).

[63] P. Heirman, W. Van Boxem and A. Bogaerts, Phys. Chem. Chem. Phys. **21,** 12881 (2019).

[64] N. C. Roy, C. Pattyn, A. Remy, N. Maira and F. Reniers, Plasma Process. Polym. **18,** 202000087 (2021).

[65] G. S. Ganesh, A. J., L. P., H. Rao, A. M. Shivapuji, P. L. Girard-Lauriault and L. Rao, J. Appl. Phys. **129,** 093303 (2021).

[66] K. Liu, Z. Yang and S. Liu, IEEE Trans. Plasma Sci. **48,** 969 (2020).

[67] Y. Gao, Z. Liu, S. Wang, B. Pang, D. Xu, D. Liu and M. G. Kong, Plasma Process. Polym. **18,** 2100038 (2021).

[68] J. Jose and L. Philip, J. Environ. Manage. **286,** 112202 (2021).

[69] E. Casado, M. C. Garcia, D. A. Krawczyk, F. J. Romero-Salguero and A. Rodero, Plasma Process. Polym. **17,** 2000030 (2020).

[70] S. Jaiswal and E. M. Aguirre, AIP Adv. **11,** 045311 (2021).

[71] M. C. García, M. Mora, D. Esquivel, J. E. Foster, A. Rodero, C. Jiménez-Sanchidrián and F. J. Romero-Salguero, Chemosphere **180,** 239 (2017).

[72] L. Yang, X. Wang, D. Zhu, Q. Zhang, T. Xi, D. Liu, J. Niu and F. Huang, IEEE Trans. Plasma Sci. **48,** 953 (2020).

[73] R. K. Singh, E. Brown, S. Mededovic Thagard and T. M. Holsen, J. Hazard. Mater. **408,** 124452 (2021).

[74] A. Moldgy, G. Nayak, H. A. Aboubakr, S. M. Goyal and P. J. Bruggeman, J. Phys. D. Appl. Phys. **53,** 434004 (2020).

[75] Z. Liu, S. Wang, B. Pang, H. Zhang, Y. Gao, D. Xu and M. G. Kong, J. Phys. D. Appl. Phys. **54,** 215203 (2021).

[76] K. Sklias, J. S. Sousa and P. M. Girard, Cancers (Basel). **13,** 615 (2021).

[77] C. Jiang, E. B. Sözer, S. Song, N. Lai, P. T. Vernier and S. Guo, Phys. Plasmas **27,** 113513 (2020).

[78] A. Lin, E. Biscop, C. Breen, S. J. Butler, E. Smits and A. Bogaerts, Oxid. Med. Cell. Longev. **2020,** 9750206 (2020).

[79] J. A. Silsby, S. Simon, J. L. Walsh and M. I. Hasan, Plasma Chem. Plasma Process. **41,** 1363 (2021).

[80] N. Akiyama, Y. Nakagawa, S. Uchida and F. Tochikubo, J. Appl. Phys. **129,** 163304 (2021).

[81] A. Stancampiano, T. Gallingani, M. Gherardi, Z. Machala, P. Maguire, V. Colombo, J. Pouvesle and E. Robert, Appl. Sci. **9,** 3861 (2019).

[82] J. Kruszelnicki, A. M. Lietz and M. J. Kushner, J. Phys. D. Appl. Phys. **52,** 355207 (2019).

[83] M. E. Hassan, M. Janda and Z. Machala, Water **13,** 182 (2021).

[84] H. Gao, G. Wang, B. Chen, Y. Zhang, D. Liu, X. Lu, G. He and K. Ostrikov, Plasma Sources Sci. Technol. **30,** 053001 (2021).

[85] T. Xia, A. Kleinheksel, E. M. Lee, Z. Qiao, K. R. Wigginton and H. L. Clack, J. Phys. D. Appl. Phys. **52,** 255201 (2019).

[86] G. Nayak, M. S. Simeni, J. Rosato, N. Sadeghi and P. J. Bruggeman, J. Appl. Phys. **128,** 243302 (2020).

[87] G. Nayak, N. Sadeghi and P. J. Bruggeman, Plasma Sources Sci. Technol. **28,** 125006 (2019).

[88] A. M. Lietz, E V Barnat, J. E. Foster and M. J. Kushner, J. Appl. Phys. **128,** 083301 (2020).

[89] Y. Luo, A. M. Lietz, S. Yatom, M. J. Kushner and P. J. Bruggeman, J. Phys. D. Appl. Phys. **52,** 44003 (2019).

[90] T. Darny, G. Bauville, M. Fleury, S. Pasquiers and J. Santos Sousa, Plasma Sources Sci. Technol. **30,** 105021 (2021).

[91] L. Invernizzi, N. Sadeghi, F. P. Sainct and P. Guillot, Plasma Sources Sci. Technol. **31,** 035002 (2022).

[92] B. Huang, C. Zhang, I. Adamovich, Y. Akishev and T. Shao, Plasma Sources Sci. Technol. **10,** 044001 (2020).

[93] B. Peng, N. Jiang, Z. Liu, X. Yao, J. Li and Y. Wu, J. Appl. Phys. **131,** 113301 (2022).

[94] K. W. Engeling, J. Kruszelnicki, M. J. Kushner and J. E. Foster, Plasma Sources Sci. Technol. **27,** 85002 (2018).

[95] M. Taguchi, Y. Ochiai, R. Kawagoe, Y. Kato, K. Teranishi, S. Suzuki and H. Itoh, EPJ Appl. Phys. **55,** 13805 (2011).

[96] S. Seyrling, E. Reisch and L. Ramoino, Ozone Sci. Eng. **40,** 356 (2018).

[97] K. Murayama, N. Matsumura, M. Taguchi, Y. Katoh, K. Teranishi, S. Suzuki and H. Itoh, EPJ Appl. Phys. **47,** 22814 (2009).

[98] H. Itoh, T. Nagai, M. Taguchi, K. Teranishi and S. Suzuki, Plasma Res. Express **3,** 035001 (2021).

[99] S. Seyrling, M. Müller and L. Ramoino, Eur. Phys. J. D **71,** 136 (2017).

[100] Y. Qin, S. Qian, C. Wang and W. Xia, Plasma Sci. Technol. **20,** 095501 (2018).

[101] M. Taguchi, K. Yamashiro, T. Takano and H. Itoh, Plasma Process. Polym. **4,** 719 (2007).

[102] W. Li, G. V. Gibbs and S. T. Oyama, J. Am. Chem. Soc. **120,** 9041 (1998).

[103] C. F. Poole, J. Chromatogr. A **1421,** 137 (2015).

[104] J. C. Soo, E. G. Lee, R. F. LeBouf, M. L. Kashon, W. Chisholm and M. Harper, J. Occup. Environ. Hyg. **15,** 351 (2018).

[105] D. W. You, Y. S. Seon, Y. Jang, J. Bang, J. S. Oh and K. W. Jung, J. Chromatogr. A **1625,** 461267 (2020).

[106] M. W. Li, A. Ghosh, R. Sharma, H. Zhu and X. Fan, Sensors Actuators B Chem. **332,** 129504 (2021).

[107] S. Narayanan, M. Agah and G. Rice, Proc. IEEE Sensors 51 (2013).

[108] H. Zhu, M. Zhou, J. Lee, R. Nidetz, K. Kurabayashi and X. Fan, Anal. Chem. **88,** 8780 (2016).

[109] D. B. VanGilder, I. D. Boyd and M. Keidar, J. Spacecr. Rockets **37,** 129 (2000).

[110] I. D. Boyd and J. T. Yim, J. Appl. Phys. **95,** 4575 (2004).

[111] K. Hara, "Development of Grid-Based Direct Kinetic Method and Hybrid Kinetic-Continuum Modeling of Hall Thruster Discharge Plasmas," Ph.D. Thesis (University of Michigan Ann Arbor, 2015).

[112] A. L. Raisanen, K. Hara and I. D. Boyd, Phys. Plasmas **26,** 123515 (2019).

[113] M. Choi, "Improving Hall Thruster Plume Simulation by Including Magnetic Field Effects," Ph.D. Thesis (University of Michigan Ann Arbor, 2016).

[114] T. D. Huismann, "Improving Hall Thruster Plume Simulation through Refined Characterization of Near-field Plasma Properties," Ph.D. Thesis (University of Michigan Ann Arbor, 2011).

[115] T. Hemke, D. Eremin, T. Mussenbrock, A. Derzsi, Z. Donkó, K. Dittmann, J. Meichsner and J. Schulze, Plasma Sources Sci. Technol. **22,** 015012 (2013).

[116] L. Bischoff, G. Hübner, I. Korolov, Z. Donkó, P. Hartmann, T. Gans, J. Held, V. Schulz-

Von Der Gathen, Y. Liu, T. Mussenbrock and J. Schulze, Plasma Sources Sci. Technol. **27,** 125009 (2018).

[117] L. Yan, P. Y. Wang, Y. H. Ou and X. L. Kang, J. Appl. Math. **2012,** 327021 (2012).

[118] M. Dünnbier, M. M. Becker, S. Iseni, R. Bansemer, D. Loffhagen, S. Reuter and K. D. Weltmann, Plasma Sources Sci. Technol. **24,** 065018 (2015).

[119] N. Balcon, G. J. M. Hagelaar and J. P. Boeuf, IEEE Trans. Plasma Sci. **36,** 2782 (2008).

[120] S. A. Norberg, E. Johnsen and M. J. Kushner, Plasma Sources Sci. Technol. **24,** 035026 (2015).

[121] D. X. Liu, J. F. Li, A. J. Yang, X. H. Wang, M. Z. Rong and M. G. Kong, High Volt. **1,** 81 (2016).

[122] Y. Liu, I. Korolov, T. Hemke, L. Bischoff, G. Hübner, J. Schulze and T. Mussenbrock, J. Phys. D. Appl. Phys. **54,** 275204 (2021).

[123] D. X. Liu, A. J. Yang, X. H. Wang, M. Z. Rong, F. Iza and M. G. Kong, J. Phys. D. Appl. Phys. **45,** 305205 (2012).

[124] J. Shi and M. G. Kong, IEEE Trans. Plasma Sci. **33,** 624 (2005).

[125] N. Y. Babaeva and G. V. Naidis, J. Appl. Phys. **128,** 203301 (2020).

[126] X. L. Wang, Y. Liu and Y. T. Zhang, IEEE Trans. Plasma Sci. **45,** 3147 (2017).

[127] S. Schröter, A. Wijaikhum, A. R. Gibson, A. West, H. L. Davies, N. Minesi, J. Dedrick, E. Wagenaars, N. De Oliveira, L. Nahon, M. J. Kushner, J. P. Booth, K. Niemi, T. Gans and D. O'Connell, Phys. Chem. Chem. Phys. **20,** 24263 (2018).

[128] S. Schröter, A. R. Gibson, M. J. Kushner, T. Gans and D. O'Connell, Plasma Phys. Control. Fusion **60,** 014035 (2018).

[129] A. M. Lietz and M. J. Kushner, J. Phys. D. Appl. Phys. **49,** 425204 (2016).

[130] D. X. Liu, P. Bruggeman, F. Iza, M. Z. Rong and M. G. Kong, Plasma Sources Sci. Technol. **19,** 025018 (2010).

[131] E. Slikboer, K. Acharya, A. Sobota, E. Garcia-Caurel and O. Guaitella, Sci. Rep. **10,** 2712 (2020).

[132] C. Y. T. Tschang, R. Bergert, S. Mitic and M. Thoma, J. Phys. D. Appl. Phys. **53,** 215202 (2020).

[133] A. K. Srivastava, M. K. Garg, K. S. Ganesh Prasad, V. Kumar, M. B. Chowdhuri and R. Prakash, IEEE Trans. Plasma Sci. **35,** 1135 (2007).

[134] D. L. Brown, M. L. R. Walker, J. Szabo, W. Huang and J. E. Foster, J. Propuls. Power **33,** 582 (2017).

[135] U. of Rochester, https://www.lle.rochester.edu/index.php/education/graduate-studies/h-e-d-physics/

[136] K. Takashima, I. V. Adamovich, Z. Xiong, M. J. Kushner, S. Starikovskaia, U. Czarnetzki and D. Luggenhlscher, Phys. Plasmas **18,** 083505 (2011).

[137] A. El-Zein, M. Talaat, G. El-Aragi and A. El-Amawy, IEEE Trans. Plasma Sci. **48,** 1022 (2020).

Chapter 2 Description of the Models

This chapter highlights three of the computational models used in this dissertation. First, the Model for the Erosion Of Wires due to Sputtering (*MEOWS*) is detailed. This model is used in Chapters 3 and 4. Descriptions of *nonPDPSIM* and *GlobalKin* follow, and those models comprise the remaining chapters in this dissertation. The author's contributions to these models are detailed in Section 2.4.

2.1 Model for the Erosion Of Wires due to Sputtering (*MEOWS*)

This section describes the numerical model for erosion of wires by ion-impact sputtering, *MEOWS*, developed by the author. A diagram of the notional wire layout and erosion of the wire is shown in Figure 2.1, and a flow chart is shown in Figure 2.2. In *MEOWS*, the cross-section of the wire is discretized into small, planar surfaces. *MEOWS* then calculates the erosion of each small, planar surface for small time steps until the desired end time is reached. The erosion depth of a flat surface due to sputtering is calculated by

$$\Delta h = \frac{j_i}{q}\frac{m_m}{\rho_m}\Delta t Y\left(E,\theta\right), \tag{2.1}$$

where Δh is the erosion depth of the surface, j_i is the ion current density, q is the fundamental charge, m_m is the mass of the target material, ρ_m is the density of the target material, Δt is the time step, and Y(E, θ) is the sputtering yield (atoms removed per incident ion) that depends on ion energy E and incident angle θ with respect to the surface normal. The erosion depth scales linearly with j_i and Y(E, θ). The ions are assumed incident on the wire from the -y direction and assumed to be singly-charged. The output of *MEOWS* is a profile of the eroded wire. *MEOWS* was first developed in Python and then transferred to C++ to decrease runtime.

First, the sputtering yield models implemented in *MEOWS* are described in Section 2.1.1. The initialization of *MEOWS* is discussed in Section 2.1.2, and the process at each time step is described in Section 2.1.3.

2.1.1 Sputtering Yield Models

The sputtering yield is a dominant factor in determining the erosion of a surface in the plume of a Hall thruster. Physically, sputtering occurs when an energetic ion transfers energy to an atom in the material and dislodges the atom. The dislodged atom then must travel through the material and reach the gas phase, where it becomes sputtered. The sputtering yield varies for different incident ion as well as target materials. This dissertation considers only the sputtering yield of molybdenum and gold with incident xenon atoms.

The sputtering yield $Y(E, \theta)$ depends on both energy of the incident ion E and angle of incidence with respect to the surface normal θ ($\theta = 0°$ refers to normal incidence). Most works assume the energy and angular dependence can be modeled separately. The total sputtering yield is then

$$Y\left(E,\theta\right)=Y\left(E\right)Y\left(\theta\right), \tag{2.2}$$

where $Y(E)$ is the normal incidence sputtering yield that depends only on E and $Y(\theta)$ is the angular factor that depends only on θ. Occasionally, the assumption of separation of variables is broken (see Section 2.1.1.2).

Many different models for the normal incidence sputtering yield and angular factor exist [1–7]. These are all semi-empirical models, requiring the tuning of model parameters to best fit the measured sputtering yields. Therefore, the models and reported model parameters depend on the quality of measurements. The measurements in the literature do not often report quantities like surface roughness or spread in the ion energy that influence sputtering yield. A Bayesian approach to estimating the model parameters and quantifying the uncertainty in the sputtering yield models is detailed in Chapter 4.

2.1.1.1 Normal Incidence Sputtering Yield Models

Three forms of the normal incidence sputtering yield model are considered in this dissertation. These forms all have a threshold energy E_{th} as one of the model parameters, and sputtering does not occur below the threshold energy.

For the sputtering yield of gold, one of the normal incidence sputtering yield models is taken from Ikuse et al. [6] and is

$$Y(E) = a\left(1-\sqrt{\frac{E_{th}}{E}}\right)^{5/2}\left(1+b\left(\sqrt{\frac{E}{E_{th}}}-1\right)\right), \tag{2.3}$$

where a, b, and E_{th} are model parameters. From Ikuse et al., a = 0.378, b = 5.36, and E_{th} = 28.6 eV.

The Bohdansky formula is one of the normal incidence sputtering yield models for molybdenum. The Bohdansky formula depends on the nuclear stopping cross-section $s_n(\varepsilon)$ based on the Krypton-Carbon potential [7,8], represented as

$$s_n(\varepsilon) = \frac{0.5\log(1+1.2288\varepsilon)}{\varepsilon+0.1728\sqrt{\varepsilon}+0.008\varepsilon^{0.1504}}. \tag{2.4}$$

ε is the reduced energy, calculated by

$$\varepsilon = E\frac{m_m}{m_m+m_i}\frac{0.03255}{Z_i Z_m\sqrt{Z_i^{2/3}+Z_m^{2/3}}}, \tag{2.5}$$

where m_i and Z_i are the atomic mass and atomic number of the incident ion (xenon), m_m and Z_m are the atomic mass and atomic number of the target material, and E is the incident ion energy in eV. The sputtering yield is then

$$Y(E) = Qs_n(\varepsilon)\left(1-\left(\frac{E_{th}}{E}\right)^{2/3}\right)\left(1-\frac{E_{th}}{E}\right)^2 . \tag{2.6}$$

where Q is a model parameter, and E_{th} is the threshold energy, treated as a model parameter. From Tartz et al., Q = 23.1 and E_{th} = 39.3 eV [5].

One of the normal incidence sputtering yield models used is from Eckstein and Preuss [1]. This is based on the revised Bohdansky formula [7] but has been adjusted to better match the sputtering from low-energy ions [1]. The sputtering yield is calculated by

$$Y(E) = Qs_n(\varepsilon)\frac{\left(\frac{E}{E_{th}}-1\right)^{\mu}}{\frac{\lambda}{w}+\left(\frac{E}{E_{th}}-1\right)^{\mu}} \tag{2.7}$$

and used for sputtering of both gold and molybdenum. ε is again the reduced energy, and $s_n(\varepsilon)$ is the nuclear stopping cross-section. w is defined as

$$w = \varepsilon + 0.1728\sqrt{\varepsilon} + 0.008\varepsilon^{0.1504}, \tag{2.8}$$

and the model parameters are Q, λ, μ, and E_{th}, taken from Yim [9]. Q adjusts the magnitude of the sputtering yield based on the incident ion and target material. λ gives an estimate of the energy where the sputtering yield starts decreasing, and μ is the exponent in the interatomic potential.

These normal incidence sputtering yield models are shown in Figure 2.3 for both gold and molybdenum. All of the models are nonlinear, increasing very rapidly in the low-energy regime and increasing less rapidly at higher energies. Molybdenum sputters less than gold, indicating that a gold surface will erode more quickly than a molybdenum surface.

2.1.1.2 Angular Factor Models

Two angular factor models with different behaviors at larger angles of incidence are considered in this dissertation. One is given by

$$Y(\theta)=\left(\frac{1}{\cos\theta}\right)^{f}\exp\left(-f\cos\theta_{opt}\left(\frac{1}{\cos\theta}-1\right)\right) \tag{2.9}$$

and comes from Yamamura and Shindo [2]. The model parameters include f and θ_{opt}, where θ_{opt} is the optimal angle, or angle where the angular factor is maximum. For a gold surface, f = 6.8 and θ_{opt} = 49.0° [10]. Tartz et al. used energy-dependent expressions for f and θ_{opt} for a molybdenum surface, relying on model parameters f_{sig} and p instead. These energy-dependent expressions in the angular factor also means the sputtering yield is not separated into an energy-dependent part and an angular factor as shown in Eq. (2.2). θ_{opt} is expressed as

$$\theta_{opt}=90^{\circ}-286.0\left(\frac{p}{\sqrt{E}}\right)^{0.45}, \tag{2.10}$$

and f_{sig} is expressed as

$$f=f_{sig}\left(1+2.5\frac{\sqrt{\frac{E_{th}}{E}}}{1-\sqrt{\frac{E_{th}}{E}}}\right), \tag{2.11}$$

where E_{th} is the threshold energy given by the normal incidence sputtering yield model. Tartz et al. reports f_{sig} = 2.1 and p = 0.15 [5].

The other angular factor is from Wei et al. [3] and is expressed as

$$Y(\theta)=\frac{\alpha}{A}\cos\theta\exp\left(\frac{a^{2}}{2\alpha^{2}}\left(1-\frac{\alpha^{2}}{A^{2}}\cos^{2}\theta\right)\right), \tag{2.12}$$

where $A^{2}=\alpha^{2}\cos^{2}\theta+\beta^{2}\sin^{2}\theta$ and a, α, and β are model parameters. The longitudinal and transverse straggling ranges are represented by α and β, respectively, and the projected energy range is represented by a. Following Yim [9], this model can be rewritten to cast a/α and β/α as model parameters by

$$Y(\theta) = \frac{1}{\sqrt{1+\left(\frac{\beta}{\alpha}\right)^2 \tan^2\theta}} \exp\left(\frac{1}{2}\left(\frac{a}{\alpha}\right)^2 \left(1 - \frac{1}{1+\left(\frac{\beta}{\alpha}\right)^2 \tan^2\theta}\right)\right). \tag{2.13}$$

Values for a/α and β/α are given by Yim [9].

The angular factor is shown for gold and molybdenum in Figure 2.4 for each model. The maximum in the angular factor does not occur at normal incidence but is at the optimal angle, typically between 30° and 60°. Physically, this maximum occurs not at normal incidence because the sputtered atom is not as deep in the material and can easily reach the gas phase without becoming trapped. At large incident angles nearing 90°, the energy transfer of the gas phase ion to an atom in the material is less and not enough to remove the atom. At large incident angles, the angular factor from Yamamura and Shindo rapidly decreases to zero due to the exponential term. However, the angular factor from Wei et al. smoothly decreases to zero at 90°. As will be shown in Chapters 3 and 4, this results in more peaked structures when the model from Yamamura and Shindo is used.

2.1.2 Initialization

The first step in initializing *MEOWS* is reading the input file, as shown in Figure 2.2. The input file contains information about the geometry of the wire (radius of the wire r_{wire}, depth of coating around the wire, and the materials of both the core and the coating). The total time to model the erosion of the wire for is also specified, as well as the interval to write the profile to the output file. These parameters are constant for all of the cases (eroded wire profiles) specified in the input file, as more than one case can be specified in the input file. Each case then has case-specific parameters, including the number of flat surfaces to discretize the circular cross-section into and the time step to take.

Plume properties, specifically the ion current density j_i and ion energy distribution $f(E_i)$, are also required. The ion current density and ion energy distribution are taken from either high-fidelity plume simulations or experimental measurements at different locations in the plume. Each set of measurements or simulation output contains the ion current density and ion energy distribution at different angles from the thruster centerline, so the angle from the thruster centerline to calculate erosion for is specified. Note that the ion energy distribution is required to be normalized so $\int f(E)dE = 1$.

The final parameters required are the sputtering yield models to use. Different normal incidence sputtering yield models can be specified for the coating and core material, but the same angular incidence sputtering yield model must be used for the coating and core materials. The sputtering yield models are semi-empirical, and model parameters from the literature are hard-coded into the model. To assess the role of uncertainty on the profiles, the model parameters can also be sampled from a distribution generated by Bayesian analysis. The process of generating the distributions is described in detail in Chapter 4. In this mode, the number of sampled model parameter sets are also specified in the input file, and each model parameter set is treated as a separate case.

After reading in the input file, the minimum threshold energy for sputtering between the core and the coating is determined over all the cases, and the ion energy distribution is saved for energies above the minimum threshold energy.

At the beginning of each case, the initially circular cross-section of the wire is discretized into the given number of surfaces. The angle between the points in the discretized cross-section is $2\pi/N$, where N is the specified number of surfaces. The initial array of points that make up the discretized surfaces is enforced to be symmetric. The index of each initial point in the array is also stored and can be used to calculate the maximum erosion on the wire. Endpoints are indexed counterclockwise from $(0, -r_{wire})$.

2.1.3 Time Integration

After initialization, the loop over time begins, one case at a time. A flow chart is shown in Figure 2.2. This section describes the process at each time step. The profile will remain symmetric around the y axis, as the ions are incident from the -y direction.

2.1.3.1 Shadowed Endpoint Identification

As the ions are assumed to be incident from the -y direction, some of the points in the cross-section will not be exposed to the ions, as they are "shadowed" from the incident ions. A notional diagram is shown in Figure 2.5. The endpoints that are shadowed are determined by first finding the local maxima in x with coordinates (x_{max}, y_{max}), or any endpoints that have a larger absolute x value than both their neighbors. For each local maximum with $x_{max} \geq 0$, all endpoints i with $y_i < y_{max}$ and $x_i \geq 0$ are found. Of those endpoints, if $x_i < x_{max}$, it is stored as an endpoint that is shadowed from the incident ions. Similarly, for each local maximum with $x_{max} < 0$, all endpoints i with $y_i < y_{max}$ and $x_i < 0$ are found, and if $|x_i| < |x_{max}|$, it is stored as an endpoint that is shadowed. Initially, all of the endpoints with $y_i < 0$ are shadowed. No erosion occurs for the endpoints that are shadowed.

2.1.3.2 Calculating Angle of Incidence

After determining the endpoints that are shadowed, the angle of incidence of the ions θ is calculated for each surface. The midpoint of the surface is also calculated. To calculate the incident angle, the slope m is first calculated by

$$m = \frac{y_{i+1} - y_i}{x_{i+1} - x_i}, \tag{2.14}$$

and the midpoint (x_m, y_m) is calculated by

$$\left(x_m, y_m\right) = \left(\frac{x_i + x_{i+1}}{2}, \frac{y_i + y_{i+1}}{2}\right), \tag{2.15}$$

where (x_i, y_i) and (x_{i+1}, y_{i+1}) are the coordinates of the two endpoints of the surface. With the midpoint and the slope, a point along the tangent line (x_t, y_t) is necessary to complete the right triangle and determine the incident angle of the ions relative to the surface normal. The y coordinate y_t is assigned to $2r_{wire}$ if $x_i - x_{i+1} \geq 0$ and $-r_{wire}$ otherwise. The x coordinate x_t is then calculated by

$$x_t = m\left(y_m - y_t\right) + x_m. \tag{2.16}$$

The incident angle is then calculated by

$$\begin{aligned} \theta &= \arctan\left(\frac{\left|x_t - x_m\right|}{\left|y_t - y_m\right|}\right) \text{ if } x_i - x_{i+1} \leq 0 \\ \theta &= \arctan\left(-\frac{\left|x_t - x_m\right|}{\left|y_t - y_m\right|}\right) \text{ if } x_i - x_{i+1} > 0. \end{aligned} \tag{2.17}$$

If the slope is infinite ($x_i = x_{i+1}$), the incident angle is set to -90°, and the slope is set to either -10^6 or 10^6 depending on the sign of x_i and $y_{i+1} - y_i$.

2.1.3.3 Peak Identification

After determining the incident angle of the ions on each surface, each endpoint is examined to see if it forms a peak. Peaks form when large amounts of erosion have occurred. Peaks are determined by going through the endpoints and looking at their neighbors. An example of a peak is shown in Figure 2.6.

Take two endpoints, i and i+1. If $x_i > 0$, then x_i is further from the y axis than x_{i+1} and should have a smaller y coordinate if a peak has not formed. Therefore, if $y_i > y_{i+1}$, a peak has formed. Conversely, if $x_i \leq 0$, then x_{i+1} is further away from the y axis, and if $y_{i+1} > y_i$, a peak has formed. A stencil stores whether each surface forms a peak, and peaks are checked as described in Section 2.1.3.6 after calculating the erosion in the time step.

2.1.3.4 Calculating the Erosion Depth

With the shadowed endpoints and peaks identified, and the angle of incidence calculated, the sputtering yield and erosion depth of each surface can be calculated. This section describes the process for one surface.

First, the distance between the midpoint and the center of the circle is calculated, determining the material of the surface. Then, the ion energy distribution is iterated through. First, after determining the appropriate material, the normal incidence sputtering yield is calculated using the models described in Section 2.1.1. The sputtering yield is zero if the energy is below the threshold energy E_{th}. Then, parameters for the angular incidence sputtering yield model are set, as the model from Yamamura and Shindo can have model parameters that depend on energy. The appropriate mass m_m and density ρ_m based on the material are also set, as these properties are required in Eq. (2.1) to calculate the erosion depth. Then, the sputtering yield at the given energy $Y(E_i, \theta)$ is calculated. The sputtering yield is only calculated if the angle of incidence is greater than 0. This sputtering yield is added to the total sputtering yield, weighted by the ion energy distribution f(E_i), by

$$Y(E,\theta)=\sum_i Y(E_i,\theta)\, f(E_i). \tag{2.18}$$

Using the total sputtering yield Y(E, θ), the erosion depth Δh is calculated by Eq. (2.1).

2.1.3.5 Eroding the Profile

After Δh has been calculated for all surfaces, the endpoints of the surfaces are moved. The movement is only performed if the endpoints are not shadowed as described in Section 2.1.3.1. A diagram of the movement is shown in Figure 2.7.

For each endpoint i, the erosion of each adjacent surface (i and i-1) is considered. First, a point on the tangent line for each surface is calculated. The y coordinate y_t is set to 0 in both cases, and the x coordinates $x_{t,i-1}$ and $x_{t,i}$ are calculated by

$$\begin{aligned} x_{t,i-1} &= x_i + m_{i-1} y_i \\ x_{t,i} &= x_i + m_i y_i . \end{aligned} \tag{2.19}$$

The distance between the tangent points (d_{i-1} and d_i) and (x_i ,y_i) are determined by

$$\begin{aligned} d_{i-1} &= \sqrt{\left(x_i - x_{t,i-1}\right)^2 + y_i^2} \\ d_i &= \sqrt{\left(x_i - x_{t,i}\right)^2 + y_i^2} . \end{aligned} \tag{2.20}$$

The x and y coordinates the endpoint would move to based on the erosion of surfaces i and i-1 is then calculated (($x_{e,i}$, $y_{e,i}$) and ($x_{e,i-1}$, $y_{e,i-1}$), respectively). For $x_i \geq 0$, these values are

$$\begin{aligned} x_{e,i-1} &= x_{t,i-1} - c_{i-1}\left(d_{i-1} - \Delta h_{i-1} \sin\theta_{i-1}\right) \\ y_{e,i-1} &= d_{i-1} - \Delta h_{i-1} \cos\theta_{i-1} \\ x_{e,i} &= x_{t,i} - c_i\left(d_i - \Delta h_i \sin\theta_i\right) \\ y_{e,i} &= d_{i-1} - \Delta h_i \cos\theta_i , \end{aligned} \tag{2.21}$$

Where Δh_{i-1} and θ_{i-1} are the erosion depth and angle of incidence of surface i-1 and Δh_i and θ_i are the erosion depth and angle of incidence of surface i. The constants c_{i-1} and c_i are either +1 or -1, depending on the slope m of the surface. If $m_i \geq 0$, $c_i = 1$, and if $m_i < 0$, $c_i = -1$. If θ is less than 0 for either surface, the respective $x_{e,i-1}$ or $x_{e,i}$ is set to x_i. For $x_i < 0$, $x_{t,i-1}$, $x_{t,i}$, d_{i-1}, d_i, c_{i-1}, and c_i are calculated in the same manner as for $x_i \geq 0$. However, $x_{e,i-1}$, $y_{e,i-1}$, $x_{e,i}$, and $y_{e,i}$ differ and are instead calculated as

$$\begin{aligned}
x_{e,i-1} &= x_{t,i-1} + c_{i-1}\left(d_{i-1} + \Delta h_{i-1}\sin\theta_{i-1}\right) \\
y_{e,i-1} &= -\left(d_{i-1} + \Delta h_{i-1}\cos\theta_{i-1}\right) \\
x_{e,i} &= x_{t,i} + c_i\left(d_i + \Delta h_i\sin\theta_i\right) \\
y_{e,i} &= -\left(d_i + \Delta h_i\cos\theta_i\right).
\end{aligned} \tag{2.22}$$

The new endpoint coordinates ($x_{i,n}$, $y_{i.n}$) are then an average of where the endpoint would move to based on each adjacent surface as

$$\begin{aligned}
x_{n,i} &= \frac{1}{2}\left(x_{e,i-1} + x_{e,i}\right) \\
y_{n,i} &= \frac{1}{2}\left(y_{e,i-1} + y_{e,i}\right).
\end{aligned} \tag{2.23}$$

2.1.3.6 Correcting Erosion of Peaks and Removing Unphysical Loops

After all the endpoints have been moved, the profile is checked to ensure it remains physical. First, the erosion of peaks is checked to ensure over-erosion did not occur. If it did, the erosion must be corrected, as shown notionally in Figure 2.8.

To correct the erosion, both the old coordinates and new coordinates of endpoints must be used. Correcting the erosion begins by iterating through the previously identified peaks (Section 2.1.3.3). If the adjacent endpoint further from the y-axis is also part of a peak, this endpoint is ignored. Additionally, (0, $-r_{wire}$) is ignored. This section will describe the process for $x_i > 0$, as a mirror image process occurs for $x_i < 0$.

First, it is determined if the endpoint needs to be reset. If surface i is previously determined to be a surface forming a peak, its endpoint i is the peaked endpoint. Resetting needs to occur if $x_i > x_{i-1,old}$, where $x_{i-1,old}$ is the coordinate of the endpoint i-1 before erosion occurred in this time step. The new slope of surface i m_i is calculated, where $m_i=10^6$ if m_i is infinite. Using the previous slope of surface i-1 ($m_{i-1,old}$), the new coordinates for endpoint i are calculated by the intersection between the old surface i-1 and new surface i. These coordinates are

$$\begin{aligned} x_i &= \frac{y_{i+1} + m_{i-1,old}x_{i-1,old} - y_{i-1,old} - m_i x_{i+1}}{m_{i-1,old} - m_i} \\ y_i &= y_{i-1,old} + m_{i-1,old}\left(x_i - x_{i-1,old}\right). \end{aligned} \tag{2.24}$$

After resetting the endpoint coordinates of peaks, unphysical loops are checked for and removed. These loops form when large amounts of erosion have occurred. A schematic for their removal is shown in Figure 2.9.

By iterating through all surfaces i, the intersection of surface i and any other surface j from i+2 to the end are checked. Adjacent surfaces are not checked for intersection, as they intersect at their shared endpoint. The algorithm for checking for loops for positive x coordinates is described here, and negative x follows a similar algorithm.

The x coordinate of the intersection point $x_{intersect}$ of surfaces i and j is computed by the coordinates of their endpoints i and j by

$$x_{intersect} = \frac{y_j - y_i - m_j x_j + m_i x_i}{m_i - m_j}. \tag{2.25}$$

Note that if both slopes are equal, the surfaces do not intersect. If $x_i < x_{intersect} < x_{i+1}$ and $x_j < x_{intersect} < x_{j+1}$, the surfaces intersect and the endpoints between i and j need to be removed as a loop has formed. The endpoints are added to a list to be removed after going through all the surfaces. The coordinates of endpoint i+1 are reset to the intersection of surfaces i and j with coordinates ($x_{intersect}$, $y_{intersect}$), and $y_{intersect}$ is calculated by

$$y_{intersect} = y_i + m_i \left(x_{intersect} - x_i \right). \tag{2.26}$$

If a loop forms on the y axis, $x_{intersect}$ is set identically to zero.

Another check is performed to ensure no endpoints eroded outside of the pre-erosion wire profile. If the distance between an endpoint and (0,0) is larger than $r_{wire} + 10^{-15}$, the endpoint added to the list to be removed.

Then, the endpoints to be removed by distance or unphysical loops are removed, and a new array of x and y coordinates is formed. If one or zero endpoints remain, or if the endpoint on the y axis has a distance larger than $r_{wire} + 10^{-15}$ from (0,0), the entire wire has been eroded, and this case is completed.

A final check is performed to ensure neighboring endpoints do not have the same coordinates. If two endpoints do, one of them is removed from the simulation.

2.1.3.7 Completing the Time Step

At every user-specified output time, the eroded wire profile is written to a file. Additionally, the maximum erosion on each profile can be calculated and written to a file. The maximum erosion is calculated by determining the maximum distance between the endpoint and the pre-erosion position of the endpoint, using an array storing the index the endpoint started at that is updated when endpoints are deleted.

If no erosion occurred in the time step ($\Delta h_i = 0$ for all surfaces i) or all endpoints are deleted, the case is completed, regardless if the end time was reached.

2.2 *nonPDPSIM*

nonPDPSIM is a 2D computational plasma model that solves for plasma discharges over time on an unstructured mesh. *nonPDPSIM* leverages time-slicing techniques to model processes that happen on vastly different timescales (ps for electron motion, μs for fluid flow). *nonPDPSIM* is also described in detail in Norberg et al. [11].

A flow chart of *nonPDPSIM* as used in this dissertation is shown in Figure 2.10. The inputs to *nonPDPSIM* include a numerical mesh, a namelist, and a reaction mechanism. The mesh defines the geometry of the system, as well as the nodes. The namelist specifies which modules of *nonPDPSIM* to use, as well as properties like time steps and error criteria. The reaction mechanism file first lists all the species included and properties of those species like molecular weights, charge, Lennard-Jones coefficients, enthalpies of formation, and interactions at the walls. Following the species, the reaction mechanism file lists the reactions between these species. These reactions are often specified in Arrhenius form. For those reactions that do not match Arrhenius form well (i.e., electron-impact reactions), a reference to an internal database of cross-sections is included. A stationary solution of Boltzmann's equation provides the electron-impact rate coefficients at specified E/N (electric field/gas number density) from the cross-sections.

The bulk of the computational load in *nonPDPSIM* is in solving the plasma discharge equations. Voltages are applied over time to metals. These voltages can either be directly specified as a function of time or as a sinusoidal waveform with specified magnitude and frequency. First, the electron temperature T_e is updated using an electron temperature equation having heating sources from the interpolated electric field. Following the electron temperature update, a Newton-Raphson method is used to solve for the potential, charged species, and charge accumulated in or on materials. Neutral species are solved using their continuity equations. These three processes all occur at the plasma time step, which is automatically chosen based on the ideal number of Newton-Raphson iterations, further limited by dielectric relaxation time and Courant considerations.

Time-slicing allows other modules to be used at different time steps than the plasma time step. These modules include fluid flow, the surface kinetics module, and the neutral plasma option [12,13]. The modules used in this dissertation include the gas temperature module, electron Monte Carlo simulation (eMCS), and the capacitively-coupled power (CCP) module.

In this section, each part of *nonPDPSIM* used in this dissertation is described. The geometry and mesh are discussed in Section 2.2.1. Following that, the calculation of the electron-impact rate coefficients from Boltzmann's equation and T_e are discussed in Sections 2.2.2 and 2.2.3, respectively. The Newton-Raphson method for determining the potential and charged species densities is detailed in Section 2.2.4, and sources of ions due to photoionization are detailed in Section 2.2.5. The neutral species transport is examined in Section 2.2.6. The time-slicing modules are then discussed in Sections 2.2.7, 2.2.8, and 2.2.9. Finally, post-processing scripts developed by the author are discussed in Section 2.2.10.

2.2.1 Geometry and Mesh

The unstructured mesh that is required as input to *nonPDPSIM* is made using an external mesh generator. In this dissertation, the commercial software Pointwise was used to generate the meshes. Updates to *nonPDPSIM* were made by the author to include the ability to read in meshes generated by the open source mesh generator Gmsh. A new subroutine was added to *nonPDPSIM* to allow for correct reading of the files output by Gmsh, and a tutorial demonstrating how to use Gmsh was developed. While Gmsh was not used for meshes in this dissertation, adding support allows others to generate meshes without requiring a license for Pointwise.

An example of a geometry used in *nonPDPSIM* is shown in Figure 2.11. This geometry is a double dielectric barrier discharge and will be used in Chapter 8 of this dissertation. Each node in the mesh is associated with a different material. If the node is on the boundary between two materials, the node belongs first to the metal, then to the highest permittivity dielectric or material with the higher conductivity, and lastly to the plasma. Properties of each material are specified in the namelist file, including relative permittivity, conductivity, and secondary electron and photoelectron emission coefficients. The plasma itself can be divided into different zones. Specifying different zones allows for different initial gas compositions or for liquids to be included.

In this dissertation, the geometries are all Cartesian geometries, though there is the option to use cylindrically symmetric geometries in *nonPDPSIM*. A symmetric boundary condition on the left boundary can be employed in Cartesian coordinates. The author worked on adding the ability to have symmetric boundary conditions on the top, bottom, and right boundaries in addition to the left boundary.

Triangular elements in the mesh that are far from equilateral can cause numerical hotspots to occur. It is also necessary for the first few rows of nodes in the plasma to be equidistant from whatever material they are in contact with. If they are not equidistant, large gradients in electric fields can appear between the nodes and lead to numerical hotspots.

After the mesh has been imported to *nonPDPSIM*, the cells around the nodes are formed using the intersection of perpendicular bisectors of the chords between cells. Discretization is accomplished using a finite volume method. In Cartesian systems, the volume is determined by multiplying by the depth of the mesh that is specified in the namelist.

2.2.2 Boltzmann Table for Electron-Impact Rates

Since the electron energy distribution in low-temperature plasmas is not well represented by a Maxwell-Boltzmann distribution as discussed in Chapter 1, obtaining the rate coefficients for electron-impact reactions is not straightforward. In *nonPDPSIM*, the electron-impact rate coefficients are calculated from electron velocity/energy distributions obtained using Boltzmann's equation, which is

$$\frac{\partial f}{\partial t} + \vec{v} \cdot \nabla_{\vec{r}} f + \frac{1}{m} \sum_i \overline{F_i} \cdot \nabla_{\vec{v}} f = \left(\frac{\partial f}{\partial t} \right)_{collisions}, \tag{2.27}$$

where $f\left(\vec{r}, \vec{v}, t\right)$ is the electron velocity distribution, $\vec{v}$ is the velocity, $\vec{r}$ is the spatial vector, m is the mass of the electron, and $\overrightarrow{F}$ is the force on the electrons, typically due to electric fields. The right-hand side of Boltzmann's equation is the collision term. The collision term is based on the cross-sections for the electron-impact reactions included. The cross-sections for electron-impact reactions are stored in a database internal to *nonPDPSIM*. To solve for $f\left(\vec{v}\right)$ the two-term spherical harmonic approximation for $f\left(\vec{v}\right)$ is used. The two-term spherical harmonic approximation is

$$f\left(\vec{v}\right) = f_0\left(\left|\vec{v}\right|\right) + f_1\left(\left|\vec{v}\right|\right)\cos\theta, \tag{2.28}$$

where the first term $f_0\left(\left|\vec{v}\right|\right)$ is the isotropic distribution and the second term is the anisotropic distribution along the direction of the applied electric field. Values of E/N are specified by the user, and the electron temperature T_e is solved for each bin of E/N using the spherical harmonic expansion. T_e can then be used to calculate the electron-impact rate coefficients, resulting in a lookup table of rate coefficients for various E/N. The lookup table can be updated throughout the simulation to reflect changes in gas composition.

2.2.3 Electron Temperature

A successive over-relaxation (SOR) method is used to update the electron energy equation for T_e. The electron energy equation is

$$\frac{\partial}{\partial t}\left(\frac{3}{2}n_e k_B T_e\right) = \overline{J}_e \cdot \overline{E} - \sum_i \Delta\varepsilon_i R_i - \nabla \cdot \left(\frac{5}{2}\overline{\Gamma}_e k_B T_e - \kappa_e\left(T_e\right)\cdot \nabla T_e\right), \tag{2.29}$$

where subscript e refers to electrons, n_e is the electron density, and k_B is Boltzmann's constant. The first term on the right-hand side is the Joule heating of the electrons, with the electron current J_e and electric field E. J_e is calculated as σ E, where σ is the conductivity. The second term on the right-hand side refers to energy gained or lost in reaction i $\Delta\varepsilon_i$ with rate R_i. This term includes heating from processes like Penning ionization. R_i is calculated by

$$R_i = k_i\left(T_e\right)\prod_j n_j^{a_{ij}^{(L)}}, \tag{2.30}$$

where k_i is the rate coefficient that depends on T_e, n_j is the density of reactant j, and $a_{ij}^{(L)}$ is the number of times species j appears on the left-hand side of the reaction. The rate coefficient for electrons is typically calculated from the cross-section for the collisions, using the Boltzmann table as described in Section 2.2.2. The third term in the electron energy equation refers to loss due to electron flux Γ_e and electron thermal conductivity κ_e.

2.2.4 Newton-Raphson Iteration

Poisson's equation, the charged species continuity equations, and the charge density in materials are coupled; each of them depend on the potential, charged species density, and charge density accumulated in materials. These three equations are solved together using a Newton-Raphson method for the Jacobian matrix. Typically, this is the most computationally expensive part of *nonPDPSIM*.

Poisson's equation for the potential Φ is

$$\nabla \cdot \left(\varepsilon \nabla \Phi\right) = -\left(\sum_j q_j n_j + \rho_s\right), \tag{2.31}$$

where ε is the permittivity of the material, q_j is the charge of species j with density n_j, and ρ_s is the charge accumulated on or within material s. The continuity equation for charged species densities n_j is

$$\frac{\partial n_j}{\partial t} = -\nabla \cdot \overline{\Gamma_j} + S_j + \left[\sum_j -\nabla \cdot \overline{\Gamma_j}\gamma_j + \sum_p -\nabla \cdot \overline{\Gamma_p}\gamma_p\right]_b, \tag{2.32}$$

where Γ_j is the flux formulated by the Scharfetter and Grummel method [14]. The second term S_j is the source of species j due to reactions, including photoionization (discussed further in Section 2.2.5) and from the electron Monte Carlo simulation (discussed further in Section 2.2.8). The third term in brackets only applies when the charged species is electrons and when the node in question neighbors a material that is not plasma. The first term in the brackets refers to secondary electron emission with coefficient γ_j, and the second term in the brackets refers photoelectron emission with coefficient γ_p and photon flux Γ_p. The final equation for the material charge density is

$$\frac{\partial \rho_s}{\partial t} = \nabla \cdot \left(\sigma_s \Phi\right) + \left[\sum_j q_j \left(-\nabla \cdot \overline{\Gamma_j}\left(1+\gamma_j\right)\right) + \sum_p e\Gamma_p \gamma_p\right]_b \tag{2.33}$$

where σ_s is the conductivity of material s and e is the electron charge, and . The second term in brackets applies only at the boundary between the plasma and material. The first term in the brackets represents the loss of charge due to secondary electron emission, and the second term represents the loss of charge due to photoelectron emission. Secondary and photoelectron emission coefficients are specified in the namelist and do not vary with ion energy. This assumption is appropriate, as the ion temperature is similar to the neutral gas temperature in atmospheric pressure LTPs.

Poisson's equation, the charged species continuity equations, and the equation for charge density in materials are solved using an implicit Newton-Raphson method. The Jacobian matrix A_{jk} is constructed for all of the variables discussed in this section at all of the nodes. The elements of the Jacobian matrix are $\frac{\partial N_{ji}}{\partial M_{km}}$, where indices i and m refer to different nodes and N_j and M_k refer to different variables expressed in finite volume formulation. Since nodes that are not neighbors have a Jacobian element of zero, the matrix is sparse. The sparse matrix is solved implicitly using the SPARSKIT solver developed by Saad [15]. Two preconditioners can be used: generalized minimum residual method with incomplete lower-upper threshold (ILUT) and biconjugate gradient (BiCG) with ILUT [15]. In many cases, the GMRES/ILUT preconditioner performs the best; however, in geometries with materials that have high relative permittivities ε_r, the BiCG/ILUT preconditioner results in a much faster runtime.

Analytical expressions for the Jacobian elements A_{jk} at each node are calculated by

$$A_{jk} = \frac{1}{\Delta t}\left(\delta_{jk} - \frac{\partial N_j}{\partial M_k}\right), \tag{2.34}$$

where Δt is the time step and δ_{jk} is the Kronecker delta function ($\delta_{jk} = 1$ if $j = k$, $\delta_{jk} = 0$ otherwise). One example of the analytical expression for the density of species s at node i is

$$\frac{\partial n_{si}}{\partial n_{si}} = \beta \sum_j \frac{\alpha\left(D_{si} + D_{sj}\right)}{1 - \exp\left(\alpha \Delta x_{ij}\right)} \frac{A_{ij}}{V_i} \Delta t, \tag{2.35}$$

where β is the implicitness factor, α relates to the Scharfetter and Gummel method of calculating flux, j refers to the neighbors of node i. D_{si} and D_{sj} are diffusion coefficients (discussed further in Section 2.2.6). Δx_{ij} is the distance between nodes i and j, A_{ij} is the face area between nodes i and j, V_i is the volume of the cell around node i, and Δt is the time step. Further description can be found in Lietz [13]. Once the residual is below the user-specified threshold (typically around 10^{-6}), the iterations of the Newton-Raphson method are completed for the plasma time step.

Plasma time steps can be automatically chosen based on the number of iterations of the Newton-Raphson method. The ideal number of iterations is specified by the user. The time step is increased if the iterations were lower than the ideal number of iterations, and the time step is decreased if the iterations were higher than the ideal number.

2.2.5 Photoionization

One source of charged species is due to photoionization of the species. In *nonPDPSIM*, emission from species i photoionizes species l. The emitted radiation is calculated using a Green's function approach. The Green's function for emission from species i is

$$G_i\left(\overline{r_j},\overline{r_k}\right)=\frac{1}{4\pi\left|\overline{r_j}-\overline{r_k}\right|^2}\exp\left(-\frac{\left|\overline{r_j}-\overline{r_k}\right|}{\lambda_i}\right), \tag{2.36}$$

where r_j and r_k are the positions of two nodes and λ_i is the mean free path of photon species i, determined by the absorption cross-sections for the gas through with the photon passes. The Green's function is initialized at the beginning of the simulation. The source term for photoionization of species l is then

$$S_{photo,l}\left(\overline{r_k}\right)=N_i\left(\overline{r_k}\right)\sum_i A_i\int\sigma_{il}N_i\left(\overline{r_j}\right)G_i\left(\overline{r_j},\overline{r_k}\right)d^3r_j, \tag{2.37}$$

where A_i is the Einstein coefficient of species i and σ_{il} is the absorption cross-section of species l from photon i. Both A_i and σ_{il} are specified in the reaction mechanism.

2.2.6 Neutral Species

After the potential, charged species densities, and charge in materials are updated, the neutral species are updated. The neutral species, unlike the charged species, do not depend on the electric field for transport. A neutral species is updated using its continuity equation, which is

$$\frac{\partial n_j}{\partial t} = -\nabla \cdot \left(\vec{v} n_j - D_j \nabla n_j \right) + S_{vj} + \left[S_{sj} \right]_b, \tag{2.38}$$

where the first term on the right-hand side is due to advective velocity v and diffusion with diffusion coefficient D_j. While *nonPDPSIM* can solve the Navier-Stokes equations for the advective velocity in the fluid module, the fluid module was not used in this dissertation, and the advective velocity is assumed to be zero. The second term on the right-hand side is the source of species j S_{vj} due to reactions in the volume, and the third term is the source at the boundaries between the plasma and the surface S_{sj}. The source at the boundaries is based on the sticking and giving coefficients and species specified in the reaction mechanism. The continuity equations are solved implicitly using a SOR method for each species. Explicit options using first, second, or third order Runge-Kutta methods are also available [12].

The diffusion coefficients for neutral species are calculated by

$$D_{ij} = 0.001858 \sqrt{\frac{m_i + m_j}{m_i m_j}} \frac{T_g^{3/2}}{P \sigma_{ij} \Omega}, \tag{2.39}$$

where D_{ij} is the diffusion coefficient of species i due to species j, m_i and m_j are the masses of the species i and j, T_g is the gas temperature, P is the gas pressure, and Ω is the collision integral [16]. σ_{ij} is the average of the Lennard-Jones radii of the two species. Fluxes of all species, including photons, to the surfaces can be recorded.

2.2.7 Gas Temperature Module

One of the time-slicing modules available for *nonPDPSIM* is the gas temperature module. The gas temperature module calculates T_g assuming fluid flow is not included. If fluid flow is included (the Navier-Stokes equations are solved), T_g is instead calculated in the fluid module. The gas temperature module is called less frequently than the plasma timestep, and the gas temperature module can be integrated for longer than the time between calls to the module.

The energy equation for T_g is solved using a SOR method. The energy equation is

$$\frac{\partial}{\partial t}\left(N_g c_v T_g\right) = \sum_j \overline{J_j} \cdot \overline{E} - \sum_k R_k \Delta H_k - \nabla \cdot \left(-\kappa \nabla T_g\right), \tag{2.40}$$

where N_g is the total gas density and c_v is the specific heat at constant volume. The first term is Joule heating of the ion species j with current J_j and electric field E. The second term is heating or cooling due to change in enthalpy ΔH_k in reaction k with rate R_k. The third term is cooling due to thermal conductivity κ of the materials in contact with the plasma. The Joule heating of the ions can be averaged over a user-specified time.

2.2.8 Electron Monte Carlo Simulation

Another time-slicing module available for *nonPDPSIM* is the electron Monte Carlo Simulation (eMCS). When a node has a large value of E/N, the fluid approximation for electrons emitted from materials is not necessarily accurate, and a kinetic Monte Carlo approach is used. Nodes with large values of E/N typically reside in the sheaths formed around surfaces. The eMCS allows secondary electrons and photoelectrons to be treated kinetically and transferred to the fluid when their energy is below a certain user-specified threshold.

The eMCS is performed over a user-specified area, typically in the sheaths around materials that have a large E/N. The eMCS overlays a structured mesh onto the unstructured mesh generated by Pointwise. The spacing specified by the user of the eMCS mesh should be similar to the spacing of the unstructured mesh to easily interpolate between the unstructured and structured meshes. The electric field is required input to the eMCS and is transferred from the unstructured to structured mesh. After performing the eMCS, the source of fluid electrons is then transferred back to the unstructured mesh.

At each call to the eMCS, a specified number of macroparticles are emitted from each surface node residing in the eMCS mesh. These macroparticles of electrons have an initial electron energy of 4 eV. Once the energy of the macroparticle falls below 90% of the initial energy, the macroparticle is removed from the eMCS and becomes a source to the fluid electrons in Eq (2.32) . Macroparticles can also be lost by surfaces, recombination, or attachment. Once a macroparticle exits the eMCS mesh, it also becomes a source to the fluid electrons.

When this option is used, 150 macroparticles are emitted from each MCS surface node, and the eMCS is updated every 0.1 ns. This is typically larger than the plasma timestep of 1 ps - 10 ps. At each plasma timestep, the sources to the fluid electrons from the eMCS are held constant.

2.2.9 Capacitively-Coupled Power Module

In *nonPDPSIM*, the voltage is specified as a function of time to the electrodes. The voltage is either directly written as a function of time, in the case of pulsed systems, or it can be specified as a sinusoidal waveform. However, in radio frequency (RF) systems with capacitively-coupled power (CCP), the power deposited in the plasma is the more relevant parameter than the voltage.

However, specifying the power deposited directly in *nonPDPSIM* is challenging. Instead, *nonPDPSIM* can calculate the power deposited in a given time period (typically one RF cycle) and normalize the voltage to achieve the desired power. The averaged power P over the RF cycle is first calculated by integrating the power over the RF cycle by

$$P = \frac{1}{\tau}\int_0^{\tau}\int \overline{J}\left(\vec{r},t\right)\cdot \overline{E}\left(\vec{r},t\right) d^3 r dt, \qquad (2.41)$$

where τ is the RF cycle period. The magnitude of the sinusoidal voltage is then adjusted by

$$V_{new} = V_{old}\sqrt{\frac{P}{P_{specified}}} \qquad (2.42)$$

where V_{old} is the previous voltage magnitude, V_{new} is the new voltage magnitude, and $P_{specified}$ is the desired power. An upper limit on the adjustment is specified to ensure smooth transitions between RF cycles. The number of RF cycles until the desired power is reached depends solely on how good the initial estimate of the voltage was.

2.2.10 Post-Processing Scripts

The outputs of *nonPDPSIM* are written as Tecplot files. These include a 2D Tecplot file over the geometry at different times, a 1D volume-averaged file giving volume-averaged densities over time, and a 1D file containing the fluxes to surfaces versus the location on the surface at different times. However, due to the structure of the files, some post-processing is required if a species density over time at a particular location is desired. To that end, the author has developed many post-processing scripts written in Python and using PyTecplot, the Python library that interfaces with Tecplot. The scripts described here are primarily used in Chapter 5, and the source code is displayed in Appendix A.

One of the scripts, average_over_time, takes the 2D Tecplot file and averages over the time in the file, which is useful for cases that were restarted to obtain finer temporal resolution once a quasi-steady state was reached. The displacement current J_d and conduction current J_c over the geometry can also be calculated using the script displacement_current. J_d and J_c are

$$\begin{aligned}\overrightarrow{J_d} &= \varepsilon \frac{\partial}{\partial t} \vec{E} \\ \overrightarrow{J_c} &= \sigma \vec{E}.\end{aligned} \qquad (2.43)$$

J_d relies on the time derivative of E, calculated using a forward-difference method at each node in the geometry. J_c is proportional to E at each time. This script outputs another 2D Tecplot file which includes the conduction and displacement currents.

The variation of quantities over time at a specific location is also often required. A variety of scripts can read in the 2D Tecplot file and extract the quantities over time at specific locations. One example is extracting quantities along a line across the plasma gap, extract_1d_lines. The output of extraction along a line is a 1D Tecplot file, containing the quantities across the plasma gap at various times. The times are specified as different “zones” available for plotting. Another example is extracting quantities at a specific location, extract_over_cycle. In this case, the output 1D Tecplot file contains time as a variable, so electron density versus time can be easily plotted. Another similar script, extract_over_cycle_flux1d, can extract quantities at a specific location from the 1D Tecplot file containing the fluxes. This script outputs a 1D file containing time as a variable, as the Tecplot file containing fluxes has location as a variable and time as different “zones.” Another script, calculate_phase, calculates the phase of the oscillation of the electron density relative to the oscillation of the RF voltage.

Two scripts were developed to compare to experimental results in Chapter 5. The first script, he_metastable_calculation, takes the extraction across the plasma gap of time-averaged 2D Tecplot file to determine the He metastable states ($He(2^3S)$ and $He_2(a^3\Sigma_u^+)$). The densities of the He metastables are smoothed over 200 µm to match the experimental resolution. The density of $He_2(a^3\Sigma_u^+)$ is estimated from the lumped state of He_2^* included in the reaction mechanism by multiplying by the ratio of $He(2^3S)$ divided by the total He excited state density. The other script, compare_emissivities, takes the 1D file extracted across the plasma gap at various times and calculates the emissivity from each location at each time. The emissivity is then averaged across the plasma and over the RF cycle, giving an estimate of emissivity versus wavelength.

2.3 *GlobalKin*

GlobalKin is a 0D plasma chemistry model. The species densities n, electron temperature T_e, and gas temperature T_g are calculated for over time using the well-stirred reactor approximation. Time-slicing modules are also implemented. *GlobalKin* is described in detail in Lietz and Kushner [17]. Since *GlobalKin* is a 0D model, it has a much faster runtime than the 2D *nonPDPSIM*.

The flow chart of *GlobalKin* as used in this dissertation is shown in Figure 2.12. The input files include a namelist and a reaction mechanism. The namelist specifies properties of the system like power deposition and diffusion length and which modules of *GlobalKin* to use. The reaction mechanism is similar to *nonPDPSIM*, with the species and their properties listed first, followed by the reactions. The reactions can be specified in Arrhenius form or solved for from their cross-sections using the Boltzmann tables. The Boltzmann tables are constructed in the same way as described in Section 2.2.2 and can be updated throughout the simulation.

After initialization, *GlobalKin* solves for n, T_e, and T_g over time. The power deposition into the plasma is specified as a function of time, and the power profile can be repetitively pulsed. The electron energy equation is used to solve for the electron temperature. The electron energy equation is

$$\begin{aligned}\frac{d}{dt}\left(\frac{3}{2}n_e k_B T_e\right) &= \vec{J}\cdot\vec{E} + n_e\sum_i \Delta\varepsilon_i k_i n_i + \sum_i \Delta\varepsilon_i k_i n_{1i} n_{2i} \\ &-\sum_i \frac{3}{2} n_e \nu_{mi}\left(\frac{2m_e}{m_i}\right) k_B\left(T_e - T_i\right),\end{aligned} \tag{2.44}$$

where n_e is the electron density and k_B is Boltzmann's constant. The first term on the right-hand side refers to Joule heating of the electrons, where J is the current and E is the electric field. The second term refers to energy deposited into the electrons by electron-impact reactions, where $\Delta\varepsilon_i$ is the energy deposited from reaction i with rate constant k_i and other reactant n_i. The third term is the energy deposited into the electrons by reactions without electrons as a reactant with reactants n_{1i} and n_{2i}. The fourth term is the loss of energy due to momentum-transfer collisions with ions and neutral species. Here, ν_{mi} is the momentum transfer collision frequency, m_e is the electron mass, m_i is the other particle mass, and T_i is the temperature of species i (gas temperature).

Following the update of T_e, the species densities n_i are determined by their continuity equations. The continuity equation for species i is

$$\begin{aligned}\frac{dn_i}{dt} &= \sum_j \left(\left(a_{ij}^{(R)} - a_{ij}^{(L)} \right) k_j \prod_l n_l^{a_{ij}^{(L)}} \right) + \frac{1}{\tau_{flow}} \left(n_{i0} - n_i \left(1 + \frac{P - P_0}{P} \right) \right) \\ &+ \sum_m \left(-\frac{D_i n_i}{\Lambda^2} f_m S_{im} + \sum_k \frac{D_k n_k}{\Lambda^2} f_m S_{km} g_{ikm} \right). \end{aligned} \tag{2.45}$$

The first term refers to source and loss due to reaction j, where $a_{ij}^{(R)}$ and $a_{ij}^{(L)}$ are the number of times species i appears on the right- and left-hand sides of the reaction, respectively. The second term is the source or loss due to gas flow, where τ_{flow} is the residence time of the gas, n_{i0} is the density of species i that flows into the reactor, P is the current pressure, and P_0 is the specified operating pressure. The third term corresponds to loss of species i due to diffusion, as well as a source due to the sticking and giving coefficients specified in the reaction mechanism file. Here, D_i is the diffusion coefficient of species i, Λ is the diffusion length of the system, f_m is the fractional area of material m, S_{im} is the reaction probability of species i on material m, and g_{ikm} is the fraction of flux of species k to material m that returns as species i. The diffusion coefficient is calculated by

$$D_i = \frac{k_B T_g}{\sum_j \frac{1}{\mu_{ij}} \frac{n_j}{N_{STP}}}, \tag{2.46}$$

where μ_{ij} is the mobility and N_{STP} is the number density of gas at standard temperature and pressure (2.5×10^{19} cm^{-3}). The mobility for neutral species is calculated by

$$\begin{gathered} \mu_{ij} = \sqrt{\frac{m_i m_j}{m_i + m_j}} \sqrt{\frac{\pi}{8 k_B T_g}} \frac{1}{m_i N_{STP} \sigma_{ij}} \\ \sigma_{ij} = \pi \left(\frac{\sigma_i + \sigma_j}{2} \right)^2, \end{gathered} \tag{2.47}$$

where m_i and m_j are masses of species i and j and σ_i and σ_j are Lennard-Jones radii of species i and j. For charged species, the mobilities are typically tabulated in *GlobalKin* instead of estimated from Lennard-Jones parameters. The diffusion coefficient is then the ambipolar diffusion coefficient.

Lastly, the gas temperature is updated by the energy equation, which is

$$\begin{aligned} \frac{d}{dt}\left(\frac{3}{2} N_g c_p T_g \right) &= P_{ion} + \sum_i \frac{3}{2} n_e \nu_{mi} \left(\frac{2 m_e}{m_i} \right) k_B \left(T_e - T_i \right) + \sum_i \Delta \varepsilon_i^{fc} R_i - \sum_i \Delta H_i R_i \\ &+ \frac{1}{\tau_{flow}} \left(N_{g0} c_{p0} T_{g0} - N_g c_p T_g \left(\frac{P}{P_0} \right) \right) - \frac{\kappa}{\Lambda^2} \left(T_g - T_w \right). \end{aligned} \tag{2.48}$$

where N_g is the total gas density and c_p is the specific heat. The first term on the right-hand side is P_{ion}, or the Joule heating into the ions. The second term is the heating of the gas due to momentum-transfer collisions with electrons. The third term is heating due to dissociation of the gas, otherwise known as Franck-Condon heating. Here, $\Delta\varepsilon_i^{fc}$ is the energy released in reaction i with rate R_i. The fourth term is heating due to the change in enthalpy, where ΔH_i is the change in enthalpy of reaction i. The fifth term is advective heating or cooling of the gas due to flow into the reactor. N_{g0}, c_{p0}, and T_{g0} refer to the gas density, specific heat, and gas temperature of the gas flowing into the reactor. The final term is loss of heat due to thermal conduction, where κ is the thermal conductivity and T_w is the wall temperature. The electron energy equation, species continuity equations, and gas temperature energy equation are solved by an ordinary differential equation solver called DVODE [18]. The maximum residual ranges from 10^{-8} to 10^{-5}.

Similar to *nonPDPSIM*, *GlobalKin* has many modules that can be used. Some, like the liquid module and plug-flow module, are used at the same timestep as the plasma. Others, like the surface kinetics module (SKM), utilize time-slicing and can be called more or less frequently than the plasma updates. The two modules used in this dissertation are the liquid droplet module and the SKM, and these are described in detail in Sections 2.3.1 and 2.3.2, respectively. One post-processing script was written for the output of *GlobalKin* and is described in Section 2.3.3.

2.3.1 Liquid Module

GlobalKin can simulate plasma-liquid interaction using the liquid module, described in detail in Lietz and Kushner [17]. Each gas phase species has a liquid phase counterpart, though liquid phase species do not require a gas phase counterpart. Reactions are required to only involve species of a single phase. Diffusion is the primary interaction between the gas and liquid phases, and the liquid phase is assumed to be a second well-stirred volume.

From the perspective of the gas phase, the liquid is simply another surface in contact with the plasma with sticking coefficients for each gas phase species. For species i, the sticking coefficient on the liquid surface $S_{i.liquid}$ is based on dimensionless Henry's law constant h_i. The sticking coefficient is calculated by

$$S_{i,liquid} = \frac{h_i n_{i,gas} - n_{i,liquid}}{h_i n_{i,gas}}, \tag{2.49}$$

where $n_{i,gas}$ is the gas phase density of species i and $n_{i.liquid}$ is the corresponding liquid phase density.

To calculate the liquid phase densities, a continuity equation for the liquid phase species is used. This continuity equation is

$$\begin{aligned} \frac{dn_{i,liquid}}{dt} = {} & \sum_j \left(\left(a_{ij}^{(R)} - a_{ij}^{(L)} \right) k_j \prod_l n_l^{a_{ij}^{(L)}} \right) + \frac{D_{i,gas} n_{i,gas}}{\Lambda^2} f_{liquid} S_{i,liquid} \frac{V_{gas}}{V_{liquid}} \\ & - \max\left(0, \frac{D_{i,gas} \left(n_{i,liquid} - h_i n_{i,gas} \right)}{\Lambda^2} \frac{V_{gas}}{V_{liquid}} \right). \end{aligned} \tag{2.50}$$

The first term, similar to the gas phase, is the source or loss of species i in the liquid due to reactions. The second term refers to diffusion into the liquid from the gas, providing a source of species i. Here, f_{liquid} is the fractional area of the plasma in contact with the liquid, V_{gas} is the volume of the gas phase, and V_{liquid} is the volume of the liquid phase, specified by the user or calculated internally for droplets (Section 2.3.1.1). The third term allows for a flux of species i back into the gas phase if the liquid phase is saturated beyond its Henry's law concentration.

Evaporation of the liquid is included in *GlobalKin*. Evaporation is specified by adding a flux of the solvent (typically H_2O) from the liquid phase to the gas phase. This flux is given by

$$\Gamma_i = \frac{D_i \left(n_{i,s} - n_{i,gas} \right)}{\Lambda^2} \frac{V_{gas}}{A_{liquid}}, \tag{2.51}$$

where A_{liquid} is the surface area of the liquid in contact with the plasma and $n_{i,s}$ is the saturated vapor pressure of the solvent.

2.3.1.1 Droplet Module

The liquid module described above was initially developed to simulate a layer of liquid residing on one of the surfaces in contact with the plasma. In this geometry, the diffusion length to the walls well represented the diffusion of radicals produced in the plasma to the liquid. This assumption of one constant diffusion length for both the liquid and walls is not correct when the liquid is a droplet is immersed in the plasma. The diffusion length of radicals to the droplet is not that of the radicals to the walls of the reactor; in fact, the radicals are produced very close to the droplet. Therefore, the droplet module in *GlobalKin* allows for a second diffusion length to be specified in the namelist, used solely for diffusion to the liquid droplet.

Upon encountering the droplet, radicals will react quickly and only be present within a small layer on the surface of the droplet. Therefore, the well-stirred reactor approximation for the liquid is not necessarily correct, as radicals will not interact throughout the entire liquid volume. Another option in the droplet module in *GlobalKin* divides the droplet into two volumes; a reactive layer and a nonreactive core. The reactive layer thickness R_{layer} is specified by the user, and if the reactive layer is larger than the specified droplet radius, the entire droplet is assumed to be reactive. The volume of the droplet then assumed to be the volume of the reactive layer V_{layer}. V_{layer} is calculated by

$$V_{layer} = \frac{4}{3}\pi\left(R_{droplet}^{3} - \left(R_{droplet} - R_{layer}\right)^{3}\right), \tag{2.52}$$

where $R_{droplet}$ is radius of the droplet. The surface area of the droplet in contact with the plasma is calculated by

$$A_{liquid} = 4\pi R_{droplet}^{2}. \tag{2.53}$$

The nonreactive core does not undergo reactions, and species densities in the nonreactive core do not change. The nonreactive core and reactive layer do not interact.

The output of *GlobalKin* is only the densities of the species within the reactive layer. The density throughout the droplet n_{total} (reactive layer and nonreactive core) can be calculated by

$$n_{total} = \frac{x_{initial}(3.347\times10^{22}\,cm^{-3})(V_{core}) + n_{layer}V_{layer}}{V_{total}}, \tag{2.54}$$

where $x_{initial}$ is the initial mole fraction in the liquid phase, 3.347 × 10^{22} cm^{-3} is the density of liquid H_2O, V_{core} is the nonreactive core volume, n_{layer} is the density in the reactive layer, and V_{total} is the total volume of the droplet. If $x_{initial}$ is zero, n_{total} reduces to

$$n_{total} = \frac{V_{layer}}{V_{total}} n_{layer}. \tag{2.55}$$

2.3.2 Surface Kinetics Module

The other module of *GlobalKin* used in this dissertation is the Surface Kinetics Module (SKM). The SKM resolves the occupancy of surface sites over time based on fluxes of gas phase species to the walls. A separate reaction mechanism file with the surface species and reactions is required as input to the SKM. Reactions in the SKM can be between a gas phase species and surface site or between surface sites. The SKM is called at a user-specified interval that does not match the plasma timestep. The SKM can also be integrated for times longer than the time between calls to the SKM, allowing a faster convergence of the surface site occupancy. The rate equation for the surface site occupancy of species i θ_i is

$$\frac{d\theta_i}{dt} = \sum_{j,k} \theta_k \Gamma_j p_{ijk} + \sum_{k,l} \theta_k \theta_l p'_{ikl} - \theta_i \left(\sum_j \Gamma_j p_{ji} + \sum_k \theta_k p'_{ik} \right), \tag{2.56}$$

where the first term on the right-hand side is the source of surface species i due to reactions between gas phase species j and surface species k with probability p_{ijk} and flux Γ_j. The second term is the source of surface species i due to reactions between surface species k and l with probability p'_{ikl}. The third term is the loss of surface species i due to reactions with the gas phase species j with probability p_{ji} and due to reactions with surface species k with probability p'_{ik}.

2.3.3 Post-Processing Script

One post-processing script, parameter_sweep, has been developed by this author for *GlobalKin*. This script is used in Chapters 6 and 7. This script reads in multiple output files from *GlobalKin* in a specified parameter sweep, such as droplet diameter. The script then extracts specified quantities at specified times, like the OH_{aq} concentration at 10.1 ms. The output is a Tecplot file that plots the specified quantities versus the swept value (i.e., OH_{aq} concentration at 10.1 ms versus droplet diameter). The source code for this script is shown in Appendix A.

2.4 Author's Contributions

MEOWS, described in Section 2.1, was written by the author using sputtering yield models found in the literature. The model was first written in Python and was then rewritten in C++ to improve runtime.

Additions to *nonPDPSIM* were made by this author. As described in Section 2.2.1, support in *nonPDPSIM* for meshes generated by the open-source mesh generator Gmsh was added. Symmetric boundary conditions on the top, bottom, and right boundaries of the mesh were also improved, allowing for plasma to be in contact with those boundaries.

Other changes to *nonPDPSIM* involved updates to the liquid module, which is not used in this dissertation. Previous versions of *nonPDPSIM* included automatic solvation of ions and neutral species from the gas phase into the liquid phase. The author added the capability to automatically solvate electrons in addition to the ions and neutral species, eliminating the need for a fast electron solvation reaction in the reaction mechanism file that necessitated slow time steps.

Further changes to *nonPDPSIM* involved updates to the neutral plasma option, which is not used in this dissertation. The neutral plasma option does not solve Poisson's equation and instead treats the charged species like neutral species. Therefore, much larger time steps can be taken in the neutral plasma option compared to during the plasma discharge. The author ensured the CCP module does not occur during the neutral plasma option. The author also added the ability to use electron-impact rate coefficients that have been averaged over a user-specified time in the neutral plasma option in addition to the gas temperature and fluid modules.

Finally, a modified interpolation method for the electric field was implemented. In the previous method, neighboring nodes were sorted into quadrants, and the nodes closest to the x and y axes were used to interpolate the electric field at the central node. This method resulted in large electric fields at the surface of two materials with different permittivities. The new method only uses nodes with the same permittivity to interpolate.

The author has also written post-processing scripts for *nonPDPSIM*, detailed in Section 2.2.10, and for *GlobalKin*, detailed in Section 2.3.3.

2.5 Figures

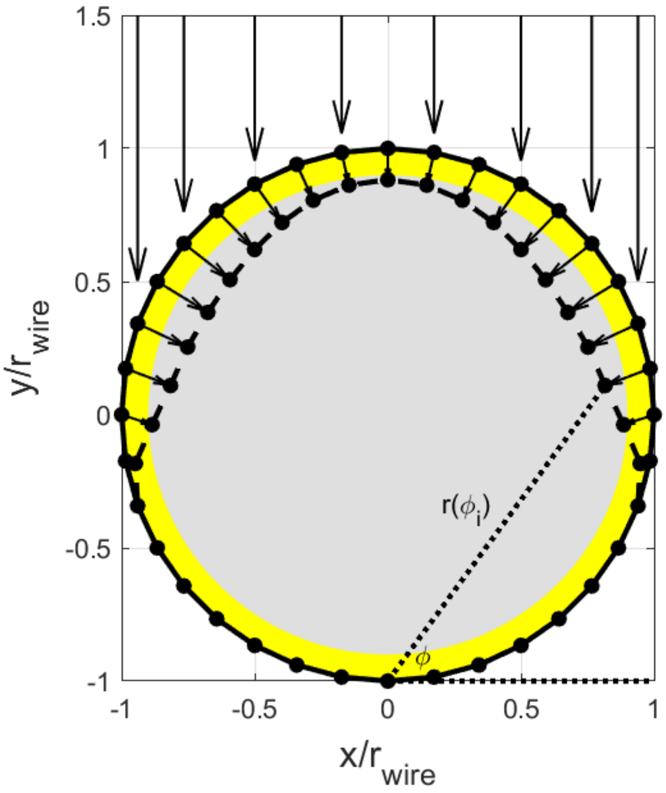

Figure 2.1. Example of erosion from the pre-erosion profile (solid) to eroded profile (dashed). The incident ion flux is shown by the black arrows. Notional gold cladding on molybdenum core is shown. Reproduced from Meyer et al. [19].

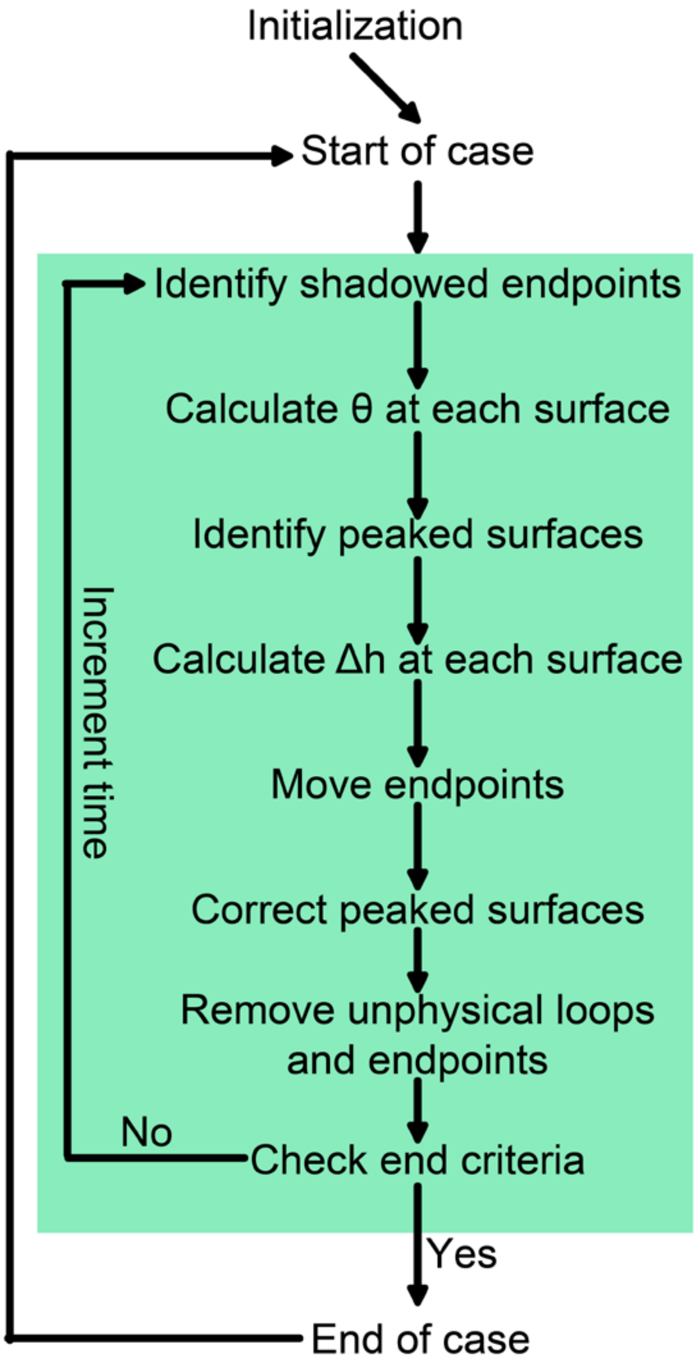

Figure 2.2. Flow chart of *MEOWS*.

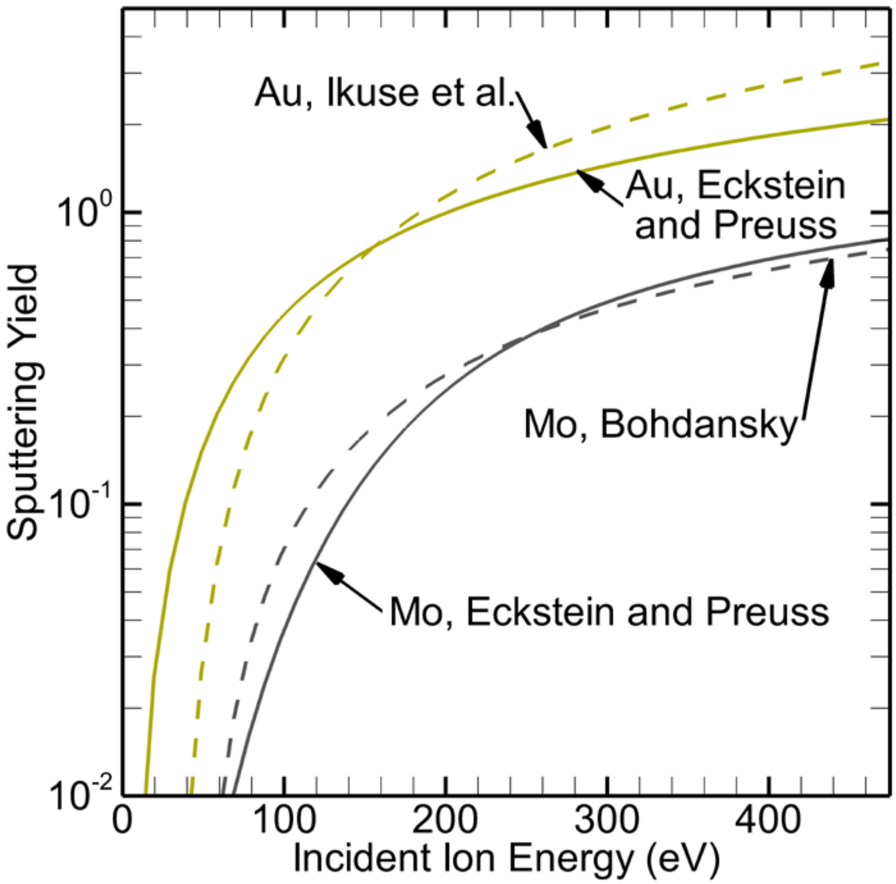

Figure 2.3. Comparison of normal incidence sputtering yield models for gold and molybdenum.

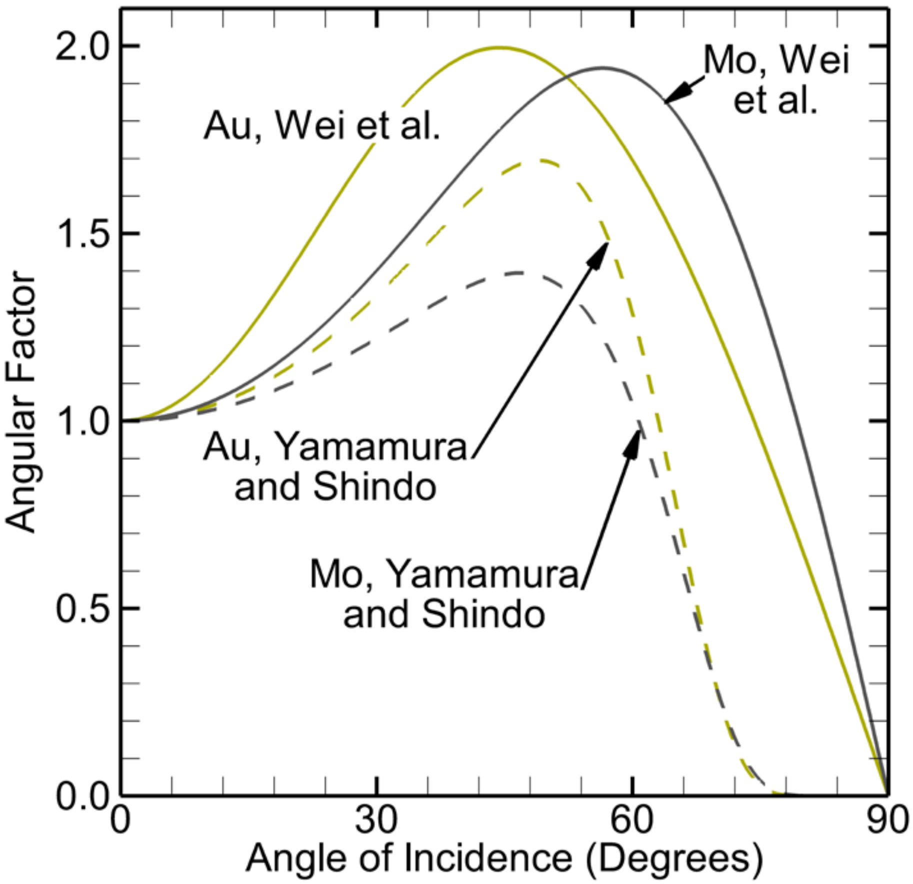

Figure 2.4. Comparison of angular factors for gold and molybdenum.

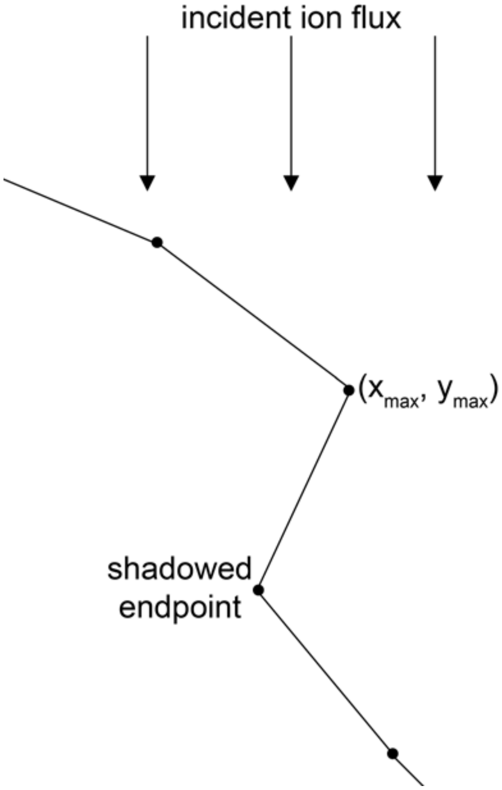

Figure 2.5. Notional determination of shadowed points for positive x values.

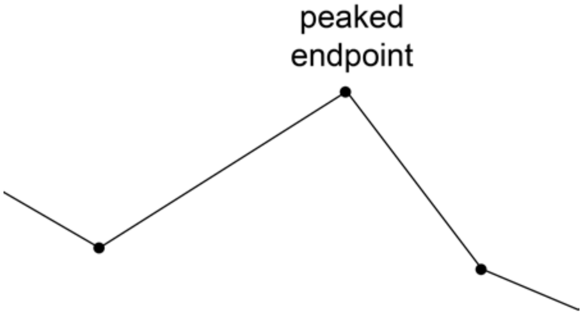

Figure 2.6. Peak identification for positive x values.

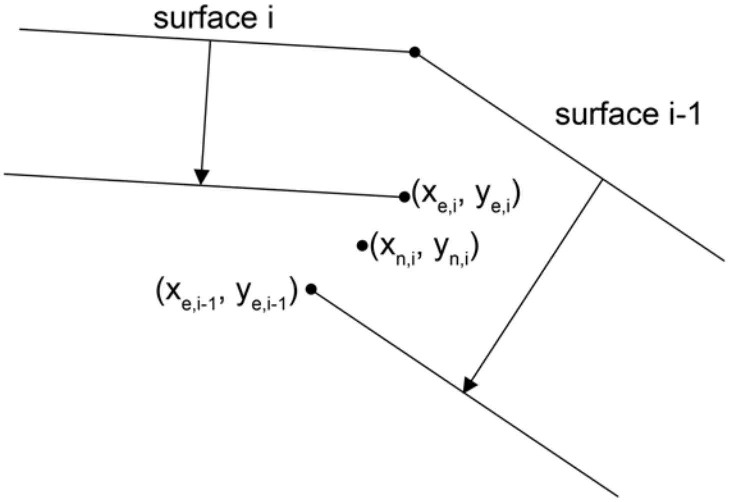

Figure 2.7. Calculating new coordinates of the endpoints.

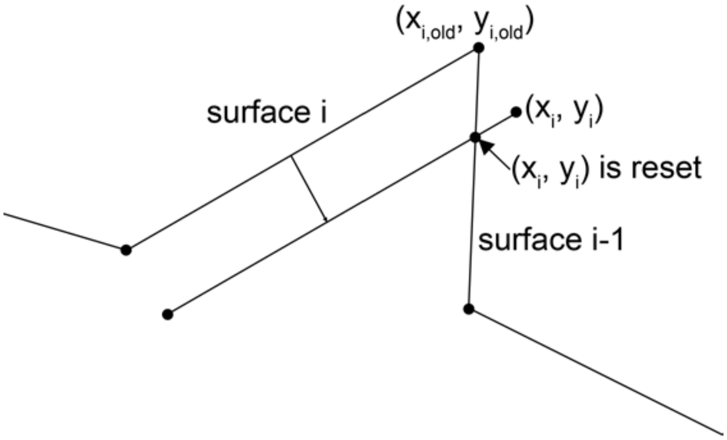

Figure 2.8. Resetting of peaked endpoint (x_i, y_i).

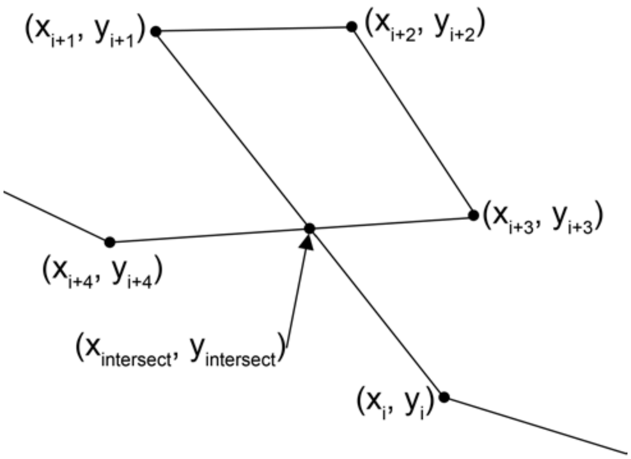

Figure 2.9. Removing of loop. (x_{i+2}, y_{i+2}) and (x_{i+3}, y_{i+3}) are removed, and (x_{i+1}, y_{i+1}) is reset to $(x_{intersect}, y_{intersect})$.

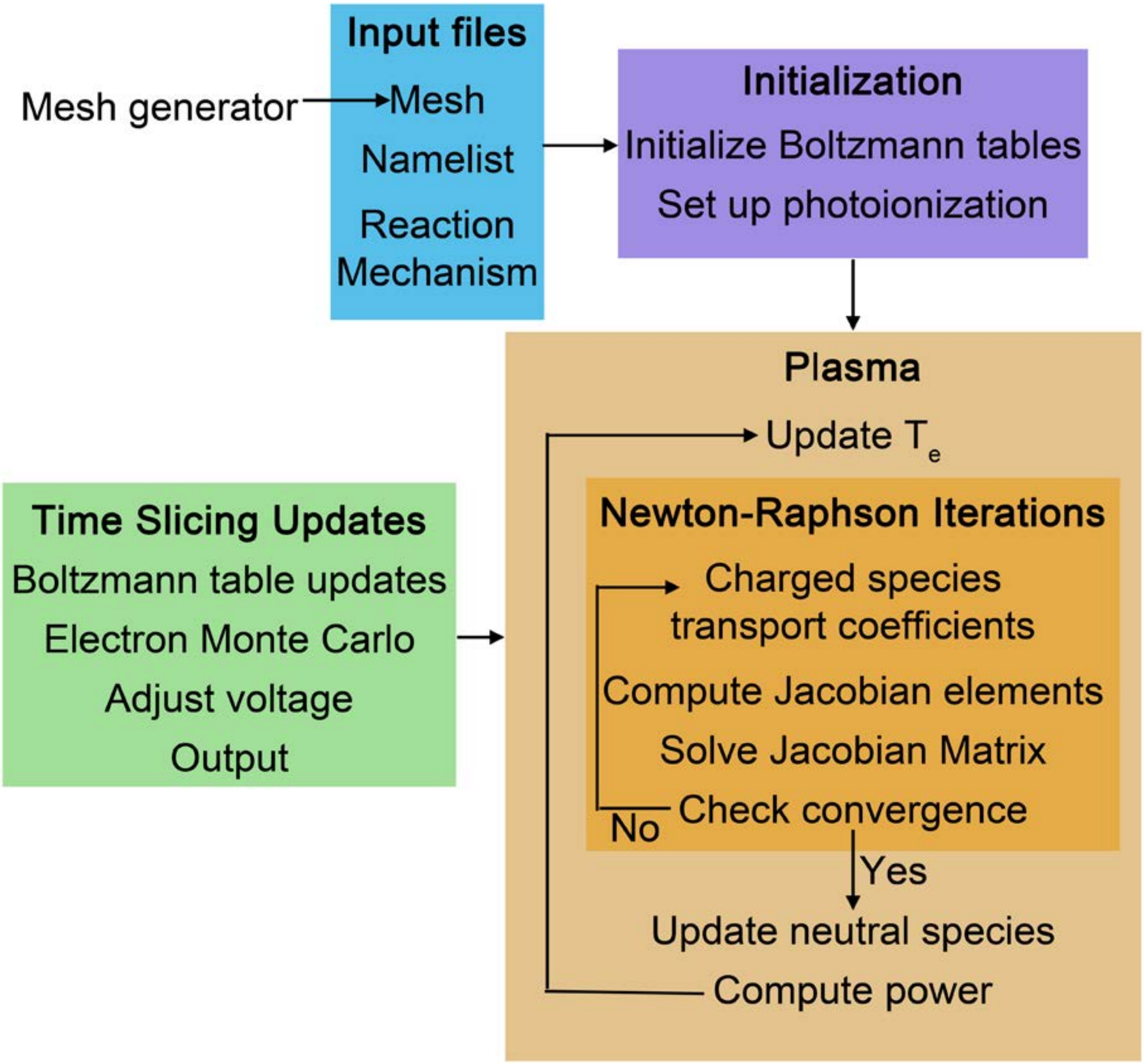

Figure 2.10. Flow chart of *nonPDPSIM*.

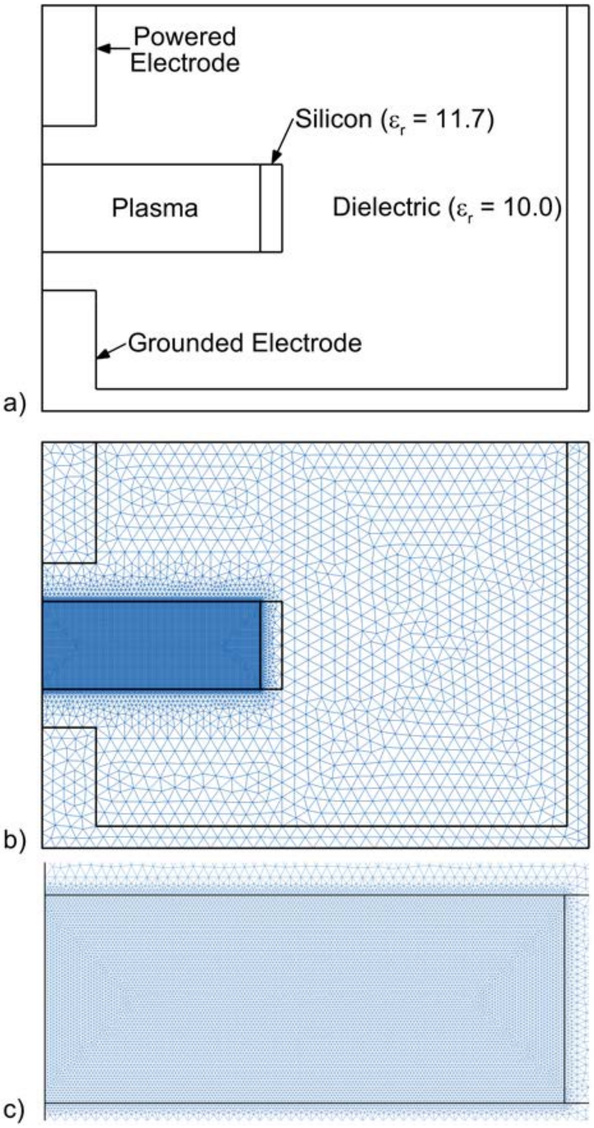

Figure 2.11. Example of geometry and mesh used in *nonPDPSIM* from Chapter 8. (a) Symmetric Cartesian geometry, (b) numerical mesh, and (c) numerical mesh of the plasma region.

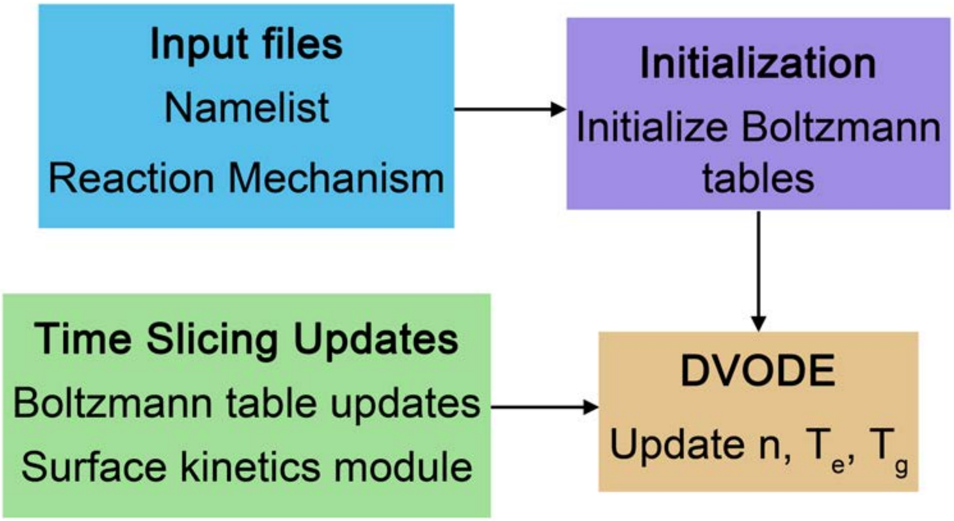

Figure 2.12. Flow chart of *GlobalKin*.

2.6 References

[1] W. Eckstein and R. Preuss, J. Nucl. Mater. **320,** 209 (2003).

[2] Y. Yamamura and S. Shindo, Radiat. Eff. **80,** 57 (1984).

[3] Q. Wei, K.-D. Li, J. Lian and L. Wang, J. Phys. D. Appl. Phys. **41,** 172002 (2008).

[4] B. Rubin, Topper J L, C. C. Farnell and A. P. Yalin, Rev. Sci. Instrum. **80,** 103506 (2009).

[5] M. Tartz, T. Heyn, C. Bundesmann, C. Zimmermann and H. Neumann, Eur. Phys. J. D **61,** 587 (2011).

[6] K. Ikuse, S. Yoshimura, K. Hine, M. Kiuchi and S. Hamaguchi, J. Phys. D. Appl. Phys. **42,** 135203 (2009).

[7] J. Bohdansky, Nucl. Instruments Methods Phys. Res. B **2,** 587 (1984).

[8] C. García-Rosales, W. Eckstein and J. Roth, J. Nucl. Mater. **218,** 8 (1995).

[9] J. T. Yim, 35th International Electric Propulsion Conference, Paper IEPC-2017-060 (2017).

[10] I. D. Boyd and M. L. Falk, AIAA 37th Joint Propulsion Conference, AIAA Paper 2001-3353 (2001).

[11] S. A. Norberg, E. Johnsen and M. J. Kushner, Plasma Sources Sci. Technol. **24,** 035026 (2015).

[12] J. A. Kruszelnicki, "Controlling Plasma Reactivity Transfer to Gases , Solids and Liquids," Ph.D. Thesis (University of Michigan, 2021).

[13] A. M. Lietz, "Atmospheric Pressure Plasma Sources for Plasma Medicine," Ph.D. Thesis (University of Michigan, 2019).

[14] D. L. Scharfetter and H. K. Gummel, IEEE Trans. Electron Devices **16,** 64 (1969).

[15] Y. Saad, *SPARSKIT: A basic tool-kit for sparse matrix computations*, (2005).

[16] J. O. Hirschfelder, C. F. Curtiss and R. B. Bird, *Molecular Theory of Gases and Liquids*,

Wiley (1954).

[17] A. M. Lietz and M. J. Kushner, J. Phys. D. Appl. Phys. **49,** 425204 (2016).

[18] P. N. Brown, G. D. Byrne and A. C. Hindmarsh, SIAM J. Sci. Stat. Comput. **10,** 1038 (1989).

[19] M. E. Meyer, M. P. Byrne, I. D. Boyd and B. A. Jorns, J. Spacecr. Rockets **59,** 988 (2022).

Chapter 3 Erosion of a Meshed Reflector in the Plume of a Hall Effect Thruster[1]

A model for the erosion of a meshed reflector, *MEOWS*, by sputtering in the plume of a Hall effect thruster is presented, and results are compared to experimental measurements. The ion current density and ion energy distribution function at the location of the meshed reflector are required to determine the erosion. These properties are obtained through both numerical simulation and experimental measurements. The sputtering yield as a function of energy and angle of incidence is also required to determine the erosion, and this chapter considers several models. The erosion is then modeled by discretizing the cross-section of a single wire in the meshed reflector and modeling how each discretized surface erodes over time. The results of the model using different sputtering yield models are compared to experimental measurements of the eroded wire profiles to assess and validate *MEOWS*. The average of these results using different sputtering yield models accurately predicts the experimentally measured eroded wire profiles to within 35% of the wire radius at different locations in the plume. With this validated model, the erosion of meshed reflectors in the plume of other electric propulsion devices can be determined.

3.1 Introduction

Electric propulsion (EP) devices, including Hall effect thrusters, are being used increasingly on Earth-orbiting satellites and for deep-space missions. While these devices offer a high specific impulse compared to chemical propulsion systems, there is a risk of causing damage

---

[1] The results discussed and portion of the text in this chapter have been previously published in M.E. Meyer et al., “Erosion of a meshed reflector in the plume of a Hall effect thruster, Part 1: Modeling”, AIAA Propulsion and Energy 2019 Forum, AIAA Paper 2019-3987 (2019).

to the spacecraft components. Since these low thrust devices need to operate for long periods of time, their highly energetic propellant can lead to ion-impact erosion of key spacecraft components [1]. Understanding how material erodes in the plume of an EP device is therefore a critical aspect of integrating these devices onto a spacecraft. One example of a spacecraft component that is particularly critical for commercial systems is the meshed reflector. Meshed reflectors are parts of antenna used on satellites and can lose functionality after a certain level of erosion. Erosion of this level can offset the gains in specific impulse and lifetime afforded by the EP device.

Since the meshed reflectors are typically made of a mesh of molybdenum wires coated with gold, the erosion of wires due to sputtering by the ions in the plume of an EP device needs to be understood. While the erosion of a planar surface in the plume of a Hall effect thruster has been previously investigated [2–4], the erosion of a cylindrical surface in these conditions has not been studied. The goal of this chapter is to examine the modeling of the erosion of a meshed reflector in the plume of a Hall effect thruster. The development of *MEOWS,* an erosion model for the meshed reflectors, is detailed. *MEOWS* considers the erosion of a single wire, as each wire in the meshed reflector will erode in the same manner. The experimental setup is described by Byrne et al. [5]. The results of the experimental testing include the plume properties and eroded wire profiles at different locations in the plume. The wire profiles are used to verify the results of *MEOWS* calculated using the experimentally measured plume properties.

This chapter is organized as follows. First, the methods of modeling the plume, sputtering yield, and wire erosion are discussed. Results of the plume modeling and wire erosion modeling are then presented, and those results are compared to the corresponding experimental measurements. The implications of these results for spacecraft are discussed.

3.2 Modeling

Several key components are necessary for evaluating the erosion of a wire. Plume properties such as the ion current density and ion energy distribution function at the surface of the wire are required. These properties are obtained through a plume simulation. The sputtering yield, or atoms emitted from the surface per incident ion, is determined using the ion energy distribution. With the sputtering yield and the ion current density, the erosion of a wire can be modeled by discretizing the cross-section of the wire into small, planar surfaces and calculating how those surfaces erode over time.

The sputtering yield models and *MEOWS* are discussed in Section 2.1. This section presents the plume simulation that can provide ion current density and ion energy distribution.

3.2.1 Plume Modeling

The ion current density and ion energy distribution are required to determine the erosion of a wire. While experimental measurements give the best estimates of these quantities, high fidelity numerical simulations enable the prediction of erosion in the plume of other EP devices by estimating the required plume properties. This section describes one such high fidelity model.

Plume properties such as the ion current density and ion energy distribution vary at different locations in the plume. The xenon ions accelerated by the axial electric field in a Hall effect thruster form a high density beam of energetic ions that diverges about 30° from the thruster centerline. At larger angles from the thruster centerline, charge-exchange collisions dominate. These collisions occur when an electron is transferred from a neutral xenon atom to an energetic ion, resulting in a slow-moving ion and a fast-moving neutral atom. These slow-moving ions are less energetic than the ions in the beam, and the density of ions at large angles from the thruster centerline is lower than the density of ions in the beam.

The ion current density and ion energy distribution can be determined by the 2D axisymmetric simulation *MONACO-PIC* (*MPIC*). This steady state simulation uses the particle-in-cell (PIC) and direct simulation Monte Carlo (DSMC) methods to model the ion and neutral atom motion and describes the electrons by the three fluid conservation equations. The simulation uses macroparticles to represent a large number of ions and neutral atoms. Both momentum exchange and charge-exchange collisions between the ions and neutral atoms are considered. The DSMC method performs the collisions of the macroparticles by randomly selecting pairs of macroparticles to collide in a given cell. This method conserves both momentum and energy. The five types of collisions considered are neutral atom and neutral atom momentum exchange, neutral atom and singly charged ion momentum exchange and charge-exchange, and neutral atom and doubly charged ion momentum exchange and charge-exchange. The effects of background pressure are included by introducing neutral atoms in each cell that collide with other particles but do not move themselves. The PIC method moves the ions according to the force F from the local electric field E

$$\vec{F} = q\vec{E}. \tag{3.1}$$

New macroparticles are injected into the simulation at the inlet boundary. The velocity of these macroparticles is determined from a drifting Maxwell-Boltzmann velocity distribution function with specified drift velocity and specified temperatures in each direction. In this work, the inlet boundary is an effective inlet along a magnetic field line in the near-field plume, as described in Huismann [6].

Since the electrons adjust to the local electric field faster than the ions due to the mass of electrons being much smaller than that of the ions, the electrons can be described using a detailed fluid model, as documented in Boyd and Huismann [6,7]. Assuming quasi-neutrality, the electron number density n$_e$ is determined by the ion number density. This detailed fluid model solves for the plasma potential ϕ, electron temperature T$_e$, and electron velocity v$_e$ using the electron continuity equation, the electron momentum equation, and the electron energy equation:

$$\frac{\partial}{\partial t} n_e + \nabla \cdot \left(n_e \overrightarrow{v_e} \right) = n_e n_a C_i \tag{3.2}$$

$$\frac{\partial}{\partial t}\left(m_e n_e \overrightarrow{v_e} \right) + m_e n_e \left(\overrightarrow{v_e} \cdot \nabla \right) \overrightarrow{v_e} = e n_e \vec{E} - \nabla p_e + \frac{e n_e}{\sigma} \overrightarrow{J_e} \tag{3.3}$$

$$\begin{gathered} \frac{\partial}{\partial t}\left(\frac{3}{2} n_e k_B T_e \right) + \frac{3}{2} n_e \left(\overrightarrow{v_e} \cdot \nabla \right) k_B T_e + p_e \nabla \cdot \overrightarrow{v_e} = \nabla \cdot \kappa_e \nabla T_e + \\ 3\left(\overrightarrow{J_e} \cdot \vec{E} \right) \frac{m_e}{m_i} \nu_e n_e k_B \left(T_e - T_H \right) - n_e n_a C_i \varepsilon_i \end{gathered} \tag{3.4}$$

The electron pressure is p$_e$ = n$_e$k$_B$T$_e$. The classical electrical conductivity σ is

$$\sigma = \frac{e^2 n_e}{m_e \nu_e}, \tag{3.5}$$

and the electron thermal conductivity κ_e is

$$\kappa_e = \frac{2.4}{1 + \frac{\nu_{ei}}{\sqrt{2}\nu_e}} \frac{k^2 n_e T_e}{m_e \nu_e}. \tag{3.6}$$

The total electron collision frequency ν_e is the sum of the ion-electron collision frequency ν_{ei} and the neutral-electron collision frequency ν_{en}. The ionization rate C$_i$ is taken from Ahedo [8] and is

$$C_i = \sigma_r c_e \left(1 + \frac{T_e \varepsilon_i}{\left(T_e + \varepsilon_i \right)^2} \right) \exp\left(-\frac{\varepsilon_i}{T_e} \right), \tag{3.7}$$

where T$_e$ is expressed in eV.

In steady state, all of the time derivatives in the fluid equations are neglected. The electron continuity equation, in terms of the stream function $\nabla \psi = n_e \overrightarrow{v_e}$, can be rewritten as

$$\nabla^2 \psi = n_e n_a C_i . \tag{3.8}$$

The electron momentum equation can be represented as a generalized Ohm's law

$$\overline{J_e} = \sigma \left(-\nabla \phi + \frac{1}{e n_e} \nabla \left(n_e k_B T_e \right) \right). \tag{3.9}$$

By applying charge continuity in steady state ($\nabla \cdot \overline{J_e} = 0$), this equation can be solved for ϕ. The electron energy equation can be solved for the T_e

$$\begin{gathered} \nabla^2 T_e = \nabla \log\left(\kappa_e \cdot \nabla T_e \right) + \frac{1}{\kappa_e} (-\overline{J_e} \cdot \overline{E} + \frac{3}{2} n_e \left(\overline{v_e} \cdot \nabla \right) k_B T_e + p_e \nabla \cdot \overline{v_e} + \\ \frac{3 m_e}{m_i} \nu_e n_e k_B \left(T_e - T_H \right) + n_e n_a C_i \varepsilon_i). \end{gathered} \tag{3.10}$$

With the plasma potential calculated from the above equations, the local electric field $\vec{E} = \nabla \phi$ can be derived and used to calculate the motion of the ions. Further details about *MPIC* can be found in Huismann [6].

The results of *MPIC* include the ion current density and ion energy distributions along an arc of specified distance from the thruster at various angles from the thruster centerline, as illustrated in Figure 3.1. These plume properties are necessary to determine the erosion of a wire.

3.3 Results

Experimental measurements of the plume properties and eroded wire profiles are compared to the results from *MEOWS*. Experimental testing of the erosion of a meshed reflector was conducted at the Large Vacuum Test Facility at the University of Michigan with the H6US thruster. This thruster has been studied extensively [9–11]. The first stage of experimental testing measured plume properties including the ion current density and ion energy distributions along an arc at 1 m from the thruster. These results were compared to the results of *MPIC*. The second stage of experimental testing placed samples of the meshed reflector at 1 m from the thruster and various angles from the thruster centerline. The samples were exposed to the plume of the thruster for 10 hours. After experimental testing was completed, wires of the meshed reflectors were measured by optical profilometry at five different locations on the wire to obtain height profiles. More details on the experimental testing can be found in Byrne et al. [5].

This section first compares the experimentally measured plume properties to the results of *MPIC*. Then, results of *MEOWS* are presented. Results at 18°, 33°, 48°, and 63° from the thruster centerline are examined. These locations are chosen because they have very different plume properties, so a variety of eroded wire profiles are achieved. Therefore, plume properties were measured and meshed reflector samples were placed at these locations during the experimental testing.

3.3.1 Plume Modeling Results

The experimentally measured ion energy distributions are compared to the results of *MPIC*. The initial results of *MPIC* did not match the experimentally measured ion energy distributions well, especially at low angles from the thruster centerline. To better match the experimentally measured ion energy distributions at these low angles, the ion and neutral atom velocity and temperature at the effective inlet were adjusted.

Figure 3.2 shows the ion energy distributions at 18°, 33°, 48°, and 63° from the thruster centerline that are used to model the erosion of a wire. The experimentally measured data and the simulation results after the boundary conditions were adjusted are shown in these figures. The experimentally measured ion energy distributions are an energy per charge distribution, while the results of *MPIC* are the ion energy distributions of only the singly charged ions. At 18° from the thruster centerline, the experimentally measured ion energy distribution has a peak near 280 eV. This peak is the energy of the ions in the beam from the thruster. The simulation accurately captures both the location and height of the peak in the ion energy distribution. This peak is also seen at 33° and 48° from the thruster centerline, but it has a lower magnitude. A peak is seen at energies below 50 eV at 48° and 63° from the thruster centerline. This peak is due to charge-exchange ions, and its location is predicted well by the simulation.

In addition to the ion energy distributions, the experimentally measured ion current density is compared to the ion current density from the simulation in Figure 3.3. While the value of the ion current density on the thruster centerline is well predicted by the simulation, the simulation slightly overestimates the ion current density for angles less than 35° from the thruster centerline and underestimates the ion current density at larger angles from the thruster centerline.

While these ion energy distributions and ion current density agree qualitatively, the results are not exact. These discrepancies are influenced by various factors. An effective inlet along a magnetic field line in the near-field plume is used as the simulation does not account for magnetic field effects. The ion and neutral atom velocity and temperature at this inlet were initially derived from the results of another simulation, *HPHall*, as discussed in Huismann [6]. These boundary conditions were then adjusted to match the operating condition of the thruster and to better match the experimentally measured ion energy distributions. Experimental measurements of the ion and neutral atom velocity and temperature at the effective inlet could improve the agreement, as well as including magnetic field effects.

3.3.2 Wire Erosion Modeling Results

MEOWS is used to predict the profile of an eroded wire that is exposed to the plume for 10 hours at 18°, 33°, 48°, and 63° from the thruster centerline. The experimental measurements and simulation results provide the ion current density and ion energy distributions at those locations. First, the convergence of *MEOWS* with varying time steps is presented. Convergence of *MEOWS* with varying numbers of initial surfaces is not considered in this work. Then, the results of *MEOWS* are compared to the experimentally measured wire profiles.

3.3.2.1 Convergence of the Model

The convergence of *MEOWS* is assessed by varying the time step dt. To measure convergence, the profile after 10 hours of thruster operation is calculated for decreasing values of dt. Convergence is achieved when the difference between all endpoints that start at the same location is within 1% of the wire radius for two successive values of dt.

Results from *MEOWS* with different time steps are shown in Figure 3.4 at 18°, 33°, 48°, and 63° from the thruster centerline using the normal incidence model from Eckstein and Preuss, the angular incidence model from Wei et al., and experimentally measured plume properties. At 18° from the thruster centerline, the profiles converge at dt = 0.05 s. However, at the other three angles considered, the profiles converge at dt = 10 s. Results using other combinations of sputtering yield models or the plume properties from the simulation at 18° from the thruster centerline converge at time steps as high as dt = 0.5 s or have yet to converge for time steps as low as dt = 0.05 s, and results at 33°, 48°, and 63° from the thruster centerline converge at dt = 10 s. As the size of the time step decreases, the erosion depth of each surface per time step decreases. Since the convergence depends on the erosion depth per time step, profiles at different angles from the thruster centerline converge at different time steps. At 18° from the thruster centerline, the erosion depth per time step is high due to the high current density and high energy of most of the ions. Therefore, the time step required to reach convergence is much smaller than the other angles from the thruster centerline.

3.3.2.2 Comparison to Experimentally Measured Profiles

The converged results from *MEOWS* or results with the lowest time step using the experimental measurements and simulation plume properties can be compared to the experimentally measured profiles. These profiles were measured at five different points along the wire and are averaged by x value to give one profile with error bars corresponding to the standard deviation. Since the experimentally measured wire profiles were measured with a profilometer, the exact height is not known. The experimentally measured profiles are then placed at heights that most closely match the results from *MEOWS* in each figure. Figures 3.5, 3.6, 3.7, and 3.8 show the results from *MEOWS* with the plume properties from experiment and simulation at 18°, 33°, 48°, and 63° from the thruster centerline with different combinations of normal and angular incidence sputtering yield models.

Most of the results from *MEOWS* using the plume properties from simulation at 18° from the thruster centerline predict significantly more erosion than the results using the plume properties from experiment and the experimentally measured profiles. The amount of erosion is overestimated because of the difference in the plume properties predicted by the simulation and measured experimentally at this location. The ion current density is higher in the simulation results than in the experimental measurements, and the ion energy distribution in the simulation results predicts more ions will have a higher energy than in the experimental measurements. This difference in the ion energy distribution leads to an increase in the sputtering yield when the plume properties from the simulation are used.

One combination of sputtering yield models predicts less erosion near $x/r_{wire} = 0$ when using the plume properties from simulation than the experimentally measured profiles show, as seen in Figure 3.5d. This difference is due to the dependence of the model parameters of the angular incidence model from Yamamura and Shindo for molybdenum on threshold energy. Since the angular incidence model from Yamamura and Shindo with the threshold energy of the Bohdansky formula predicts more sputtering at the optimal angle than the model with the threshold energy of the normal incidence model from Eckstein and Preuss at its optimal angle, the decrease of the sputtering yield to zero is faster for the model with the threshold energy of the Bohdansky formula than the decrease of the model with the threshold energy of the normal incidence model from Eckstein and Preuss. Peaks are able to form at larger y values due to the sputtering yield decreasing to zero more quickly.

The difference in the results using the simulation data in Figures 3.5a and 3.5c is explained by the differing sputtering yield predicted by the normal incidence sputtering yield models for gold. At energies above 200 eV, the normal incidence model from Ikuse et al. predicts more sputtering than the normal incidence model from Eckstein and Preuss. Therefore, the gold layer erodes away faster when the normal incidence model from Ikuse et al. is used. Since the gold layer coats the wire, this difference in the sputtering yields affects the profile even when a large amount of erosion has occurred.

The results using the experimentally measured plume properties and the angular incidence sputtering yield model from Yamamura and Shindo at 18° from the thruster centerline predict a taller peak than the results using the angular incidence model from Wei et al. This taller peak forms because the angular incidence model from Yamamura and Shindo predicts the sputtering yield rapidly decreases to zero at angles of incidence beyond the optimal angle, as shown previously in Figure 2.3. Therefore, very little erosion of surfaces with large angles of incidence occurs. Since the angular incidence model from Wei et al. does not approach zero as quickly as the angular incidence model from Yamamura and Shindo, the tall peak is not seen in the profiles using the angular incidence model from Wei et al. The results at 18° from the thruster centerline using the experimentally measured plume properties and the angular incidence sputtering yield model from Wei et al. capture the height of the peak of the experimentally measured profiles. The small, jagged features in the results form because adjacent surfaces have different angles of incidence, which leads to different amounts of erosion of each surface.

At 33° from the thruster centerline, the results from *MEOWS* using the plume properties from the simulation predict more erosion than the results using the experimentally measured plume properties, as shown in Figure 3.6. This overestimation is again due to the ion current density from the simulation results being higher than the experimentally measured ion current density. While all results shown in Figure 3.6 predict the erosion near $x/r_{wire} = 0$ well, the angular incidence model from Yamamura and Shindo with the experimental dataset best captures the erosion depth near $x/r_{wire} = \pm 1$. This is because the model from Yamamura and Shindo predicts low sputtering yields at angles of incidence beyond the optimal angle. The results from *MEOWS* at 48° and 63° from the thruster centerline predict a small amount of erosion, as seen in Figures 3.7 and 3.8. The differences between the predictions using different datasets or different sputtering yield models are not significant. All results at these angles predict the experimentally measured profiles well.

At each location in the plume, the results from *MEOWS* using the four different combinations of sputtering yield models can be averaged to produce an average profile. The average is calculated by first determining the angle between the line segment from $(0, -r_{wire})$ to each endpoint in the profile from the line $y = - r_{wire}$. The endpoints with the closest angle are then averaged. The average profiles using the plume properties from experiment and simulation are shown in Figure 3.9, with error bars corresponding to the standard deviation. At 18° from the thruster centerline, the averaged profile using the plume properties from simulation again overestimates the amount of erosion. The averaged profile using the plume properties from experiment matches the experimentally measured profile relatively well, as the endpoints in the average profile agree with the measured points with the closest x value to within 20% of a wire radius. The tall peak seen previously in the profiles using the angular incidence model from Yamamura and Shindo has been reduced because the profiles using the angular incidence model from Wei et al. do not have that feature.

At 33° from the thruster centerline, both averaged profiles capture the erosion near $x/r_{wire} = 0$. However, neither averaged profile accurately captures the profile near $x/r_{wire} = \pm 1$ because the sputtering yield predicted by the angular incidence model from Wei et al. does not decrease to zero as rapidly as the sputtering yield predicted by the angular incidence model from Yamamura and Shindo does, leading to more erosion at large angles of incidence. The averaged result using the experimentally measured plume properties agrees with the average measured profile to within 35% of a wire radius, with the differences more than 20% of the wire radius near $x/r_{wire} = -1$. At 48° and 63° from the thruster centerline, the averaged profiles predict the experimentally measured data relatively well. Differences between the average measured profile are within 20% of the wire radius at all endpoints except near $x/r_{wire} = \pm 1$.

While the results from *MEOWS* using the plume properties from experiment best predict the experimentally measured wire profiles, the results using the simulated plume properties give a good estimate of the erosion. This estimate captures the experimentally measured profiles relatively well at 33°, 48°, and 63° from the thruster centerline. While the erosion at 18° from the thruster centerline is not accurately captured by results using the plume properties from simulation, the results using the simulated plume properties still predict that the wire will be significantly eroded. Therefore, *MEOWS* can be used with simulated plume properties to estimate the erosion of a wire in the plume of EP devices if experimentally measured properties are not available.

3.4 Discussion

Because the erosion of a wire differs from the erosion of a planar surface due to the change in angle of incidence around the wire, estimates of erosion of meshed reflectors assuming these reflectors are planar surfaces can underestimate the erosion experienced by the reflector. The erosion depth of a flat molybdenum surface coated with gold is shown in Figure 3.10 after being exposed to the plume for 10 hours. This erosion depth is calculated using the normal incidence model from Eckstein and Preuss, the angular incidence model from Wei et al., and the experimentally measured plume properties at 18° from the thruster centerline. The maximum modeled erosion depth on a wire after being exposed to the plume for the same amount of time is also shown using the same sputtering yield models and plume properties. At angles of incidence near the optimal angle of the angular incidence model from Wei et al. for molybdenum, the erosion depth assuming a planar surface matches the maximum erosion depth on a wire. However, at angles of incidence above or below the optimal angle, the erosion depth assuming a planar surface is much less than the maximum erosion depth on a wire under the same conditions. Since significant amounts of erosion can damage the meshed reflector, underestimating the erosion can lead to unexpected decreased performance or failure of the meshed reflector.

Averaging the results from *MEOWS* across the different sputtering yield models produces better agreement with the experimentally measured profiles than considering one combination of sputtering yield models. While the angular incidence sputtering yield models from Wei et al. and Yamamura and Shindo predict different sputtering yields at various angles of incidence, these differences are averaged out when the average of the profiles is taken, as seen in Figure 3.9a. The averaging can also reduce the uncertainties associated with the sputtering yield models. While the model parameters of the sputtering yield models have an uncertainty, using two different sputtering yield models and averaging those results can better estimate the actual sputtering yield.

3.5 Concluding Remarks

EP devices used on satellites can affect many components of the satellite, including meshed reflectors that are composed of small wires. This chapter detailed the validation of *MEOWS* to predict the eroded profile of a single wire exposed to the plume of an EP device. *MEOWS* discretized the cross-section of a wire into planar surfaces and calculated how those surfaces erode through time. *MEOWS* required the ion energy distribution and the ion current density at the location of the wire in the plume to calculate the erosion depth of each discretized surface. These parameters were either determined by a plume simulation or measured experimentally.

Experimental testing was conducted at the University of Michigan to measure the plume properties and the eroded wire profiles, which is detailed in Byrne et al. [5]. The results of the experimental testing were compared to the results of the plume simulation *MPIC* and to the results of *MEOWS*. Using different normal and angular incidence sputtering yield models in *MEOWS* produced different profiles. The differences between these sputtering yield models were especially prominent in the profile at 18° from the thruster centerline, where a large amount of erosion occurs in 10 hours. The profiles with different sputtering yield models were averaged at each location in the plume, and these averaged profiles provided good agreement with the experimentally measured profiles.

While the experimentally measured plume properties best predict the experimentally measured profiles, the plume properties from the simulation predicted the amount of erosion relatively well, especially at large angles from the thruster centerline. Therefore, *MEOWS* can be used to predict the erosion of a wire in the plume of other electric propulsion devices, even if the experimentally measured ion current density and ion energy distributions are not available. This prediction is valuable as the amount of erosion can affect the performance of meshed reflectors.

3.6 Figures

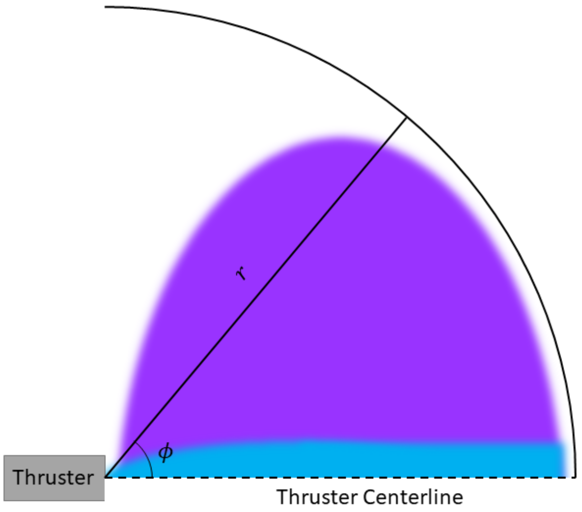

Figure 3.1. Location on an arc of distance r and angle ϕ from the thruster centerline.

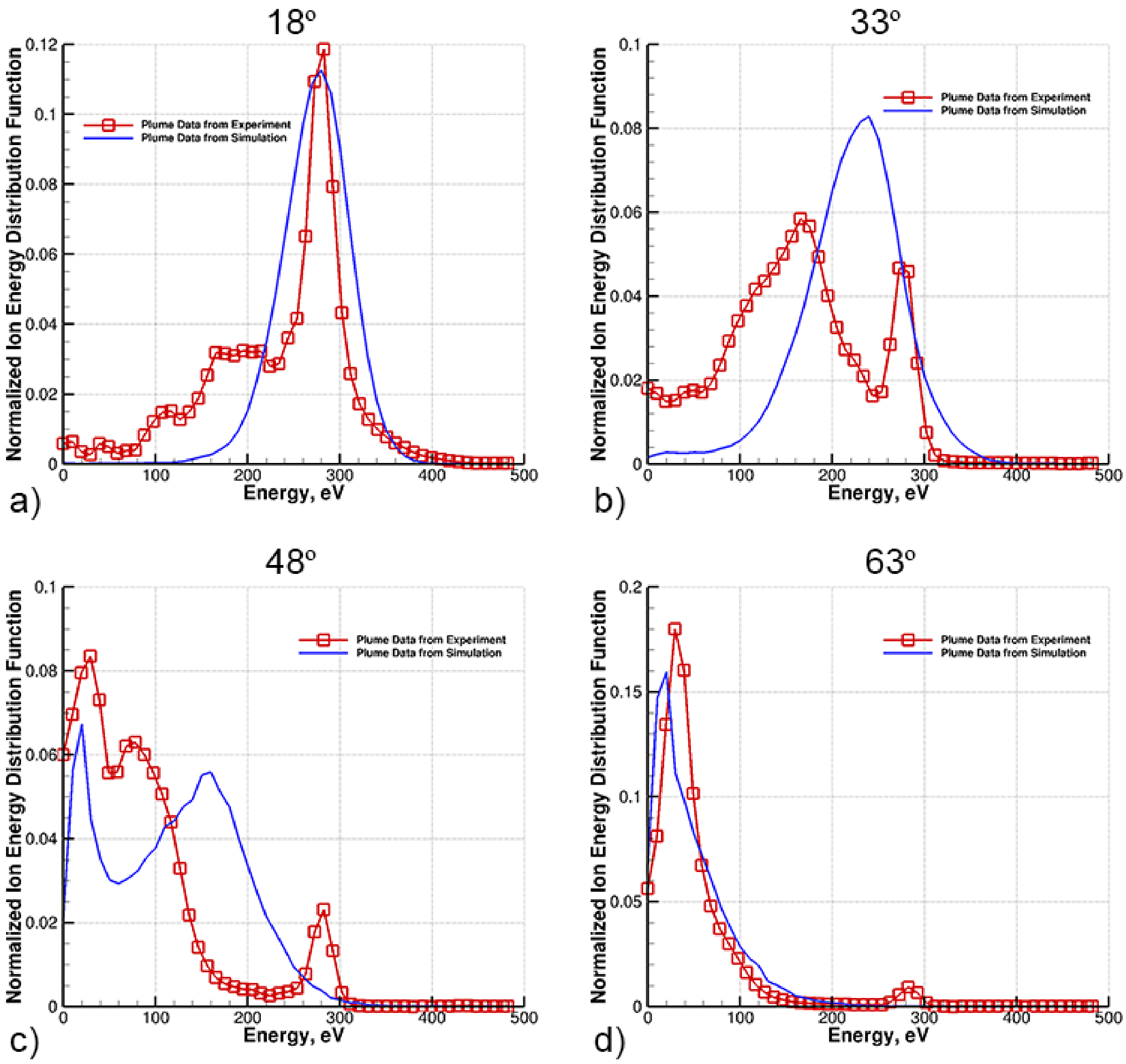

Figure 3.2. Ion energy distributions at 1 m from the thruster exit at (a) 18°, (b) 33°, (c) 48°, and (d) 63° from the thruster centerline.

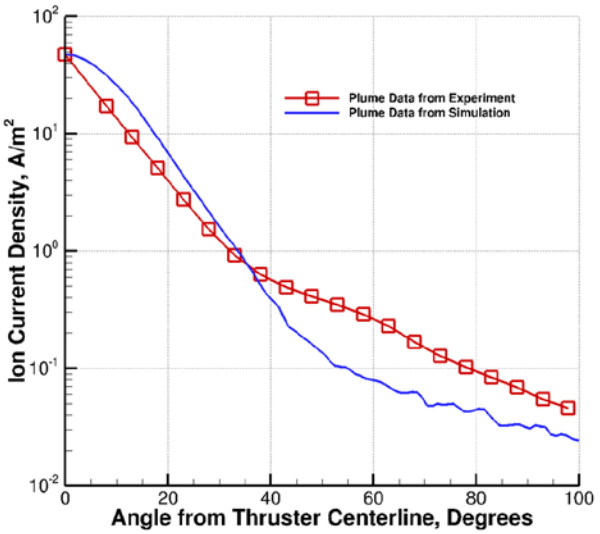

Figure 3.3. Ion current density at 1 m from the thruster exit.

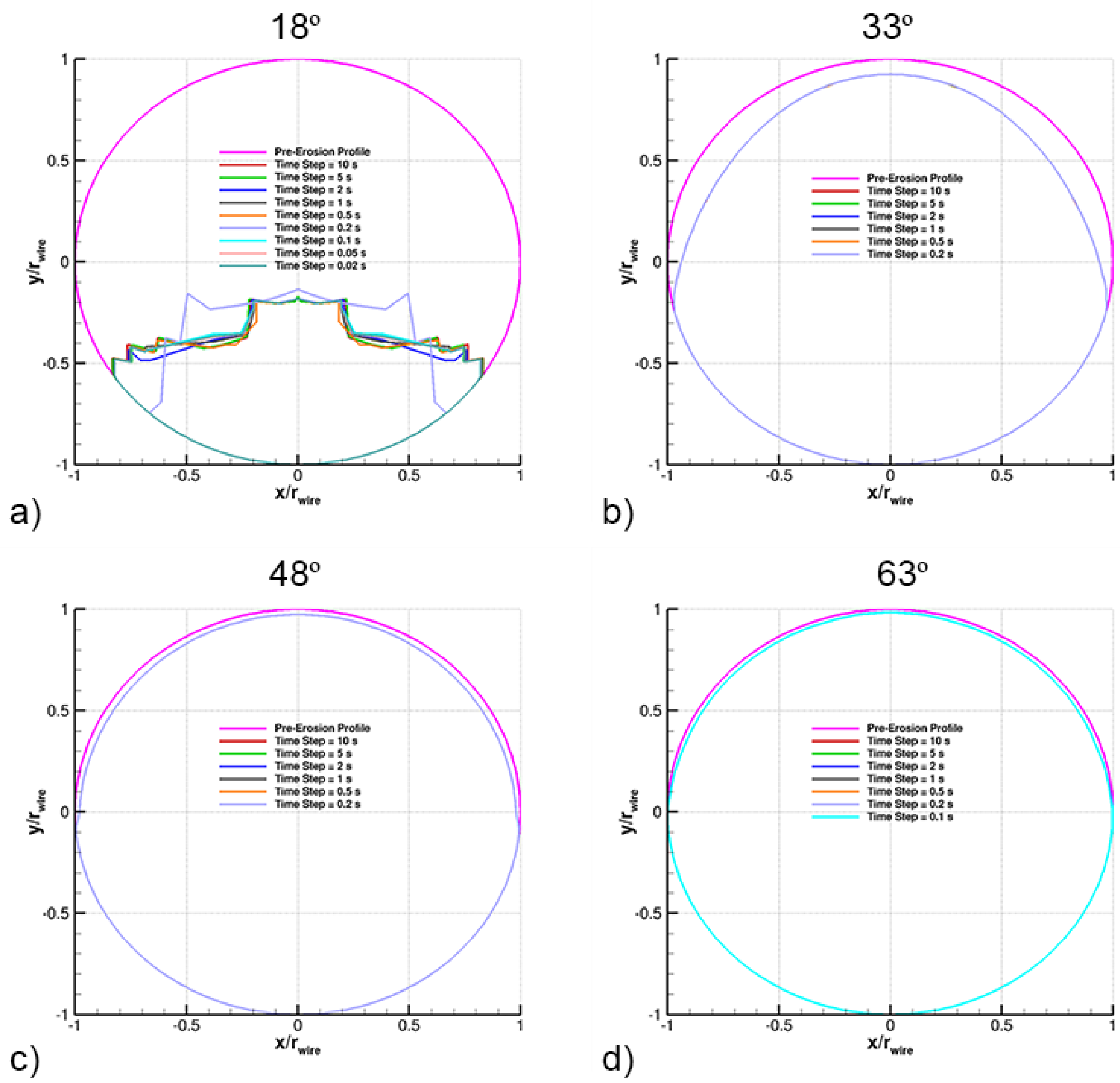

Figure 3.4. Convergence of *MEOWS* with the normal incidence model from Eckstein and Preuss and angular incidence model from Wei et al. at (a) 18°, (b) 33°, (c) 48°, and (d) 63° from the thruster centerline. Plume properties taken from experimental measurements.

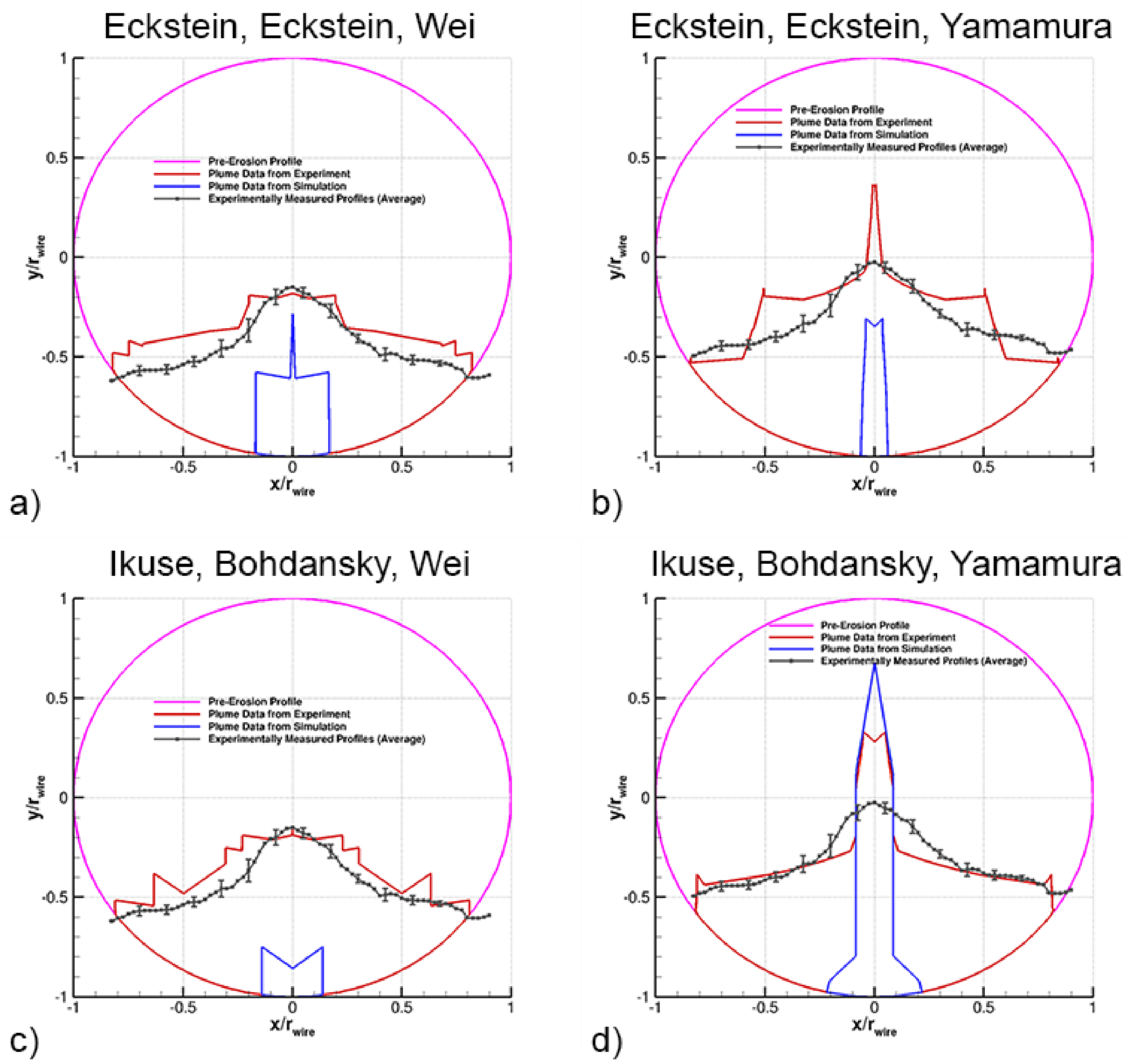

Figure 3.5. Comparison of the results from *MEOWS* and experimentally measured profiles at 18° from centerline. Results using (a) normal incidence model from Eckstein and Preuss and angular incidence model from Wei et al., (b) normal incidence model from Eckstein and Preuss and angular incidence model from Yamamura and Shindo, (c) normal incidence model from Ikuse et al. for gold, normal incidence model from Bohdansky for molybdenum, and angular incidence model from Wei et al., (d) normal incidence model from Ikuse et al. for gold, normal incidence model from Bohdansky for molybdenum, and angular incidence model from Yamamura and Shindo.

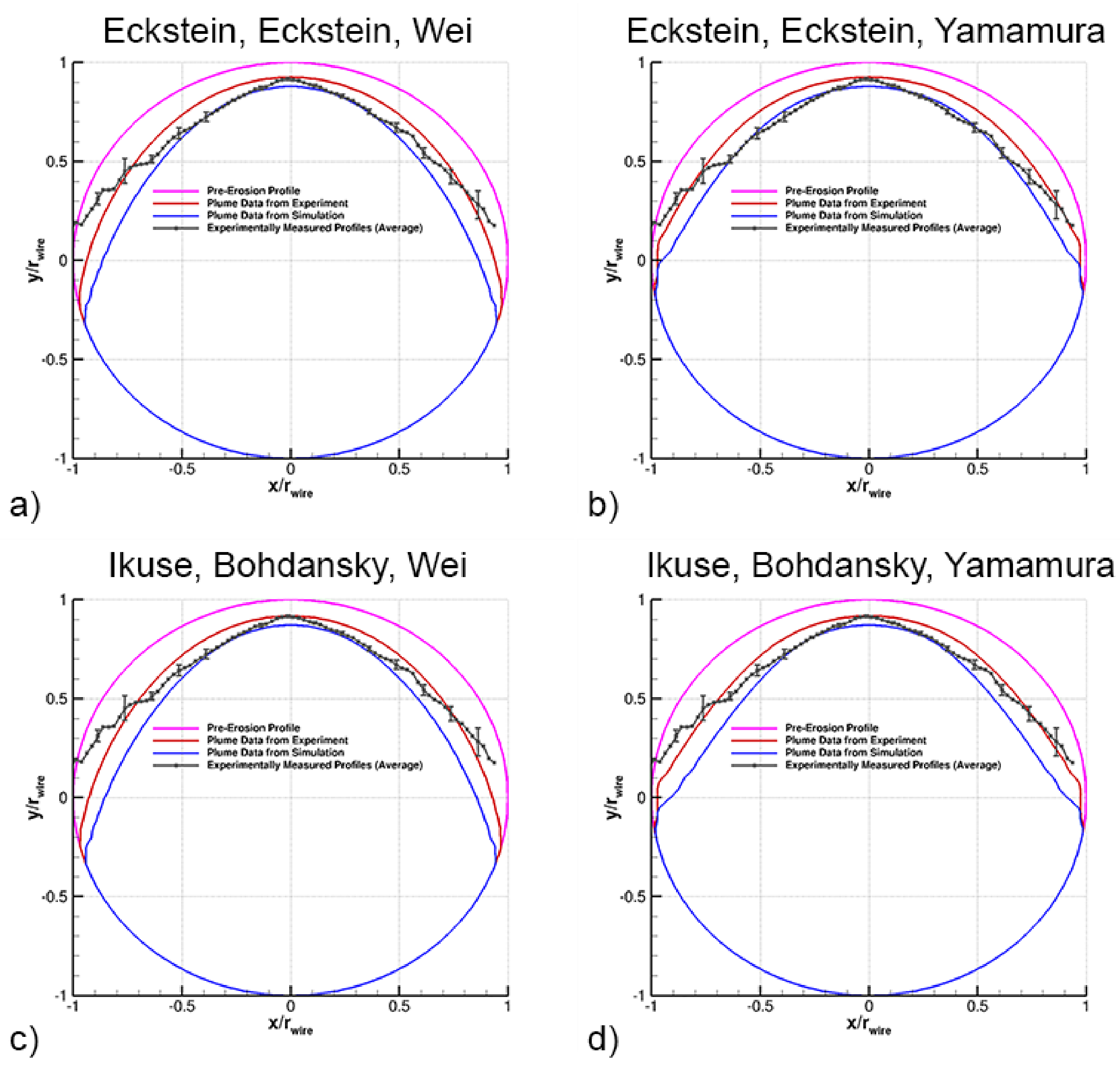

Figure 3.6. Comparison of the results from *MEOWS* and experimentally measured profiles at 33° from centerline. Results using (a) normal incidence model from Eckstein and Preuss and angular incidence model from Wei et al., (b) normal incidence model from Eckstein and Preuss and angular incidence model from Yamamura and Shindo, (c) normal incidence model from Ikuse et al. for gold, normal incidence model from Bohdansky for molybdenum, and angular incidence model from Wei et al., (d) normal incidence model from Ikuse et al. for gold, normal incidence model from Bohdansky for molybdenum, and angular incidence model from Yamamura and Shindo.

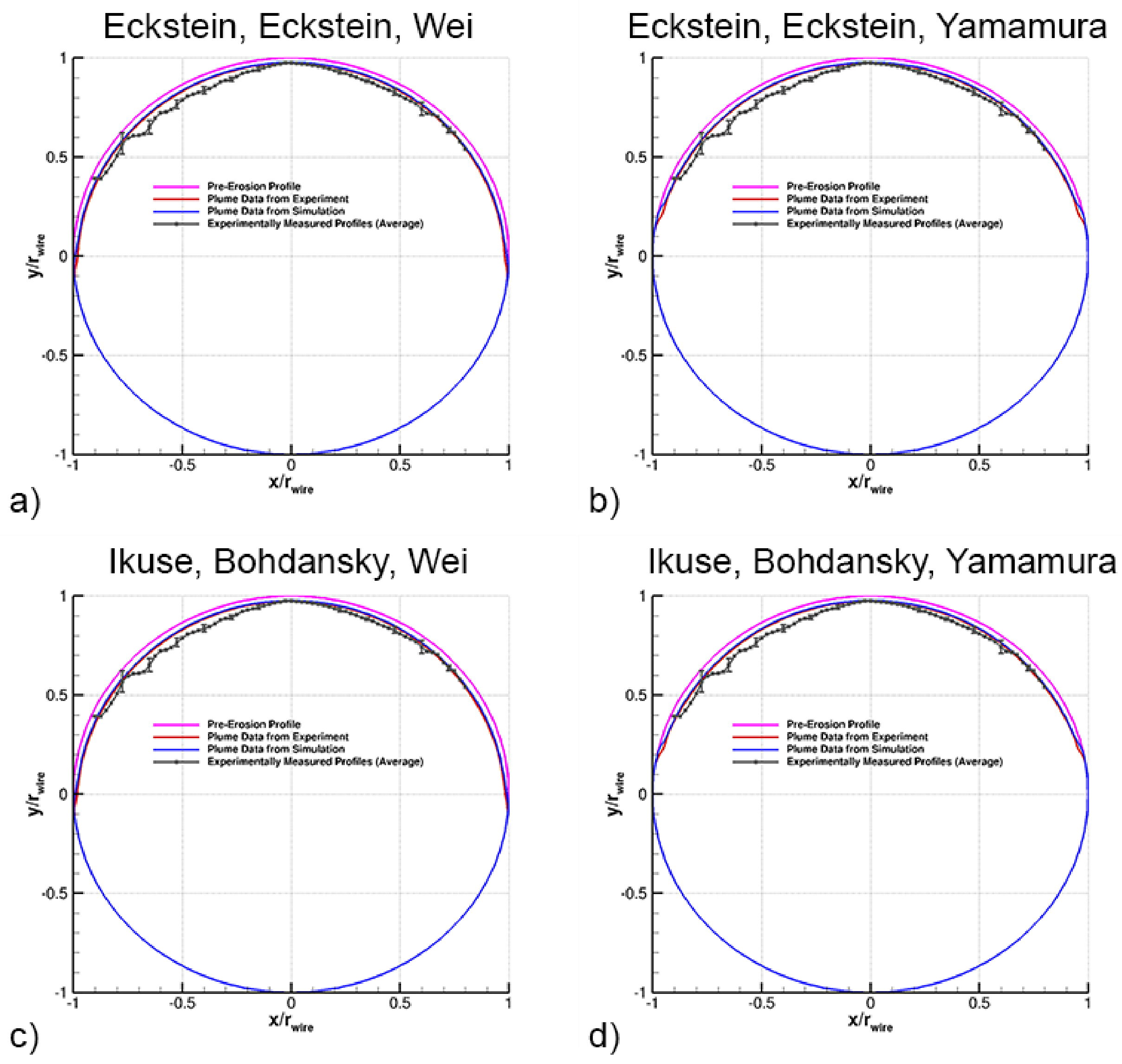

Figure 3.7. Comparison of the results from *MEOWS* and experimentally measured profiles at 48° from centerline. Results using (a) normal incidence model from Eckstein and Preuss and angular incidence model from Wei et al., (b) normal incidence model from Eckstein and Preuss and angular incidence model from Yamamura and Shindo, (c) normal incidence model from Ikuse et al. for gold, normal incidence model from Bohdansky for molybdenum, and angular incidence model from Wei et al., (d) normal incidence model from Ikuse et al. for gold, normal incidence model from Bohdansky for molybdenum, and angular incidence model from Yamamura and Shindo.

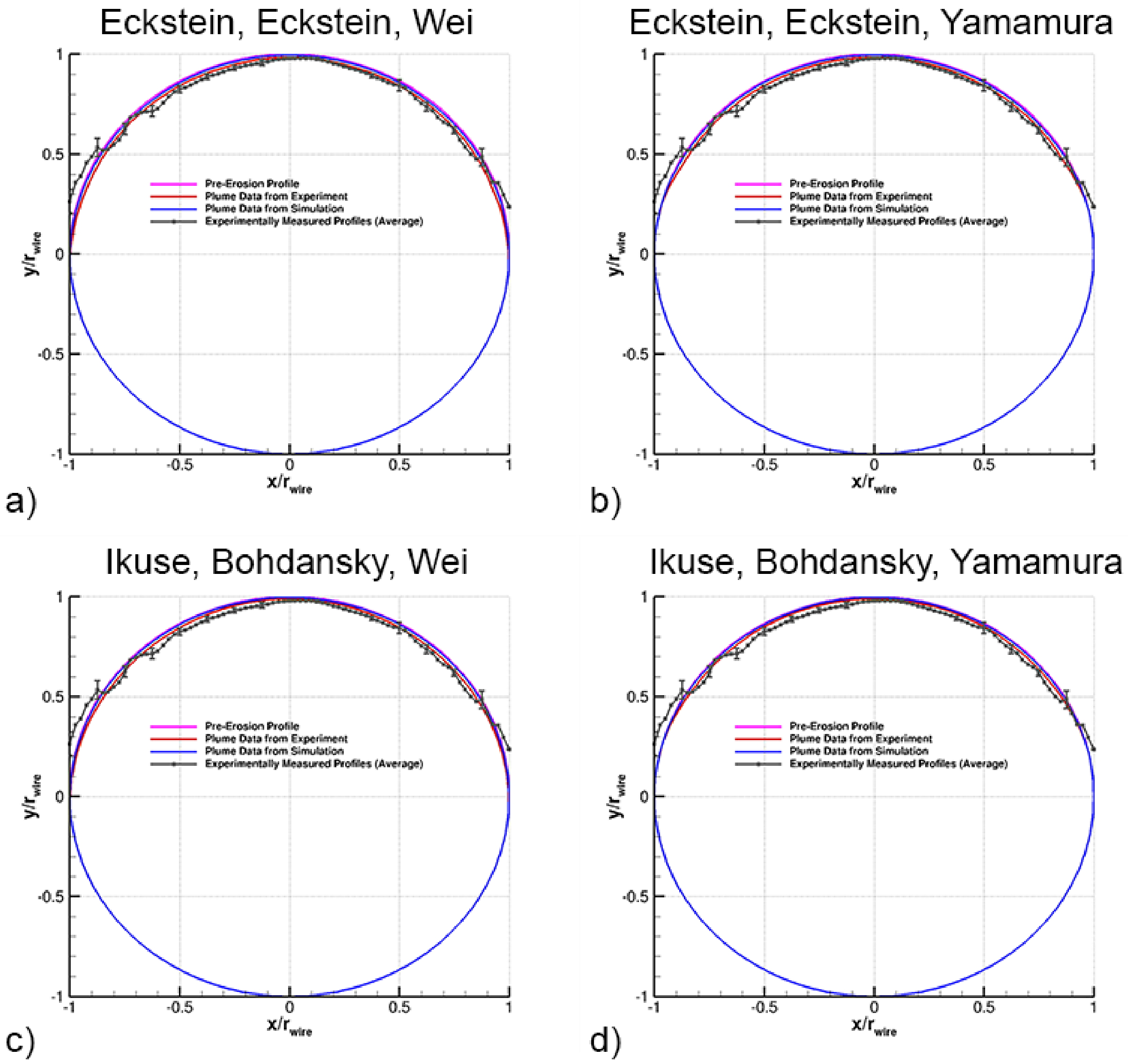

a) Eckstein, Eckstein, Wei

b) Eckstein, Eckstein, Yamamura

c) Ikuse, Bohdansky, Wei

d) Ikuse, Bohdansky, Yamamura

Figure 3.8. Comparison of the results from *MEOWS* and experimentally measured profiles at 63° from centerline. Results using (a) normal incidence model from Eckstein and Preuss and angular incidence model from Wei et al., (b) normal incidence model from Eckstein and Preuss and angular incidence model from Yamamura and Shindo, (c) normal incidence model from Ikuse et al. for gold, normal incidence model from Bohdansky for molybdenum, and angular incidence model from Wei et al., (d) normal incidence model from Ikuse et al. for gold, normal incidence model from Bohdansky for molybdenum, and angular incidence model from Yamamura and Shindo.

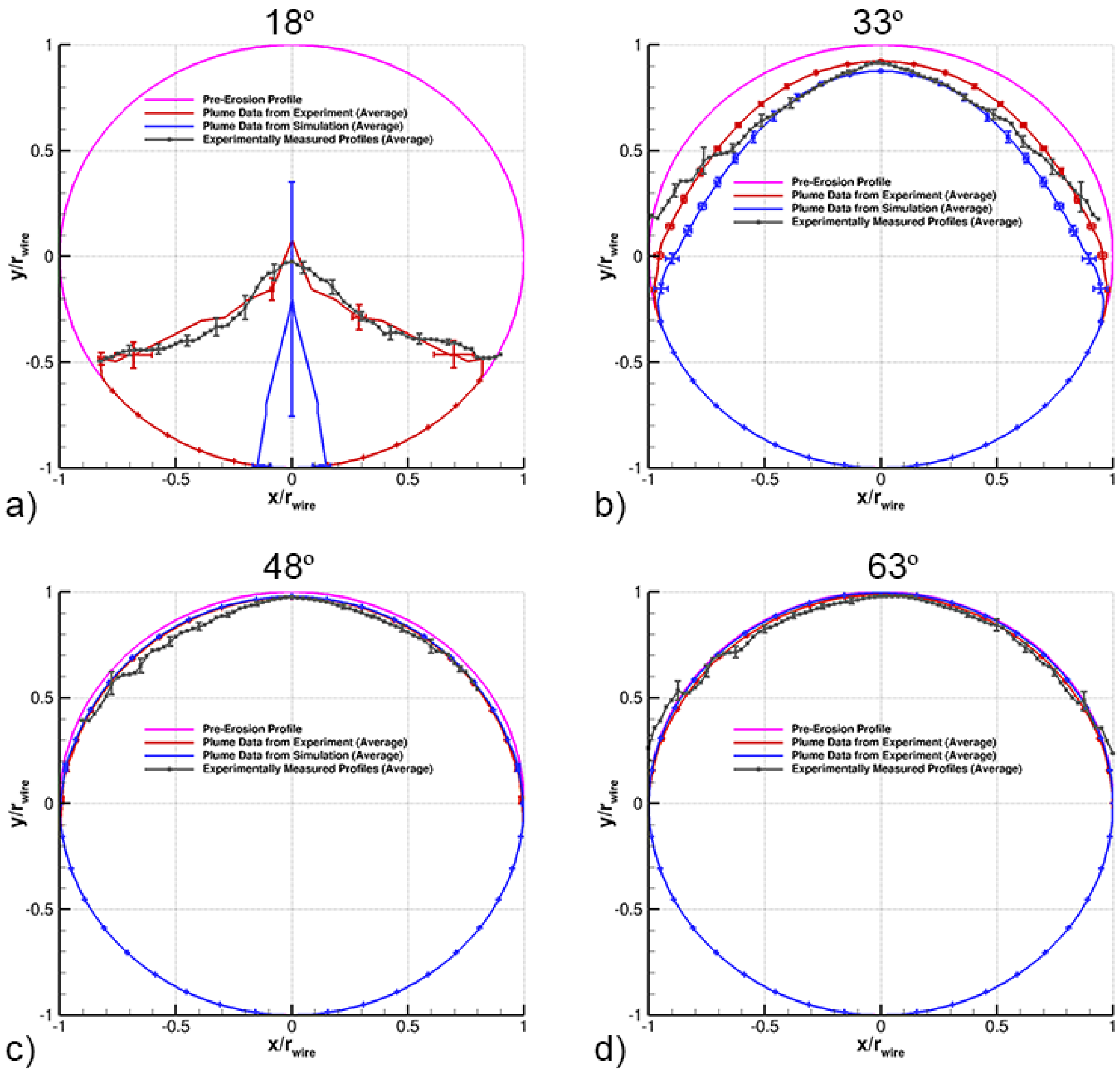

Figure 3.9. Comparison of the average of the results from *MEOWS* and experimentally measured profiles at (a) 18°, (b) 33°, (c) 48°, and (d) 63° from the thruster centerline.

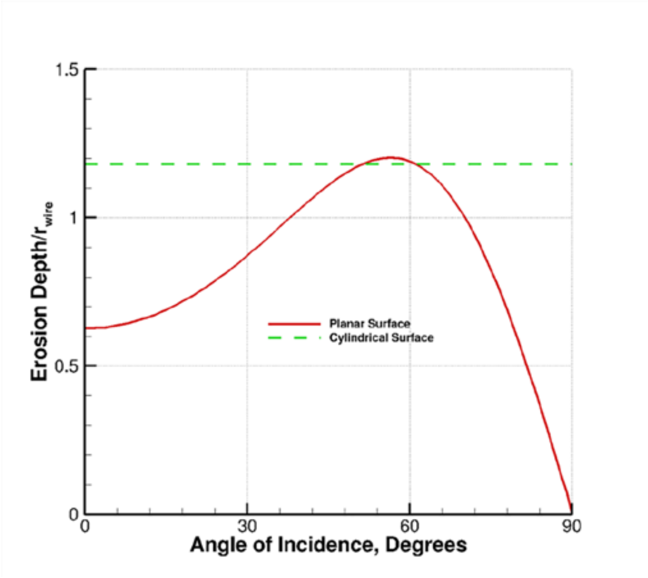

Figure 3.10. Erosion depth of a planar surface for different angles of incidence. The maximum erosion depth on a wire is plotted for reference.

3.7 References

[1] D. Y. Oh, D. E. Hastings, C. M. Marrese, J. M. Haas and A. D. Gallimore, J. Propuls. Power **15,** 345 (1999).

[2] I. D. Boyd and M. L. Falk, AIAA 37th Joint Propulsion Conference, AIAA Paper 2001-3353 (2001).

[3] J. T. Yim, 35th International Electric Propulsion Conference, Paper IEPC-2017-060 (2017).

[4] B. Rubin, Topper J L, C. C. Farnell and A. P. Yalin, Rev. Sci. Instrum. **80,** 103506 (2009).

[5] M. P. Byrne, M. E. Meyer, I. D. Boyd and B. A. Jorns, AIAA Propulsion and Energy 2019 Forum, AIAA Paper 2019-3988 (2019).

[6] T. D. Huismann, "Improving Hall Thruster Plume Simulation through Refined Characterization of Near-field Plasma Properties," Ph.D. Thesis (University of Michigan Ann Arbor, 2011).

[7] I. D. Boyd and J. T. Yim, J. Appl. Phys. **95,** 4575 (2004).

[8] E. Ahedo, P. Martínez-Cerezo and M. Martínez-Sánchez, Phys. Plasmas **8,** 3058 (2001).

[9] D. L. Brown, "Investigation of low discharge voltage Hall thruster characteristics and evaluation of loss mechanisms," Ph.D. Thesis (University of Michigan Ann Arbor, 2009).

[10] B. M. Reid, "The influence of neutral flow rate in operation of Hall thrusters," Ph.D. Thesis (University of Michigan Ann Arbor, 2009).

[11] R. Shastry, "Experimental Characterization of the Near-Wall Region in Hall Thrusters and its Implications on Performance and Lifetime," Ph.D. Thesis (University of Michigan Ann Arbor, 2011).

[12] M. Tartz, T. Heyn, C. Bundesmann, C. Zimmermann and H. Neumann, Eur. Phys. J. D **61,** 587 (2011).

[13] K. Ikuse, S. Yoshimura, K. Hine, M. Kiuchi and S. Hamaguchi, J. Phys. D. Appl. Phys. **42,** 135203 (2009).

Chapter 4 Quantifying Uncertainty in Predictions of Spacecraft Erosion Induced by a Hall Thruster[2]

The impact of sputtering yield model uncertainty on the predicted erosion of a meshed reflector wire exposed to a Hall effect thruster plume was investigated. Quantifying this uncertainty is critical for making informed assessments of reflector lifetime. The erosion is modeled by *MEOWS* and assumes known ion current density and energy distribution at the location of the wire. The wire surface is then discretized, and wear is evaluated incrementally over time. The confidence in model predictions is quantified where the major source of uncertainty is assumed to stem from the material sputtering yield. *MEOWS* is run to simulate reflector erosion after 10 h of exposure to a 3 kW class Hall thruster operating at 300 V. The simulated results then are compared to experimental measurements from a dedicated wear test performed on a series of mesh coupon samples. The experimental results are shown to fall largely within the 95% credible intervals from model predictions, though the uncertainty in the maximum predicted erosion is found to be up to 190% of the maximum predicted erosion. These results are discussed in the context of predicting lifetime of reflectors on orbit and the need for margin in this component design.

4.1 Introduction

The Hall effect thruster is a form of in-space propulsion that has a higher propellant efficiency compared to more traditional chemical rockets. This high fuel efficiency, which stems

---

[2] The results discussed and portion of the text in this chapter have been previously published in M.E. Meyer et al., “Quantifying Uncertainty in Predictions of Spacecraft Erosion Induced by a Hall Thruster,” Journal of Spacecraft and Rockets, **59**, 988 (2021).

from the ability of these devices to accelerate their propellant to high speeds (> 20 km/s), makes the Hall thruster ideally suited for a wide range of applications, such as orbit raising and station keeping, where propellant efficiency is paramount. Yet, while Hall thrusters have been shown to be a reliable technology, there are a number of systems-level challenges with integrating these devices on spacecraft. Most notably, the energetic xenon exhaust of these systems can impinge on and erode surfaces mounted adjacent to the thruster through ion-impact sputtering. Over sufficiently long exposure times, this erosion poses a risk to these nearby components [1–4].

There is a major potential source of uncertainty in most modeling efforts performed to date that stems from how the sputtering yield (the number of eroded particles per incident ion) of the material is modeled. This uncertainty can lead to significant variance in prediction for the key erosion processes.

The large uncertainty in the sputtering models stems from the fact that they are primarily semi-empirical. They must be calibrated against datasets where the quality, applicability, and sparsity in the data all contribute to the model uncertainty [5–15]. For example, in many cases, the data employed to calibrate the models are generated under controlled conditions that are not representative of the plume environment. Similarly, many datasets do not extend to the lower energies (< 100 eV) typical of the peripheries of Hall thruster plumes. To capture the erosion of spacecraft materials, extrapolation thus must be performed based on the model. This can lead to high levels of uncertainty, often multiple orders of magnitude, in the estimated sputtering yield. This effect is compounded by the fact that many sputtering models are highly nonlinear in the lower energy regime [16]. As the rate of erosion of materials scales linearly with the sputtering yield of the material, this uncertainty in principle could translate to low levels of confidence in spacecraft erosion predictions. In light of the critical challenge posed by the plume-spacecraft interaction, there is a pressing need to quantify the impact of this uncertainty on the confidence in model predictions for erosion.

The goal of this chapter is to assess the role of sputtering yield uncertainty on the results of *MEOWS*, a recently-validated model for the erosion of coated rounded wires subject to the plume of a xenon-based Hall effect thruster [17,18]. This particular application is motivated by the widespread use of this type of thin wire geometry in communications antennae. This chapter is organized in the following way. In Section 4.2, the framework for performing forward uncertainty quantification for erosion predictions is described. In Section 4.3, following the approach first described by Yim [16] and employed by others [19–21], Bayesian inference is applied to quantify the uncertainty in sputtering yield for the two constituent materials in the coated wire, gold and molybdenum. In Section 4.4, the details of the experimental setup and data that were used to validate the model developed in the previous chapter are briefly reviewed [17,18]. In Section 4.5, the model predictions under uncertainty are compared to experimental datasets. In Section 4.6, the results are discussed in the context of the limitations of the model and future implications for assessing erosion due to plume-spacecraft interactions. Concluding remarks are given in Section 4.7.

4.2 Model Description

MEOWS and the sputtering yield models employed are discussed in Section 2.1. In Chapter 3, the best agreement between the model predictions and experimentally measured wire profiles occurred when the normal incidence from Eckstein and Preuss and angular factor from Wei et al. were used [5,8]. To illustrate how the angular factor affects the predicted wire profiles, the angular factor from Yamamura and Shindo is also used [6], assuming f and θ_{opt} are independent of incident ion energy. The cross-section of the wire is divided into 200 planar surfaces. In this section, the quantification of the confidence in the model predictions due to uncertainty in the sputtering yields is discussed.

4.2.1 Uncertainty Quantification in Model Predictions

There are multiple sources of uncertainty for *MEOWS* as described in Section 2.1. These include uncertainty in the model inputs as well as uncertainty in the model parameters in the sputtering yields. However, since experimental measurements for the plasma properties are used, which are taken with a high degree of certainty, the dominant source of uncertainty is assumed to stem from the model parameters, $\Theta = (\lambda, f, ...)$ in the sputtering yield models. The uncertainty associated with these parameters is represented by treating them as random variables described by probability distribution $P(\Theta)$. Provided this distribution of parameters is known (discussed in Section 4.3), the impact of model uncertainty on the predictions of erosion can be quantified by random sampling from the distribution and running the model multiple times.

To this end, for a given measured input of ion current density and ion energy distribution, this distribution of model parameters is randomly sampled from 10,000 times, and these values are applied in *MEOWS* to produce 10,000 unique eroded wire profiles. These profiles are correlated by placing the endpoints from each segment into bins based on angle ϕ from the point $(0, -r_{wire})$ and line segment defined by $y = -r_{wire}$ and the positive x direction. As depicted in Figure 4.1, the center of the bins ϕ are chosen based on the angle of the initial points on the discretized surface, and the bounds of the bins are the averages of the two adjacent angles. The inclusivity of the bounds of the bins are chosen to be symmetric around $\phi = 90°$, where the point farthest from $\phi = 90°$ is inclusive and the other is exclusive, except at $\phi = 90°$, where both are inclusive. At the edges, the bins are between $\phi \in [0°, \phi_1/2)$ and $\phi \in ((\phi_n + 180°)/2, 180°]$ where ϕ_n represents the angle of the last point as measured counterclockwise from $(0, -r_{wire})$.

The 10,000 profiles are binned into data sets, and the distribution of distance $r(\phi_i)$ of the endpoints from the point $(0, -r_{wire})$ in each bin are known. From these, the median $(r_{50}(\phi_i))$, 5th percentile $(r_5(\phi_i))$, and 95th percentile $(r_{95}(\phi_i))$ distances from $(0, -r_{wire})$ are calculated. These distances are then translated into points, $(x(\phi_i), y(\phi_i))$ for the i^{th} bin, by using the angle at the center of the bin. In this way, predictions for the median erosion profile and credible intervals are created based on the variance in the sputtering yield measurements. The uncertainty of the erosion is also calculated by taking the distance between the 5th percentile and median in each bin, $r_{50}(\phi_i) - r_5(\phi_i)$, and the distance between the 95th percentile and median in each bin, $r_{95}(\phi_i) - r_{50}(\phi_i)$. These values represent the uncertainty of the upper and lower limits of erosion, respectively. The erosion depth of the median profile is determined by taking the distance between the median distance and the point on the initial profile in each bin, $r_{initial} - r_{50}(\phi_i)$, where $r_{initial}$ is the distance between the initial point in each bin and $(0, -r_{wire})$. The maximum erosion of the median profile is reported with + and - margins, where the + value corresponds to the maximum distance between the 5th percentile and median and the - value corresponds to the maximum distance between the 95th percentile and median. Note these maximum quantities are not necessarily found in the same angular bin. The relative uncertainty, or the maximum distance between the 5th percentile and median divided by the maximum erosion of the median, is also calculated. This relative uncertainty represents the worst-case scenario of uncertainty in the erosion estimates. To assess convergence with number of samples, the relative uncertainty was computed for varying numbers of samples. The relative uncertainty differs by less than 2 percentage points after 6000 samples. Similarly, to calculate the maximum erosion of the experimental measurements, the points in the experimental measurements are sorted into the same bins and calculate $r_{initial} - r_{exp}$, where r_{exp} is the distance of the experimental profiles from $(0, -r_{wire})$. The maximum is then taken.

4.3 Model Parameter Inference for Sputtering Yield Models

As discussed in Section 2.1.1, the sputtering yield can be represented as

$$Y(E,\theta)=Y(E)Y(\theta), \tag{4.1}$$

where Y(E) is the energy dependent normal incidence model and Y(θ) is the angular factor. Both the normal incidence model and angular factor employed for sputtering are semi-empirical. Thus, while the form of each model is rooted in a physical understanding of the process of sputtering, they must be calibrated against experimental data. The resulting model parameters inferred from this calibration have inherent uncertainty that stem from both variance in the data and the fidelity of the model. This uncertainty in model parameters Θ is represented with the characteristic probabilistic distributions P(Θ) introduced in Section 4.2.1. This section describes the method for inferring these distributions from sputtering datasets compiled from previous work. This is based on the same analysis technique used by Yim [16] and is rooted in a Bayesian approach.

Following this Bayesian approach to model inference, the model parameters are treated as random variables where their probability distribution can be inferred from experimental data,

$$P(\Theta)\propto L(d\,|\,\Theta)\pi(\Theta), \tag{4.2}$$

where π(Θ) is the joint prior probability distribution of the parameters and L(d | Θ) is the likelihood function of data set d. The prior probability distribution is based on a prior belief about the distribution of the parameter. For this work, following the approach of Yim [16], uniform distributions for all model parameters are chosen where the possible ranges of each of these distributions are based on previously published parameter fits [5,6,8,16]. The likelihood function indicates the probability that, assuming the model with model parameters Θ is correct, measurements would yield the data set d. While it is a common practice to employ a Gaussian distribution for the likelihood, following Yim, this chapter uses a likelihood function based on a log-normal distribution, given by

$$L\left(d \mid \Theta\right) = \prod_{j=1}^{N} \frac{1}{\sigma\sqrt{2\pi}} \exp\left(-\frac{1}{2\sigma^2} \left(\log\left(\frac{y_j}{M\left(x_j;\Theta\right)} \right) \right)^2 \right), \tag{4.3}$$

where x_j and y_j are independent and dependent elements, respectively, of the data set d, N is the number of points in the data set, $M(x_j; \Theta)$ is the model, and σ is assumed to be 1. σ is assumed to be 1 due to the high variance in the disparate data sets used. Since the stated error σ in these data does not come close to encompassing this variance in the data points, it is not included in this analysis. If σ was on the order of the variance in the data points, it could be included in this formulation.

The experimental data used in the likelihood function was extracted from data sets from several previous sputtering studies [7,9–15]. These consisted of measurements of both the normal incidence sputtering as a function of energy (Figure 4.2) and the angular factor of sputtering (Figure 4.3) for xenon ions on both gold and molybdenum. As can be seen, the magnitudes of the reported data can vary significantly depending on the study (c.f. Figure 4.2b). This underscores the inherent uncertainty in these data that results from variance in the test and testing conditions. With this in mind, the compiled datasets were substituted into Eq. (4.2), and the probability distribution of the model parameters was generated by employing a nested sampling Markov chain Monte Carlo routine [22]. For the analysis of each model, 10,000 live points were used, which are iterated upon approximately 200,000 times. A representative result of the probability distributions generated by inferring the parameters from the Eckstein and Preuss normal incidence model for xenon sputtering of molybdenum is shown in Figure 4.4. The probability distribution in this case is represented in two ways: with joint distributions and marginal distributions. The joint distributions show the partially marginalized probability distribution as a function of two of the model parameters. Each distribution is normalized such that the labeling indicates the total percentage of samples that are contained below the contour. The marginal distributions plot the probability of the single model parameter.

The probability distributions are a graphical indication of the model parameters that best match the data and the relative confidence in these parameters. The peaks in each distribution correspond to the most probable value for the parameter. The characteristic width of the marginal distributions represents the relative uncertainty in the parameters. This uncertainty ultimately stems from the spread in the experimental data as well as the limited fidelity of the semi-empirical models.

By sampling from these joint distributions, the impact of parameter uncertainty on the model predictions can be represented. By assuming that the most probable model fits are the ones most likely to represent reality, the uncertainty in the fits can be propagated to predict the most likely erosion rates. To this end, one of the elements Θ from the joint distribution is selected as described previously to evaluate the sputtering yield at each energy E (for normal incidence, $Y(E)$) and angle θ (for the angular factor, $Y(\theta)$). This process is repeated for all samples to yield a data set of predicted sputtering at the given energy or angle. The resulting median of these data sets (solid line) along with 5th and 95th percentiles (dashed lines) are shown in Figures 4.2 and 4.3. To be clear, the credible intervals for sputtering yield are not the variation in sputtering yield but are a quantification of the belief that a particular sputtering yield will be observed. In the case of the normal incidence model for molybdenum (Figure 4.2a), the median and credible intervals are tightly constrained. This is in large part driven by the availability of data points at the lower incident ion energies where the model is highly non-linear. This nonlinearity weights the fit to these datapoints. On the other hand, the model fit to gold (Figure 4.2b) exhibits uncertainty exceeding an order of magnitude. This underscores the impact of both the disparity in data sets and the relative sparsity of data where the model is most nonlinear, near the threshold energy for sputtering of approximately 20 eV. As shown in Section 4.5, this uncertainty can contribute to wide variances in erosion predictions.

For the angular dependence of sputtering yield $Y(\theta)$ shown in Figure 4.3, while the median lines generally follow the data, the credible intervals extend to ranges on the order of the value of the median. This is a function of the relative sparsity of the data as well as the nonlinearity of the model. The disparity is particularly pronounced for the sputtering of gold where there is only one available data set. With that said, while the credible intervals are relatively large compared to the median, the magnitude in the uncertainty in the angular dependence of sputtering yield is only on the order of unity. This uncertainty thus will have less of an impact on sputtering compared to the larger order of magnitude variance in the normal incidence models.

In summary, the approach for quantifying model uncertainty for the normal incidence and angular dependence models for sputtering has been described in this section. In Section 4.5, sampling methods are employed to investigate how the uncertainty in these sputtering yields impacts confidence in wire erosion predictions. Before proceeding with this analysis, however, the experimental measurements for validation of *MEOWS* are discussed.

4.4 Experimental Measurements for Model Inputs and Validation

To inform the input conditions for *MEOWS* as well as validate its predictions, experimental measurements of wire erosion in a Hall thruster plume are required as well as local plasma measurements of the environment near the wire. To this end, data was employed from a previous experimental study. The nature of the measurements and key findings are briefly described here. Additional details can be found in Byrne et al. [18].

4.4.1 Test Article and Erosion Measurements

The experimental layout from Byrne et al. [18] for performing a controlled erosion study of mesh wire is shown in Figure 4.5. The H6, 6 kW class Hall thruster [23–27], was employed as the plasma source in this work. This laboratory device (Figure 4.5a) was jointly developed by the University of Michigan, the Air Force Research Laboratory, and the Jet Propulsion Laboratory. It has a centrally mounted cathode and operates on xenon gas.

The erosion of the wire was experimentally characterized in four mesh reflector coupons placed in the plume of the H6 thruster when operated at a discharge voltage of 300 V and power of 3 kW (Figure 4.5b). These coupons were placed equidistant from one another, one meter from the thruster centerline, and facing the thruster. The exposure time of 10 h and sample locations were chosen to accelerate the erosion while simultaneously sampling a broad range of plume locations.

The erosion of these mesh surfaces was quantified using a laser confocal microscope. While the mesh coupons include many wires, one wire in the coupon was chosen to quantify the erosion. The erosion measurements consisted of the average of profiles taken at five different locations along the wire axis (Figure 4.6). The reported experimental measurements and uncertainty represent the average and standard deviation from these five profiles. As discussed in Byrne et al. [18], due to the structure of the samples, the absolute height of the profile could not be determined from the measurements. In this chapter, the absolute height is determined by having the most experimentally measured data points fall within the credible intervals of the results of *MEOWS*.

4.4.2 Plume Properties

To inform the predictions of *MEOWS* for the mesh wire coupons, the plasma measurements from Byrne et al. [18] that were taken at the same locations of the wire samples were used. The generated data included the ion energy distribution $f_i(E)$, as inferred with a retarding potential analyzer, and the ion current density j_i, as measured with a Faraday probe. These results have been reproduced from Byrne et al. [18] in Figure 4.7. The ion current density as a function of angle measured from thruster centerline is shown in Figure 4.7a. As can be seen here, the ion current density is at its maximum on the thruster centerline and decreases with angle. This is a typical feature of Hall thruster plumes [28]. The ion energy distribution at the four angular locations of the coupons is shown in Figure 4.7b. Near the thruster centerline (18°), the energy distribution shows a most probable energy of 280 eV, which is comparable to the discharge voltage. This is expected for the centerline where the main beam of the exhaust is directed. As the angle from the thruster centerline increases to locations at the periphery of the main beam, the most probable energy decreases in magnitude, and a population starts to grow with a most probable value of 30 eV. This lower-energy population is likely attributed to the formation of charge-exchange ions that result from collisions of the main beam with ambient neutrals. As was discussed and ultimately showed in Chapter 3, the wire samples located closest to the thruster centerline are subject to the highest rates of erosion. This is due to the combination of higher ion energy and flux to the target. The samples farther from centerline experience diminishing levels of erosion. The wide range of erosion rates provides a diverse data set for comparison with the model.

4.5 Results

In this section, the results of the impact of sputtering model uncertainty on erosion predictions are presented. To this end, *MEOWS*, described in Section 2.1, is used with the experimentally measured plume properties detailed in Section 4.4.2 to model the erosion of wires over 10 h of exposure to the plume of the H6 Hall thruster. The joint probability distributions of model parameters described in Section 4.3 is sampled from 10,000 times to generate 10,000 unique eroded wire profiles. These profiles are combined to obtain a median profile with quantified uncertainty as described in Section 4.2.1.

The eroded wire profiles at 1 m from the thruster and at four angles from the thruster centerline (18°, 33°, 48°, and 63°) are examined, shown notionally in Figure 4.5b. Time steps of 1 s at 18° from the thruster centerline and 10 s at the other three locations are used. These time steps are based on the convergence study described in Section 3.3.2.1. Convergence was defined as the difference between locations of endpoints that start at the same location on the wire being less than 1% of a wire radius. Convergence was achieved for 33°, 48°, and 63° from the thruster centerline at a time step of 10 s. While convergence at 18° required time steps of 0.05 s, taking these time steps would have been prohibitively computationally expensive. Instead, a time step of 1 s was chosen as relatively little variation in the final wire profiles was seen. The eroded wire profiles calculated using the previously described model at these four locations are shown in Figures 4.8, 4.9, 4.10, and 4.11. At each location, the results for both angular incidence sputtering yield models are included. The normal incidence model was from Eckstein and Preuss, as the best comparison to experiments was found with this normal incidence model in Chapter 3. For comparison, the experimentally measured profiles from Byrne et al. [18] and described in Section 4.4.1 are plotted.

The results at 18° from the thruster centerline are shown in Figure 4.8. This location exhibits the highest erosion out of the four coupons because both the ion current density and ion energies are highest at this location. As can be seen, both sputtering models (Wei et al. and Yamamura and Shindo) qualitatively agree with the experimental results. Most notably, they successfully predict a characteristic peak, which (as is discussed in the following section) is due to the preferred erosion that occurs at the optimal angle of the angular incidence sputtering yield. Similarly, the maximum erosion predicted on the median profile is 114% of a wire radius from model from Wei et al. (+ 49% of a wire radius, - 42% of a wire radius) and 94% when the model from Yamamura and Shindo is used (+ 55% of a wire radius, - 35% of a wire radius). This compares favorably to the experimental result which shows over 97% of the experimentally measured profile lies within the credible intervals.

Despite the quantitative and qualitative agreement with data, for both cases, the credible intervals of the models are large compared to the median prediction. This result underscores the large degree of uncertainty that stems from the uncertainty in sputtering yield. Indeed, because the maximum credible intervals are on the order of the maximum erosion, the lifetime of the reflector could be substantially overestimated. The implications of this result are expanded upon in the following section.

The results at 33° from the thruster centerline are shown in Figure 4.9. Due to the lower ion current density (Figure 4.7a) and lower number of high-energy ions (Figure 4.7b), there is less erosion at this location than at 18° from the thruster centerline. As with the 18° case, the shape of the eroded wire profile differs between the two angular incidence sputtering yield models. More erosion is seen near $x/r_{wire} = \pm 1$ when the model from Wei et al. is used than when the model from Yamamura and Shindo is used. Quantitatively, the maximum erosion in the median profile is 14%

of the wire radius (+ 7% of a wire radius, - 5% of a wire radius) when the model from Wei et al. is used and 13% of the wire radius (+ 15\% of a wire radius, - 6\% of a wire radius) when the model from Yamamura and Shindo is used. The experimentally measured profile agrees well with the model predictions with over 89% of the experimentally measured profile lying within the credible intervals. With respect to model confidence, the maximum credible intervals are smaller than those at 18°. This is ultimately because the wire erodes less in 10 h due to the lower ion current density and less-energetic ions striking the wire. The perhaps more relevant metric, however, is the relative magnitude of the uncertainty, which in this case is on the order of the maximum erosion. This result thus illustrates again the driving role of uncertainty in lowering the confidence in the erosion prediction.

The results at 48° from the thruster centerline are shown in Figure 4.10. At this location, the ion current density is less than half of the ion current density at 33° from the thruster centerline, and the ion energy distribution shows most ions have energies below 150 eV. Therefore, less erosion is predicted and measured here than at 18° and 33° from the thruster centerline. The predictions from the two models are qualitatively similar. Quantitatively, the maximum erosion on the wire is 4.1% of the wire radius (+ 3.5% of a wire radius, - 3.3% of a wire radius) when the model from Wei et al. is used and 4.1% of a wire radius (+ 4.1\% of a wire radius, - 3.3% of a wire radius) when the model from Yamamura and Shindo is used. Over 74% of the experimentally measured profile lies within the credible intervals. In terms of model confidence, the credible intervals are smaller in magnitude at 48° from the thruster centerline than at 33° from the thruster centerline because there is less erosion of the wire overall. However, the maximum credible intervals are approximately the size of the maximum erosion on the median profile, indicating a large relative uncertainty in the erosion prediction.

The results at 63° from the thruster centerline are shown in Figure 4.11. This location exhibits the lowest ion current density (less than half of the ion current density at 48° from the thruster centerline), and the ion energy distribution shows most of the ions have an energy below 50 eV with the most probable energy at 29 eV. The lowest amount of erosion is therefore seen at this location. Indeed, it is barely discernible from the initial wire profile, and the gold coating has not been removed. The maximum erosion on the median profile is 2.0% of a wire radius (+ 3.3% of a wire radius, - 1.5% of a wire radius) and 1.9% of a wire radius (+ 3.6% of a wire radius, - 1.4% of a wire radius) when the models from Wei et al. and Yamamura and Shindo are used, respectively. The predictions of *MEOWS* again agree quantitatively with the experimentally measured profile, with 85% of the experimentally measured profile falling within the credible intervals. While the absolute value of uncertainty is lower than in the other, higher erosion cases, because the maximum credible interval can be nearly double the maximum erosion on the wire, the relative uncertainty in the erosion is larger for this outermost angle.

For a side-by-side comparison, the results from all four angles are combined in Figure 4.12a, in which both the predicted and measured maximum erosion as a function of angle from the thruster centerline are plotted. This graphically illustrates how the maximum erosion of the experimental measurements agrees well, within credible intervals, with the maximum erosion of the predictions. Moreover, as discussed in the preceding, the maximum erosion decreases with angle from thruster centerline. This is the result of the decrease in current density and ion energy with increasing angle.

With that said, while the magnitude of the credible intervals for the erosion scales with the magnitude of median erosion, the relative uncertainty (maximum distance between the 5th percentile and median divided by the maximum erosion of the median) does not decrease with angle in the same way (Figure 4.12b). Rather, the relative uncertainty is the lowest at 18° from the thruster centerline and generally increases, with the exception of the model from Yamamura and Shindo at 33°, with angle from the thruster centerline. This result shows that the prediction for the periphery of the plume has the highest degree of uncertainty; the relative confidence is at least the same magnitude as the value of the median prediction. This is a notable result as it is the location where spacecraft components will be placed. Potential reasons for why the relative uncertainty is higher at this location are discussed in Section 4.6.

In summary, when model-based uncertainty is systematically accounted for, the predictions for the eroded wire profiles match the experimental results within uncertainty. With that said, the uncertainty in the sputtering yield does have a substantial impact on the confidence in model prediction. Indeed, the maximum credible intervals calculated yielded variances in the erosion that are on the order of the median predictions. These variances in turn (particularly in the periphery of the plasma) could translate to large uncertainty (up to 190%) in spacecraft component lifetime when exposed to a thruster plume. The implications of these results are discussed in the following section.

4.6 Discussion

In this section, the implications of the findings are discussed. The unusual shape of the eroded profiles is first commented on. The implications of the results for assessing lifetime, the role of the uncertainties that were not assessed, the limitations of the model, and recommendations for improving confidence in erosion predictions are then discussed.

4.6.1 Physical Implications of Erosion Results

As seen in the previous section, the experimentally measured and predicted eroded wire profiles (Figure 4.8) show an unusual structure; they become progressively peaked when subject to more bombardment. This shape is a physical manifestation of the fact that the sputtering depends on the angle of incidence between the surface and the incoming ions. As shown in Figure 4.3, the optimal angle, or angle where the sputtering yield is maximized, is not at normal incidence (0°) but instead is between 20° and 60°. In fact, the sputtering yield at the optimal angle can be three times as large as the sputtering yield at normal incidence. Therefore, for the same ion current density and ion energy distribution, a surface at the optimal angle will experience three times the erosion compared to a surface at normal incidence. Because more sputtering occurs at surfaces near the optimal angle, more erosion on the wire at locations off axis from the direction of normal beam incidence is seen. This leads to the gradual steepening of the wire profile. This peak is especially pronounced when the wire has been substantially eroded, such as at 18° from the thruster centerline (Figure 4.8).

Both the model uncertainty and model choice impact the predicted shape of this steepening. As shown in Section 4.3, the uncertainty in the angular sputtering model can lead to wide variance in the predicted optimal angle for erosion. This is captured by the fact that the credible intervals show profiles that exhibit different degrees of steepening in Figure 4.8. Moreover, in reviewing the sputtering fits for both the models from Wei et al. and Yamamura and Shindo (Figure 4.3), the model from Yamamura and Shindo more rapidly decays to zero at higher angle of incidence. This in turn can explain the more step-like structure exhibited in the predicted erosion from this model (Figure 4.8b). Finally, for all the sputtering yield models, particularly the model from Yamamura and Shindo in Figure 4.3, there is a high degree of uncertainty at oblique angles (greater than 80°).

This likely contributes to the qualitative disagreement in model predictions at the edges of the wire ($x/r_{wire} = \pm 1$) in Figures 4.8 and 4.9 where the angle of ion incidence is largest.

4.6.2 Implications of Uncertainty on Lifetime Assessments

Quantifying the impact of sputtering uncertainty on erosion estimates is complicated by the fact that the sputtering models are nonlinear and the plasma properties are nonmonotonic. Indeed, in some cases (Figure 4.2b), the sputtering models can have uncertainty exceeding an order of magnitude, and the ion energy spectrum can exhibit values ranging from 0 to 300 eV (Figure 4.7b). With that said, despite the variability in both sputtering yields and data, for a wide range of erosion rates (Figures 4.8 - 4.11), the variance in the erosion predictions is only on the order of 190%.

One possible explanation for this relatively low variance stems from the wire geometry. The sputtering model with the largest uncertainty is the normal incidence for sputtering of gold. However, the gold-coated layer on the wires is relatively thin and in fact erodes very quickly at 18° and 33° from the thruster centerline. The majority of the erosion instead is the result of the sputtering of the underlying molybdenum. The contribution to uncertainty from the gold erosion may not drastically impact the overall confidence. On the other hand, the sputtering yields for normal incidence on molybdenum as well as for the angular sputtering yields all only have variances on the order of 150%. This level of uncertainty is commensurate with the uncertainty in erosion predictions reported in the previous section.

With that said, while the gold layer is completely removed at most locations considered, this surface does not completely erode at 63° from the thruster centerline. This location correspondingly exhibits higher relative uncertainty (greater than 150%), as shown in Figure 4.12b for both angular incidence sputtering models. Because the gold layer is not completely eroded and the variance in the sputtering yield model for gold is larger than that of molybdenum (Figure 4.2), the relative uncertainty in the erosion is expected to be high at this location. Another potential factor adding to the higher relative uncertainty at this angular location is the nonlinearity of the sputtering yield at low energies. At 63° from the thruster centerline, most of the ions have energies below 50 eV (Figure 4.7b). These energies correspond to the highest variances in the gold sputtering yield model (Figure 4.2b), as the sputtering yield is highly nonlinear near the threshold energy. Additionally, the variance in the threshold energy itself significantly changes the sputtering yield. While most ions at 63° can sputter gold if the threshold energy is 10 eV, most ions cannot sputter gold if the threshold energy increases to 30 eV.

In practice, the confidence in the erosion estimates suggests a potential guideline for wire design: adopting at least 190% in margin on the wire radius. This may be sufficient to mitigate the uncertainty in erosion prediction. Indeed, the fact that this 190% appears valid for a wide range of plasma conditions and erosion (Figure 4.12b) further supports its adoption as a general guideline. With that said, it is possible that the simulations and experiments may not have captured all representative conditions for a thruster on orbit. This may suggest that 190% is not a universally sufficient margin.

4.6.3 Sources of Uncertainty Beyond Sputtering Yield

While there are other sources of uncertainty that may impact the erosion estimates such as uncertainty in the local plasma properties, these are neglected as small when compared to the order of magnitude variance in the sputtering yield. This assumption is justified, as the experimental measurements were performed in a controlled environment. This is borne out by the quantitative agreement of the model predictions with experiment. In practice, however, for making predictions of erosion on spacecraft surfaces in orbit, these plasma-based uncertainties must be considered.

This stems in large part from the fact that on-orbit measurements for the plasma environment are not available and that plume models for the space environment are limited [29]. Indeed, the ion energies and fluxes at the periphery of the plasma are highly susceptible to the background pressure in the test facility [30,31], and the variation in these properties with pressure is not well understood. This results in a large degree of uncertainty as to what these plume properties will be on orbit where the background pressure is absent. As the ion energies in the plume are closest to the regions of highest uncertainty in the sputtering yield (i.e., near the threshold energies), on-orbit predictions may be particularly susceptible to the variance in the sputtering yield models. With that said, this additional uncertainty can be incorporated into the formalism introduced here by treating the plasma properties as probabilistic as well and sampling over their distributions. This ultimately will be a critical step for fully quantifying the uncertainty in predictions for spacecraft component erosion in space.

4.6.4 Limitations of *MEOWS*

While the results of *MEOWS* match the experimentally measured profiles well, this approach does have limited fidelity. For example, even though studies have shown that surface roughness can impact the sputtering yield by a factor of two [32], this effect has been neglected. This decision was largely motivated by the fact that reduced fidelity, analytical models for this effect are still under investigation. With that said, the calibrated model does in some sense implicitly account for the uncertainty due to material surface conditions. As discussed in Section 4.3, the experimental conditions and properties of the target materials (such as roughness) used for generating the data sets varied across studies. This can in part explain the relatively large variance in sputtering yield both as a function of energy and angle. The model inference method inherently accounts for this uncertainty in the calibration.

Redeposition of sputtered material on the wires has also been neglected. As the wires in the mesh reflector coupons are close to each other, sputtered material from one wire could redeposit on an adjacent wire. Additionally, sputtered material could redeposit on the same wire. However, the redeposition of material is expected to be small compared to the erosion of the wire.

Another limitation of *MEOWS* is that only the effects of singly charged ions were considered, neglecting the impact of charge-exchange neutral particles and multiply charged species. The expectation is that these higher-energy particles could lead to higher rates of erosion. This modeling approach could be adapted to account for these higher energy species by treating each charge species separately with its own associated current density. This would require an estimate of the relative species concentration of each charge state. With that said, given the relatively large uncertainty in the erosion predictions (Figure 4.8) as well as the relatively low fraction of higher charge states in Hall thrusters [28], this effect may be comparatively small.

Finally, the ions are currently assumed to impact the wire from one direction. Incorporating a two-dimensional ion velocity distribution would capture the differing flux of ions from different directions, giving a better estimate of erosion. In fact, using the ion velocity distribution would capture erosion around the entire wire; assuming the ions impact the wire from one direction gives no erosion on the side of the wire not facing the ions. This effect is anticipated to be relatively small close to the thruster centerline (less than 30°). The ions in this region are primarily moving in one direction because they have been accelerated by the axial electric field in the thruster. However, at the periphery of the plume, ions are largely formed by charge-exchange collisions with neutrals. The velocity of the neutrals is not influenced by the electric field, and the motion of the low-energy ions formed in charge-exchange collisions is susceptible to the local electric field. Therefore, at these periphery regions, the incident ions may not all originate from the thruster beam.

4.6.5 Recommendations for Improving Accuracy of Erosion Assessments

The central thesis of this chapter is that the uncertainty in sputtering yield models can translate to high degrees of uncertainty in sputtering erosion. To reduce the uncertainty in the eroded wire profiles, the uncertainty in the sputtering models needs to be reduced. As discussed in the preceding section, some of the inherent uncertainty stems from the variance across data sets. This likely can be attributed to the varying experimental conditions that were employed for these disparate studies. Improved fidelity could be achieved by performing additional sputtering studies on material states (i.e., roughness) and under conditions that more accurately reflect the spacecraft surface.

The shapes of the median fits and credible intervals in Figures 4.2 and 4.3 also suggest potential follow-up experiments that could be performed to improve model fidelity. For example, there is a high degree of variability in the model fit for higher energies (exceeding 50 eV) in Figure 4.2b. This stems in large part from the fact that there are only data available at these higher energies where the underlying model is relatively flat and not as easily constrained. The model uncertainty could be reduced by generating more data near the threshold energy (approximately 20 eV) where the underlying equation is more nonlinear. This points to the need for additional experiments to selectively target these lower energies for gold sputtering.

The model fits in the angular sputtering yields, Figure 4.3, also would benefit from additional data, particularly for the sputtering yields for gold. However, with the exception of the model from Wei et al. for molybdenum (Figure 4.3b), the shape of the median fits and credible intervals for the angular model show qualitatively less agreement with the data. This suggests that the underlying physics-based models for the angular dependence may be missing key elements of the physical processes. Indeed, this variance may in large part be attributed to attempting to fit a functional shape that does not conform to the data. Ultimately, the reduced applicability of the model may not be surprising as the preponderance of sputtering yield data and models has been derived for higher energy levels (greater than 500 eV). Other physical phenomena may play at role at these lower energies. With this in mind, a more pressing recommendation for reducing uncertainty for the angular dependence is to revisit the underlying theory for the governing equations.

4.7 Concluding Remarks

In summary, the goal of this chapter has been to quantify the impact of uncertainty in sputtering yield on predictions for erosion due to spacecraft interactions with the plume of a Hall effect thruster. This is a critical question, as the high-energy ions from this source can lead to component failure over time. Understanding the predicted erosion and being able to identify the margin for this erosion to guarantee spacecraft life are thus of practical interest. With this in mind, this chapter has investigated a model, *MEOWS*, to predict the eroded profile of a key element for spacecraft: the gold-coated molybdenum rounded wires in mesh reflectors. *MEOWS* discretizes the cross-section of the wire and takes inputs for the local current density, ion energy distribution, and sputtering yield to track how those discretized surfaces erode through time. To assess the impact of sputtering yield uncertainty on the erosion predictions, Bayesian inference was applied to determine the probability distributions for three known semi-empirical models for the sputtering yield of xenon on molybdenum and gold. Sampling from these distributions of the model parameters, *MEOWS* was ran 10,000 times to build statistical estimates for the wire erosion.

Experimental data for the plume of a 6 kW Hall thruster provided input plasma data for *MEOWS* [18]. The model predictions for erosion were compared to experimental measurements of wire samples. These samples were placed at four angles from the thruster centerline and 1 m downstream of the thruster. The eroded states varied from nearly complete erosion to only minor erosion on the wire surface layer, thus providing a varied data set for comparison. At all locations, the experimental measurements largely fell within the credible intervals for the predicted eroded wire profiles. In particular, at high erosion rates, the model was able to predict an unusual peak like structure in the wire shape. This was attributed to the nonmonotonic dependence of angular sputtering on the incident angle.

In terms of the role of uncertainty, the largest relative uncertainty was in the regions of the plume where the energies are closest to the threshold energy for erosion. Because the gold is not completely eroded at this location, this may in part be explained by the lower confidence in the sputtering of gold compared to molybdenum. With that said, despite the fact that sputtering model uncertainty can vary by an order of magnitude, the confidence in erosion prediction only varied by 190%. This may in part be explained by the fact that at most locations examined, the majority of the erosion occurs in the molybdenum substrate of the wire where sputtering is modeled with higher confidence.

This work has discussed the results in the context of improving predictions for spacecraft erosion on orbit. In particular, these results would suggest that, despite the large variance in sputtering models at some energies and angles of incidence, for typical Hall thruster plumes, it may be sufficient to employ material margins with only 190% to ensure service life. However, the model does invoke a number of simplifying assumptions, such as the neglect of multiply charged species and surface roughness, and in space the plasma conditions may trend more to the regions of higher uncertainty in the sputtering yields. This conclusion also holds for materials with similar levels of uncertainty in the sputter yield. Regardless, this chapter has established a rigorous framework for propagating and quantifying the role of sputtering uncertainty on erosion prediction. This is a critical, practical consideration for the design and margin choices of spacecraft components that may be subject to plume impingement.

4.8 Figures

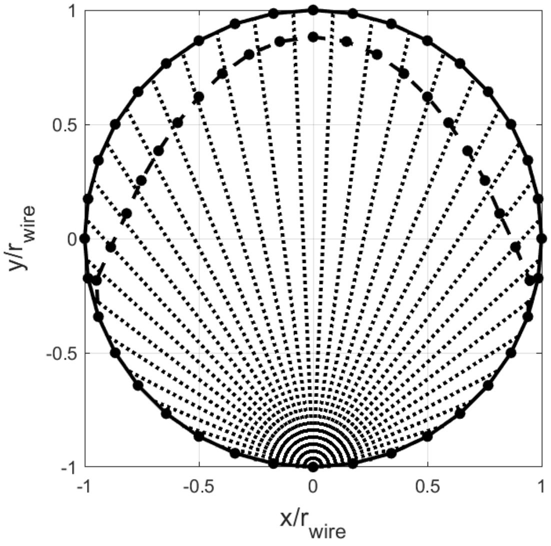

Figure 4.1. Points in the final profile (dashed) are sorted into bins based on their angle ϕ from $(0, -r_{wire})$ and positive x values in $y = -r_{wire}$.

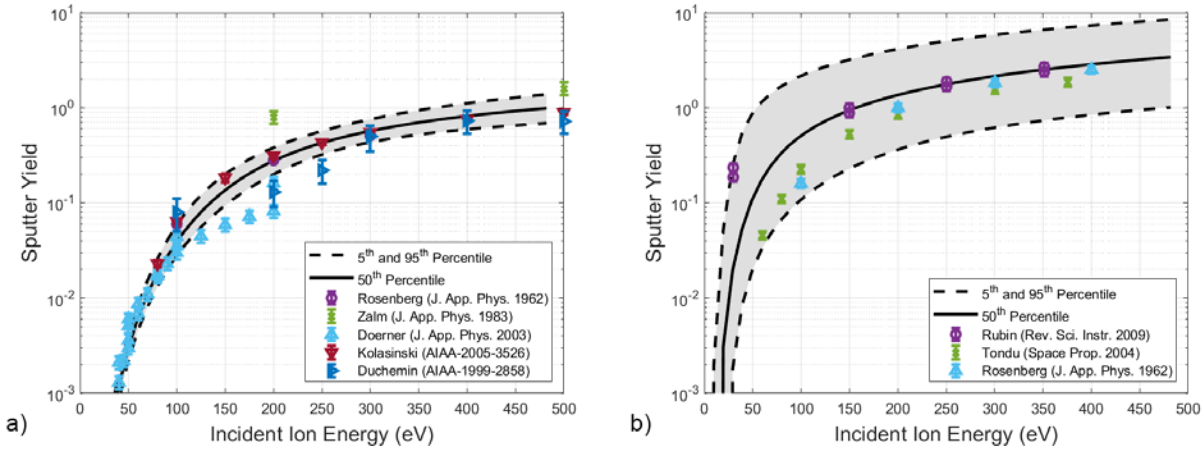

Figure 4.2. Experimental data and model fits for normal incidence sputtering yield models for xenon incident on (a) molybdenum [9–13] and (b) gold [9,14,15].

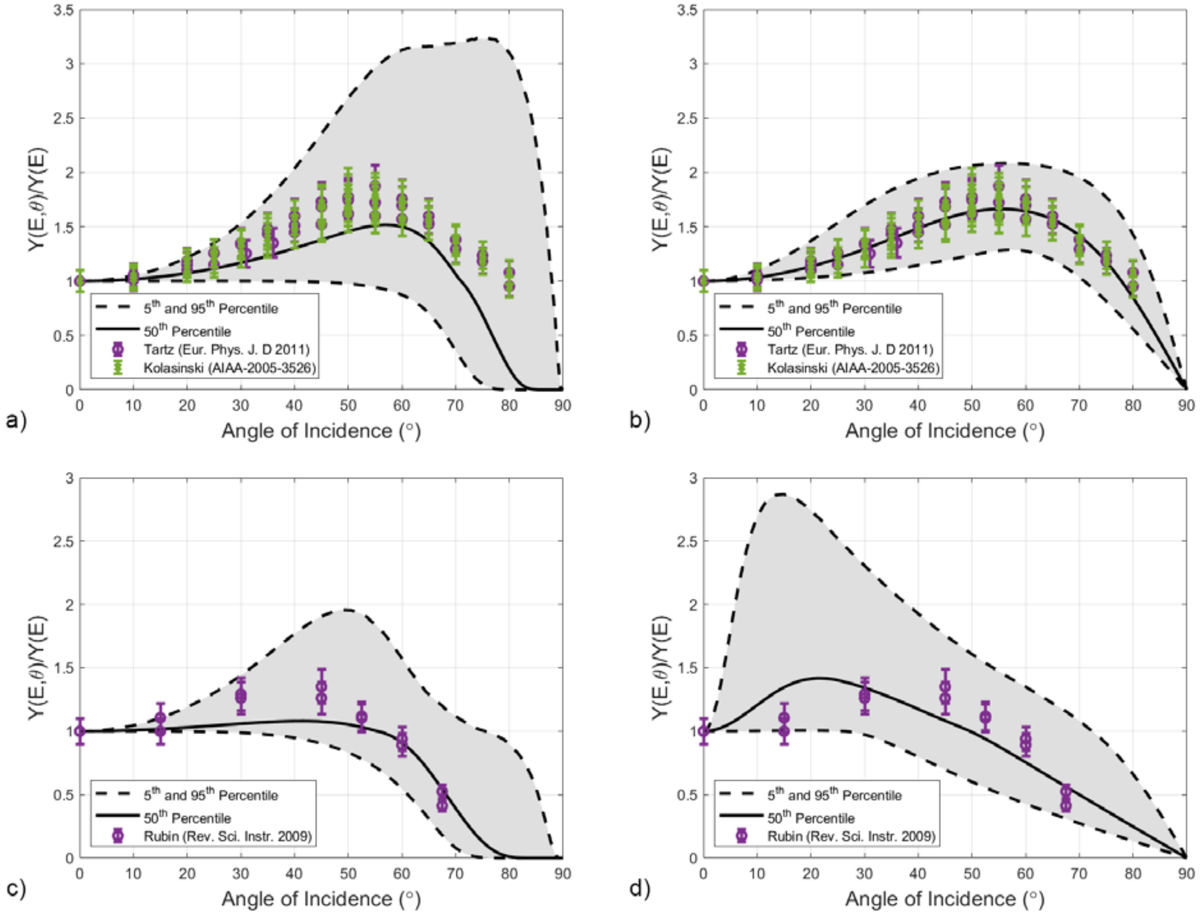

Figure 4.3. Experimental data and model fits for angular incidence sputtering yield models for xenon incident on molybdenum and gold. (a) Model from Yamamura and Shindo for molybdenum [7,12], (b) model from Wei et al. for molybdenum [7,12], (c) model from Yamamura and Shindo for gold [14], and (d) model from Wei et al. for gold [14].

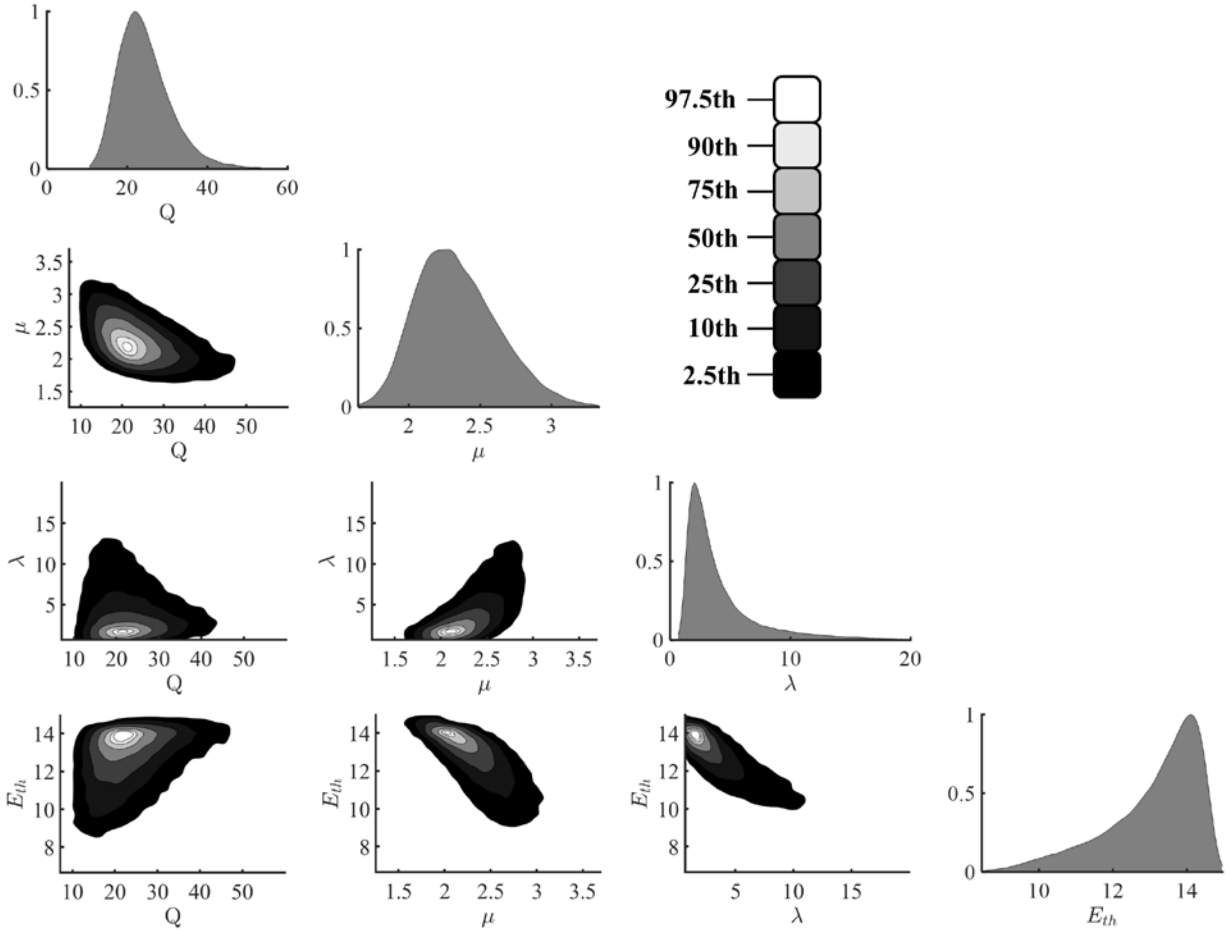

Figure 4.4. Joint and marginal probability distributions for model parameters of the sputtering model from Eckstein and Preuss for molybdenum. Labeling indicates percentage of samples contained below the contour.

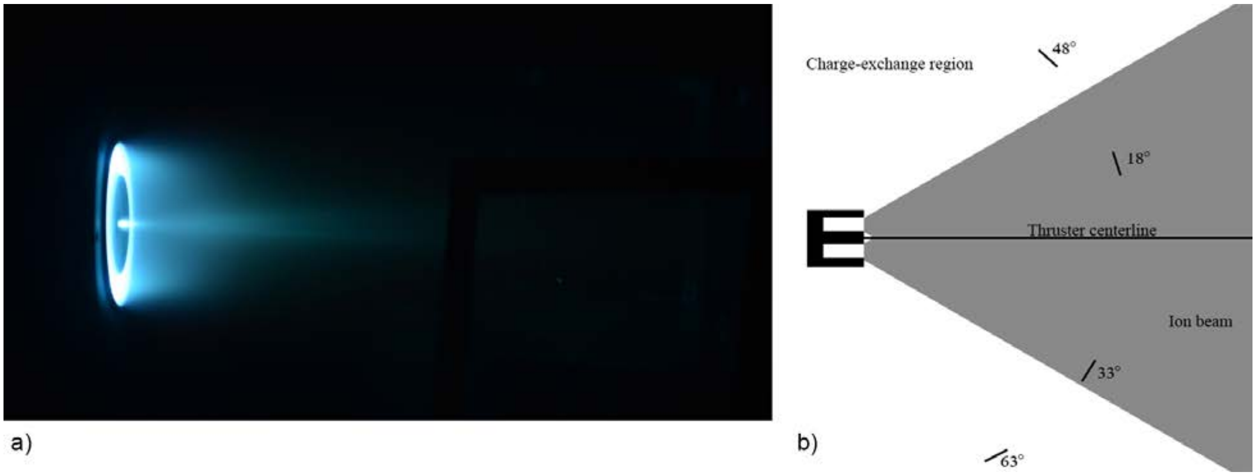

Figure 4.5. Experimental setup. (a) The H6 6 kW Hall effect thruster, operating at 300 V and 3 kW, during a mesh material wear test [18] in the Large Vacuum Test Facility at the University of Michigan and (b) notional layout of sample placement for wire erosion measurements.

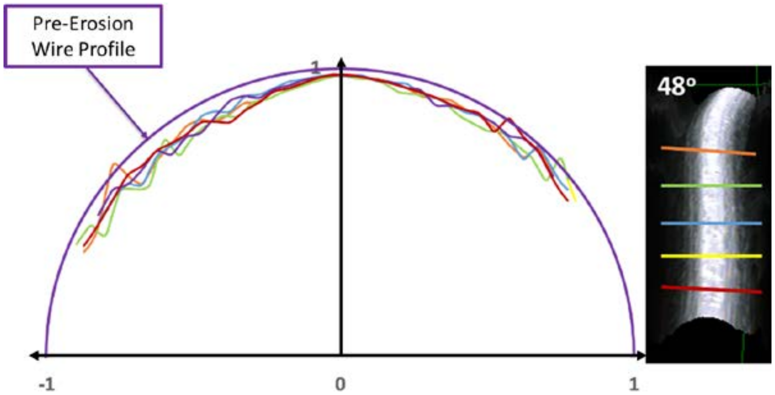

Figure 4.6. Each wire segment is characterized at a series of higher focal planes, producing a three-dimensional map of its surface. Five height profiles were extracted.

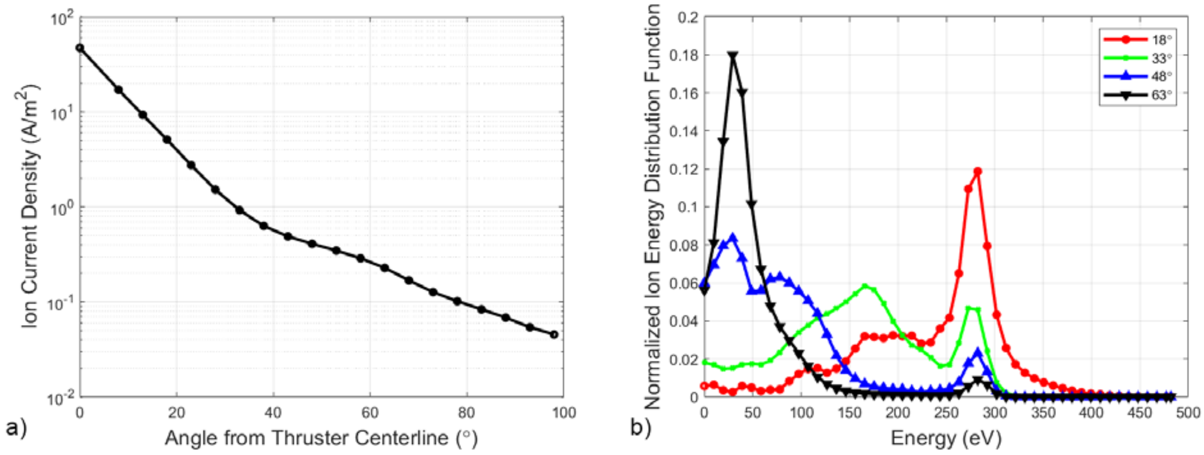

Figure 4.7. Plasma properties. (a) Ion current density and (b) ion energy distributions for the H6 Hall thruster operating at 300 V and 3 kW. Measurements performed at 1 m from thruster. Data from Byrne et al. [18].

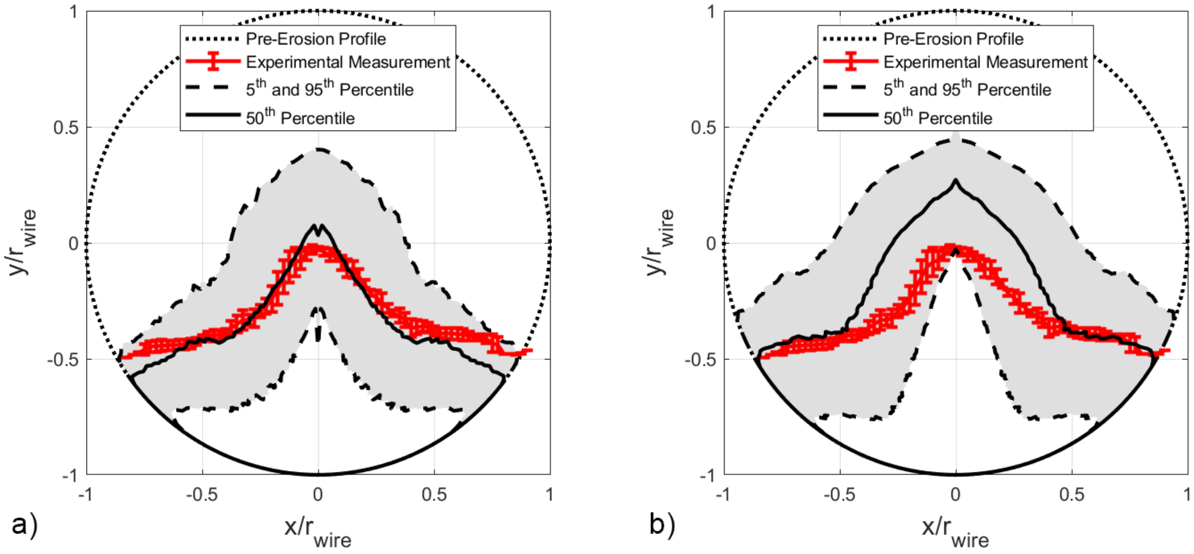

Figure 4.8. Eroded wire profiles at 18° from the thruster centerline using the angular incidence model from (a) Wei et al. and (b) Yamamura and Shindo.

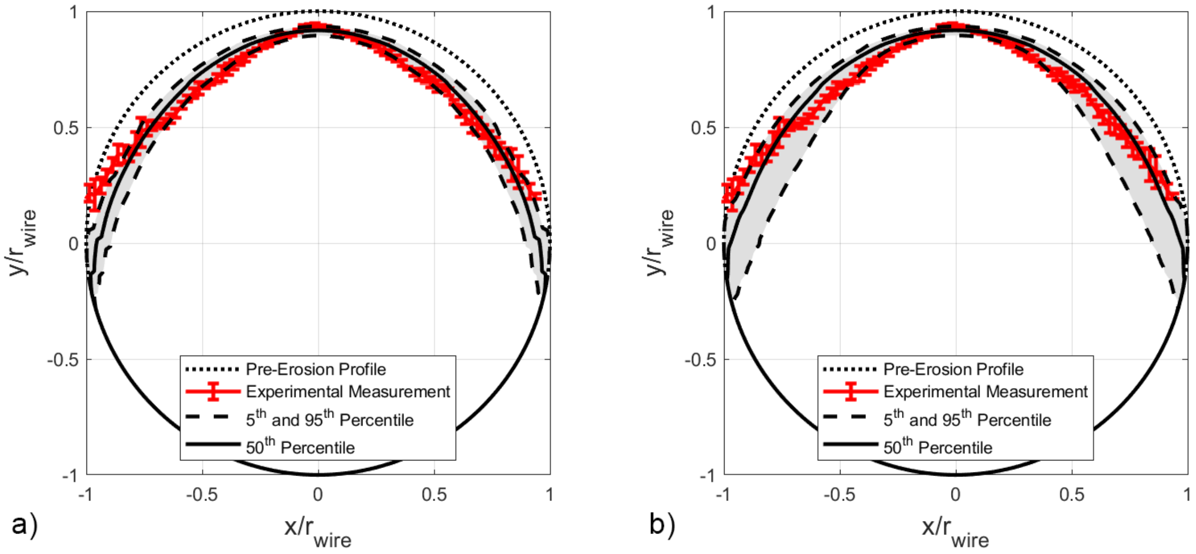

Figure 4.9. Eroded wire profiles at 33° from the thruster centerline using the angular incidence model from (a) Wei et al. and (b) Yamamura and Shindo.

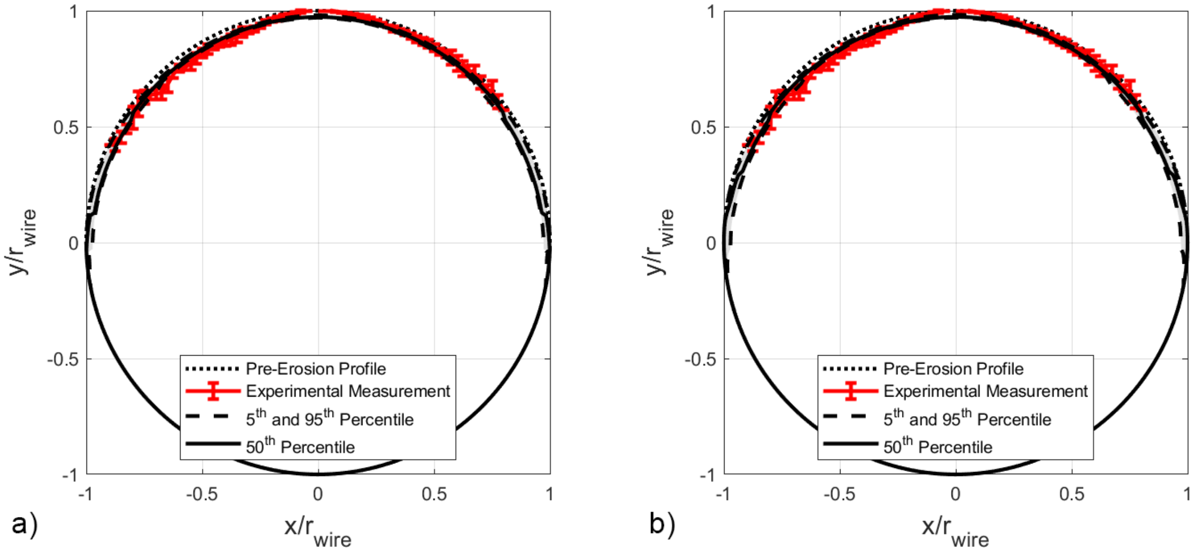

Figure 4.10. Eroded wire profiles at 48° from the thruster centerline using the angular incidence model from (a) Wei et al. and (b) Yamamura and Shindo.

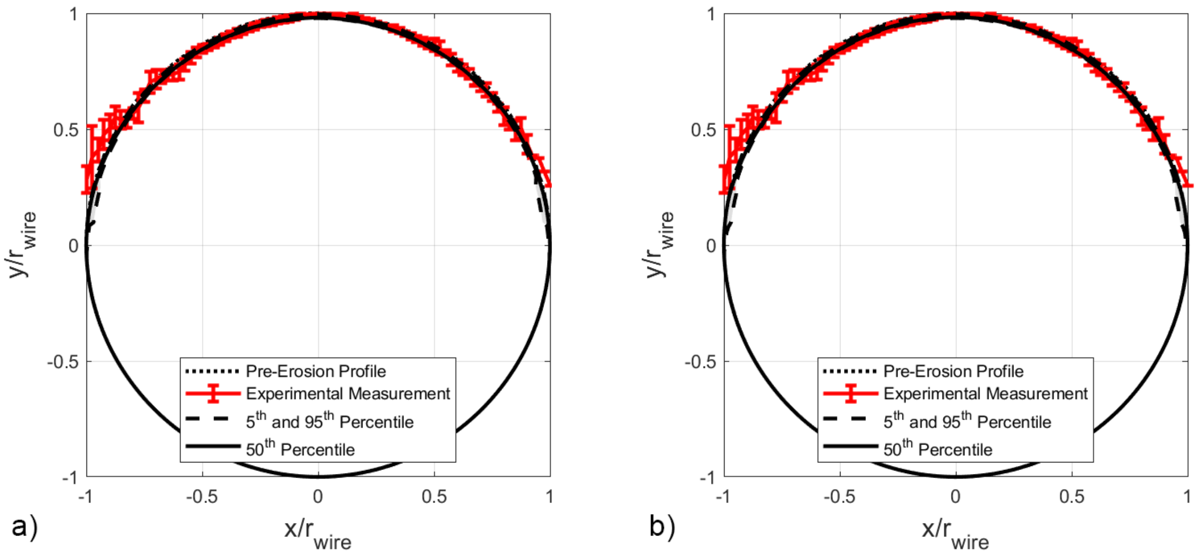

Figure 4.11. Eroded wire profiles at 63° from the thruster centerline using the angular incidence model from (a) Wei et al. and (b) Yamamura and Shindo.

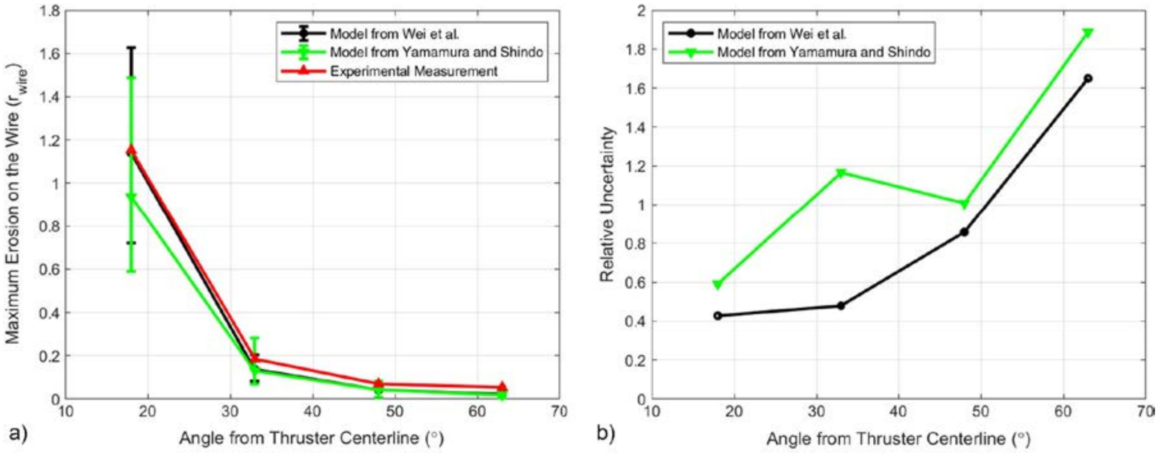

Figure 4.12. Dependence on angle from thruster centerline of (a) maximum erosion on the wire (error bars on the model results show the maximum erosion of the 5th and 95th percentile credible intervals) and (b) relative uncertainty.

4.9 References

[1] D. Y. Oh, D. E. Hastings, C. M. Marrese, J. M. Haas and A. D. Gallimore, J. Propuls. Power **15,** 345 (1999).

[2] E. J. Pencil, T. Randolph and D. Manzella, AIAA 32nd Joint Propulsion Conference, AIAA Paper 1996-2709 (1996).

[3] Randolph T, E. Pencil and D. Manzella, AIAA 30th Joint Propulsion Conference, AIAA Paper 1994-2855 (1994).

[4] D. Y. Oh and D. E. Hastings, 32nd Joint Propulsion Conference and Exhibit, AIAA Paper 1996-3299 (1996).

[5] W. Eckstein and R. Preuss, J. Nucl. Mater. **320,** 209 (2003).

[6] Y. Yamamura and S. Shindo, Radiat. Eff. **80,** 57 (1984).

[7] M. Tartz, T. Heyn, C. Bundesmann, C. Zimmermann and H. Neumann, Eur. Phys. J. D **61,** 587 (2011).

[8] Q. Wei, K.-D. Li, J. Lian and L. Wang, J. Phys. D. Appl. Phys. **41,** 172002 (2008).

[9] D. Rosenberg and G. K. Wehner, J. Appl. Phys. **33,** 1842 (1962).

[10] P. C. Zalm, J. Appl. Phys. **54,** 2660 (1983).

[11] R. P. Doerner, D. G. Whyte and D. M. Goebel, J. Appl. Phys. **93,** 5816 (2003).

[12] R. D. Kolasinski, 41st AIAA/ASME/SAE/ASEE Joint Propulsion Conference and Exhibit, AIAA Paper 2005-3526 (2005).

[13] O. B. Duchemin and J. E. Polk, 35th Joint Propulsion Conference and Exhibit, AIAA Paper 1999-2858 (1999).

[14] B. Rubin, Topper J L, C. C. Farnell and A. P. Yalin, Rev. Sci. Instrum. **80,** 103506 (2009).

[15] T. Tondu, V. Inguimbert, F. Darnon and J. F. Roussel, 4th International Spacecraft

Propulsion Conference, Paper 2004ESASP.55E.105T (2004).

[16] J. T. Yim, 35th International Electric Propulsion Conference, Paper IEPC-2017-060 (2017).

[17] M. E. Meyer, M. P. Byrne, B. A. Jorns and I. D. Boyd, (2019).

[18] M. P. Byrne, M. E. Meyer, I. D. Boyd and B. A. Jorns, AIAA Propulsion and Energy 2019 Forum, AIAA Paper 2019-3988 (2019).

[19] B. A. Jorns and M. P. Byrne, Plasma Sources Sci. Technol. **30,** 15012 (2021).

[20] M. M. Saravia, A. Giacobbe and T. Andreussi, Rev. Sci. Instrum. **90,** 23502 (2019).

[21] M. P. Byrne and B. A. Jorns, Proceedings of the 36th International Electric Propulsion Conference, Paper IEPC-2019-630 (2019).

[22] D. Sivia and J. Skilling, *Data analysis: a Bayesian tutorial*, OUP Oxford (2006).

[23] M. S. McDonald and A. D. Gallimore, 31st International Electric Propulsion Conference, Paper IEPC-2009-113 (2009).

[24] M. S. McDonald, "Electron Transport in Hall Thrusters," Ph.D. Thesis (University of Michigan Ann Arbor, 2012).

[25] D. L. Brown, "Investigation of low discharge voltage Hall thruster characteristics and evaluation of loss mechanisms," Ph.D. Thesis (University of Michigan Ann Arbor, 2009).

[26] B. M. Reid, "The influence of neutral flow rate in operation of Hall thrusters," Ph.D. Thesis (University of Michigan Ann Arbor, 2009).

[27] R. R. Hofer, "Development and Characterization of High-Efficiency, High-Specific Impulse Xenon Hall Thrusters," Ph.D. Thesis (University of Michigan Ann Arbor, 2004).

[28] D. M. Goebel and I. Katz, *Fundamentals of Electric Propulsion: Ion and Hall Thrusters*, John Wiley & Sons, Incorporated (2008).

[29] J. Laube, N. Massaccesi, B. Zitouni and M. Peukert, 36th International Electric Propulsion

Conference, IEPC-2019-294 (2019).

[30] W. Huang, H. Kamhawi and T. Haag, 52nd AIAA/SAE/ASEE Joint Propulsion Conference, AIAA Paper 2016-4828 (2016).

[31] D. L. Brown, M. L. R. Walker, J. Szabo, W. Huang and J. E. Foster, J. Propuls. Power **33,** 582 (2017).

[32] M. Kuestner, W. Eckstein, V. Dose and J. Roth, Nucl. Instruments Methods Phys. Res. Sect. B Beam Interact. with Mater. Atoms **145,** 320 (1998).

Chapter 5 Sheath Formation Around a Dielectric Droplet in a He Atmospheric Pressure Plasma[3]

Interactions at the interface between atmospheric pressure plasmas and liquids are being investigated to address applications ranging from nanoparticle synthesis to decontamination and fertilizer production. Many of these applications involve activation of droplets wherein the droplet is fully immersed in the plasma and synergistically interacts with the plasma. To better understand these interactions, 2D modeling of radio frequency (RF) glow discharges at atmospheric pressure operated in He with an embedded lossy dielectric *droplet* (tens of microns in size) was performed. The properties of the sheath that forms around the droplet were investigated over the RF cycle. The electric field in the bulk plasma polarizes the dielectric droplet while the electron drift in the external electric field is shadowed by the droplet. The interaction between the bulk and sheath electric fields produces a maximum in E/N (electric field/gas number density) at the equator on one side of the droplet where the bulk and sheath fields are aligned in the same direction and a minimum along the opposite equator. Due to resistive heating, the electron temperature T_e is maximum 45° above and below the equator of the droplet where power deposition per electron is the highest. Although the droplet is, on the average, negatively charged, the charge density on the droplet is positive on the poles and negative on the equator, as the electron motion is primarily due to diffusion at the poles but due to drift at the equator.

---

[3] The results discussed and portion of the text in this chapter have been published in M. Meyer et al., "Sheath Formation Around a Dielectric Droplet in a He Atmospheric Pressure Plasma", Accepted to Journal of Applied Physics (2022).

5.1 Introduction

Interactions between atmospheric pressure plasmas and liquids are being investigated for applications such as plasma medicine and water treatment [1–4]. The plasma produces reactive oxygen and nitrogen species (RONS) that solvate into the liquid to chemically activate the fluid. This chemical activation can remediate complex organic molecules in the liquid such as benzene or methyl blue dye [5,6]. These reactive species have also been shown to reduce viability of bacteria and cancer cells [7–9].

The interaction of plasmas and liquids is actively being studied, with emphasis on both short-lived and long-lived reactive species. Modeling by Heirman et al. has shown that only limited RONS (H_2O_{2aq}, HNO_{2aq} and $NO_2^-{}_{aq}$, and HNO_{3aq} and $NO_3^-{}_{aq}$) are present in solutions in large concentrations 15 s after plasma exposure [10]. (The “aq” subscript indicates a solvated or in-liquid species.) Short-lived RONS such as OH_{aq} react quickly at the plasma-liquid interface, while other long-lived RONS such as HO_{2aq}, $ONOOH_{aq}$, and O_{3aq} react or de-solvate into the gas phase within 10 s of liquid exposure, though these times scales are system dependent. De-solvation occurs most rapidly for systems having a large surface-to-volume ratio (SVR), such as droplets. We note that species may be continually generated, but reactive species may have low concentrations. Roy et al. experimentally observed RONS formation in a filamentary dielectric barrier discharge operated at varying N_2/O_2 fractions where the water was in contact with the ground electrode [11]. They found that the $NO_3^-{}_{aq}$ density in the liquid increases as the fraction of O_2 in the gas increases as O_{aq}, $O_2^-{}_{aq}$, and O_{3aq} are precursors to $NO_3^-{}_{aq}$.

Plasma-induced electrochemistry also depends on the transport of plasma-produced species into solutions. For example, nanoparticles can be produced in metal ion containing solutions exposed to atmospheric pressure plasmas. Zheng et al. showed that in an $AgNO_{3aq}$

solution, neutral Ag_{aq} clusters form when the solvated electron concentrations are higher than the Ag^+_{aq} concentration, and Ag_{aq} ion clusters form when the reverse is true [12]. Other studies have focused on processes at the interface between the plasma and the liquid. Akiyama et al. performed Monte Carlo simulations to determine how far electrons penetrate into water before they become solvated electrons. They showed that solvated electrons can be produced 17 nm from the water surface for incident electron energies relevant to atmospheric pressure plasmas [13].

Transport is the limiting factor in chemical activation of liquids as the plasma generated RONS need to transport to the interface of the gas and liquid and then diffuse into the bulk liquid. These transport limitations can be mitigated to some degree. A high surface-to-volume ratio (SVR) of the liquid can shorten the time the RONS require to diffuse from the interface to the bulk liquid. Another mitigation strategy is to form the RONS very close to the liquid surface, shortening the distance between the RONS and the interface.

Previous studies have examined these transport limits at the interface. Liu et al. varied the surface to volume ratio of water and found that the concentration of long-lived RONS (H_2O_{2aq}, $NO_2^-{}_{aq}$, $NO_3^-{}_{aq}$, and H^+_{aq}) increased as the SVR increased [14]. In particular, $NO_2^-{}_{aq}$, $NO_3^-{}_{aq}$, and $H_3O^+_{aq}$ increased nearly linearly with SVR, while the density of H_2O_{2aq} saturated at higher SVRs. Hassan et al. investigated the transport of H_2O_2 and O_3 into electrosprayed water droplets [15]. While H_2O_{2aq} and O_{3aq} concentrations in the droplets increased with treatment time, the H_2O_{2aq} concentration was 4 orders of magnitude larger than O_{3aq}, due to the higher Henry's law constant of H_2O_2. While O_{3aq} in the liquid reached saturation without coming close to depleting the gas phase, H_2O_2 in the gas phase was depleted before the liquid became saturated. The total surface area of the droplets also increased H_2O_{2aq} and O_{3aq} concentrations in the liquid. Delgado et al. used a 1D reaction-diffusion model to investigate a general transport limited reaction involving solvated electrons and a general scavenger represented by S ($e_{aq} + S^n \rightarrow S^{n-1}$) [16]. Once S at the surface is depleted, the reaction becomes transport limited as S must diffuse to the surface of the liquid. To increase the yield of the scavenger reaction, they suggest pulsing the plasma, decreasing the electron flux, and using a multiphase system where the liquid is interspersed in the plasma. Silsby et al. used a global model to investigate one-film and two-film transport theory at the interface between the gas and liquid [17]. Using Sherwood numbers (ratio of convective mass transfer to diffusive mass transfer) specific to each species, they showed that two-film transport theory more accurately captures the gas-liquid interface than one-film transport theory.

In this chapter, atmospheric pressure plasma interactions with dielectric droplets as a proxy for liquid droplets were computationally investigated for a radio frequency (RF) plasma sustained in He. This chapter builds on previous experimental work in the same system to investigate transport processes into liquid droplets. The experimental system had a 2 mm gap between electrodes and electrode length of 9.5 mm [18]. To characterize the plasma, Nayak et al. measured He metastable densities produced by broadband absorption spectroscopy [18]. They found that the densities of both He metastables He(2^3S) and He_2^* were maximum close to the electrodes. Adding 50 ppm of H_2O to the gas mixtures reduces both monomer and dimer He excited state densities due to quenching by H_2O. In a companion study, Nayak et al. used broadband absorption and optical emission spectroscopy to estimate the electron temperature and density for both He and Ar plasmas [19]. They measured the plasma emission and estimated the emissivity using Maxwellian and non-Maxwellian electron energy distributions (EEDs). The best fit of the emissivity was found with a non-Maxwellian EED which produced an electron temperature of 3.5 eV and electron density of 1.2×10^{11} cm^{-3} for a He plasma. Having characterized the plasma, Oinuma et al. investigated the transport of OH into a water droplet by flowing water droplets through the plasma and collecting them for later analysis [20]. $HCOO^-_{aq}$ was dissolved in the droplet, and its degradation over time provided an estimate of OH radicals solvating into the droplet from the plasma. Based on a 1D reaction-diffusion model that matches the experimental results, OH_{aq} reacts with $HCOO^-_{aq}$ primarily at the surface of the droplet. $HCOO^-_{aq}$ degradation is therefore limited by $HCOO^-_{aq}$ diffusion from the bulk to the surface of the droplet. The effects of other reactive species, including O, H, $O_2(a^1\Delta_g)$, O_3, metastable He atoms, and metastable Ar atoms, on $HCOO^-_{aq}$ degradation were analyzed by Nayak et al. [21]. O was found to possibly contribute to the degradation of $HCOO^-_{aq}$, and a lower bound on that reaction rate was estimated to be 1.66×10^{-13} cm^3/s.

The plasma treatment of liquid droplets affects the surrounding in several ways. The droplet will likely evaporate, producing a region of high vapor density around the droplet that will affect plasma transport properties and plasma chemistry. The droplet may act as a sink for plasma-produced reactive species or a source of in-liquid produced species which transport into the plasma. The droplet is also electrically active. That is, the droplet will electrically charge as a floating body in a plasma, producing a sheath at its boundary with the plasma. Droplets with large electrical permittivities will polarize in the applied and plasma generated electric fields. The polarization electric fields then modify plasma properties.

The plasma chemistry and electrical consequences of droplets in plasmas occur simultaneously. In order to investigate and isolate the electrical consequences of droplets in atmospheric pressure plasmas, the results discussed here focus on the plasma-surface interactions of a dielectric, non-reactive droplet. The system is an atmospheric pressure RF generated plasma sustained in He, similar to the experiments conducted by Nayak et al. and Oinuma et al. [18–21]. The sheath around the droplet is asymmetric due to the horizontally applied electric field and polarization of the droplet. While the sheath oscillates over the RF cycle, the applied voltage and sheath oscillation are 50-60° out of phase, a consequence of the RC-like behavior of the current flow (capacitance due to sheaths and the droplet, and resistivity due to the bulk plasma). The electric field around the droplet is the sum of the electric field in the bulk plasma resulting from the applied voltage, the sheath electric field surrounding the droplet, and the electric field due to polarization of the dielectric droplet. This combination produces a maximum in E/N (electric field/gas number density) on one side of the droplet, where these electric fields constructively interfere, and a minimum in E/N on the opposite side of the droplet, where these electric fields destructively interfere. Changing the relative permittivity ε_r, diameter, and conductivity of the droplet primarily affects the sheath surrounding the droplet by changing the polarization and allowing charge transport through the droplet.

The conditions for the chapter and model are described in Section 5.2. Comparison of the model to experimental results of plasma properties are presented in Section 5.3. The bulk plasma properties and properties of the sheath surrounding the droplet are described in detail in Section 5.4. Results of varying the properties of the droplet (relative permittivity ε_r, diameter, conductivity) are discussed in Section 5.5, and results of varying properties of the plasma (RF frequency, power deposited) discussed in Section 5.6. Concluding remarks are in Section 5.7.

5.2 Description of the Model and Experiment

The conditions investigated in this chapter are patterned after the experiments conducted by Nayak et al. and Oinuma et al. [18–21]. The reactor is an atmospheric pressure RF glow discharge sustained in He and operated at 13.56 MHz. The two parallel plate electrodes are separated by 2 mm and are surrounded by polytetrafluoroethylene (Teflon). As described by Oinuma et al. [20], water droplets (36 µm – 56 µm in diameter) are dispensed and flow with the gas through the reactor for fundamental studies of plasma-droplet interactions. These droplets are collected by an aluminum insert kept at a temperature below freezing to preserve the droplets for later chemical analysis.

To investigate the sheath that forms around the droplet immersed in the RF plasma, the 2D model *nonPDPSIM* was used. *nonPDPSIM* is described in in Section 2.2 and will not be redescribed here. In this chapter, secondary electron emission from surfaces in contact with the plasma was included with a yield for all positive ions of 0.1 on metal surfaces and 0.01 on dielectric surfaces. With the plasma being largely confined between the metal electrodes, the plasma properties are not particularly sensitive to the value of the secondary electron emission coefficient on the bounding dielectrics. The temperature of these secondary electrons was assumed to be the electron temperature at that location. The Boltzmann table was updated every 5 ns during integration of the plasma transport equations to reflect changes in composition of the gas. Photoionization was not included. The capacitively-coupled power module was used to obtain the desired power, and the desired power was typically produced after 20 RF cycles.

Two geometries for the atmospheric pressure RF glow discharge were investigated in this chapter. The first 2D Cartesian geometry closely replicated the experimental reactor and is shown in Figures 5.1a and 5.1b. The droplet is not included in this geometry to better compare model results with experimental measurements of the plasma. The mesh contains 9,077 total nodes and 6,379 gas phase nodes. The left electrode and boundary of the computational domain were grounded. The right electrode and boundary of the computational domain were powered. The electrodes are separated by 2 mm. The Teflon (ε_r = 2.1) above and below the electrodes is separated by 3 mm. The depth of the reactor was 1.91 cm. To compare with experiments, the plasma was sustained in He with air impurities (6 ppm N_2, 2.3 ppm H_2O, and 1.5 ppm O_2), and the RF frequency was 13.56 MHz [18].

The second 2D geometry was used to investigate the sheath around the droplet and is shown in Figure 5.1c. The numerical mesh has 9,695 total nodes and 7,344 gas phase nodes. This 2D Cartesian geometry was similar to the experimental reactor with the exception of the electrode gap which was increased to 3 mm. The gap between the Teflon above and below the electrodes was 4 mm. The increase in the gap was made to better isolate the sheath dynamics around the droplet from the sheath dynamics occurring at the electrodes. The depth of the reactor was 1.91 cm. The plasma was sustained in He with dry air impurities (16 ppm N_2 and 4 ppm O_2). The RF frequency was 10 MHz or 50 MHz, and the power deposition was varied from 1 W to 15 W. Evaporation from the droplet is not included in the model. The model was typically executed for over 135 cycles in each case to achieve quasi-steady state over an RF cycle.

A dielectric droplet was placed at the center of the gap between the electrodes with its diameter varied from 40 µm to 80 µm. The numerical mesh near the droplet is shown in Figure 5.2. The relative permittivity ε_r of the droplet was varied from 1 to 80, and the conductivity was varied from 0 to 10^{-1} S/cm. The droplet is treated as a dielectric as opposed to an active liquid plasma. This choice was made in order to isolate the sheath dynamics which are more universal behavior from the plasma-chemical processes that may be particular to a given system. Since we used a 2D Cartesian geometry, the droplet is effectively represented as a cylindrical rod in the model. The differences caused by the droplet being a cylinder as opposed to a sphere in the experiment are mentioned during discussion of the results.

The reaction mechanism consisted of 15 charged species, 11 neutral species, and 18 excited states with 796 reactions. The species included in the model are listed in Table 5.1. A limited number of oxygen and nitrogen species were included to account for the dry air impurities. Given their small densities, higher order species such as nitrogen oxides were not included in the mechanism. The reaction mechanism was based on Van Gaens and Bogaerts [24] with updates to include He made by Norberg [25]. Updates based on branching ratios to excited states of recombination of He^+ and He_2^+ were obtained from Emmert et al. [26], and radiation trapping factors were computed in the manner described by Lietz et al. [27].

5.3 Comparison of Results from the Model to Experiments

Predictions of the model were compared to the results of experiments performed by Nayak et al. [18,19]. These experiments measured the electron density and temperature as well as the density of the metastable states $He(2^3S)$ and He_2^*. These measurements were made without water droplets in the plasma. The power deposition was 15 W at an RF frequency of 13.56 MHz.

The bulk plasma properties obtained from the model are shown in Figure 5.3a time-averaged over one quasi-steady state RF cycle – electron density, E/N and T_e. The time-averaging was performed using average_over_time, one of the post-processing scripts described in Section 2.2.10. The electron density peaked at the sheath edge at the electrodes (8.7×10^{11} cm^{-3}) with the density in the center of the gap a factor of two lower (4×10^{11} cm^{-3}). This profile is enabled by dissociative recombination of molecular ions in the bulk plasma dominating electron loss. With the electron density peaking near the sheath edge, this plasma may operating in a combination of a γ-mode or a Penning mode [28,29]. In the γ-mode, ionization is dominated by secondary electron emission, acceleration in the sheaths at the electrodes and subsequent electron-impact ionization. The Penning mode produces ionization in the sheaths by Penning ionization from excited states produced in the sheath. For these conditions, the time-averaged rate of direct electron-impact ionization in the sheaths has a maximum value of 1.6 × 10^{18} $cm^{-3}s^{-1}$. The rate for Penning ionization is 4.1 × 10^{18} $cm^{-3}s^{-1}$.

E/N peaks in the sheaths at the electrodes with a maximum value of 30 Td (1 Td = 10^{-17} V-cm^2), while E/N in the bulk plasma is an order of magnitude lower at 2 Td. The sheath thickness at the electrodes is about 300 µm on a time-averaged basis. Since T_e is largely determined by E/N, T_e also peaks in the sheaths near the electrodes at 4 eV while T_e in the bulk plasma is 1.5 eV. These results mirror those for modeling atmospheric pressure He capacitively coupled discharges having similar gaps and power deposition [28,30–32]. The power deposition also peaks in the sheaths near the electrodes. T_e at various times throughout the RF cycle is shown in Figure 5.3b across the plasma gap. This profile across the plasma gap is taken at the center of the electrodes. At 18.4 ns (25% through the RF cycle when the powered electrode is at its peak voltage), T_e reaches 6.5 eV near the grounded electrode and is 1.1 eV near the powered electrode. The maximum T_e in the bulk plasma is 1.8 eV. The opposite is true at 52.3 ns (75% through the RF cycle) when the voltage on the powered electrode is at its most negative. The time-averaged T_e is also shown in Figure 5.3b.

To determine the electron density and T_e, Nayak et al. measured the absolute optical emission from the plasma. They calculate the emissivity due to Bremsstrahlung as a function of wavelength, $\varepsilon_{ea}(\lambda)$, from

$$\varepsilon_{ea}\left(\lambda\right)=C_{ea}\frac{n_e[He]}{\lambda^2}\int_{\frac{hc}{\lambda}}^{\infty}\sigma_m(\varepsilon)\varepsilon^{3/2}\left(1-\frac{hc}{2\lambda\varepsilon}\right)\sqrt{1-\frac{hc}{\lambda\varepsilon}}f(\varepsilon)d\varepsilon, \tag{5.1}$$

where λ is the emission wavelength, ε is the electron energy, C_{ea} = 1.77 W m^2 $J^{-3/2}$ sr^{-1}, n_e is the electron density, [He] is the He density (2.45 × 10^{19} cm^{-3}), h is Planck's constant, c is the speed of light, $\sigma_m(\varepsilon)$ is the momentum transfer cross-section for electrons colliding with He [33], and f(ε) is the electron energy distribution. They compared these emissivity estimates to their experimentally measured emission spectra to determine n_e and T_e. These values of n_e and T_e are temporal and spatial averages over the volume from which photons were collected over the RF cycle.

To compare results of the model to the temporal and spatially averaged experimental results, the emissivity at discrete points across the plasma gap was calculated by using time-resolved n_e and T_e at each location across the gap, as provided by the model, and a Maxwell-Boltzmann electron energy distribution, which is a simplifying assumption, using compare_emissivities, a post-processing script for *nonPDPSIM* described in Section 2.2.10. The emissivity was only calculated for those locations with electron temperatures above 1.37 eV (energy of a 900 nm photon, lowest wavelength measured). The emissivity was then averaged over time and across the plasma gap. The predicted emissivity from the model is shown in Figure 5.4a. Experimentally, the electron density and temperature required to reproduce measured emissivity are $n_e = 2.0 \times 10^{11}$ cm^{-3} and $T_e = 2.5$ eV when using a Maxwell-Boltzmann energy distribution [19]. The emissivity predicted by the Maxwell-Boltzmann energy distribution is also shown in Figure 5.4a. The best fit reported by Nayak et al. was for a non-Maxwellian energy distribution (1.2×10^{11} cm^{-3} and 3.5 eV). As shown in Figure 5.4a, the emissivity predicted by the model closely matches the experimental results, indicating that the model accurately represents the experimental conditions.

Measurements were also made of the densities of two He metastable states ($He(2^3S)$ and $He_2(a^3\Sigma_u^+)$) [18]. The densities predicted by the model are compared to the experimental measurements in Figure 5.4b. The time-averaged densities from the model results were extracted along a line perpendicular to the electrodes and at the center of the electrode height using the post-processing script extract_1d_lines described in Section 2.2.10. The modeled densities were also smoothed by averaging within 0.2 mm using he_metastable_calculation described in Section 2.2.10. To estimate the value of $He_2(a^3\Sigma_u^+)$ from the lumped He_2^* state in the model, the density of He_2^* is multiplied by the fraction of $He(2^3S)$ divided by the total He excited state density, since $He(2^3S)$ forms $He_2(a^3\Sigma_u^+)$ at each point across the plasma gap. Both He metastable densities from the model are maximum near the electrodes and decrease by at least three orders of magnitude in the bulk plasma due to the higher T_e near the electrodes and quenching of these states by impurities. The experimentally measured densities are normalized to span the entire plasma gap. The experimentally measured densities are also maximum close to the electrodes and decrease significantly in the bulk plasma. The model results reproduce the spatial dependence of the densities measured in the experiments, albeit with higher maximum densities. The difference in peak densities are attributed to uncertainties in the precise densities of impurities.

5.4 Plasma Properties with an Immersed Dielectric Droplet

Properties of the bulk plasma and the sheath surrounding the dielectric droplet are discussed in this section. The base case was an RF glow discharge operating at 10 MHz with 5 W power deposition. The plasma was sustained in He with 20 ppm of dry air impurity (16 ppm N_2 and 4 ppm O_2). The initially nonconductive 80 μm diameter dielectric droplet with $\varepsilon_r = 80$ was placed in the center of the plasma.

5.4.1 Bulk Plasma Properties

The bulk plasma properties averaged over one quasi-steady state RF cycle are shown in Figures 5.5 - 5.8 for the base case (5 W) as well as the parameter sweeps discussed in the next two sections. The voltage amplitude to deliver 5 W was 326 V. (There is essentially no DC bias in this geometrically symmetric system.) The bulk electron density is 7.5 × 10^{11} cm^{-3} on the central axis several droplet diameters away from the droplet. At low power deposition (5 W being at the top of that range), the 80 µm diameter droplet influences the electron density across the width of the bulk plasma. The droplet produces a shadow of electron density on either side. The electric field in the bulk plasma a few diameters away from the droplet oscillates with an amplitude of about 80 V/cm or an E/N of 0.33 Td for which the drift velocity of electrons in pure He is 2.7 × 10^5 cm-s^{-1}. During ¼ of the 100 ns RF cycle, electrons drift about 35 µm, so at least a portion of the electron exclusion is due to physical shadowing or obscuration of the electrons' horizontal motion by the droplet. This effect is likely exaggerated by the 2D simulation, in which the droplet appears to be a rod, and so provides no avenue for electrons moving horizontally to avert the droplet at the axial location of the droplet (perpendicular to the computational domain). If the droplet was spherical, electrons drifting horizontally at the height of the droplet would have the option of drifting around the droplet.

The time-averaged E/N has a maximum value of 23 Td (5625 V/cm) in the sheaths that form at the electrodes. The instantaneous maximum is 51 Td (12,500 V/cm). The time-averaged E/N value in the bulk plasma is less than 0.25 Td (61 V/cm) with an instantaneous maximum of 0.35 Td (86 V/cm). The electron temperature T_e is largely determined by heating by the oscillating sheath at the electrodes and secondarily by Joule heating in the bulk plasma. The time-averaged maximum T_e is 3.75 eV at the sheath edge at the electrodes with an instantaneous maximum of 6 eV. In the bulk plasma (on axis), the time-averaged T_e is 0.2 eV with instantaneous maximum of 0.3 eV. This range of T_e is similar to that reported in modeling by Liu et al. [30]. The thickness of the sheath at the electrodes was 500 µm on a time-averaged basis.

Primary ionization and excitation of He is dominated by the sheath heated electrons within 300-400 µm of the electrodes. Ionization is dominated by Penning processes of He excited states and the air impurities in the bulk plasma where the net electron-impact ionization source is negative. That is, the rate of direct electron-impact ionization is lower than losses by dissociative recombination. The electron temperature is lower in the bulk plasma compared to, for example, the COST plasma jet due to the larger inter-electrode gap. With sheath heating dominating, plasmas having a smaller gap between the electrodes will have higher electron temperatures on axis [28,30–32].

Volume-averaged densities are shown in Figure 5.9 as a function of time over the RF cycle. With the exception of He^+, the charged particle densities are nearly constant over the RF cycle. The electron density is 1.8×10^{11} cm^{-3} with N_2^+ and O_2^+ having densities near 1.4×10^{11} and 5.4×10^{10} cm^{-3}, respectively, being the dominant positive ions. While N_2 and O_2 have only impurity level densities, the ionization potentials of N_2 and O_2 are lower than that of He, leading to N_2^+ and O_2^+ becoming the dominant positive ions through charge-exchange and Penning ionization processes. He_2^+ is the dominant helium ion, with a density near 10^9 cm^{-3}. The negative ions O_2^- and O^- are primarily formed by three-body and dissociative attachment to O_2, respectively, and have densities near 10^8 cm^{-3}. The density of He^+ oscillates between 3×10^7 cm^{-3} – 10^8 cm^{-3} over the RF cycle. This oscillation indicates He^+ is produced and consumed at different times during the RF cycle. In spite of the rate of formation of He^+ by electron impact at the sheath edge being the largest of all ions due to its large mole fraction, its rapid rate of dimerization to form He_2^+ and charge-exchange with impurities rapidly depletes its density. Since T_e in and adjacent to the sheaths oscillates over the RF cycle, the production of He^+ also oscillates over the RF cycle.

Neutral radicals and excited states are shown in Figures 5.9b and 5.9c during the RF cycle. The volume-averaged densities of metastable electronic states (e.g., $N_2(A)$, $O_2(^1\Delta)$, $O_2(^1\Sigma)$, $He(2^3S)$), vibrationally excited molecules, and radicals do not significantly oscillate over the RF cycle due to their low rates of quenching and reaction. The excited states of He with shorter radiative lifetimes or trapped lifetimes have moderate oscillation.

5.4.2 Sheath Surrounding the Droplet

As an electrically floating body in the plasma, the droplet will acquire an electrical charge which, on a time-averaged basis, balances the currents of positive and negative species to the surface. In doing so, the surface of the droplet charges, and a sheath is formed at the surface of the droplet. In an electropositive plasma, the droplet should charge negatively compared to the local plasma potential to reflect a portion of the higher thermal flux of electrons compared to positive ions. In an isotropically uniform, quiescent plasma in which the electric field in the bulk plasma is small compared to the electric fields in the sheath, the surface charge on the droplet and sheath around the droplet should both be uniform. That is, a spherical or cylindrical droplet should have a sheath with a uniform thickness and sheath potential as a function of azimuthal position that is uniform.

The electron density, E/N, T_e, and charge density on the droplet are shown in Figure 5.10 over the first half of a quasi-steady state RF cycle at 5 ns intervals in the 100 ns (10 MHz) period. (The second half of the RF cycle is not shown because the results mirror those of the first half.) The time-averages of these quantities over the RF cycle are shown in the last row of Figure 5.10. A sheath forms around the droplet, indicated by the lower electron density and larger E/N in the vicinity of the droplet shown in Figures 5.10a and 5.10b. The mean free path for electrons and ions at 1 atm is less than 2 µm, whereas the average thickness of the sheath is more than 100 µm resulting in the sheath being collisional. (Sheath thickness around the droplet is defined in this work as the location where the net charge density is 0.01 that of the positive ion density to capture where charge separation begins to occurs in the sheath. Since the gradient in charge density is steep at this location, our conclusions are not particularly sensitive to the precise value of charge density that designates the edge of the sheath.) The sheath is not circular and is elongated along the equator (in the horizontal direction) due, in part, to the influence of the applied horizontal electric field and the polarization of the droplet. During the RF cycle along the equator, the sheath thickness varies from 20 µm to 130 µm. At the poles (in the vertical direction), the sheath thickness varies from 70 µm to 90 µm. The Debye length in this system is 16.4 µm, which is typically smaller than the sheath thickness around the droplet based on the average charge. This is also consistent with the classic derivation of sheath thickness based on the Bohm criterion.

The properties of the sheath around the droplet, including the electron density, oscillate over the RF cycle out of phase with the sinusoidal applied voltage. The applied voltage to the powered electrode is maximum at 25 ns into the RF cycle which does not coincide with the maximum deformation in the sheath. The charging and discharging of the droplet can be viewed as that of a capacitor, and so the response of the droplet can be approximated as an RC circuit. The impedance of the RC circuit is complex due to the capacitor, leading to a phase difference ϕ between the voltage and the current. This phase angle is given by

$$\cos(\phi) = \frac{R}{\sqrt{R^2 + \left(\frac{1}{\omega C}\right)^2}}, \tag{5.2}$$

where R is the series resistance, ω is the radian frequency of the voltage oscillation, and C is the series capacitance. The series capacitance is due to the capacitance of the sheath at the electrode, the sheath around the droplet, and the droplet itself. The capacitance of the sheaths at the electrodes $C_{s,e}$ [34] in series with the droplet is

$$C_{s,e} = \frac{1.226\varepsilon_0 A}{\lambda_D}, \tag{5.3}$$

where ε_0 is the permittivity of free space, $A = \pi R_p^2$ is the cross-sectional area of the droplet with radius R_p, and λ_D is the Debye length, used as an estimate of sheath thickness. Note $C_{s,e}$ is the capacitance of the sheath at one electrode and must be accounted for twice in calculating the series capacitance of the system. The capacitance of the sheath around the droplet $C_{s,d}$ is approximately

$$C_{s,d} = \frac{4\pi\varepsilon_0}{\frac{1}{R_p} - \frac{1}{R_s}}, \tag{5.4}$$

where R_s is the radius of the sheath, estimated to be the semimajor axis of the elliptical sheath. The capacitance of the droplet C_d is

$$C_d = 4\pi\varepsilon_0\varepsilon_r R_p, \tag{5.5}$$

where ε_r is the relative permittivity of the droplet. Plasma resistance was calculated from the bulk plasma conductivity σ

$$\sigma = \frac{e^2 n_e}{m_e \nu_m}, \tag{5.6}$$

where e is the fundamental charge, n_e is the bulk electron density, m_e is the electron mass, and ν_m is the momentum transfer collision frequency of electrons in the bulk plasma (3.5×10^{11} s^{-1}). From the conductivity, the resistance of the plasma was

$$R = \frac{L}{\sigma A}, \tag{5.7}$$

where L is the gap between the electrodes. With this analysis performed by the post-processing script calculate_phase, the phase of the oscillation of the sheath was estimated to be 53°, closely matching the results of the model (54°).

In the absence of plasma, the polarization of the droplet by the horizontal external electric field produces a maximum in electric field at the surface of the droplet at the horizontal equator and a minimum at the axial poles. The polarization electric field outside a droplet of relative permittivity ε_r is

$$\vec{E} = E_0 \cos\theta \left[1 + 2\left(\frac{R_p}{r}\right)^3 \frac{\varepsilon_r - 1}{\varepsilon_r + 2} \right] \hat{a}_r - E_0 \sin\theta \left[1 - \left(\frac{R_p}{r}\right)^3 \frac{\varepsilon_r - 1}{\varepsilon_r + 2} \right] \hat{a}_\theta, \qquad (5.8)$$

where θ is measured from the direction of the external electric field having magnitude E_0. The E/N in the vicinity of the droplet, Figure 5.10b, results from the superposition of the electric field in the bulk plasma and the sheath electric field, modified by the polarization of the droplet. The electric field in the sheath surround the droplet is continuously directed inwards towards the droplet, while the electric field in the bulk plasma oscillates over the RF cycle. The superposition of these two electric fields enhances the total E/N at the equator on that side of the droplet (and phase in the RF cycle) that the sheath and bulk electric field both point in the same direction. The maximum of E/N near the droplet at the equator is 4 Td. The superposition of these two electric fields minimizes the total E/N at the equator on that side of the droplet (and phase in the RF cycle) that the sheath and bulk electric field point in opposite directions. This superposition produces a zero in E/N when the sheath and bulk electric fields are equal. With the bulk applied electric field having a purely horizontal orientation, and the electric field in the sheath being axially directed, there is no direct competition between the bulk and sheath electric fields at the poles. The sheath thickness at the poles therefore experiences less modulation during the RF cycle than at the equator.

There is some degree of shadowing of the electron drift motion by the droplet that contributes to the asymmetry in the sheath. In pure He, the drift velocity for E/N = 2 Td is about 10^6 cm/s, which during ¼ of the RF cycle produces drift distance of about 300 μm. This distance exceeds the diameter of the droplet. With virtually no axial component of the bulk electric field, the droplet effectively shadows electron drift motion at the equator, a shadow that must be filled in by diffusion. This shadowing lowers the average electron density along the equator on the opposite side of the droplet, which then translates to a thicker sheath.

T_e over the RF cycle is shown in Figure 5.10c in the vicinity of the droplet. T_e oscillates with the same phase as the electron density and E/N. The maximum in T_e near the droplet is 0.35 eV and occurs at about 45^o above and below the horizontal plane. It is in this region that the power deposition per electron is the highest. It is also at this location that the polarization electric field is zero. However, the time-averaged maximum in T_e occurs at the poles. It is at these locations that the E/N is always finite and does not experience a zero-crossing. The time-averaged minimum in T_e occurs at the equator of the droplet as this is where the E/N is, on the average, lowest due to the canceling of bulk and sheath fields. While T_e does vary over the RF cycle near the droplet, the variation is small for these conditions (< 0.35 eV). Therefore, reactive species fluxes to the droplet will likely not vary based on the change in T_e near the droplet. The majority of reactive species are produced further away near the sheaths at the electrodes. That said, rotational and vibrationally excited species fluxes may change based on this small change in T_e.

The charge density on the droplet is shown in Figure 5.10d. Since the droplet is nonconductive, and its charging time exceeds the RF period, the charge density on the surface does not significantly change over the RF cycle after coming into equilibrium following approximately 20 RF cycles or about 2 μs. With the droplet being a floating dielectric in an electropositive plasma, the total charge density on the particle must be negative, as it is here. The total average charge is -1.5 × 10^7q (where q = 1.6 × 10^{-19} C), producing a time-averaged sheath potential of -1.5 V along the equator and -1.4 V along the poles, commensurate with the low time-averaged electron temperature.

The distribution of the charge on the droplet is non-uniform. The surface is charged negatively at the equator and is charged positively at the poles. This disparity in charging is due in part to the directed drift of electrons and due in part to the polarization electric fields. With there being shadowing of the electron drift motion by the droplet, the drift component of the electron flux into the sheath is smallest at the poles and largest at the equator. In fact, the decrease in horizontal electric field at the poles reduces the drift component. Electron transport to the sheath is dominated by drift at the equator while being dominated by diffusion to the poles. The ions, with lower mobility, largely respond to the time-averaged sheath electric field which transports ions by drift to the surface of the particle throughout the RF cycle at all surface points. The lack of a drift component of electrons in the flux of the surface at the poles and dominance of the drift component of the electron flux at the equator leads to the differential charging. With there being no conductivity to redistribute these charges, an asymmetric charge distribution can be supported. This differential charging of the surface is allowed by the net charge on the droplet being negative, thereby placing the droplet, on the average, at a more negative potential with respect to the low plasma potential. The differential charging of the surface provides for the local changes in sheath potential that are required to balance electron and ion fluxes to that location.

The fluxes of the charged species to the droplet over the RF cycle are shown in Figure 5.11. These results were extracted on the equator (left and right) and on the poles (top and bottom) using extract_over_cycle_flux1d as described in Section 2.2.10. Fluxes to the equator of the droplet are shown in Figures 5.11a and 5.11b. With fluxes of electrons into the sheath being dominated by drift, the fluxes collected at the left and right equators are asymmetric and 180^o out of phase. Here, the polarization of the droplet produces large enough electric fields that even the ion fluxes have significant modulation. The maximum in ion flux coincides with a minimum in electron flux, which corresponds to that portion of the RF cycle that the opposing electric fields (sheath and bulk plasma) produce a maximum at the equator. The maximum in ion flux and minimum in electron flux are out of phase with the applied RF voltage, as shown in Figure 5.11. The maximum of electron flux occurs at the minimum extension of the sheath when the electric fields in the sheath and bulk plasma oppose each other. At all locations, the peaks in the oscillation of all the fluxes were out of phase with the applied voltage and in phase with the oscillation of the sheath.

The fluxes of ions to the surface do not significantly vary over the RF cycle at the poles of the droplet, as shown in Figures 5.11c and 5.11d. The flux of electrons is highly modulated over the RF cycle as the electrons with a higher mobility respond to the changing electric field more quickly than the ions. The flux of electrons to the poles peaks twice over the RF cycle at $2 – 4 \times 10^{15}$ cm^{-2} s^{-1}. Transport of electrons to the poles is dominated by axial diffusion which is not particularly sensitive to the direction of the horizontal electric field. However, the availability of electrons in the vicinity of the poles which are then available to diffuse to the poles is sensitive to the horizontal electric fields. Fluxes to the top and bottom poles are essentially the same.

5.5 Sheath Characteristics for Different Droplet Properties

5.5.1 Permittivity

With the droplet being an electrically floating body in the plasma, its charging and discharging during the RF cycle will be a function of its electrical permittivity, or its capacitance. The RF cycle averaged electron density, E/N, and T_e of the bulk plasma are shown in Figures 5.5b, 5.6b, and 5.7b for $\varepsilon_r = 1$ to 80. The influence of the droplet on the plasma is in large part manifested by the exclusion of bulk plasma by the sheath around the droplet, and the charge accumulation (and discharging) during the RF cycle. The charging and discharging of the droplet during an RF cycle is approximately 1.1×10^6q for all permittivities, which is a small fraction of the electron inventory in the vicinity of the droplet. As a result, the capacitive nature of the droplet does not significantly affect the bulk plasma. The permittivity of the droplet does affect the time to charge the droplet (larger permittivity, larger RC time constant).

However, near the droplet, ε_r of the droplet does affect the sheath, the spatial distribution of charge on the droplet, and the local electron density. The time-averaged electron density and charge on the droplet for $\varepsilon_r = 1$ to 80 are shown in Figure 5.12a. As ε_r increases, the eccentricity of the sheath increases. In particular, the sheath extends further along the equator as ε_r increases whereas there is little change in sheath properties at the poles. This extension in the sheath is attributable to the more intense polarization electric fields at the equator with increasing ε_r. With $\varepsilon_r =1$, there are no polarization electric fields to perturb the sheath. The disparity in the shape of the sheath is then fully attributable to the drift component of the electron flux in the horizontal direction and shadowing of electron flux.

The azimuthal charge density on the surface of the droplet is a function of ε_r. With $\varepsilon_r = 1$, the droplet is negatively charged at all azimuthal positions with the largest negative charge density being at the poles. With the absence of polarization electric fields at $\varepsilon_r = 1$, the shadowing of the drift flux in the horizontal direction produces, on the average, lower electron fluxes to the equator compared to the poles. The time-averaged sheath potential at the equator is -1.0 V and at the poles is -1.3 V. As ε_r increases to 4, the negative charge density at the equator increases in magnitude. With $\varepsilon_r = 20$, positive charge density emerges at the poles of the droplet and negative density intensifies at the equator, while the average charge density on the droplet remains negative. The time-averaged sheath potential at both the equator and poles is -1.5 V. This charging pattern is retained with $\varepsilon_r = 80$ with the magnitude of the charge density increasing by a factor of 4 relative to $\varepsilon_r = 20$ to account for the larger capacitance of the droplet. The time-averaged sheath potential at the equator is -1.5 V and at the poles is -1.4 V.

The oscillation of the electron density a distance $2R_p$ from the center of the droplet along the left equator is shown in Figure 5.12b for $\varepsilon_r = 1$ to 80. The oscillation was extracted using the post-processing script extract_over_cycle described in Section 2.2.10. With an increase in ε_r, the electron density decreases, which is largely a consequence of the sheath being thicker with larger ε_r producing a smaller electron density near the surface. With the polarization electric field saturating for $\varepsilon_r > 10\text{-}20$, the electron density is similar with $\varepsilon_r = 20$ and 80. The phase of the electron density oscillation is similar for all ε_r, ranging from 54° for $\varepsilon_r = 80$ to 58° for $\varepsilon_r = 1$. These results match the predicted phases of oscillation, which varied from 53° for $\varepsilon_r = 80$ to 59° for $\varepsilon_r = 1$. Since the phase of oscillation is similar for all ε_r, the capacitance of the droplet is not the dominant factor in determining the phase.

The dynamics of E/N over one quasi-steady state RF cycle as well as the time-averaged values are shown in Figure 5.13 for $\varepsilon_r = 1$, 4, 20 and 80. With $\varepsilon_r = 1$, E/N is maximum at the poles of the droplet. In the absence of polarization electric fields, there is no decrease in the applied electric field at the poles. The electric fields and formation of sheaths at the poles are solely due to diffusion of electrons and positive ions from the bulk plasma. However, in the absence of polarization of the droplet, the E/N still has a zero at the equator when the sheath and applied electric fields oppose each other. The end result is that the time-averaged E/N is maximum at the poles, leading to an oblate shape.

The maximum instantaneous E/N occurs on the equator of the droplet for $\varepsilon_r = 4$. However, the maximum of the time-averaged E/N occurs at the poles due to the lack of competition between the sheath electric field and the bulk electric field. As ε_r increases to 20 and 80, the magnitude of E/N increases, and the maximum of the time-averaged E/N shifts to the equator due to the increased polarization of the droplet.

5.5.2 Diameter

The diameter of the droplet was decreased from 80 µm to 60 µm and 40 µm. The bulk electron density does not significantly vary with the diameter of the droplet except along the equator of the droplet, where the electron density increases as the diameter of the droplet decreases. This increase in electron density occurs because the cross-sectional area of the droplet decreases, allowing more electrons to move around instead of becoming obscured and shadowed by the droplet. E/N and T_e in the bulk plasma also do not significantly change as a function of diameter of the droplet.

While the bulk plasma does not significantly change, sheath properties near the droplet do depend on the diameter of the droplet, as shown by the time-averaged values in Figure 5.14. The maximum E/N increases and E/N becomes more azimuthally symmetric as the diameter decreases. The polarization of the droplet is independent of diameter; however, the extent of the polarization electric field beyond the surface of the droplet scales with the size of the droplet. With the sheath thickness largely a function of the bulk plasma properties, and so relatively constant with diameter of the droplet, the polarization electric field for the smaller droplets produces a smaller perturbation. With the shadowing of the electron flux being less severe with smaller diameters of the droplet, there is less horizontal elongation of the sheath. The spatial dependence of T_e is qualitatively the same for all diameters. With the droplet size being commensurate (or smaller) than the sheath thickness, we expect some dependence of sheath properties on droplet size independent of polarization and RF electric fields. For example, the curvature of the sheath increases as the ratio of the sheath thickness to droplet size increases.

The charge density on the droplet also varies with diameter. With small droplet sizes where the polarization electric fields are less influential and shadowing less severe, the uniformity of the surface charging improves. The same trend occurs when varying the permittivity of the droplet. The charge distribution for $\varepsilon_r = 1$ and $\varepsilon_r = 4$ is more uniform due to the smaller influence of the polarization of the droplet by the plasma. The same process is occurring with smaller diameters.

5.5.3 Conductivity

The previous discussion addressed the sheath properties surrounding a nonconductive dielectric droplet. The conductivity of water can range from 5×10^{-8} S/cm (ultrapure water) to 5×10^{-2} S/cm (sea water). To examine how the conductivity of the droplet affects the sheath around the droplet, the conductivity of the dielectric droplet was varied from 0 to 10^{-1} S/cm. The bulk plasma properties (electron density, E/N, and T_e) do not significantly vary as the conductivity of the droplet was increased, as shown in Figures 5.5c, 5.6c, and 5.7c. The charging and discharging of the droplet over the RF cycle is about 1.2×10^6q, which is not enough to affect the bulk plasma.

Regardless of the conductivity of the droplet, the droplet is a floating electrical body in the plasma which, on a time-averaged basis, should collect no net charge. In this regard, the charging potential, total charge, and sheath properties should not be a sensitive function of droplet conductivity. The time-averaged total charge on the droplet increases slightly from -1.5×10^7q on the nonconductive droplet to -1.9×10^7q for a droplet with a conductivity of 10^{-1} S/cm. However, the distribution of charge and how the droplet maintains the floating potential do depend on the droplet conductivity, as shown in Figure 5.15. The charge density on the droplet is shown every 25 ns during the first 50 ns of the quasi-steady state RF cycle, along with the time-averaged values for droplet conductivities of $\sigma = 10^{-1}$, 10^{-5} and 10^{-7} S/cm. The charge density on the least conductive droplet, 10^{-7} S/cm, essentially does not oscillate over the RF cycle and has regions of positive and negative charge, as is the case for the nonconductive droplet. With an increase in conductivity to 10^{-5} S/cm and larger, there is a distinct change in the charge distribution to being uniformly negatively charged. The magnitude of the negative charge density at the poles of the of $\sigma = 10^{-5}$ S/cm droplet is 1 order of magnitude less than that at the equator, a remnant of the positive charging of less conductive droplets. The charge density still does not oscillate significantly over the RF cycle.

With an increase in conductivity to 10^{-3} S/cm, the droplet remains uniformly negatively charged while the charge density oscillates over the RF cycle, side-to-side on the equator. The oscillation in charge density increases as the conductivity increases to 10^{-1} S/cm, as shown in Figure 5.15a. The higher conductivity is able to redistribute net positive charging at the poles produced with low conductivity to be an average surface charge over the entire droplet. With the net charge on the droplet being negative, this results in a negative surface charge over the entire droplet. With moderate conductivity, this redistribution occurs over many RF cycles. With the highest conductivity, this redistribution occurs in real time during a single RF cycle.

Current continuity must be maintained through the droplet. With the bulk plasma properties being a weak function of the droplet conductivity, the current flowing through the droplet should also be a weak function of conductivity. While the total current flowing through the droplet should not change with conductivity, the proportion of current that is displacement current and conduction current does change with conductivity. This change in character of the current is shown in Figure 5.16, displaying the conduction and displacement current density at the center of the droplet over one quasi-steady state RF cycle. The displacement and conduction currents were calculated by the post-processing scripts displacement_current and extract_over_cycle as described in Section 2.2.10. The current is entirely displacement current when the droplet is nonconductive. Displacement current dominates for conductivities up to 10^{-5} S/cm. As shown in Figure 5.15, the charge density on the surface of the droplet does not oscillate over the RF cycle for this range of conductivity. For droplet conductivities of 10^{-3} S/cm and higher, the conduction current is the same order of magnitude as the displacement current, as the conductivity is large enough to support charge transport through the center of the droplet. With a droplet conductivity of $\sigma = 10^{-1}$ S/cm, the conduction current through the droplet dominates over the displacement current. Although not calculated here as part of the simulation, the droplet may be heated by these conduction currents. For example, the power deposition at the center of the droplet is 40 µW cm^{-3}.

5.6 Sheath Characteristics for Different Plasma Properties

5.6.1 RF Frequency

The time-averaged electron density, E/N, and T_e for the entire discharge are shown in Figure 5.8 for RF frequencies of 10 MHz and 50 MHz while keeping the power constant at 5 W.

Time-averaged values of electron density, E/N, T_e, and charge density near the droplet are shown in Figure 5.17. The magnitude of the bulk electron density was similar between the two frequencies, as shown in Figure 5.8. However, the sheath is more symmetric at the higher frequency. While the ions do not significantly drift during the RF period for either frequency, electrons do significantly drift over half the RF cycle. That distance is approximately 30 µm at 50 MHz and 300 µm at 10 MHz. The former is commensurate with the diameter of the droplet whereas the latter is larger than the droplet diameter. This drift distance is 10 times lower at 50 MHz than at 10 MHz due both to the shorter period and the lower bulk electric field resulting from the lower applied voltage – 159 V at 50 MHz and 326 V at 10 MHz. The end result is that there is little shadowing of the electron flux by the droplet at 50 MHz while having significant shadowing by the droplet at 10 MHz. The greater shadowing at the lower frequency produces a more asymmetric sheath.

The asymmetry in the sheath surrounding the droplet at 50 MHz is largely due to the polarization of the droplet and less due to shadowing of the electron flux. The time-averaged sheath potential at 50 MHz (-5.4 V at the equator and -3.7 V at the poles) is at least 2.5 times larger than at 10 MHz (-1.5 V at the equator and -1.4 V at the poles) which then produces commensurate increases in E/N in the sheaths. These differences largely account for the increase in T_e surrounding the droplet that occurs at 50 MHz (0.65 eV) compared to 10 MHz (0.23 eV). T_e is also more uniformly distributed around the droplet at the higher frequency.

The distribution of charge density on the surface of the droplet does not significantly depend on RF frequency, as the poles are positively charged and the equator is negatively charged at both frequencies. However, at 50 MHz, the magnitudes of the positive and negative charges are at least three times higher than at 10 MHz, a consequence of the higher bulk T_e. Given that the charge distribution is nearly independent of frequency while shadowing is sensitive to frequency, the bipolar charge distribution is largely attributable to polarization of the droplet.

The oscillation of the electron density at $2R_p$ from the center of the droplet along the left equator and the top pole is shown in Figure 5.18a over one RF cycle for frequencies of 10 MHz and 50 MHz. While the electron densities at the equator are commensurate at 10 MHz and 50 MHz, the electron density at the pole is almost 3 times larger at 10 MHz than 50 MHz. The electron density is higher at 10 MHz because the sheath is more asymmetric, being thinner at the pole than along the equator due to the dominance of shadowing. The electron density at $2R_p$ from the center of the droplet is then more reflective of the bulk plasma density. The phase of the electron density oscillation at 50 MHz, -1.8°, is nearly in phase with the applied voltage. The dynamics of E/N are shown in Figure 5.18b at 5% of a diameter away from the left equator and from the top pole of the droplet. At the poles of the droplet, E/N does not oscillate significantly, with E/N twice as large at 50 MHz (4.1 Td) than at 10 MHz (2.1 Td) due to the lack of drift current directed into the poles. The same relative increase in E/N occurs at the equator where there is significant oscillation - 1.5 Td at 10 MHz and 3.5 Td at 50 MHz.

5.6.2 Power Deposition

The time-averaged electron density, E/N, and T_e for the entire discharge are shown in Figures 5.5a, 5.6a, and 5.7a, for power deposition of 1, 5, 10 and 15 W. With the increase in power deposition, the plasma transitions from the α-mode (dominated by bulk ionization) to the γ-mode or Penning mode (dominated by sheath ionization). The α-mode has the highest electron density in the bulk plasma, while the γ-mode has the highest electron density near the sheath edge [28,29]. The time-averaged bulk electron density at 1 W is 1.4×10^{11} cm^{-3} (applied voltage amplitude 235 V) and 7.7×10^{11} cm^{-3} at 5 W (326 V), both operating in α-mode. At 10 W (278 V), the electron density in the bulk plasma increases to 9.9×10^{11} cm^{-3} while the maximum shifts to the sheath edge at 1.5×10^{12} cm^{-3}, indicative of the start of the γ-mode or Penning mode. The bulk and sheath edge electron densities are 3.8×10^{11} cm^{-3} and 1.3×10^{12} cm^{-3} at 15 W (355 V). This voltage decrease is characteristic of the transition between the α- and γ- modes [28,29]. While the maximum time-averaged E/N occurs in the sheaths near the electrodes at all powers, as shown in Figure 5.6a, the maximum time-averaged E/N increases from 1 W (7 Td) to 10 W (30 Td) and slightly decreases at 15 W (29 Td). Similar to E/N, the maximum T_e occurs at the sheath edges, with cycle averaged T_e in the bulk plasma decreasing from 0.3 eV at 1 W to 0.16 eV at 5 W and increasing to 0.22 eV at 10 W and 1 eV at 15 W. The maximum T_e in the bulk plasma increases from 0.4 eV at 1 W to 1.7 eV at 15 W.

Since the electron density and T_e vary as a function of power, the relative abundances of ions and excited states change as well. The volume-averaged densities ions as a function of power are shown in Figure 5.19. To compare ion composition between powers, these densities are normalized to the volume-averaged electron density at each power. The normalized densities of N_2^+ and O_2^+ do not significantly change as a function of power. Charge-exchange reactions are rapid enough that helium monomer and dimer ions are consumed by reactions with the impurities at all powers. The relative density of O_2^- decreases with increasing power as the rate coefficient for three-body attachment to O_2 is proportional to T_e^{-2}, thereby decreasing its rate of formation as electron temperature increases with power. Although T_e increases with power, the rate of formation of O^- by dissociative attachment is low at all powers. The relative density of O^- decreases in large part because the rate of ion-ion neutralization increases with power. The relative densities of He^+ and He_2^+ increase with power in large part due to the increase in T_e.

The time-averaged sheath properties near the droplet are shown in Figure 5.20 for powers from 1 – 15 W. With the increase in bulk plasma density, the sheath thickness decreases from 1 W to 10 W, and the sheath becomes more symmetric. However, at 15 W, the sheath again becomes asymmetric due to shadowing by the increasing contribution of drift current. The maximum of the time-averaged E/N occurs at the equator of the droplet for all powers with the symmetry improving from 1-10 W and becoming asymmetric at 15 W. The pattern of droplet charging is the same at all powers, negative at the equator and positive at the poles.

5.7 Concluding Remarks

An important aspect of plasma-liquid interactions and the plasma-activation of liquids is the sheath that forms at the liquid surface. This is particularly important in plasma activation of droplets due to their high surface-to-volume ratio. In this chapter, the properties of sheaths around droplets immersed in an atmospheric pressure RF He plasma with air impurities were investigated using *nonPDPSIM*. The droplet was modeled as a dielectric to isolate the electrical properties of the plasma-droplet interactions from those resulting from chemistry. The reactor conditions were an electrode separation of 3 mm, length of 9.5 mm with power deposition of 1-15 W at a frequency of 10 MHz or 50 MHz. Droplet diameters of 40-80 μm, relative permittivities of 1-80, and conductivities up to 0.1 S/cm were investigated.

For most of the conditions investigated, the sheath surrounding the droplet was asymmetric, elongated in the horizonal direction aligned with the applied electric field. This asymmetry results from polarization of the droplet that maximizes the electric field on the equator of the droplet and shadowing of the horizontal drift motion of electrons due to the bulk electric field. With the charge on the droplet and bulk plasma properties being in a quasi-steady state during the RF cycle for most conditions, the sheath forming at the surface of the droplet should be symmetric, producing electric fields pointing radially inward towards the droplet. However, both the polarization electric field produced by the droplet and the bulk electric field alternate in direction and magnitude every half-cycle and are largest in the horizontal direction. The vector sum of the natural sheath electric field and the bulk electric field produces maxima and minima in the total electric field on opposite sides of the droplet along the equator. The end result is oscillation in the extent of the sheath at the equator. Since the bulk electric field is purely horizontal, there is less modulation of the sheath electric fields and less modulation in the sheath's extent at the poles of the droplet. The polarization dynamics in the sheath thickness scale with the permittivity of the droplet while being less a function of the discharge conditions.

The drift and shadowing component of the sheath asymmetry is more sensitive to plasma conditions. In He, the electron drift velocity is high enough that during a 10 MHz cycle, the electrons can drift more than the diameter of the droplet. This drift increases the electron density on one side of the droplet, thinning the sheath at the equator, and decreases electron density on the other side of the droplet, extending the sheath at the equator. Since the bulk drift current does not flow directly into the poles of the droplet, charged particle fluxes into the poles are diffusion dominated with thickness that is only weakly modulated during the RF cycle. Molecular gas mixtures having lower electron mobilities and lower drift velocities will produce less shadowing by the droplet and less modulation in the sheath properties. Operating at higher frequencies will reduce the drift contribution to the sheath asymmetry.

With the droplets being electrically floating bodies in an electropositive plasma, the droplets charge, on the average, negatively and acquire, on the average, a negative potential with respect to the local plasma potential. The net negative charge on the droplets occurred for all conditions examined. That said, the distribution of charge on the droplets is not necessarily uniform. For what may be ideal conditions – no rotation of the droplet, no photo-electron emission, negligible conductivity – the droplets generally charged positive at the poles and negative at the equator while the total charge was negative. With charged particle fluxes being diffusion dominated at the poles while electron fluxes at the equator are drift dominated, there is an excess of electron charge collected at the equator. The response of the sheaths is to flatten at the poles, letting through an excess of positive charge, to retain its needed droplet averaged charge balance. With the droplet not rotating, this is a quasi-steady state configuration. With a sufficiently high droplet conductivity, the charge distribution on the droplet becomes more uniform, becoming negative at the poles.

Conductivity of the droplet also affects the manner in which current continuity is maintained through the droplet. In most cases, the droplet has little effect on the bulk plasma properties beyond the extent of the sheath. For low conductivities, current continuity is maintained by displacement current through the droplet. While the total current through the droplet does not significantly change when increasing the conductivity of the droplet, conduction current through the droplet increases, and eventually dominates at a conductivity of 10^{-1} S/cm.

Generally, changes in droplet properties do not greatly affect the bulk plasma properties. However, the bulk plasma properties with-and-without the droplet can be affected. The plasma density at the height of the droplet was generally lower than above and below the droplet. This decrease in plasma density is largely attributed to the shadowing of the electron drift motion by the droplet. The results discussed here were produced with a 2D model of a single, stationary droplet. This modeling method and choice of conditions were likely a worst-case scenario with respect to this local reduction in plasma density. The droplet appeared to be a rod and not a sphere. In 3D, the plasma can flow around the droplet, and if the droplet moves, its shadowing is averaged over space. Our results are, however, indicative of the long-range influence that larger droplets (tens of μm) can have on the plasma.

If plasma activation of a water droplet is dominated by fluxes of neutral radicals produced far from the droplet, these sheath dynamics may not have a large effect on that activation. However, droplet activation depending dominantly on charged particles fluxes (e.g., electron solvation) will likely be sensitive to the sheath dynamics. The net positive charging at the poles of the droplet may result in a different ion chemistry than at the equator. Although these simulations were performed for a single, non-moving droplet, one can speculate on the consequences of the asymmetric sheath dynamics on a high density of droplets or for a distribution of droplet sizes. For droplet spacings commensurate with the sheath thickness, some non-ideal behavior even at atmospheric pressure may occur, perhaps leading to a weak form of the Coulomb liquids produced at low pressures. Given that the sheath dynamics are asymmetric, equator vs pole, one may also expect some degree of anisotropy in the properties of the Coulomb liquids that liquids that might occur at high densities of droplets. For example, the spacing of the droplets in the Coulomb liquid in the horizontal direction in which the sheath is most elongated would likely be larger than in the axial direction in which the width of the sheath is typically smaller. Since the sheath properties and thickness are functions of the size of the droplets, a distribution of droplet sizes would likely lead to some additional disorder in the Coulomb liquid.

This chapter focused on an electropositive plasma with only a small fraction of negative ions, about 10^{-3}. The negative ions had a negligible effect on the sheath properties. Based on prior studies of sheath properties in electronegative plasmas, the trends discussed here for sheath properties around a droplet should apply to fairly large electronegativities as long as T_e is high compared to the ion temperature. The sheath properties around the droplet in an afterglow where T_e has thermalized would likely be more sensitive to negative ions.

5.8 Tables

Table 5.1. Species included in the model.

Charged Species	e, OH^-, H_2O^+, H_3O^+, O_2^+, O_2^-, O^+, O^-, N_2^+, N^+, $H_4O_2^+$, $H_2O_3^+$, $H_5O_2^+$, He^+, He_2^+
Neutral Species	H, H_2, OH, H_2O, HO_2, H_2O_2, O_2, O, N_2, N, He
Excited States	$H_2O(v)$, $O_2(v)$, $O_2(r)$, $O_2(^1\Delta_g)$, $O_2(^1\Sigma_u)$, $O(^1D)$, $N_2(r)$, $N_2(v)$, $N_2(A^3\Sigma_u)$, $N_2(a'^1\Sigma)$, $N(^2D)$, $He(2^3S)$, $He(2^1S)$, $He(2^3P)$, $He(2^1P)$, He(3P), He(3S), He_2^*

He_2^* is a lumped state of all He excited dimers.

5.9 Figures

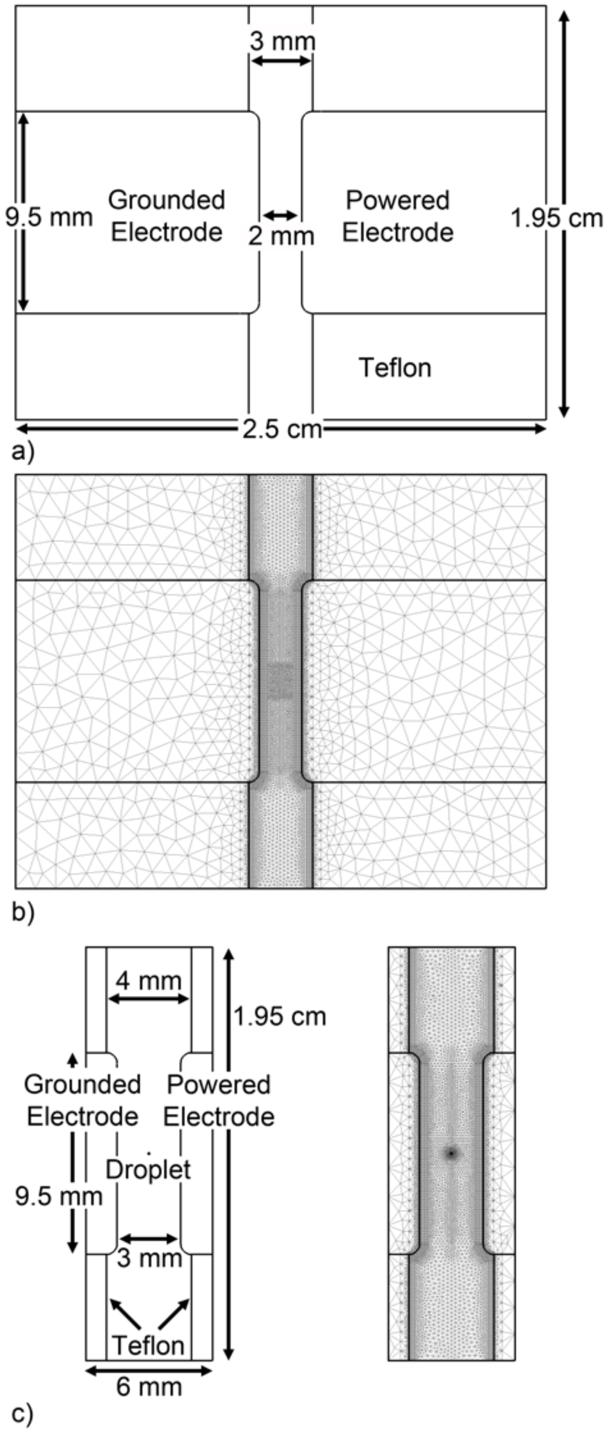

Figure 5.1. Geometry and numerical meshes used in the model. (a) Geometry and (b) numerical mesh to compare the simulated plasma properties to experimental plasma properties. (c) Geometry and numerical mesh to examine sheath properties around the droplet.

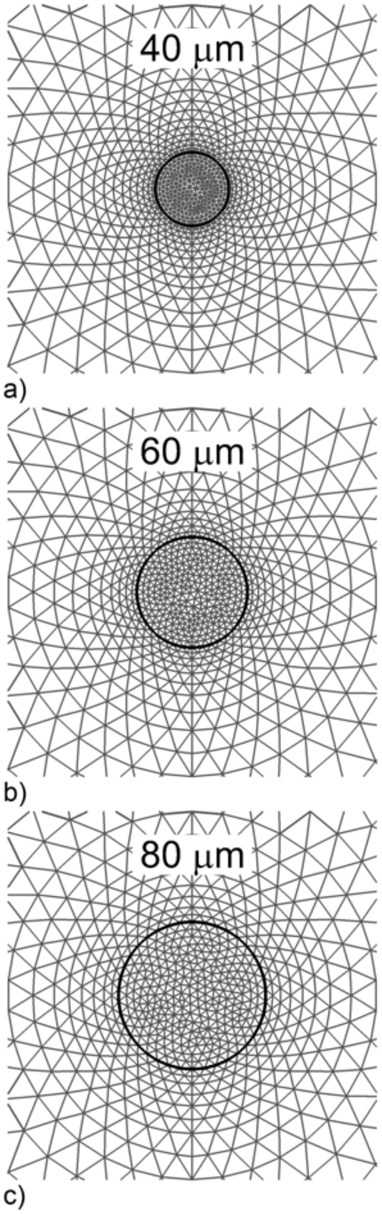

Figure 5.2. Numerical mesh near the droplet for diameters of (a) 40 µm, (b) 60 µm and (c) 80 µm.

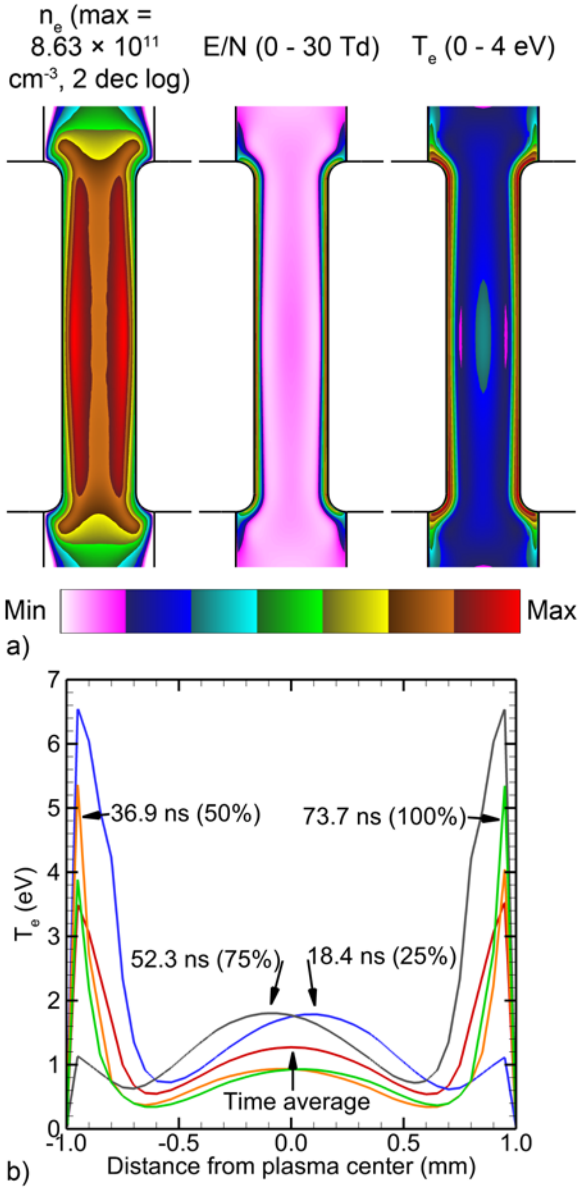

Figure 5.3. Plasma properties for the He RF discharge. (a) Time-averaged bulk plasma properties (electron density, E/N, T_e) over one quasi-steady state RF cycle. (b) T_e across the plasma gap at various times during the RF cycle.

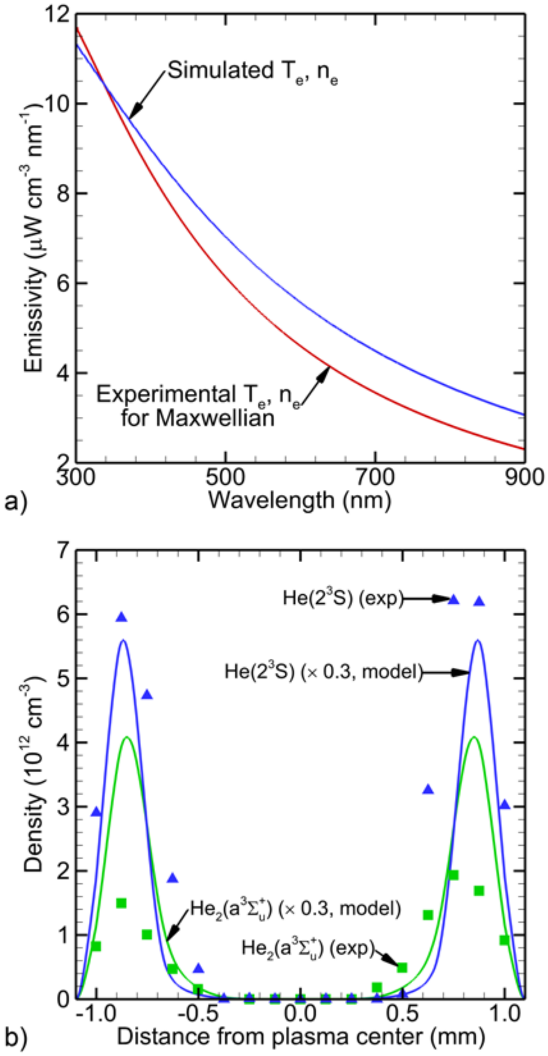

Figure 5.4. Comparison of model predictions to experimental measurements. (a) Emissivity fitted by Nayak et al. [19] (red) and emissivity calculated using model results (blue). (b) He metastable densities time-averaged over one quasi-steady state RF cycle extracted perpendicular to the electrodes and at the center of the electrode height. Model results (solid), and experimental measurements (points) for He(2^3S) (blue) and He$_2^*$ (green).

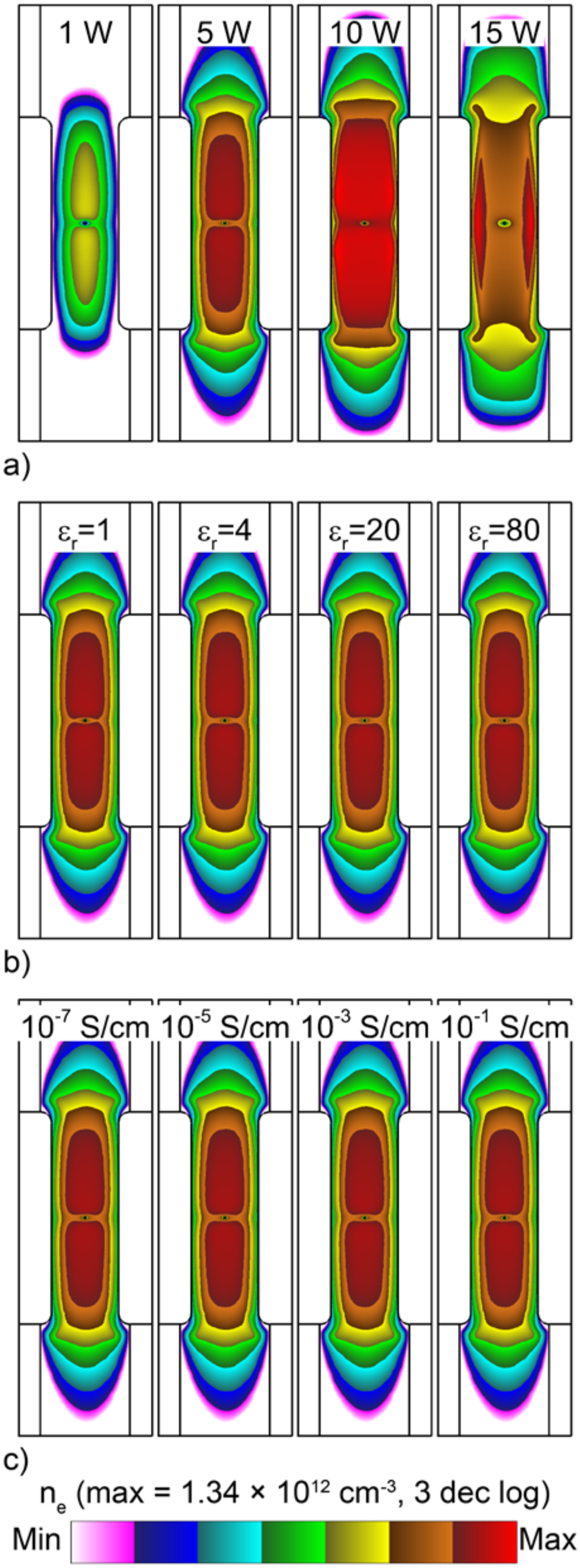

Figure 5.5. Electron density averaged over one quasi-steady state RF cycle. (a) 1 W – 15 W, (b) droplet permittivity of $\varepsilon_r = 1$ to $\varepsilon_r = 80$, and (c) droplet conductivity of 10^{-7} – 10^{-1} S/cm.

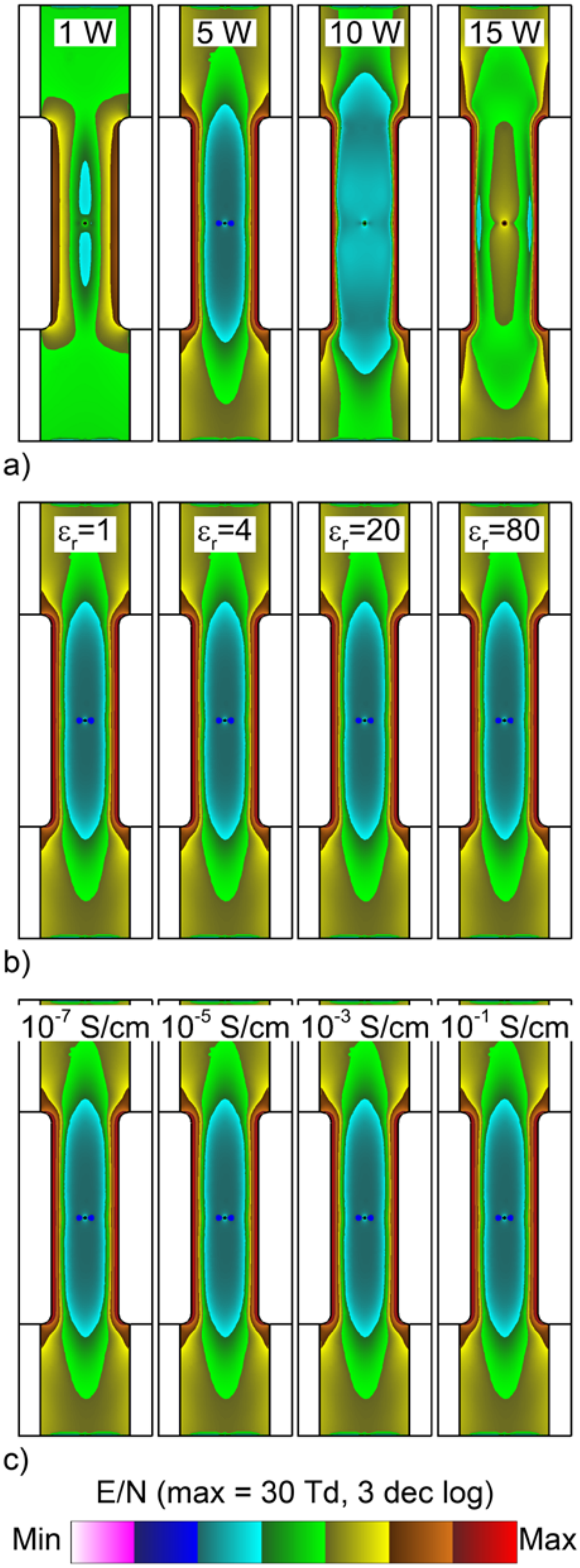

Figure 5.6. E/N averaged over one quasi-steady state RF cycle. (a) 1 W – 15 W, (b) droplet permittivity of $\varepsilon_r = 1$ to $\varepsilon_r = 80$, and (c) droplet conductivity of $10^{-7} – 10^{-1}$ S/cm.

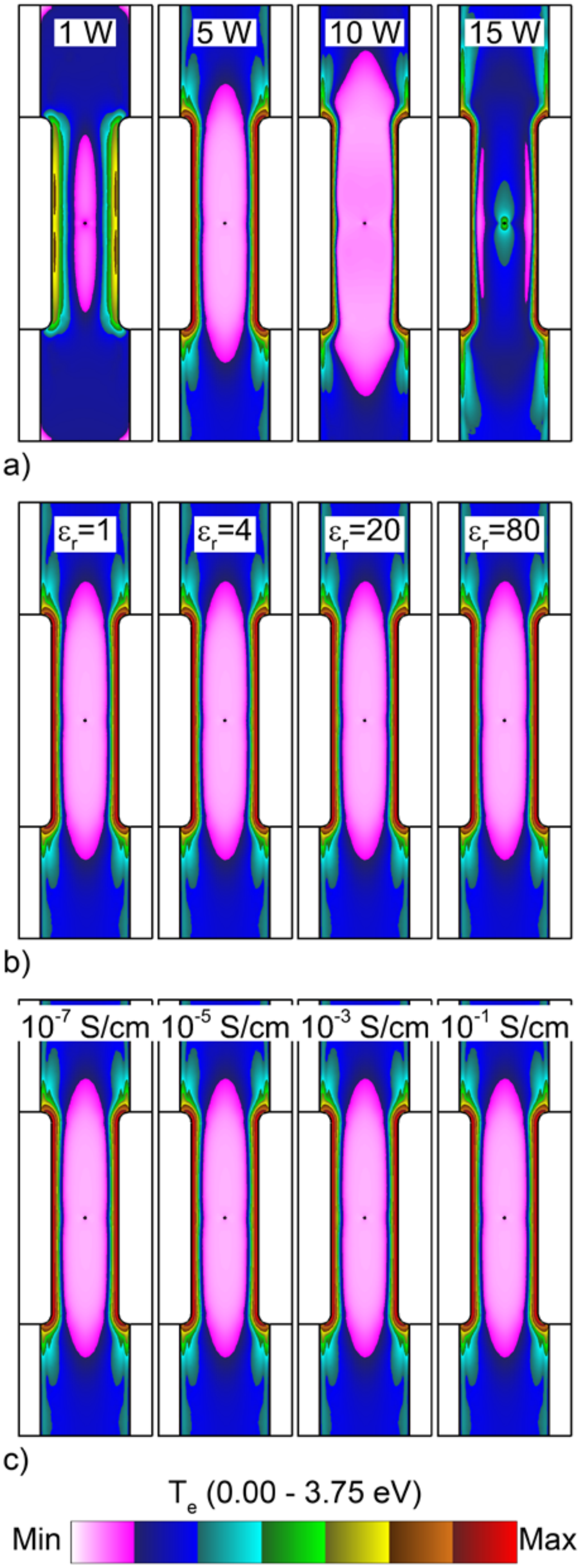

Figure 5.7. T_e averaged over one quasi-steady state RF cycle. (a) 1 W – 15 W, (b) droplet permittivity of $\varepsilon_r = 1$ to $\varepsilon_r = 80$, and (c) droplet conductivity of $10^{-7} – 10^{-1}$ S/cm.

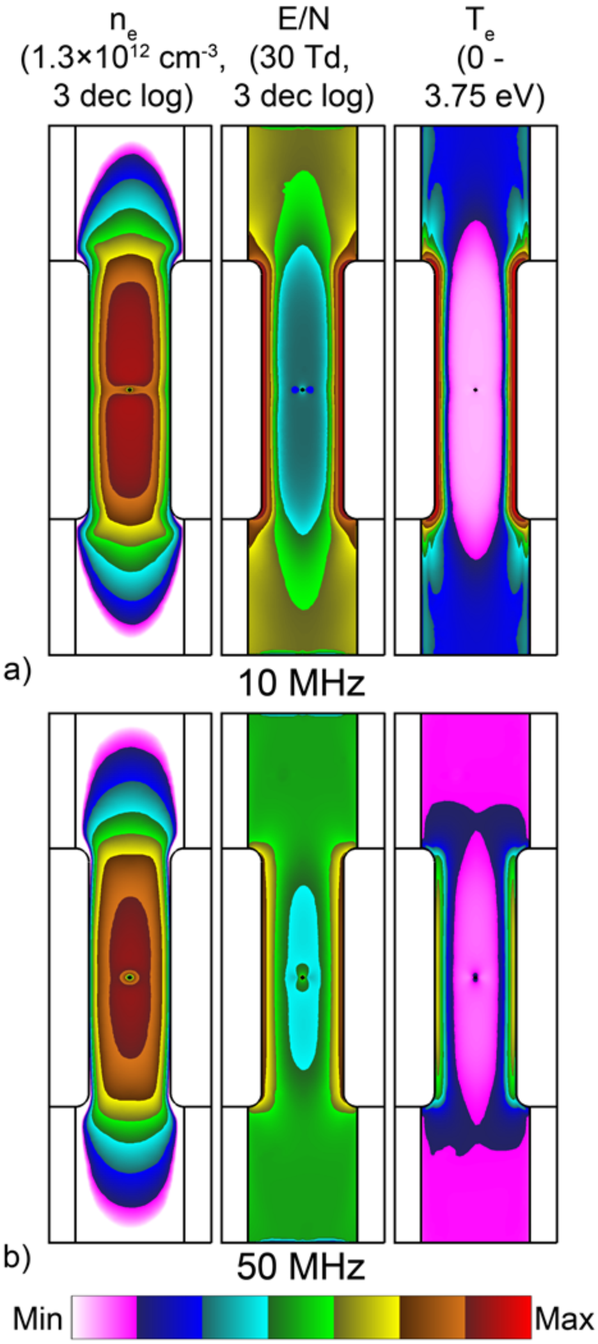

Figure 5.8. Electron density, E/N, and T_e averaged over one quasi-steady state RF cycle for (a) 10 MHz and (b) 50 MHz.

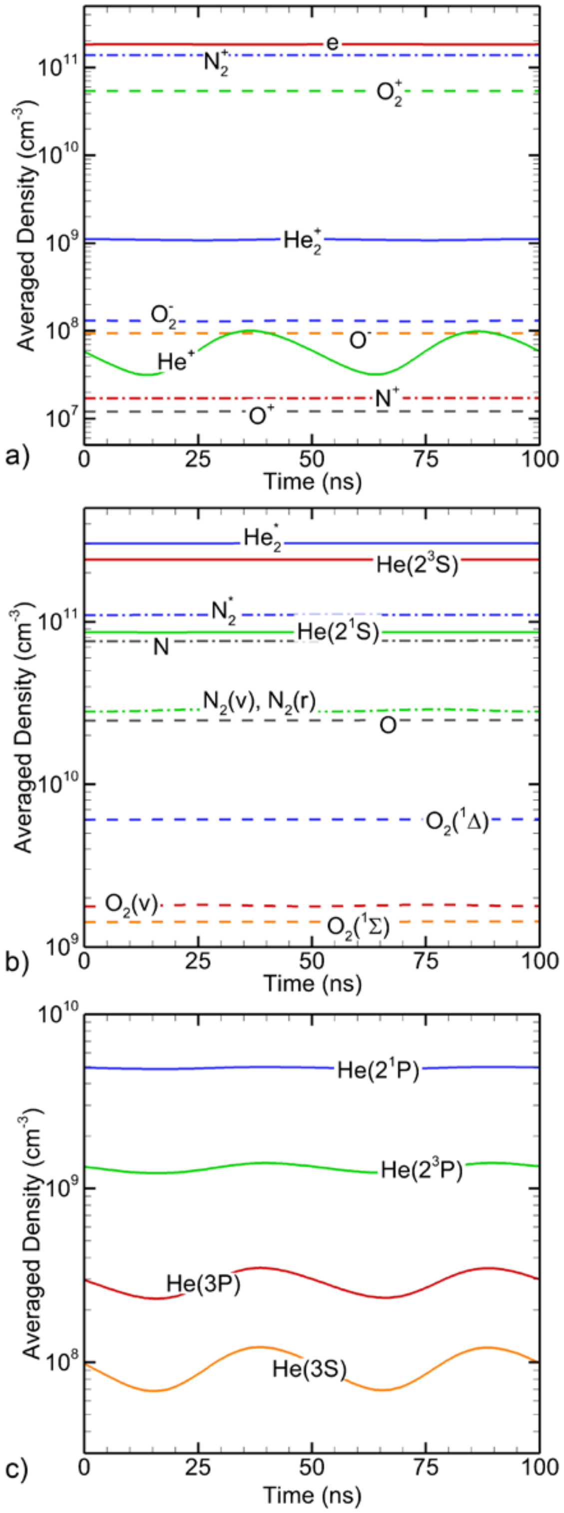

Figure 5.9. Volume-averaged species densities for the base case over one quasi-steady state RF cycle. (a) Charged species, (b) neutral species, and (c) neutral species with densities that oscillate over the RF cycle.

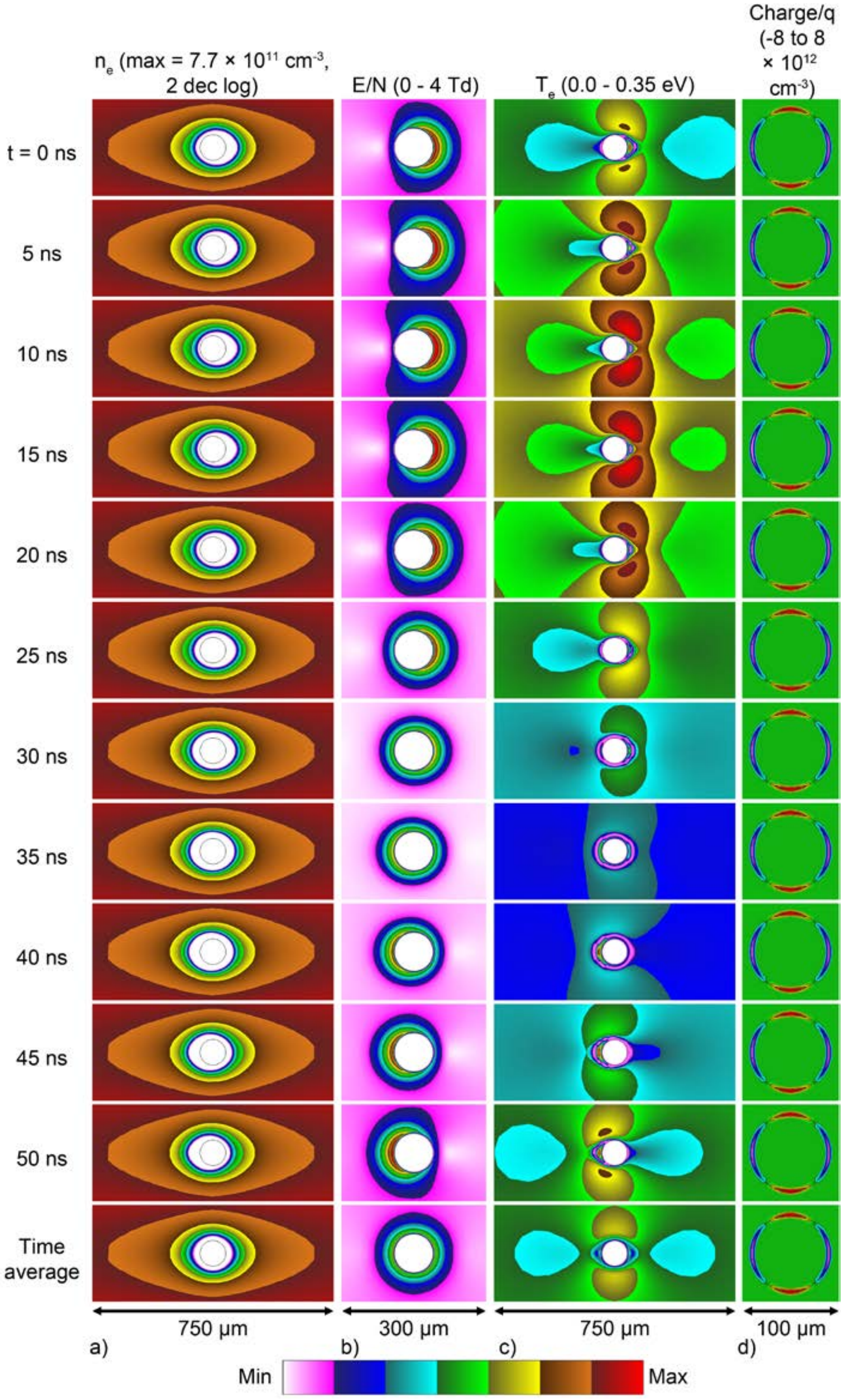

Figure 5.10. Properties of the sheath near the droplet over half of one quasi-steady state RF cycle at 10 MHz (0 – 50 ns). (a) Electron density, (b) E/N, (c) T$_e$, and (d) charge density on the droplet. The last row shows the time-average of these quantities over one quasi-steady state RF cycle.

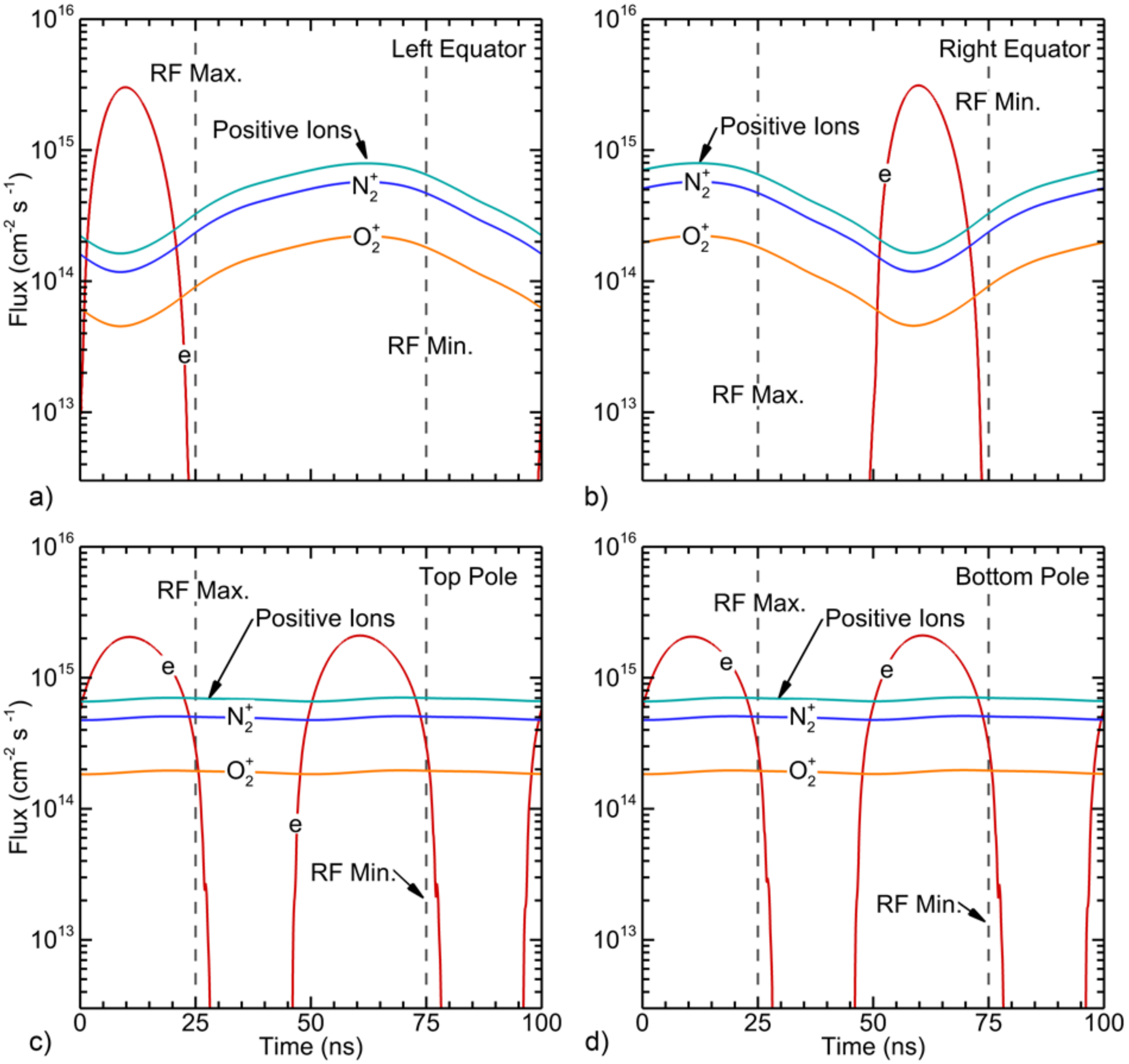

Figure 5.11. Flux of charged species to the (a) left equator, (b) right equator, (c) top pole, and (d) bottom pole of the droplet over one quasi-steady state 10 MHz RF cycle.

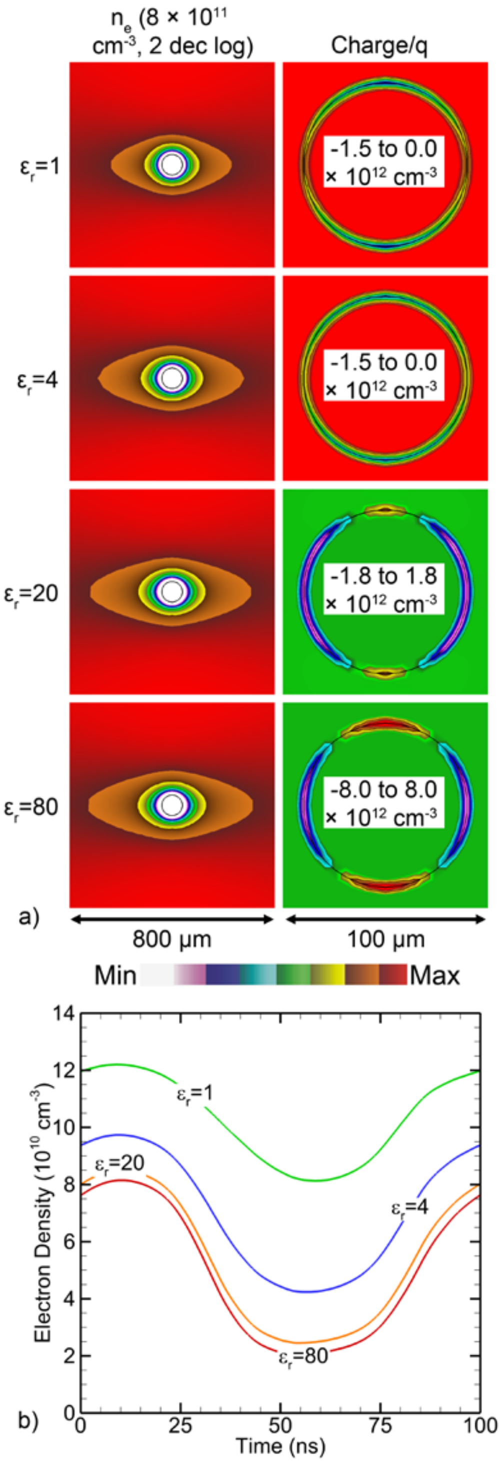

Figure 5.12. Sheath properties for droplet permittivities of $\varepsilon_r = 1$ to $\varepsilon_r = 80$. (a) Time-averaged electron density and charge density on the droplet over one quasi-steady state RF cycle. (b) Electron density at $2R_p$ from center of droplet along left equator of the droplet over one quasi-steady state RF cycle.

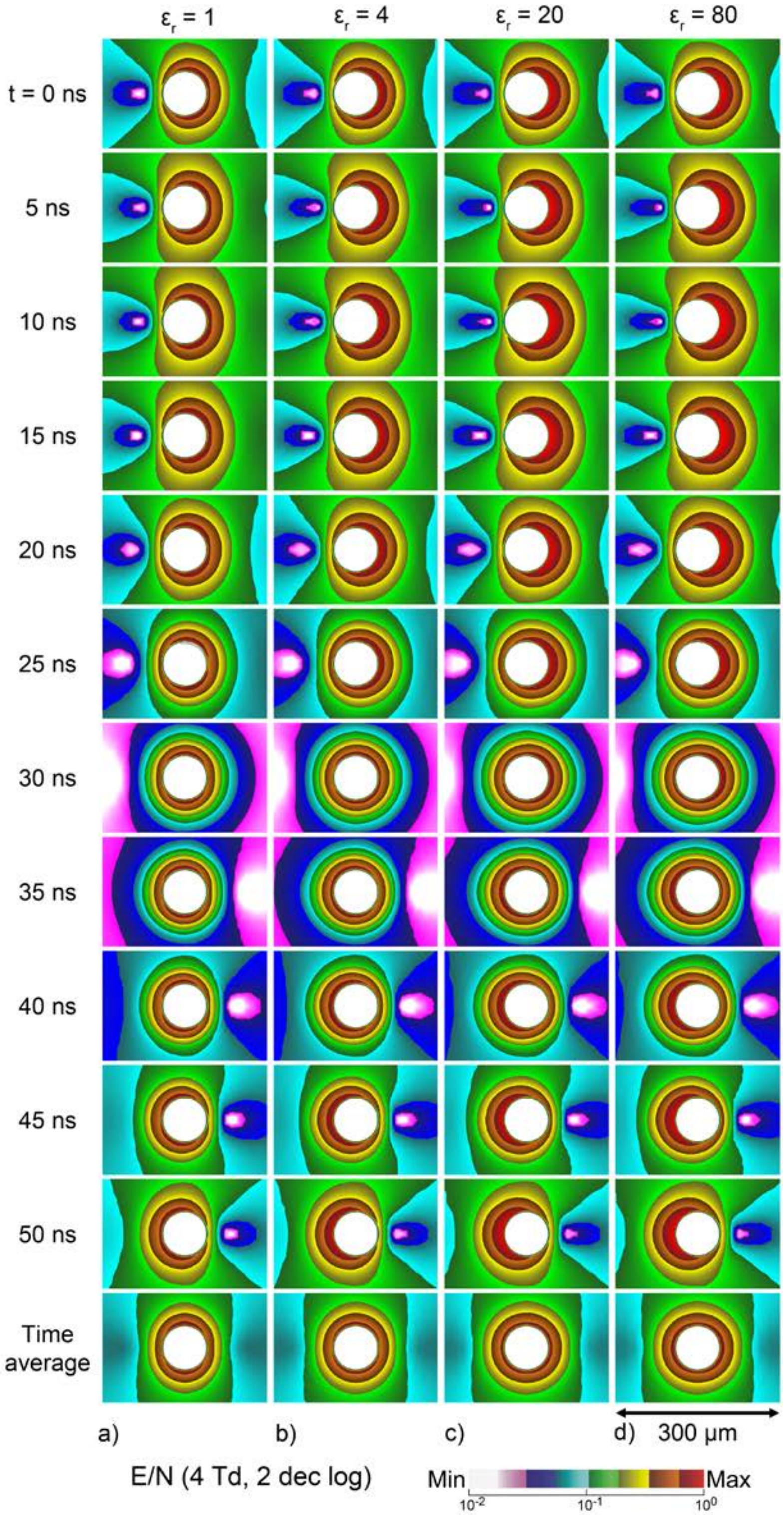

Figure 5.13. E/N over half of one quasi-steady state 10 MHz RF cycle (0 – 50 ns) for different permittivities of the droplet. The last row shows the time-average of E/N over the RF cycle. (a) ε_r =1, (b) ε_r = 4, (c) ε_r = 20, and (d) ε_r = 80.

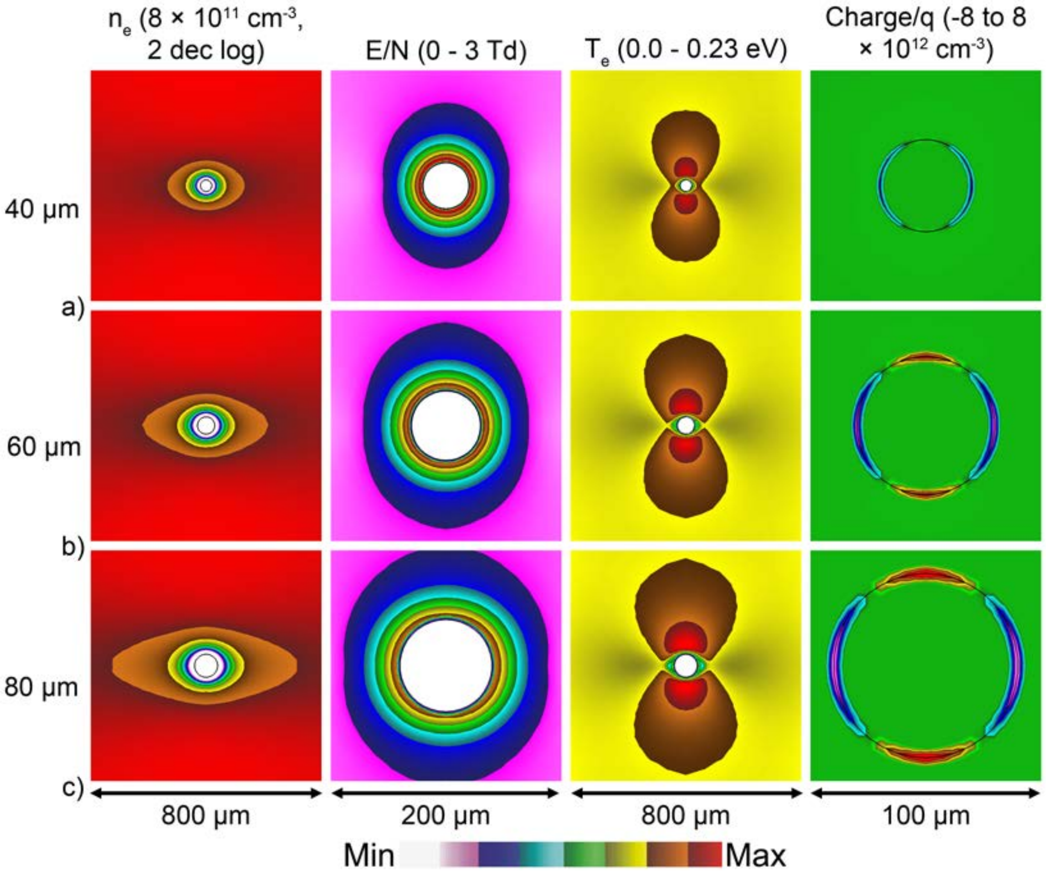

Figure 5.14. Time-averaged electron density, E/N, T_e, and charge density on the droplet over one quasi-steady state 10 MHz RF cycle for different diameters of the droplet. (a) 40 µm, (b) 60 µm, and (c) 80 µm.

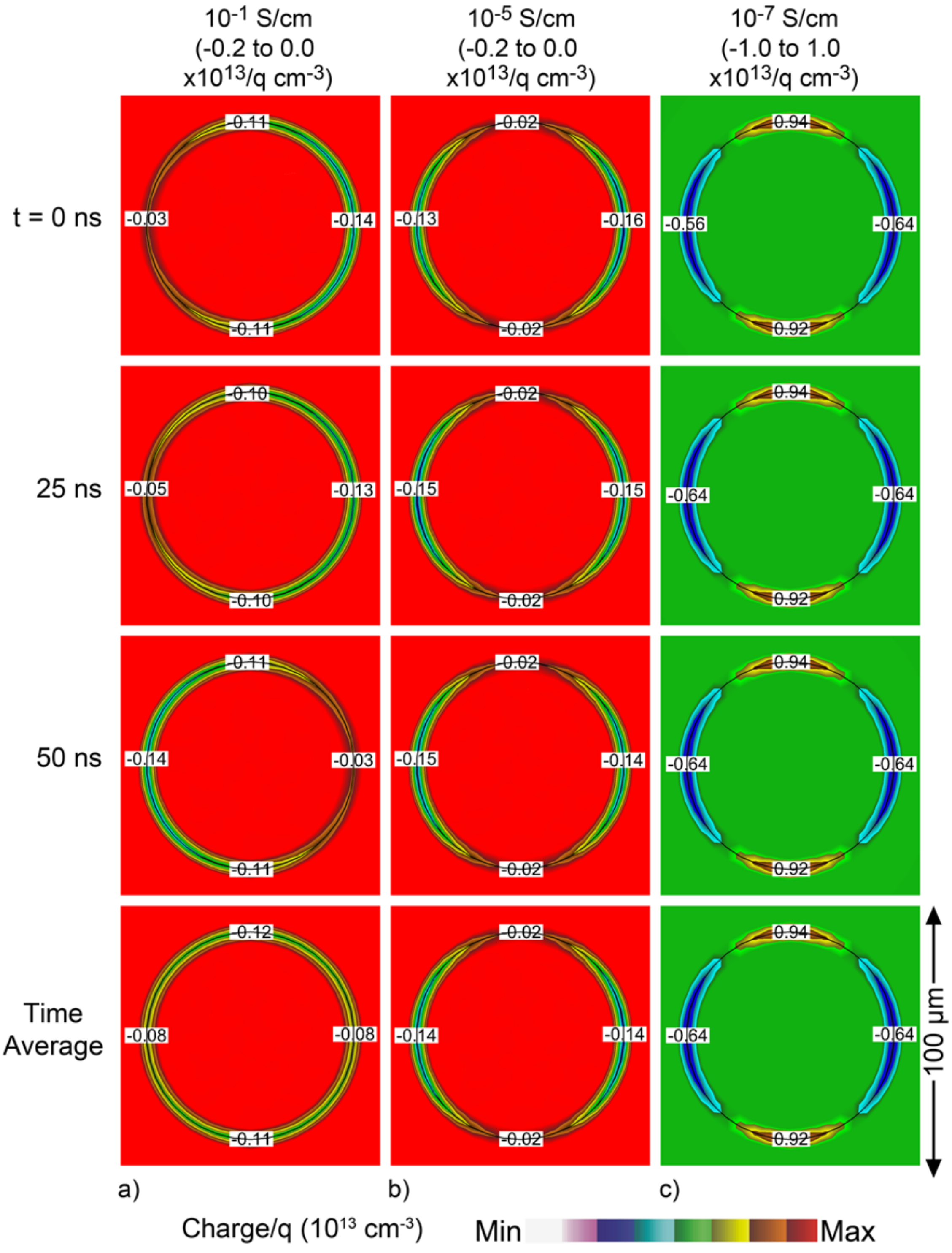

Figure 5.15. Charge density on the droplet over half of one quasi-steady state 10 MHz RF cycle (0 – 50 ns) for different conductivities of the droplet. The last row shows the time-average of these quantities over the RF cycle. (a) 10^{-1} S/cm, (b) 10^{-5} S/cm, and (c) 10^{-7} S/cm.

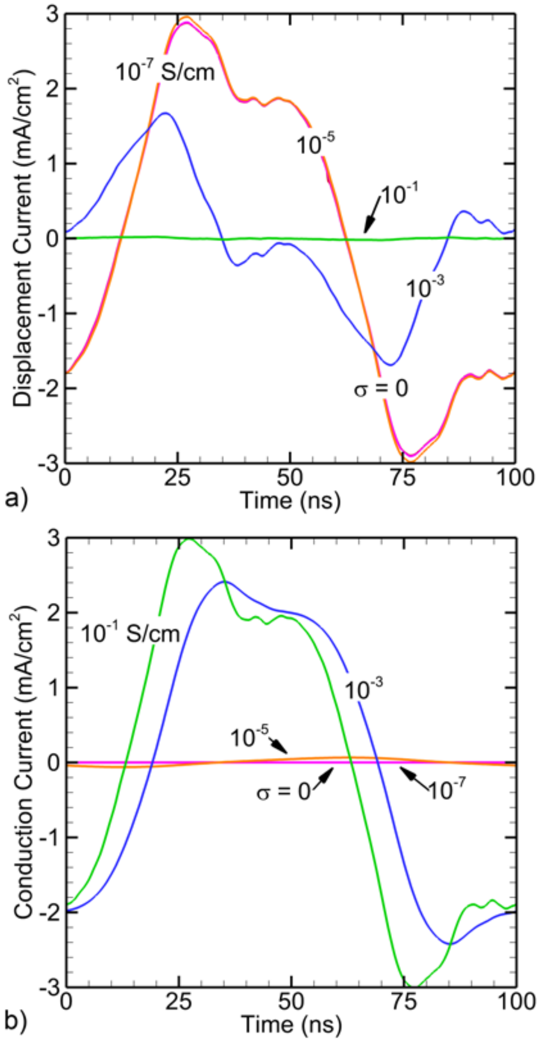

Figure 5.16. Current contributions through the center of the droplet for droplet conductivities of 10^{-1} S/cm, 10^{-3} S/cm, 10^{-5} S/cm, 10^{-7} S/cm, and a nonconductive droplet over one quasi-steady state RF cycle. (a) Displacement current density and (b) conduction current density.

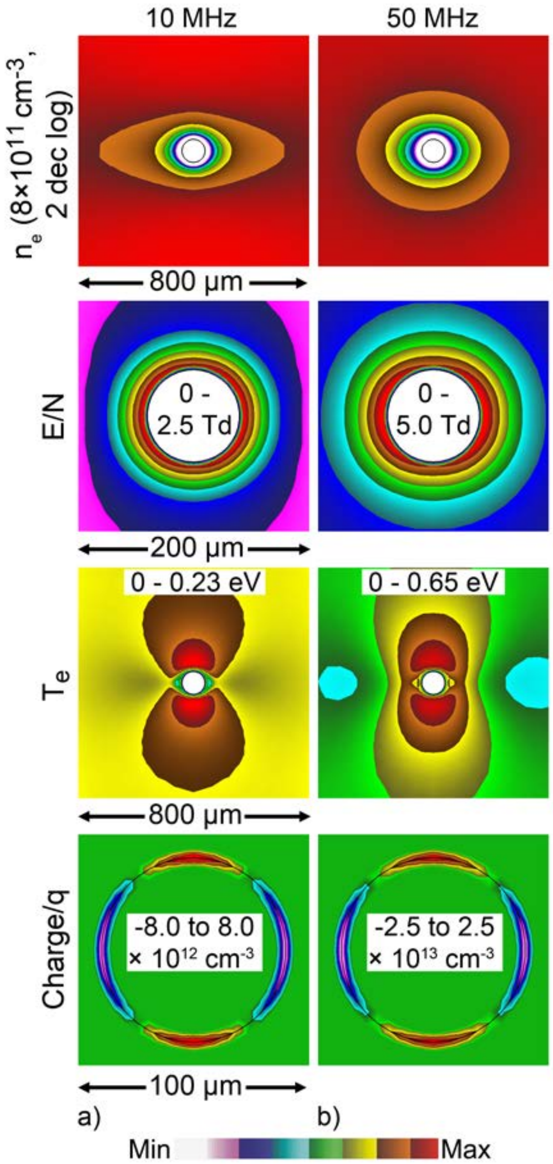

Figure 5.17. Time-averaged electron density, E/N, T_e, and charge density on the droplet over one quasi-steady state RF cycle for frequencies of (a) 10 MHz and (b) 50 MHz.

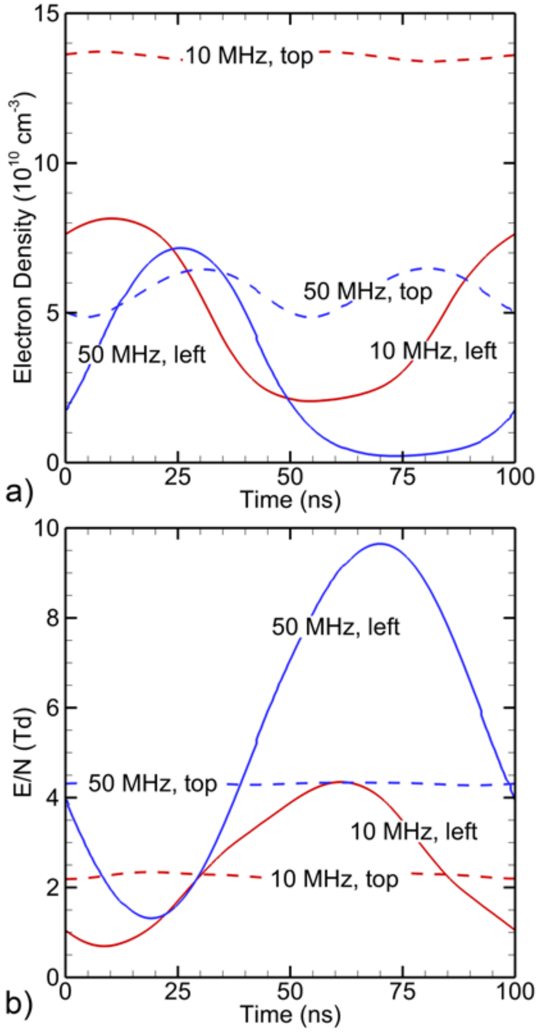

Figure 5.18. Sheath properties for RF frequencies of 10 MHz and 50 MHz over one quasi-steady state RF cycle. (a) Electron density at $2R_p$ from the center of the droplet and (b) E/N at 5% of a diameter away from left equator (solid) and top pole (dashed).

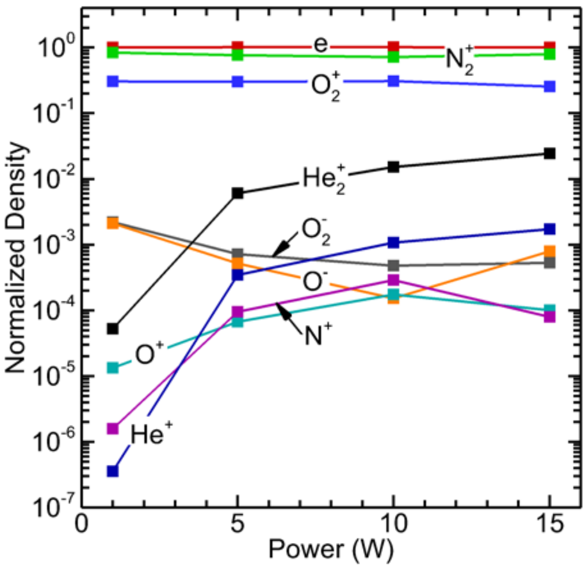

Figure 5.19. Volume-averaged charged species densities over one quasi-steady state RF cycle as function of discharge power. Densities normalized to volume-averaged electron density at each discharge power.

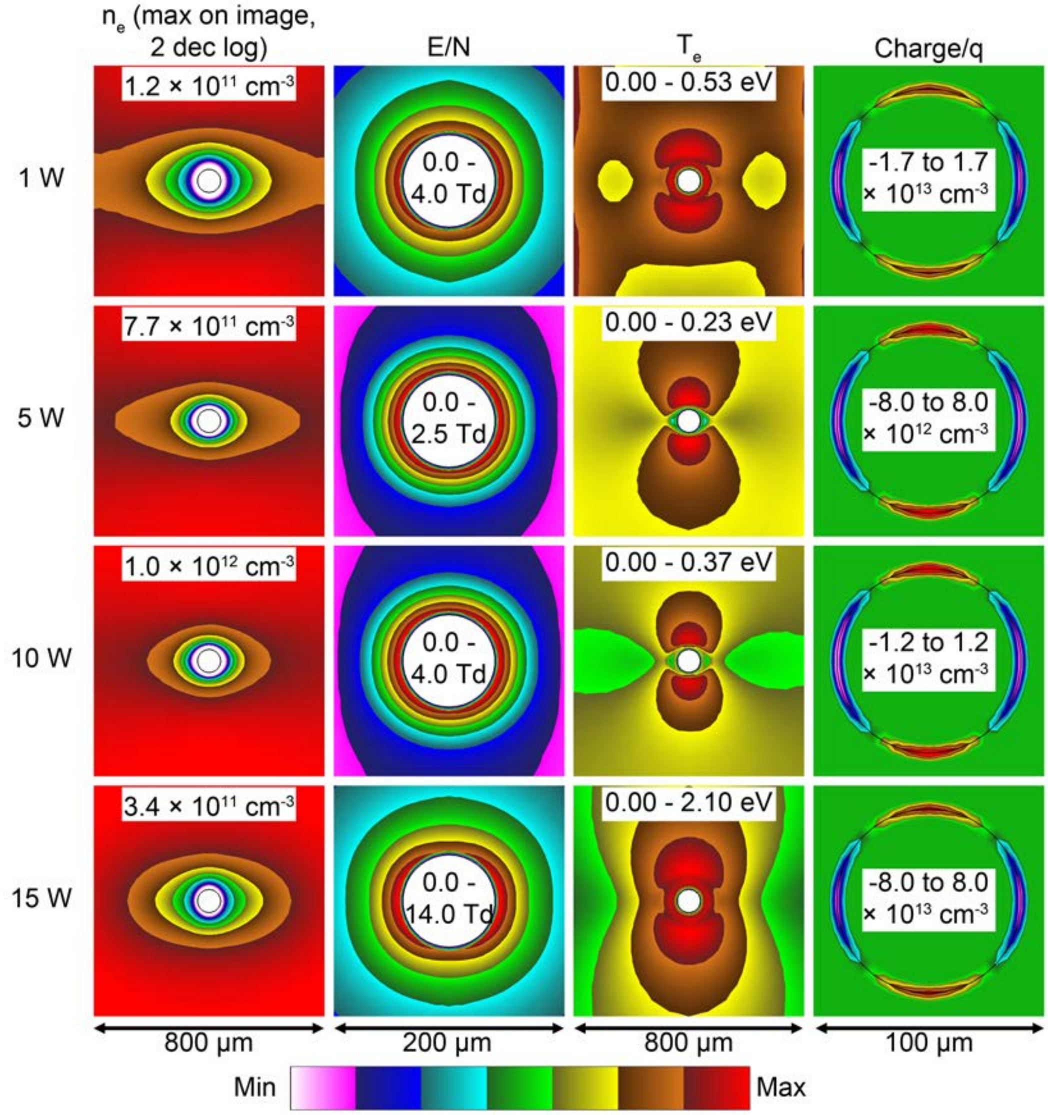

Figure 5.20. Time-averaged electron density, E/N, T_e, and charge density on the droplet over one quasi-steady state RF cycle for discharge powers of 1 W to 15 W.

5.10 References

[1] P. F. Ambrico, M. Šimek, C. Rotolo, M. Morano, A. Minafra, M. Ambrico, S. Pollastro, D. Gerin, F. Faretra and R. M. De Miccolis Angelini, Sci. Rep. **10,** 3673 (2020).

[2] Y. He, C. Ding, T. Jin, Y. Fan, Z. Wu, M. Sun, K. Wang and T. Ji, Plasma Sci. Technol. **22,** 065502 (2020).

[3] J. E. Foster, S. Mujovic, J. Groele and I. M. Blankson, J. Phys. D. Appl. Phys. **51,** 293001 (2018).

[4] T. Von Woedtke, D. Weltmann, S. Emmert, H. Metelmann, S. Rupf and K.-D. Weltmann, Phys. Plasmas **27,** 070601 (2020).

[5] E. Casado, M. C. Garcia, D. A. Krawczyk, F. J. Romero-Salguero and A. Rodero, Plasma Process. Polym. **17,** 2000030 (2020).

[6] M. C. García, M. Mora, D. Esquivel, J. E. Foster, A. Rodero, C. Jiménez-Sanchidrián and F. J. Romero-Salguero, Chemosphere **180,** 239 (2017).

[7] F. Prehn, E. Timmermann, M. Kettlitz, K. Schaufler, S. Günther and V. Hahn, Plasma Process. Polym. **17,** 2000027 (2020).

[8] M. K. J. Nicol, T. R. Brubaker, B. J. Honish, A. N. Simmons, A. Kazemi, M. A. Geissel, C. T. Whalen, C. A. Siedlecki, S. G. Bilén, S. D. Knecht and G. S. Kirimanjeswara, Sci. Rep. **10,** 3066 (2020).

[9] C. Jiang, E. B. Sözer, S. Song, N. Lai, P. T. Vernier and S. Guo, Phys. Plasmas **27,** 113513 (2020).

[10] P. Heirman, W. Van Boxem and A. Bogaerts, Phys. Chem. Chem. Phys. **21,** 12881 (2019).

[11] N. C. Roy, C. Pattyn, A. Remy, N. Maira and F. Reniers, Plasma Process. Polym. **18,** 202000087 (2021).

[12] Y. Zheng, L. Wang and P. Bruggeman, J. Vac. Sci. Technol. A **38,** 063005 (2020).

[13] N. Akiyama, Y. Nakagawa, S. Uchida and F. Tochikubo, J. Appl. Phys. **129,** 163304 (2021).

[14] Z. Liu, S. Wang, B. Pang, H. Zhang, Y. Gao, D. Xu and M. G. Kong, J. Phys. D. Appl. Phys. **54,** 215203 (2021).

[15] M. E. Hassan, M. Janda and Z. Machala, Water **13,** 182 (2021).

[16] H. E. Delgado, G. H. Brown, D. M. Bartels, P. Rumbach and D. B. Go, J. Appl. Phys. **129,** 083303 (2021).

[17] J. A. Silsby, S. Simon, J. L. Walsh and M. I. Hasan, Plasma Chem. Plasma Process. **41,** 1363 (2021).

[18] G. Nayak, N. Sadeghi and P. J. Bruggeman, Plasma Sources Sci. Technol. **28,** 125006 (2019).

[19] G. Nayak, M. S. Simeni, J. Rosato, N. Sadeghi and P. J. Bruggeman, J. Appl. Phys. **128,** 243302 (2020).

[20] G. Oinuma, G. Nayak, Y. Du and P. J. Bruggeman, Plasma Sci. Technol. **29,** 095002 (2020).

[21] G. Nayak, G. Oinuma, Y. Yue, J. S. Sousa and P. J. Bruggeman, Plasma Sources Sci. Technol. **30,** 115003 (2021).

[22] S. A. Norberg, E. Johnsen and M. J. Kushner, Plasma Sources Sci. Technol. **24,** 035026 (2015).

[23] D. L. Scharfetter and H. K. Gummel, IEEE Trans. Electron Devices **16,** 64 (1969).

[24] W. Van Gaens and A. Bogaerts, J. Phys. D. Appl. Phys. **46,** 275201 (2014).

[25] S. Norberg, "Modeling Atmospheric Pressure Plasma Jets: Plasma Dynamics, Interaction with Dielectric Surfaces, Liquid Layers and Cells," Ph.D. Thesis (University of Michigan, 2015).

[26] F. Emmert, H. H. Angermann, R. Dux and H. Langhoff, J. Phys. D. Appl. Phys. **21,** 667 (1988).

[27] A. M. Lietz, E. V Barnat, J. E. Foster and M. J. Kushner, J. Appl. Phys. **128,** 083301 (2020).

[28] J. Shi and M. G. Kong, IEEE Trans. Plasma Sci. **33,** 624 (2005).

[29] J. J. Shi and M. G. Kong, J. Appl. Phys. **97,** 1 (2005).

[30] D. X. Liu, J. F. Li, A. J. Yang, X. H. Wang, M. Z. Rong and M. G. Kong, High Volt. **1,** 81 (2016).

[31] D. X. Liu, A. J. Yang, X. H. Wang, M. Z. Rong, F. Iza and M. G. Kong, J. Phys. D. Appl. Phys. **45,** 305205 (2012).

[32] N. Balcon, G. J. M. Hagelaar and J. P. Boeuf, IEEE Trans. Plasma Sci. **36,** 2782 (2008).

[33] Phelps database, www.lxcat.net, retrieved on August 16, 2021.

[34] M. A. Lieberman, IEEE Trans. Plasma Sci. **16,** 638 (1988).

Chapter 6 Modeling $HCOO^-_{aq}$ Degradation by OH_{aq} in an Atmospheric Pressure Glow Discharge

Plasmas in contact with liquids can degrade organic molecules present in the liquid, as reactive oxygen and nitrogen species produced in the plasma solvate into the liquid. Immersing small droplets (tens of microns in diameter) in the plasma can more rapidly activate the liquid compared to treating a large volume of liquid with a smaller surface-to-volume ratio. The interactions between a radio frequency glow discharge sustained in He/H_2O and a water droplet immersed in the plasma were modeled using *GlobalKin*. $HCOO^-_{aq}$ is dissolved in the water droplet, which interacts with OH_{aq}, produced from solvation of OH from the gas phase. The resulting $HCOO^-_{aq}$ concentrations are benchmarked with previous experimental measurements. The diameter of the droplet, initial $HCOO^-_{aq}$ concentration, and gas flow rate affect only the $HCOO^-_{aq}$ concentration and OH_{aq} density, leaving the OH density in the gas phase unaffected. Power deposition, gas mixture, and percentage of H_2O in the gas mixture change both the gas and liquid phase chemistry. A general trend is observed – when $HCOO^-_{aq}$ is depleted in the reactive layer of the droplet, the OH_{aq} density increases, as the primary consumption mechanism of OH_{aq} is through the reaction with $HCOO^-_{aq}$. However, if $HCOO^-_{aq}$ is consumed well before the power turns off, reactions with $HO_2^-{}_{aq}$ and OH^-_{aq} start to consume the OH_{aq} and decrease its density in the droplet.

6.1 Introduction

Atmospheric pressure plasmas in contact with liquids are used in a wide variety of applications, including water treatment and plasma medicine [1–3]. These applications rely on plasma-produced reactive oxygen and nitrogen species (RONS) solvating into the liquid and chemically activating the liquid.

In most reactor configurations, transport limits the activation of the liquid through both solvation of the RONS in the gas into the liquid and diffusion of the RONS in the liquid. RONS produced in the plasma need to transport to the surface of the liquid to solvate. If the liquid is immersed in the plasma in the form of droplets, the distance between where the RONS are produced and the liquid can be shortened, and this transport limit can be mitigated. Once the RONS reach the surface of the liquid, these species need to diffuse from the surface into the bulk liquid. One way to mitigate this limit is to have a high surface-to-volume ratio (SVR) of the liquid, which decreases how long it takes for the RONS to diffuse from the surface to the bulk liquid. Using small water droplets (aerosols) in the plasma mitigates the limits imposed by transport [4].

Experiments have shown how SVR influences the concentrations of RONS in the liquid. Hassan et al. compared the solvation of H_2O_2 (high Henry's law constant) and O_3 (low Henry's law constant) into bulk liquid and electrosprayed droplets [5]. They showed that increasing the surface area between the gas and liquid increased the concentration of H_2O_{2aq} and O_{3aq}. (The aq subscript denotes a solvated or aqueous species.) However, their results showed that the H_2O_{2aq} concentration was only 4 orders of magnitude larger than the O_{3aq} concentration, despite the difference in the Henry's law constants being 7 orders of magnitude. This difference was attributed to the depletion of H_2O_2 in the gas phase before the liquid reached Henry's law saturation. Liu et al. showed that the concentrations of long-lived RONS (H_2O_{2aq}, $NO_2^-{}_{aq}$, and $NO_3^-{}_{aq}$) and short-lived RONS ($ONOO^-{}_{aq}$ and $O_2^-{}_{aq}$) in water increase as the SVR increases [6]. Cancer cell containing media treated with plasma-activated water with a higher SVR was more effective at causing cell death, due to the higher concentrations of RONS in the solution.

Plasma has been proposed as an advanced oxidation process to remove organic pollutants from water [1]. Singh et al. used plasma formed in Ar to treat landfill leachate samples containing PFAS [7]. The PFAAs and precursors were transported to the liquid surface by bubbling Ar through the liquid, forming a foam at the surface. Singh et al. showed that over 90% of PFOA and PFOS and over 99.9% of long-chain PFAAs were degraded within 10 minutes of treatment by plasma. Jose and Philip used air plasma to degrade four toxic volatile organic compounds commonly found in pharmaceutical wastewater [8]. The water was sprayed into the plasma reactor and recirculated. For a hydraulic retention time of 33.3 min, over 90% of the four volatile organic compounds were removed. Using samples of pharmaceutical wastewater, instead of prepared solutions, over 90% of the volatile organic compounds were removed by plasma treatment. Jaiswal and Aguirre compared the effectiveness of He and Ar plasma jets on degrading methylene blue dye [9]. They showed that the Ar plasma jet better degraded methylene blue dye compared to the He plasma jet, and they were able to attribute this to increased $O(^1S)$ and metastable Ar states that were more present in the Ar plasma jet than the He jet. Casado et al. used an Ar plasma jet to degrade benzene present on top of a water layer [10]. They showed that phenol, catechol, and nitrobenzene were the main products formed from plasma interaction with benzene. These molecules are formed by benzene reactions with OH_{aq} and NO_{2aq}, likely formed by interactions between the ambient air and Ar excited states.

Sremacki et al. injected aerosol droplets (about 22 µm) into an Ar plasma jet to observe changes to the RONS and UV radiation from the plasma [11]. Aerosols in the plasma decreased the UV radiation by absorbing the radiation in the gas phase, and gas phase reactive oxygen species were also decreased. Products of the reactions between OH_{aq} and cysteine, used as a model biological molecule and dissolved in the aerosol, were detected. Cysteine conversion was highest when the bulk liquid was exposed to the plasma, presumably due to the increase in UV photons. Plasmas have also been shown to inactivate bacteria and viruses present in solution. Xia et al. used a packed-bed dielectric barrier discharge to inactivate viruses in aerosols in the plasma [12]. At least 2.3 log reduction in the infectious virus concentration was seen in this reactor.

With the goal of investigating the transport of plasma produced ROS (reactive oxygen species) to droplets in a plasma, the degradation of $HCOO^-_{aq}$, a model organic compound, by OH_{aq}, a short-lived reactive species has been simulated. $HCOO^-_{aq}$ is dissolved in a water droplet (tens of microns in diameter) immersed in an atmospheric pressure He/H_2O radio frequency glow discharge. Previous experimental work in this reactor is described in Nayak et al. and Oinuma et al. [13–16]. Nayak et al. measured the electron temperature and density in plasmas formed in this reactor in He and Ar, as well as He metastable densities [13,14]. In Oinuma et al., droplets with 2 mM $HCOO^-_{aq}$ flowed through the He/H_2O plasma [15]. The droplets were exposed to OH formed in the gas phase that then solvates into the droplet. The $HCOO^-_{aq}$ concentration after exposure to the plasma is measured, and the change in $HCOO^-_{aq}$ concentration gave an estimate of OH transport to the droplet. Results of a 1D reaction-diffusion model showed that the interaction between OH_{aq} and $HCOO^-_{aq}$ happened primarily at the surface of the droplet. Nayak et al. investigated the effects of other reactive species on the $HCOO^-_{aq}$ concentration in the same reactor and found that another reactive species besides OH_{aq} that may consume $HCOO^-_{aq}$ is O_{aq} [16].

Using *GlobalKin*, the interactions between the plasma-produced ROS and droplet are modeled in a reactor based on the experimental work by Nayak et al. and Oinuma et al. [13–16]. The global plasma chemistry model incorporates a local diffusion length from the plasma to the droplet and a reactive layer at the surface of the droplet to effectively model the system. The base case (1 atm, He/H2O=99.8/0.2, 14.3 W), has a water droplet 41 μm in diameter with an initial

$HCOO^-_{aq}$ concentration of 2 mM, and which has a transit time of 10 ms through the plasma. Using a reactive layer thickness of 5.5 µm in the droplet, the predicted $HCOO^-_{aq}$ concentration after plasma exposure (0.79 mM) matches the experimental measurements (0.76 mM). In the gas phase, OH and H_2O_2 come to a quasi-steady state within a few ms of plasma operation. In the liquid phase, $HCOO^-_{aq}$ decreases due to reactions with OH_{aq}. The density of OH_{aq} in the droplet increases and reaches a maximum at 9.2 ms, before the end of the droplet transit through the plasma. As the $HCOO^-_{aq}$ density decreases in the reactive layer, OH_{aq} is not consumed as quickly in the reaction with $HCOO^-_{aq}$. Near 9.2 ms, the dominant consumption mechanism of OH_{aq} changes from the reaction with $HCOO^-_{aq}$ to reactions with $HO_2^-{}_{aq}$ and OH^-_{aq}. Changing the droplet diameter, initial $HCOO^-_{aq}$ concentration in the droplet, and flow rate (residence time) of the gas does not significantly change the gas phase OH but affects the liquid phase OH_{aq} and $HCOO^-_{aq}$. Varying the power, gas mixtures, and water percentage in the inlet gas flow change species densities in both the gas phase and liquid phase. When $HCOO^-_{aq}$ is degraded in the reactive layer of the droplet, the OH_{aq} density increases, which indicates that OH_{aq} is primarily consumed through the reaction with $HCOO^-_{aq}$. However, when $HCOO^-_{aq}$ in the reactive layer is consumed a few ms before the droplet leaves the plasma, the density of OH_{aq} tends to decrease, despite there being little $HCOO^-_{aq}$ left to react with. This is due to the prevalence of other species formed from $CO_2^-{}_{aq}$, one of the products of the reaction between OH_{aq} and $HCOO^-_{aq}$, that consume OH_{aq}.

In Section 6.2, the conditions used in this study are described, as well as a brief description of the experiments the modeling is based on. The plasma properties and gas and liquid phase species densities are described in Section 6.3. The variations in the gas and liquid phase species densities with varying droplet diameter, initial $HCOO^-_{aq}$ concentration, flow rate, power, gas mixture, and water percentage in the inlet gas mixture are described in Section 6.4. Concluding remarks are shown in Section 6.5.

6.2 Description of the Model and Experiments

This investigation was performed with the global plasma chemistry model, *GlobalKin*, to simulate conditions based on the experiments performed by Nayak et al. and Oinuma et al. [15,16]. The plasma reactor used by Nayak et al. and Oinuma et al. is an atmospheric pressure radio frequency glow discharge formed between two parallel plate electrodes separated by 2 mm and which are 9.5 mm long. Water droplets are released from a dispenser and pass through the plasma entrained in the gas flow, spending around 10 ms in the plasma depending on the flow rate of the gas. After flowing through the plasma, the droplets are frozen by an aluminum insert kept below freezing to preserve the exposed liquid for later chemical analysis. For the base case, 2 mM $HCOO^-_{aq}$ is dissolved in the droplet. $HCOO^-_{aq}$ reacts with OH_{aq}, in the droplet due to solvation of OH produced in the plasma. Measuring the change in $HCOO^-_{aq}$ concentration gives a measure of the OH transport to the droplet.

GlobalKin has been described previously in Section 2.3 and will not be redescribed here. The liquid droplet module described in Section 2.3.1 is used in this chapter. The diffusion length to the droplet was set to 150 µm, and the diffusion length to the walls was set to 0.637 mm, corresponding to a gap distance of 2 mm. As shown by Oinuma et al., the $HCOO^-_{aq}$ is degraded at the droplet surface while barely changed in the center of the droplet [15]. Therefore, the reactive layer of the droplet is also used in this chapter to effectively model the droplet.

The reaction mechanism includes 112 gas phase species and 123 liquid phase species, listed in Table 6.1. Note that each gas phase species has a liquid phase counterpart, and some species only exist in the liquid. There are 3,009 gas phase reactions and 317 liquid phase reactions. The gas phase reaction mechanism is based on Van Gaens and Bogaerts [17] with updates to include He made by Norberg [18]. Updates were made based on branching ratios of recombination of He^+ and He_2^+ from Emmert et al. [19] and radiation trapping factors from Lietz et al. [20]. Two gas mixtures examined include both He and Ar, and their interactions are included and based on Tian and Kushner [21]. The liquid phase reaction mechanism is based on Tian and Kushner [22] and Lietz and Kushner [23]. The rates for interaction of He excited states and ions with H_2O_{aq} were estimated to be fast relative to other reactions and based on branching ratios from Tian and Kushner [22] and Tian et al. [24]. Additional reactions to include $HCOO^-_{aq}$ were made based on the reaction mechanism in Oinuma et al. [15]. $HCOO^-_{aq}$ is consumed only by OH_{aq}, producing H_2O_{aq} and $CO_2^-{}_{aq}$. Changes to the liquid phase reaction mechanism relative to Lietz and Kushner [23] are shown in Table 6.2. Henry's law constants are taken from Sander [25] and are listed in Table 6.3. A Henry's law constant greater than 1 indicates that, at equilibrium, the density of the species in the liquid will be larger than that in the gas, while a Henry's law constant less than 1 means the density of the species in the gas will be larger than that in the liquid.

The water droplets are prepared by dissolving 2 mM $HCOOH_{aq}$ and 2 mM $NaOH_{aq}$ into the water [15]. To determine the initial conditions used in *GlobalKin*, the liquid is initialized with 2 mM $H_3O^+_{aq}$, $HCOO^-_{aq}$, Na^+_{aq}, and OH^-_{aq}. To account for solvation of atmospheric gases, 2 s of exposure to air ($N_2/O_2/H_2O$ = 78/21/1) is simulated. The resulting aqueous mole fractions are shown in Table 6.4 for various initial concentrations of $HCOO^-_{aq}$. ($H_3O^+_{aq}$, Na^+_{aq}, and OH^-_{aq} were also adjusted to have the same initial concentration as $HCOO^-_{aq}$.) $H_3O^+_{aq}$ and OH^-_{aq} have identical mole fractions that indicate a pH of 7. Na^+_{aq} and $HCOO^-_{aq}$ also have identical mole fractions. $HCOOH_{aq}$ is present at lower mole fractions than $HCOO^-_{aq}$, and $NaOH_{aq}$ has the smallest mole fraction of all, as it is a strong base and dissociates quickly in H_2O_{aq}. N_{2aq} and O_{2aq} have concentrations that indicate they are in Henry's law equilibrium with their gas phase counterparts. The mole fractions listed in Table 6.4 are used as initial conditions in the results presented in Sections 6.3 and 6.4.

The simulations using *GlobalKin* address the volume between the electrodes in the reactor (19.1 mm × 9.5 mm × 2 mm). The flow rate varies from 0.75 slm – 3 slm, and the resulting residence times are shown in Table 6.5 [16]. The base case has a flow rate of 1 slm, corresponding to a residence time of 10 ms. The power is specified as a square wave, with a 0.1 ms ramp up and ramp down, and the power is kept constant for the residence time. The power varies depending on the gas mixture used, as shown in Table 6.6. The simulation ends at the residence time plus 10 ms, the latter period to account for the flow of the gas and droplet to the collection surface. Each gas mixture includes impurities as measured in Nayak et al. (2.3 ppm H_2O, 1.5 ppm O_2, and 6.0 ppm N_2) [14].

6.3 Degradation of $HCOO^-_{aq}$ by OH_{aq}

The reaction mechanism in the liquid primarily involves $HCOO^-_{aq}$, OH_{aq}, $CO_2^-{}_{aq}$, $O_2^-{}_{aq}$, and $HO_2^-{}_{aq}$. $HCOO^-_{aq}$ dissolved in the droplet undergoes a reaction with OH_{aq}, forming $CO_2^-{}_{aq}$ and H_2O_{aq}. This reaction is the dominant consumption mechanism of OH_{aq} in the liquid, as long as $HCOO^-_{aq}$ is not depleted. Once the power turns off, and the source of OH_{aq} from solvation decreases, this reaction will consume the remaining OH_{aq}. The $CO_2^-{}_{aq}$ that is formed from the reaction of OH_{aq} and $HCOO^-_{aq}$ then reacts with O_{2aq} in a charge-exchange reaction, forming CO_{2aq} and $O_2^-{}_{aq}$. As O_{2aq} is not a reactive species and is instead found in the liquid due to the initial conditions (Table 6.4) or due to solvation of the impurity, the charge-exchange reaction occurs when $CO_2^-{}_{aq}$ is available.

Once $CO_2^-{}_{aq}$ increases and the corresponding increase in $O_2^-{}_{aq}$ occurs, $O_2^-{}_{aq}$ reacts with H_{aq} to produce $HO_2^-{}_{aq}$. $HO_2^-{}_{aq}$ can further react with OH_{aq} in two reactions: a charge-exchange reaction to form HO_{2aq} and $OH^-{}_{aq}$ or a reaction to form H_2O_{aq} and $O_2^-{}_{aq}$. As will be shown in Section 6.4.6, the reactions of $HO_2^-{}_{aq}$ and OH_{aq} becomes the dominant consumption mechanism of OH_{aq} when $HCOO^-{}_{aq}$ is depleted. Another important consumption mechanism of OH_{aq} when $HCOO^-{}_{aq}$ is depleted is reactions with $OH^-{}_{aq}$ to form $O^-{}_{aq}$ and H_2O_{aq}.

The base case examines the degradation of $HCOO^-{}_{aq}$ in a 41 µm diameter droplet exposed to a plasma sustained in He/H_2O = 99.8/0.2 (with impurities). The flow rate is 1 slm, corresponding to a residence time of 10 ms. The power deposition is 14.3 W. The droplet initially contains 2 mM $HCOO^-{}_{aq}$.

6.3.1 Determining the Reactive Layer Thickness

Before examining the $HCOO^-{}_{aq}$ degradation and reactive species densities, the thickness of the reactive layer was determined. The droplet is divided into two zones: the reactive layer and the nonreactive core. The reactive layer and nonreactive core do not interact throughout the simulation. The thickness of the reactive layer determines the amount of $HCOO^-{}_{aq}$ that can be consumed by OH_{aq} over the simulation. The thickness of the reactive layer was determined by performing simulations for thicknesses from 1 µm to 20.5 µm, where for the maximum thickness the entire droplet is considered reactive. The reactive layer thickness was then chosen to best match the experimental measurements of 0.76 mM $HCOO^-{}_{aq}$ remaining.

The remaining $HCOO^-{}_{aq}$ concentration at the end of the simulation for varying reactive layer thicknesses is shown in Figure 6.1. As the reactive layer thickness increases, the volume of the reactive layer increases compared to the nonreactive core, and the total inventory of $HCOO^-{}_{aq}$ in the reactive layer increases. As the amount of $HCOO^-{}_{aq}$ in the reactive layer increases, more

$HCOO^-_{aq}$ can be consumed by OH_{aq} in the residence time of the droplet in the plasma. The reactive layer thickness that best matches the experimental measurements is 5.5 µm, with a remaining $HCOO^-_{aq}$ concentration of 0.79 mM. 5.5 µm is used as the reactive layer thickness throughout this work, which agrees well with the 1D simulations of Oinuma et al. [15].

6.3.2 Plasma Properties and Reactive Species Densities

The plasma properties for the base case are shown in Figure 6.2a. The electron density starts at 10^8 cm^{-3}. As the power ramps up, the electron temperature increases and is maximized at 0.017 ms at 3.7 eV, igniting the plasma. As the power continues ramping up over 0.1 ms, the electron density increases, and the electron temperature slightly decreases. After about 3.5 ms, a steady state is reached in both the electron temperature and density. The steady state value of the electron density is 1.8×10^{11} cm^{-3}, and the steady state value of the electron temperature is 2.6 eV. After the power ramps down, the electrons quickly recombine, and the electron temperature also decreases.

The densities of OH and H_2O_2 in the gas phase are shown in Figure 6.2b. When the power first turns on, OH rapidly increases to 1.9×10^{14} cm^{-3} due to electron impact dissociation of H_2O. At the location of the maximum in OH, the electron temperature is higher than its steady state value, and the electron density is increasing to its steady state value, leading to an increase in OH production. As the electron density and temperature reach their steady state values, the density OH slightly decreases to its steady state value of 1.5×10^{14} cm^{-3}, balancing losses due to reactions and solvation into the droplet and the source due to electron-impact dissociation of H_2O. Once the power turns off, and the electron temperature and density rapidly decrease, the density of OH rapidly decreases due to reactions which form H_2O_2 or H_2O.

As the power first turns on, H_2O_2 rapidly increases, formed primarily by OH combining with OH. H_2O_2 then reaches a steady state value near 4.1×10^{14} cm^{-3}. While OH continues to produce H_2O_2 throughout the power on period, H_2O_2 has a high Henry's law constant (1.92×10^6), meaning H_2O_2 will readily solvate into the liquid. Immediately after the power turns off, H_2O_2 density increases slightly. After 12 ms, H_2O_2 begins to decrease as solvation into the droplet continues depleting H_2O_2 in the gas phase while the source of H_2O_2 by reactions of OH decreases.

The densities of OH_{aq}, $HCOO^-_{aq}$, $H_2O_{2\ aq}$, $CO_2^-{}_{aq}$, $O_2^-{}_{aq}$, and $HO_2^-{}_{aq}$ are shown in Figure 6.2c. These densities are shown in the reactive layer only and are not scaled as described in Section 2.3.1.1. OH_{aq} increases quite rapidly in the first 0.2 ms, due to solvation of gas phase OH. OH_{aq} increases throughout most of the power on period. The gas phase plasma supplies a nearly constant source of OH, and since OH has a relatively high Henry's law constant of 620, OH readily solvates into the droplet. The main consumption mechanism of OH_{aq} in the droplet is its reaction with $HCOO^-_{aq}$. As the $HCOO^-_{aq}$ density decreases due to reactions with OH_{aq}, the OH_{aq} density increases because its rate of consumption decreases. OH_{aq} reaches a maximum at 9.2 ms, or 0.9 ms before the power begins ramping down, at a value of 4.1×10^{14} cm^{-3}. At this point, most of the $HCOO^-_{aq}$ in the reactive layer has been consumed. The density of $CO_2^-{}_{aq}$ increases as it is a reaction product of OH_{aq} with $HCOO^-_{aq}$. Due to the increase in $CO_2^-{}_{aq}$, $O_2^-{}_{aq}$ increases through a charge-exchange reaction. $HO_2^-{}_{aq}$ increases through reactions between H_{aq} and $O_2^-{}_{aq}$. The dominant consumption mechanism of OH_{aq} is then through reactions with $HO_2^-{}_{aq}$, not $HCOO^-_{aq}$. Another important consumption mechanism is OH_{aq} reacting with OH^-_{aq}, producing H_2O_{aq} and O^-_{aq}. When the power turns off, there is no longer a source of OH in the gas phase plasma that replenishes the consumed OH_{aq}, and the density of OH_{aq} rapidly decreases.

$HCOO^{-}_{aq}$ decreases through most of the power on period due to the consumption of $HCOO^{-}_{aq}$ by OH_{aq}. At 9 ms, the $HCOO^{-}_{aq}$ density in the reactive layer is 2.9×10^{15} cm^{-3}, almost three orders of magnitude lower than its initial value of 1.2×10^{18} cm^{-3}. However, when the $HCOO^{-}_{aq}$ in the nonreactive core is included, the total $HCOO^{-}_{aq}$ density in the droplet is 4.8×10^{17} cm^{-3} at 9 ms. Once $HCOO^{-}_{aq}$ in the reactive layer is depleted, the consumption of $HCOO^{-}_{aq}$ stops because the $HCOO^{-}_{aq}$ in the nonreactive core does not react. (From a practical perspective, there will be some replenishment of $HCOO^{-}_{aq}$ in the reactive layer by diffusion from the nonreactive core.) Overall, the $HCOO^{-}_{aq}$ concentration averaged over the droplet decreases from 2 mM at the beginning of the simulation to 0.79 mM at the end of the simulation.

H_2O_{2aq} density increases throughout the power on period because there is a source of H_2O_2 in the gas phase plasma and H_2O_{2aq} has high Henry's law constant. After the power turns off, the H_2O_{2aq} density again increases, due to the formation of H_2O_2 and H_2O_{2aq} by OH and OH_{aq}. The H_2O_{2aq} density increases through the end of the simulation as gas phase H_2O_2 solvates into the liquid.

$CO_2^{-}{}_{aq}$ is one of the products from the reaction of $HCOO^{-}_{aq}$ and OH_{aq} (the other product is H_2O_{aq}). Therefore, while the $HCOO^{-}_{aq}$ density decreases, the $CO_2^{-}{}_{aq}$ density increases. $CO_2^{-}{}_{aq}$ reaches a maximum density at 8.4 ms of 9.5×10^{17} cm^{-3} in the reactive layer, coinciding with when the $HCOO^{-}_{aq}$ density decrease slows. Once $HCOO^{-}_{aq}$ in the reactive layer is depleted, there is not a source of $CO_2^{-}{}_{aq}$, and $CO_2^{-}{}_{aq}$ density decreases through the charge-exchange reaction with O_{2aq} that produces $O_2^{-}{}_{aq}$.

$O_2^{-}{}_{aq}$ is primarily produced through the charge-exchange reaction with $CO_2^{-}{}_{aq}$ and O_{2aq}. Therefore, during the first 10 ms, $O_2^{-}{}_{aq}$ density is relatively low but increases. The main consumption mechanism of $O_2^{-}{}_{aq}$ is creation of $HO_2^{-}{}_{aq}$ by reaction with H_{aq}. However, after CO_2^{-}

$_{aq}$ reaches its maximum density, $O_2^-{}_{aq}$ density rapidly increases due to production from the charge-exchange reaction.

$HO_2^-{}_{aq}$ is primarily produced by reactions between H_{aq} and $O_2^-{}_{aq}$. During the first 10 ms, $HO_2^-{}_{aq}$ increases rapidly, consuming much of the $O_2^-{}_{aq}$. However, after the power turns off, the source of H_{aq} stops, and H_{aq} density decreases, limiting the amount of $HO_2^-{}_{aq}$ formed.

The results from the model are compared to the experimental measurements in Table 6.7. The electron density and temperature are reactor averaged values, while the experimental values result from optical emission measurements emphasizing properties where the He atoms are excited [13]. Given these differences, agreement is good. The OH density and $HCOO^-{}_{aq}$ concentration are also shown in Table 6.7. The $HCOO^-{}_{aq}$ concentration is averaged over the reactive layer and nonreactive core as described in Section 2.3.1.1. The model underpredicts the measured OH density by a factor of two. In the global model, any OH in the gas phase can solvate into the droplet. Since OH does not reach Henry's law equilibrium in the droplet, OH in the gas phase constantly solvates into the liquid phase in the model. However, in the experiments, OH must be near the droplet to solvate into the droplet. This limits the amount of OH that can solvate into the droplet and increases the OH in the gas phase relative to the model. The modeled $HCOO^-{}_{aq}$ concentration matches the experimental measurements well, as the reactive layer thickness was chosen to match the measured $HCOO^-{}_{aq}$ concentration.

6.4 OH, OH_{aq}, and $HCOO^-{}_{aq}$ Variation with Liquid and Plasma Properties

The decomposition of $HCOO^-{}_{aq}$ in the droplet depends on the properties of the droplet and the plasma. In this section, properties of the droplet (diameter and initial $HCOO^-{}_{aq}$ concentration) and of the plasma (gas flow rate, power deposition, gas mixture, and water percentage in the inlet) are varied, and the effects on densities of OH, OH_{aq}, and $HCOO^-{}_{aq}$ are examined. The reactive layer thickness was kept constant at 5.5 µm throughout this section. The post-processing script parameter_sweep was used to compute all of the results in this section.

6.4.1 Droplet Diameter

Varying the droplet diameter varies the total inventory of $HCOO^-_{aq}$ in the droplet and therefore also varies the time required to consume $HCOO^-_{aq}$. The reactive layer thickness was kept constant at 5.5 µm regardless of diameter.

The variation of the density of OH with droplet diameter and SVR is shown in Figure 6.3. OH density has been recorded at 10.1 ms, or immediately when the power begins to ramp down. The OH density does not vary with droplet diameter or SVR and is nearly constant at 1.5×10^{14} cm^{-3}. Therefore, increasing the droplet diameter does not affect the gas phase plasma. In particular, droplet diameter does not affect the H_2O density in the gas phase. This is because the majority of H_2O in the gas phase does not come from evaporation of the droplet; rather, it comes from the 0.2% H_2O in the gas mixture.

While the gas phase OH does not vary with droplet diameter or SVR, OH_{aq} and $HCOO^-_{aq}$ do vary with droplet diameter and SVR, as shown in Figure 6.3. Both the OH_{aq} density and $HCOO^-_{aq}$ concentration are averaged over the reactive layer and nonreactive core. OH_{aq} density was recorded at 10.1 ms, and $HCOO^-_{aq}$ concentration in the droplet was calculated at the end of the simulation (20 ms). At all droplet diameters, $HCOO^-_{aq}$ density in the reactive layer is low, decreasing to 1.8×10^{14} cm^{-3} at 81 µm and 2.0×10^{10} cm^{-3} at 21 µm at the end of the simulation. However, the $HCOO^-_{aq}$ density in the nonreactive core of the droplet remains constant throughout the simulation at 1.2×10^{18} cm^{-3}. At small droplet diameters, the reactive layer is most of the volume of the droplet (i.e., at 21 µm, the reactive layer is 89% of the total droplet volume). However, as the droplet diameter increases, the reactive layer is less and less of the volume of the droplet, finally decreasing to 35% of the total droplet volume at 81 μm. Therefore, as diameter increases (SVR decreases), the $HCOO^-_{aq}$ concentration remaining in the droplet becomes more dependent on the concentration in the core and therefore increases. This variation is in fact linear with SVR.

OH_{aq} is only present in the reactive layer and not in the nonreactive core of the droplet. Therefore, its density is scaled by the volume of the reactive layer over the total volume. At small droplet diameters, $HCOO^-_{aq}$ in the reactive layer is consumed well before the power turns off. Therefore, the main consumption mechanism of OH_{aq} is removed, and the OH_{aq} density increases. As droplet diameter increases (SVR decreases), $HCOO^-_{aq}$ in the reactive layer is less consumed, and OH_{aq} still has $HCOO^-_{aq}$ to react with, leading to lower OH_{aq} densities. This variation is again linear with SVR.

The $HCOO^-_{aq}$ concentrations in the droplet are compared to the experimental measurements in Table 6.8 for three different droplet diameters. At 36 μm and 41 μm, the modeled $HCOO^-_{aq}$ concentrations match the measurements within uncertainty. However, at 56 μm, the model predicts 1.04 mM of $HCOO^-_{aq}$ remaining, while the measurements show 1.61 mM of $HCOO^-_{aq}$ remaining. This discrepancy may be a consequence of the effective reactive layer thickness being smaller for a diameter of 56 μm.

6.4.2 Initial $HCOO^-_{aq}$ Concentration

Varying the initial concentration of $HCOO^-_{aq}$ in the droplet varies the total inventory of $HCOO^-_{aq}$ in the droplet and the time required to consume $HCOO^-_{aq}$. The initial concentration of $HCOO^-_{aq}$ also changes the initial mole fractions of $HCOO^-_{aq}$, Na^+_{aq}, $HCOOH_{aq}$, and $NaOH_{aq}$, as shown in Table 6.4.

The variation of OH with initial $HCOO^-_{aq}$ concentration is shown in Figure 6.4 as the power begins to ramp down (10.1 ms). As only the initial $HCOO^-_{aq}$ concentration in the droplet was changed, the OH density does not vary with initial $HCOO^-_{aq}$ concentration. This shows that the gas phase plasma is not strongly affected by the initial composition of the droplet.

While the gas phase OH does not vary, OH_{aq} at the time the power begins to ramp down (10.1 ms) and $HCOO^-_{aq}$ at the end of the simulation do vary, as shown in Figure 6.4. Both OH_{aq} and $HCOO^-_{aq}$ were averaged over the droplet. At low initial $HCOO^-_{aq}$ concentrations (0.5 mM and 1 mM), $HCOO^-_{aq}$ in the reactive layer is decreased below 10^9 cm^{-3} at the end of the simulation. The total $HCOO^-_{aq}$ concentration is then dominated by the concentration in the nonreactive core. Since $HCOO^-_{aq}$ in the reactive layer is depleted, OH_{aq} is high as the main consumption mechanism of OH_{aq} has stopped. As the initial $HCOO^-_{aq}$ concentration increases, more $HCOO^-_{aq}$ remains in the reactive layer. In fact, at 10 mM initial $HCOO^-_{aq}$ concentration, the remaining density in the reactive layer is 4×10^{18} cm^{-3} (initial density is 6×10^{18} cm^{-3}). Therefore, the total $HCOO^-_{aq}$ concentration is not only due to the nonreactive core; the reactive layer still has a significant amount of $HCOO^-_{aq}$ remaining. Above 5 mM initial $HCOO^-_{aq}$ concentration, about 2 mM of $HCOO^-_{aq}$ has been degraded by OH_{aq}. Since $HCOO^-_{aq}$ is not depleted in the reactive layer at high initial $HCOO^-_{aq}$ concentrations, OH_{aq} density is low, as it is still actively being consumed in the reaction with $HCOO^-_{aq}$.

6.4.3 Gas Flow Rate

Varying the gas flow rate changes the residence time of the droplet in the plasma. At low gas flow rates, the residence time of the droplet in the plasma is long; at high gas flow rates, the residence time of the droplet in the plasma is short. The flow rates and corresponding residence times are listed in Table 6.5 and are primarily taken from the experimental work in Nayak et al. [16].

The OH density as the power begins to ramp down is shown in Figure 6.5a. Note that this time varies depending on the flow rate. The gas phase OH density does not depend on flow rate. As shown in Figure 6.2b, OH reaches a steady state value after 2 ms. This steady state value does not depend on flow rate or residence time.

The OH_{aq} density averaged over the droplet as the power begins to ramp down is shown in Figure 6.5a, and the $HCOO^{-}_{aq}$ concentration at the end of the simulation averaged over the droplet is shown in Figure 6.5b. OH_{aq} density increases from 0.75 slm to 1.25 slm. However, the $HCOO^{-}_{aq}$ concentration at the end of the simulation remains nearly constant between 0.75 slm and 1.25 slm. At 0.75 slm (13.5 ms residence time), the OH_{aq} density reaches a maximum near 9 ms due to there being less loss of OH_{aq} in the reaction with $HCOO^{-}_{aq}$. However, at 0.75 slm, the maximum occurs 4.6 ms before the power begins to ramp down, and OH_{aq} decreases due to consumption by $HO_2{}^{-}_{aq}$. At 1 slm, the maximum in OH_{aq} occurs only 0.9 ms before the power ramps down, and so the decrease in OH_{aq} is less in 0.9 ms than 4.6 ms. At 1.25 slm, the maximum in OH_{aq} occurs just as the power begins to ramp down, and so OH_{aq} does not decrease. As the flow rate increases beyond 1.25 slm (residence time decreases below 9.2 ms), OH_{aq} density decreases and $HCOO^{-}_{aq}$ density increases. As the residence time decreases, $HCOO^{-}_{aq}$ density in the reactive layer increases simply as a result of there being less time that the OH_{aq} has to react with $HCOO^{-}_{aq}$. Therefore, OH_{aq} decreases, as it is consumed in the reaction with $HCOO^{-}_{aq}$.

The measured $HCOO^{-}_{aq}$ concentrations are also shown in Figure 6.5b. The measured $HCOO^{-}_{aq}$ concentration increases as flow rate increases. At low flow rates (< 1.5 slm), the $HCOO^{-}_{aq}$ concentration predicted by the model remains constant, while it increases with increasing flow rate in the experiments. This is because the $HCOO^-_{aq}$ in the reactive layer is depleted at these low flow rates (long residence times). However, in the experiments, $HCOO^-_{aq}$ at the surface of the droplet is depleted but can be replenished by diffusion from the interior of the droplet. This mechanism does not exist in the model. In the experiments, at lower flow rates (longer residence times), $HCOO^-_{aq}$ has more time to diffuse from the center of the droplet to the surface, resulting in more $HCOO^-_{aq}$ being consumed. At high flow rates, the model results and measurements agree within experimental uncertainty.

6.4.4 Power Deposited

The power deposition in the He/H_2O plasma was increased and decreased from the base case of 14.3 W. As the power deposition increases, the electron density increases, leading to more electron-impact collisions and more reactive chemistry.

The OH and H_2O densities in the gas phase are shown in Figure 6.6 as the power begins to ramp down (10.1 ms). The OH density does vary as the power deposited varies, as opposed to varying the droplet diameter, initial $HCOO^-_{aq}$ concentration, and flow rate. At low power (< 14.3 W), the OH density increases as the power increases because the steady-state electron density increases. However, as power increases beyond 14.3 W, the OH density decreases despite the steady-state electron density continuing to increase as the power increases. This decrease in OH density is due to the depletion of H_2O in the gas phase by reactions, as shown in Figure 6.6. Since H_2O is a precursor to OH, the depletion of H_2O leads to a reduction in OH density.

The OH_{aq} density as the power begins to ramp down (10.1 ms) and the $HCOO^-_{aq}$ concentration at the end of the simulation are also shown in Figure 6.6, both averaged over the droplet. Below 10 W, the $HCOO^-_{aq}$ concentration decreases as power increases. Therefore, as $HCOO^-_{aq}$ concentration decreases, OH_{aq} increases because the main consumption mechanism of

OH_{aq} (by $HCOO^-_{aq}$) decreases. As the power increases above 10 W, however, the $HCOO^-_{aq}$ concentration does not further decrease and instead remains constant. This is because the $HCOO^-_{aq}$ in the reactive layer is almost completely consumed. Therefore, OH_{aq} density increases, as its main consumption mechanism decreases.

6.4.5 Gas Mixtures

When the plasma is sustained in different gas mixtures, different radical species are formed in the plasma. For example, in plasmas with high levels of O_2, O and O_3 are the dominant radicals; while in plasmas with high levels of H_2O, OH is a dominant radical. The degradation of $HCOO^-_{aq}$ has been investigated with varying gas mixtures [13–16], including He with admixtures of H_2O, O_2, Ar, and Ar/H_2O. The gas mixtures examined in this section have the same level of impurities as previously measured (2.3 ppm H_2O, 1.5 ppm O_2, and 6.0 ppm N_2) [14]. The power deposition varies for each gas mixture examined and is shown in Table 6.6, as well as the ratio of gases in the mixtures.

The OH density as the power begins to ramp down (10.1 ms) for various gas mixtures is shown in Figure 6.7. The He/H_2O = 99.8/0.2 and He/Ar/H_2O = 82.8/17.0/0.2 mixtures have the highest density of OH in the gas phase since the main formation mechanism of OH is electron-impact dissociation of H_2O. While H_2O can be found in the gas phase due to impurities and evaporation of the droplet, the main source of H_2O is in the initial gas mixture and flow. The He/O_2 = 99.8/0.2 mixture has the next highest density of OH in the gas phase. O is very plentiful in the He/O_2 mixture, and O can combine with H to form OH. The other three gas mixtures (He, He/Ar = 83/17, and He/H_2 = 99.8/0.2) have OH densities nearly two orders of magnitude lower than the OH densities in the He/H_2O and He/Ar/H_2O mixtures.

The OH_{aq} density as the power begins to ramp down (10.1 ms) and $HCOO^-_{aq}$ concentration at the end of the simulation are also shown in Figure 6.7, both averaged over the droplet. In general, where OH density was high in the gas phase, OH_{aq} density is also high, since OH is formed in the gas phase and solvates into the droplet. The exception, however, is the He/O_2 mixture, where the OH density is relatively low and the OH_{aq} density is the highest of all gas mixtures examined. In this case, OH_{aq} is formed not in the gas phase, but in the liquid phase by $O_{aq} + H_2O_{aq} \rightarrow OH_{aq} + OH_{aq}$. Since the He/O_2 mixture has an abundance of O to solvate into the droplet, OH_{aq} is readily formed. For the He/H_2O, He/O_2, and $He/Ar/H_2O$ mixtures, the $HCOO^-_{aq}$ in the reactive layer is depleted, and the main consumption mechanism of OH_{aq} is decreased, leading to a high density of OH_{aq} and a constant $HCOO^-_{aq}$ concentration. For the He, He/Ar, and He/H_2 mixtures, the $HCOO^-_{aq}$ is decreased by less than 0.3 mM from its initial concentration of 2 mM. Therefore, whatever OH_{aq} is in the liquid is quickly consumed in the reaction with $HCOO^-_{aq}$, leading to a low OH_{aq} density. Since the main source of OH_{aq} is solvation of OH and OH is not plentiful in these gas mixtures, OH_{aq} density is low.

The results from the model are compared to the experimental measurements in Table 6.9. As discussed in Section 6.3.2, in the He/H_2O plasma, the model underpredicts the OH density by a factor of two while matching the $HCOO^-_{aq}$ density. For the He/O_2 plasma, the OH density was not measured, but the model shows a density of 2.4×10^{12} cm^{-3}, almost two orders of magnitude lower than the He/H_2O plasma. The $HCOO^-_{aq}$ concentration matches well, as the measurements show 0.80 mM and the model predicts 0.79 mM. For the $He/Ar/H_2O$ plasma, the model underpredicts the OH density by 20%. The $HCOO^-_{aq}$ concentration again matches within uncertainty, as the model predicts 0.79 mM and the experiments show 0.74 mM.

6.4.6 Water Percentage

While different gas mixtures produce varying levels of OH and OH_{aq}, varying H_2O percentage in the He/H_2O mixture can also change the OH and OH_{aq} levels, allowing the OH density to be tuned to the desired amount. Note that to compare with experiments, the results in this section are with a flow rate of 1.5 slm, compared to 1 slm in previous sections.

The OH density as the power begins to ramp down (8.4 ms) is shown in Figure 6.8a at a flow rate of 1.5 slm (residence time of 8.3 ms). As the H_2O percentage in the initial gas mixture increases, the OH density increases because electron-impact dissociation of H_2O is the main production mechanism of OH. The OH density underpredicts the experimental measurements of OH by about 25%, but the trends in OH density are the same between the measurements and model results.

The OH_{aq} density as the power begins to ramp down (8.4 ms) is shown in Figure 6.8a, and the $HCOO^-_{aq}$ density at the end of the simulation is shown in Figure 6.8b. Both the OH_{aq} density and $HCOO^-_{aq}$ density are averaged over the droplet. At low water percentage (< 0.2%), the $HCOO^-_{aq}$ concentration continually decreases as the $HCOO^-_{aq}$ density in the reactive layer is decreasing. As the $HCOO^-_{aq}$ density decreases, the OH_{aq} density increases as the main consumption mechanism of OH_{aq} by $HCOO^-_{aq}$ decreases. Beyond 0.2% H_2O, the $HCOO^-_{aq}$ concentration remains constant as the $HCOO^-_{aq}$ in the reactive layer has been depleted. Therefore, the OH_{aq} density is expected to increase with increasing H_2O percentage since the main consumption mechanism with $HCOO^-_{aq}$ has decreased. The OH_{aq} density does increase up to 0.3% H_2O. However, at larger H_2O percentages, OH_{aq} when the power begins ramping down begins to decrease. As the H_2O percentage increases, $HCOO^-_{aq}$ becomes depleted earlier in the power on period. Therefore, $CO_2^-{}_{aq}$, a product of the reaction between OH_{aq} and $HCOO^-_{aq}$, also increases earlier in the power on period. $O_2^-{}_{aq}$ is produced from $CO_2^-{}_{aq}$ by a charge-exchange reaction with O_{2aq}. $O_2^-{}_{aq}$ then reacts with H_{aq} to form $HO_2^-{}_{aq}$, and the dominant consumption mechanism of OH_{aq} becomes reactions with $HO_2^-{}_{aq}$ to form either HO_{2aq} and $OH^-{}_{aq}$ or H_2O_{aq} and $O_2^-{}_{aq}$. Due to the abundance of $HO_2^-{}_{aq}$ produced from $CO_2^-{}_{aq}$, this consumption mechanism becomes larger as water percentage increases. Another important consumption mechanism is OH_{aq} reacting with $OH^-{}_{aq}$ to form $O^-{}_{aq}$ and H_2O_{aq}.

The measured $HCOO^-{}_{aq}$ concentration is also shown in Figure 6.8b. At 0% H_2O (pure He), the experiments show a high level of $HCOO^-{}_{aq}$ degradation, while the model does not predict this. This mismatch could indicate that there are other reactive species besides OH_{aq} that consume $HCOO^-{}_{aq}$. These other reactive species could be excited states of He, as those states are abundant in a pure He plasma, or VUV radiation from excited He states. From 0.05% H_2O to 0.3% H_2O, the measured $HCOO^-{}_{aq}$ concentration decreases. This trend is predicted by the model up to 0.2% H_2O. After 0.3% H_2O, the measured $HCOO^-{}_{aq}$ concentration remains relatively constant, matching the predictions by the model. However, the model predicts a concentration of 0.79 mM, while the measurements show a concentration near 1.1 mM. This discrepancy is likely due to the fixed thickness of the reactive layer at 5.5 µm, chosen to match the experimental measurements at 1 slm (residence time of 10 ms). These measurements and experimental results have a higher flow rate of 1.5 slm (residence time of 8.3 ms). Therefore, in the experiments, $HCOO^-{}_{aq}$ from the interior of the droplet has less time to diffuse to the surface of the droplet to replenish the consumed $HCOO^-{}_{aq}$ at higher flow rates. Since the reactive layer thickness in the model was chosen based on 1 slm, the reactive layer encompasses both the $HCOO^-{}_{aq}$ readily available at the surface of the droplet as well as the $HCOO^-{}_{aq}$ that diffuses from the center of the droplet in the 10 ms residence time.

However, when the residence time is decreased, the model does not account for the lower amount of $HCOO^-_{aq}$ that diffuses from the center of the droplet, predicting more $HCOO^-_{aq}$ consumption.

6.5 Concluding Remarks

The degradation of $HCOO^-_{aq}$, a model organic compound, by OH_{aq} from the plasma-produced OH was modeled in an atmospheric pressure RF discharge sustained in He/H_2O mixtures using *GlobalKin*. To best match the experimental results, the droplet was modeled as two zones: a reactive layer and a nonreactive core. The best thickness of the reactive layer was determined to be 5.5 µm, so the model predictions of $HCOO^-_{aq}$ concentration would match the experimentally measured $HCOO^-_{aq}$ concentration. Over the 10 ms the droplet is exposed to the plasma, the OH density reaches a steady state value of 1.5×10^{14} cm^{-3}. In the droplet, $HCOO^-_{aq}$ decreases due to reactions with OH_{aq} that solvates from the gas phase into the liquid phase due to its high Henry's law constant. Once much of the $HCOO^-_{aq}$ in the reactive layer has been consumed (about 9 ms into plasma exposure), OH_{aq} reaches a maximum and then decreases slightly. While the main consumption mechanism of OH_{aq} is the reaction with $HCOO^-_{aq}$, other reactions become dominant once $HCOO^-_{aq}$ is degraded, including those with $HO_2{}^-_{aq}$ and OH^-_{aq}.

As discussed in Section 6.4, the variation of droplet and plasma properties affects the amount of $HCOO^-_{aq}$ consumed. While all variations examined change the species densities in the liquid, only the power deposition, gas mixture, and percentage of H_2O in the inlet change the gas phase OH density (the droplet diameter, initial $HCOO^-_{aq}$ concentration, and gas flow rate do not affect the OH density). In general, when the $HCOO^-_{aq}$ concentration is low, the OH_{aq} density is high because the primary consumption mechanism of OH_{aq} is the reaction with $HCOO^-_{aq}$. However, when $HCOO^-_{aq}$ is consumed early in the power on period (as seen at low flow rates and high H_2O percentages in the inlet), the formation of $CO_2{}^-_{aq}$ by the reaction between OH_{aq} and

$HCOO^-_{aq}$ leads to the formation of $O_2^-{}_{aq}$. $O_2^-{}_{aq}$ then forms $HO_2^-{}_{aq}$, and the increase in $HO_2^-{}_{aq}$ due to $HCOO^-_{aq}$ consumption leads to reactions between OH_{aq} and $HO_2^-{}_{aq}$ becoming the dominant consumption mechanisms of OH_{aq}. Then, the reactions of $HO_2^-{}_{aq}$ and OH_{aq} lead to decreases in OH_{aq} even when $HCOO^-_{aq}$ in the reactive layer has been consumed.

6.6 Tables

Table 6.1. Species included in the reaction mechanism.

Charged Species in the Gas Phase	e, He^+, He_2^+, HeH^+, Ar^+, Ar_2^+, ArH^+ H^+, H^-, H_2^+, H_3^+, OH^+, OH^-, H_2O^+, H_3O^+ O_2^+, O_2^-, O_4^+, O^+, O^-, O_3^-, N_2^+, N_3^+, N_4^+, N^+ NO^+, NO_2^+, NO_2^-, NO_3^-, $NO^+(H_2O)$, $NO^+(H_2O)_2$, $NO^+(H_2O)_3$, $N^+(H_2O)$, $NO^+(O_2)$ $H_2O^+(H_2O)$, $O_2^+(H_2O)$, $H_3O^+(H_2O)$, $H_3O^+(H_2O)_2$, $H_3O^+(H_2O)_3$, $H_3O^+(H_2O)_4$, $H_3O^+(H_2O)_5$, $H_3O^+(H_2O)_6$, $O_2^-(H_2O)$, $O_2^-(H_2O)_2$, $O^-(H_2O)$, $OH^-(H_2O)$, $OH^-(H_2O)_2$ CO^+, CO_2^+
Neutral Species in the Gas Phase	He, Ar H, H_2, OH, H_2O, HO_2, H_2O_2 O_2, O, O_3, N_2, N NO, NO_2, NO_3, N_2O, N_2O_3, N_2O_4, N_2O_5, NH, HNO, HNO_2, HNO_3, HNO_4 CO, CO_2, HCOOH, HCOO
Excited States in the Gas Phase	$He(2^3S)$, $He(2^1S)$, $He(2^3P)$, $He(2^1P)$, He(3P), He(3S), He_2^*, $Ar(1s_1)$, $Ar(1s_2)$, $Ar(1s_3)$, $Ar(1s_4)$, Ar(4P), Ar(4D), Ar_2^* H^*, $H_2(r)$, $H_2(v)$, H_2^*, $OH(A^2\Sigma)$, $H_2O(v)$ $O_2(v)$, $O_2(r)$, $O_2(^1\Delta)$, $O_2(^1\Sigma)$, $O(^1D)$, O_3^*, $N_2(r)$, $N_2(v)$, $N_2(A^3\Sigma_u)$, $N_2(a'^1\Sigma)$, $N(^2D)$ $N_2O(v)$ $CO(v)$, $CO_2(v)$
Charged Species Only Present in the Liquid Phase	$e(H_2O)_{aq}$, $HO_2^-{}_{aq}$, $ONOO^-{}_{aq}$, $NO_4^-{}_{aq}$, $Na^+{}_{aq}$, $HCOO^-{}_{aq}$, $CO_2^-{}_{aq}$, $NO_3^{-2}{}_{aq}$, $HNO_3^-{}_{aq}$
Neutral Species Only Present in the Liquid Phase	$ONOOH_{aq}$, $NaOH_{aq}$

Table 6.2. Aqueous reaction mechanism additions or changes from Lietz and Kushner [23].

Reaction	Rate (cm^3/s unless otherwise specified)	Note
$H_2O_{aq} + H_2O_{aq} \rightarrow H_3O^+_{aq} + OH^-_{aq}$	1.83×10^{-28}	Ref. [15][2]
$H_3O^+_{aq} + OH^-_{aq} \rightarrow H_2O_{aq} + H_2O_{aq}$	4.98×10^{-11}	Ref. [15][2]
Ion and excited state solvation		
$e_{aq} + H_2O_{aq} \rightarrow e(H_2O)_{aq}$	5.0×10^{-9}	20 fs solvation time[2]
$H_3^+{}_{aq} + H_2O_{aq} \rightarrow H_3O^+_{aq} + H_{2aq}$	5.0×10^{-15}	[1,3]
$N^+(H_2O)_{aq} + H_2O_{aq} \rightarrow H_2O^+_{aq} + N_{aq} + H_2O_{aq}$	5.0×10^{-15}	[1,3]
$OH^+_{aq} + H_2O_{aq} \rightarrow H_2O^+_{aq} + OH_{aq}$	5.0×10^{-15}	[1,3]
$Ar^+_{aq} + H_2O_{aq} \rightarrow H_2O^+_{aq} + Ar_{aq}$	5.0×10^{-15}	[1,3]
$Ar^+_{2aq} + H_2O_{aq} \rightarrow H_2O^+_{aq} + Ar_{aq} + Ar_{aq}$	5.0×10^{-15}	[1,3]
$ArH^+_{aq} + H_2O_{aq} \rightarrow H_3O^+_{aq} + Ar_{aq}$	5.0×10^{-15}	[1,3]
$H^-_{aq} + H_2O_{aq} \rightarrow H_{2aq} + OH^-_{aq}$	5.0×10^{-15}	[1,3]
$N_2(r)_{aq} + H_2O_{aq} \rightarrow H_2O_{aq} + N_{2aq}$	5.0×10^{-15}	[1,3]
$H^*_{aq} + H_2O_{aq} \rightarrow H_{aq} + OH_{aq} + H_{aq}$	5.0×10^{-15}	[1,3]
$H_2O(v)_{aq} + H_2O_{aq} \rightarrow H_2O_{aq} + H_2O_{aq}$	5.0×10^{-15}	[1,3]
$N(^2D)_{aq} + H_2O_{aq} \rightarrow NH_{aq} + OH_{aq}$	$6.03 \times 10^{-11} (T_{gas}/300)^{1.2} \exp(19300/T_{gas})$	T_{gas} in K[2]
$OH(A^2\Sigma)_{aq} + H_2O_{aq} \rightarrow OH_{aq} + H_{aq} + OH_{aq}$	5.0×10^{-15}	[1,3]
$H_2(r)_{aq} + H_2O_{aq} \rightarrow H_{2aq} + H_2O_{aq}$	5.0×10^{-15}	[1,3]
$H_2(v)_{aq} + H_2O_{aq} \rightarrow H_{2aq} + H_2O_{aq}$	5.0×10^{-15}	[1,3]
$H^*_{2aq} + H_2O_{aq} \rightarrow H_{2aq} + H_{aq} + OH_{aq}$	5.0×10^{-15}	[1,3]
$O_2(r)_{aq} + H_2O_{aq} \rightarrow O_{2aq} + H_2O_{aq}$	5.0×10^{-15}	[1,3]
$O_3^*{}_{aq} + H_2O_{aq} \rightarrow O_{3aq} + H_2O_{aq}$	5.0×10^{-15}	[1,3]
$O_2(^1\Delta)_{aq} + H_2O_{aq} \rightarrow O_{2aq} + H_2O_{aq}$	$1.50 \times 10^{-17} \exp(-200/T_{gas})$	Ref. [17], T_{gas} in K[2]

$OH(A^2\Sigma)_{aq} + H_2O_{aq} \rightarrow OH_{aq} + H_2O_{aq}$	1.20×10^{-11}	[1,3]
$N_2O(v)_{aq} + H_2O_{aq} \rightarrow N_2O_{aq} + H_2O_{aq}$	5.0×10^{-15}	[1,3]
Reactive oxygen species		
$e(H_2O)_{aq} + H_2O_{aq} \rightarrow e_{aq} + H_2O_{aq} + H_2O_{aq}$	1.0×10^{-13}	[1,3]
$e(H_2O)_{aq} + Ar_{aq} \rightarrow e_{aq} + H_2O_{aq} + Ar_{aq}$	1.0×10^{-13}	[1,3]
$e(H_2O)_{aq} + H_2O_{aq} \rightarrow H_{aq} + OH^-_{aq} + H_2O_{aq}$	3.0×10^{-20}	[1]
$e(H_2O)_{aq} + H_2O^+_{aq} \rightarrow H_{aq} + OH_{aq} + H_2O_{aq}$	1.0×10^{-9}	[1]
$H_2O^+_{aq} + H_2O_{aq} \rightarrow H_3O^+_{aq} + OH_{aq}$	1.0×10^{-17}	[1]
$H_3O^+_{aq} + O^-_{aq} \rightarrow OH_{aq} + H_2O_{aq}$	1.66×10^{-11}	Ref. [15][1]
$H_3O^+_{aq} + O_2^-{}_{aq} \rightarrow HO_{2aq} + H_2O_{aq}$	9.46×10^{-11}	Ref. [15][1]
$OH_{aq} + OH_{aq} \rightarrow H_2O_{2aq}$	1.66×10^{-12}	Ref. [15][2]
$OH_{aq} + HO_{2aq} \rightarrow O_{2aq} + H_2O_{aq}$	1.66×10^{-11}	Ref. [15][2]
$OH_{aq} + H_2O_{2aq} \rightarrow HO_{2aq} + H_2O_{aq}$	5.84×10^{-14}	Ref. [15][2]
$OH_{aq} + OH^-_{aq} \rightarrow O^-_{aq} + H_2O_{aq}$	1.99×10^{-11}	Ref. [15][2]
$OH_{aq} + O^-_{aq} \rightarrow HO^-_{2aq}$	4.48×10^{-11}	Ref. [15][2]
$OH_{aq} + HO_2^-{}_{aq} \rightarrow HO_{2aq} + OH^-_{aq}$	1.25×10^{-11}	Ref. [15][2]
$O^-_{aq} + H_2O_{aq} \rightarrow OH^-_{aq} + OH_{aq}$	2.99×10^{-15}	Ref. [15][1]
$O^-_{aq} + O_{2aq} \rightarrow O_3^-{}_{aq}$	5.81×10^{-12}	Ref. [15][2]
$O^-_{aq} + H_2O_{2aq} \rightarrow O_2^-{}_{aq} + H_2O_{aq}$	8.30×10^{-13}	Ref. [15][2]
$O^-_{aq} + HO_2^-{}_{aq} \rightarrow O_2^-{}_{aq} + OH^-_{aq}$	6.64×10^{-13}	Ref. [15][2]
$O_3^-{}_{aq} + O^-_{aq} \rightarrow O_2^-{}_{aq} + O_2^-{}_{aq}$	1.16×10^{-11}	Ref. [15][2]
$O_3^-{}_{aq} \rightarrow O_{2aq} + O^-_{aq}$	4.30×10^{3} 1/s	Ref. [15][2]
$O_2^-{}_{aq} + H_2O_{2aq} \rightarrow O_{2aq} + OH_{aq} + OH^-_{aq}$	2.66×10^{-20}	Ref. [15][2]
$HO_{2aq} + H_2O_{aq} \rightarrow H_3O^+_{aq} + O_2^-{}_{aq}$	3.33×10^{-17}	Ref. [15][2]
$H_2O_{2aq} + HO_{2aq} \rightarrow OH_{aq} + O_{2aq} + H_2O_{aq}$	8.80×10^{-19}	Ref. [26][1]
$HO_{2aq} + HO_{2aq} \rightarrow H_2O_{2aq} + O_{2aq}$	3.32×10^{-15}	Ref. [15][1]
$HO_{2aq} + O_2^-{}_{aq} \rightarrow O_{2aq} + HO_2^-{}_{aq}$	8.30×10^{-14}	Ref. [15][1]
$e(H_2O)_{aq} + H_3O^+_{aq} \rightarrow H_{aq} + H_2O_{aq} + H_2O_{aq}$	3.82×10^{-11}	Ref. [26][1]
$H_{aq} + O_2^-{}_{aq} \rightarrow HO_2^-{}_{aq}$	3.32×10^{-11}	Ref. [26][1]
$HO_2^-{}_{aq} + O_3^-{}_{aq} \rightarrow OH^-_{aq} + O_{2aq} + O_2^-{}_{aq}$	1.48×10^{-15}	Ref. [15][1]

$HO_2{}^-_{aq} + H_2O_{aq} \rightarrow H_2O_{2aq} + OH^-_{aq}$	1.83×10^{-15}	Ref. [15][1]
$OH^-_{aq} + HO_{2aq} \rightarrow O_2{}^-_{aq} + H_2O_{aq}$	1.66×10^{-11}	Ref. [15][1]
$H_2O_{2aq} + OH^-_{aq} \rightarrow HO_2{}^-_{aq} + H_2O_{aq}$	1.66×10^{-11}	Ref. [15][1]
$H_2O_{2aq} + O_3{}^-_{aq} \rightarrow O_{2aq} + O_2{}^-_{aq} + H_2O_{aq}$	2.66×10^{-15}	Ref. [15][1]
$OH_{aq} + HO_2{}^-_{aq} \rightarrow H_2O_{aq} + O_2{}^-_{aq}$	1.16×10^{-11}	Ref. [15][1]
$O^-_{aq} + O_2{}^-_{aq} + H_2O_{aq} \rightarrow OH^-_{aq} + OH^-_{aq} + O_{2aq}$	3.32×10^{-35} cm^6/s	Ref. [15][1]
$O^-_{aq} + O^-_{aq} + H_2O_{aq} \rightarrow OH^-_{aq} + HO_2{}^-_{aq}$	5.53×10^{-35} cm^6/s	Ref. [15][1]
$H_2O_{2aq} + H_2O_{aq} \rightarrow H_3O^+_{aq} + HO_2{}^-_{aq}$	1.0×10^{-21}	Ref. [15][1]
$H_3O^+_{aq} + HO_2{}^-_{aq} \rightarrow H_2O_{2aq} + H_2O_{aq}$	4.98×10^{-11}	Ref. [15][1]
$e(H_2O)_{aq} + O_2{}^-_{aq} \rightarrow OH^-_{aq} + HO_2{}^-_{aq}$	2.16×10^{-11}	[1]
$e(H_2O)_{aq} + O_3{}^-_{aq} \rightarrow OH^-_{aq} + OH^-_{aq} + O_{2aq}$	2.66×10^{-11}	[1]
$OH_{aq} + O_3{}^-_{aq} + H_2O_{aq} \rightarrow O_2{}^-_{aq} + O_2{}^-_{aq} + H_3O^+_{aq}$	3.0×10^{-34} cm^6/s	[1]
Reactive nitrogen species		
$HNO_{2aq} + H_2O_{aq} \rightarrow H_3O^+_{aq} + NO_2{}^-_{aq}$	3.0×10^{-20}	[1,3]
$HNO_{3aq} + H_2O_{aq} \rightarrow H_3O^+_{aq} + NO_3{}^-_{aq}$	3.0×10^{-18}	[1,3]
$H_3O^+_{aq} + NO_2{}^-_{aq} \rightarrow H_{aq} + NO_{2aq} + H_2O_{aq}$	6.81×10^{-10}	Based on pKa = 3.39[1]
$H_3O^+_{aq} + NO_3{}^-_{aq} \rightarrow HNO_{3aq} + H_2O_{aq}$	3.32×10^{-19}	Ref. [27][1]
$OH_{aq} + HNO_{3aq} \rightarrow NO_{3aq} + H_2O_{aq}$	2.17×10^{-13}	[1,4]
$H_{aq} + HNO_{2aq} \rightarrow NO_{aq} + H_2O_{aq}$	7.50×10^{-13}	[1,4]
$NO_3{}^-_{aq} + H_{aq} \rightarrow HNO_3{}^-_{aq}$	2.32×10^{-15}	[1]
$NO_3{}^-_{aq} + e(H_2O)_{aq} \rightarrow NO_3{}^{-2}_{aq} + H_2O_{aq}$	1.83×10^{-11}	[1]
$NO_3{}^{-2}_{aq} + H_3O^+_{aq} \rightarrow OH^-_{aq} + NO_{2aq} + H_2O_{aq}$	3.32×10^{-11}	[1]
$N_2O_{5aq} + H_2O_{aq} \rightarrow NO_{2aq} + NO_{3aq} + H_2O_{aq}$	1.46×10^{-19}	[2,4]
$ONOOH_{aq} + H_2O_{aq} \rightarrow H_3O^+_{aq} + ONOO^-_{aq}$	5.0×10^{-15}	[1,3]
$ONOO^-_{aq} + H_3O^+_{aq} \rightarrow H_2O_{aq} + ONOOH_{aq}$	1.75×10^{-6}	Based on pKa = 6.8[1]

$N_{aq} + H_2O_{aq} \rightarrow NH_{aq} + OH_{aq}$	$6.03 \times 10^{-11} (T_{gas}/300)^{1.2} \exp(-19300/T_{gas})$	T_{gas} in K[2]
$H_{aq} + HNO_{aq} \rightarrow OH_{aq} + NH_{aq}$	$2.41 \times 10^{-9} (T_{gas}/300)^{-0.5} \exp(-9010/T_{gas})$	T_{gas} in K[2,4]
$HNO_{4aq} + H_2O_{aq} \rightarrow NO_4{}^-{}_{aq} + H_3O^+{}_{aq}$	5.0×10^{-15}	[1,3]
$NO_4{}^-{}_{aq} + H_3O^+{}_{aq} \rightarrow HNO_{4aq} + H_2O_{aq}$	1.08×10^{-7}	Ref. [28][1]
$NO_4{}^-{}_{aq} \rightarrow NO_2{}^-{}_{aq} + O_{2\,aq}$	1.0 1/s	Ref. [28][1]
$HNO_{4aq} + HNO_{2aq} \rightarrow HNO_{3aq} + HNO_{3aq}$	1.99×10^{-20}	[1,4]
$HNO_{4aq} \rightarrow HNO_{2aq} + O_{2aq}$	7.0×10^{-4} 1/s	[1,4]
$HNO_{4aq} \rightarrow HO_{2aq} + NO_{2aq}$	4.60×10^{-3} 1/s	[1,4]
Carbon monoxide and carbon dioxide		
$CO_2(v)_{aq} + H_2O_{aq} \rightarrow CO_{2aq} + H_2O_{aq}$	5.0×10^{-15}	[1,3]
$CO(v)_{aq} + H_2O_{aq} \rightarrow CO_{aq} + H_2O_{aq}$	5.0×10^{-15}	[1,3]
$CO_{2aq} + H_{aq} \rightarrow CO_{aq} + OH_{aq}$	$2.50 \times 10^{-10} \exp(-13300/T_{gas})$	[2]
$CO_{2aq} + O_{aq} \rightarrow CO_{aq} + O_{2aq}$	$2.80 \times 10^{-11} \exp(-26500/T_{gas})$	[2]
$CO_{2aq} + H_2O_{aq} \rightarrow CO_{aq} + O_{aq} + H_2O_{aq}$	$8.48 \times 10^{-10} \exp(-55557/T_{gas})$	[2]
$O_2(^1\Delta)_{aq} + CO_{2aq} \rightarrow O_{2aq} + CO_{2aq}$	3.0×10^{-18}	[1]
$CO_2{}^+{}_{aq} + H_2O_{aq} \rightarrow H_2O^+{}_{aq} + CO_{2aq}$	5.0×10^{-15}	[1,3]
$CO_{aq} + H_2O_{aq} \rightarrow CO_{2aq} + H_{2aq}$	$1.70 \times 10^{-13} \exp(-3486/T_{gas})$	T_{gas} in K[2]
$OH_{aq} + CO_{aq} \rightarrow CO_{2aq} + H_{aq}$	$5.40 \times 10^{-14} (T_{gas}/300)^{1.5} \exp(250/300)$	T_{gas} in K[2]
$CO_{aq} + O_{2aq} \rightarrow CO_{2aq} + O_{aq}$	$4.20 \times 10^{-12} \exp(-24000/T_{gas})$	T_{gas} in K[2]
$CO_{aq} + HO_{2aq} \rightarrow OH_{aq} + CO_{2aq}$	$2.50 \times 10^{-10} \exp(-11900/T_{gas})$	T_{gas} in K[2]
$CO_{aq} + NO_{2aq} \rightarrow CO_{2aq} + NO_{aq}$	$1.48 \times 10^{-10} \exp(-17010/T_{gas})$	T_{gas} in K[2]
$CO^+{}_{aq} + H_2O_{aq} \rightarrow H_2O^+{}_{aq} + CO_{aq}$	5.0×10^{-15}	[1,3]
Formate and sodium hydroxide		
$HCOOH_{aq} + OH_{aq} \rightarrow HCOO_{aq} + H_2O_{aq}$	2.16×10^{-13}	Ref. [26][1]
$HCOO^-{}_{aq} + OH_{aq} \rightarrow CO_2{}^-{}_{aq} + H_2O_{aq}$	5.31×10^{-12}	Ref. [26][1]
$HCOO_{aq} + O_{2aq} \rightarrow CO_{2aq} + HO_{2aq}$	4.98×10^{-12}	Ref. [26][1]
$CO_2{}^-{}_{aq} + O_{2aq} \rightarrow CO_{2aq} + O_2{}^-{}_{aq}$	3.98×10^{-12}	Ref. [26][1]

$HCOOH_{aq} + H_2O_{aq} \rightarrow HCOO^-_{aq} + H_3O^+_{aq}$	1.66×10^{-20}	Ref. [15][1]
$HCOO^-_{aq} + H_3O^+_{aq} \rightarrow HCOOH_{aq} + H_2O_{aq}$	9.38×10^{-17}	Ref. [15][1]
$Na^+_{aq} + OH^-_{aq} \rightarrow NaOH_{aq}$	5.0×10^{-20}	[1,3]
$NaOH_{aq} + H_2O_{aq} \rightarrow Na^+_{aq} + OH^-_{aq} + H_2O_{aq}$	5.0×10^{-15}	[1,3]
Helium excited state solvation		
$M_{aq} + H_2O_{aq} + H_2O_{aq} \rightarrow He_{aq} + H_2O^+_{aq} + e(H_2O)_{aq}$ $M = He(2^1S)_{aq}, He(2^3S)_{aq}, He(2^3P)_{aq}, He(2^1P)_{aq}, He(3S)_{aq}, He(3P)_{aq}$	3.31×10^{-35} cm^6/s	[1]
$M_{aq} + H_2O_{aq} + H_2O_{aq} \rightarrow He_{aq} + H^+_{aq} + OH_{aq} + e(H_2O)_{aq}$ $M = He(2^1S)_{aq}, He(2^3S)_{aq}, He(2^3P)_{aq}, He(2^1P)_{aq}, He(3S)_{aq}, He(3P)_{aq}$	1.29×10^{-36} cm^6/s	[1]
$M_{aq} + H_2O_{aq} + H_2O_{aq} \rightarrow He_{aq} + H^+_{aq} + OH(A^2\Sigma)_{aq} + e(H_2O)_{aq}$ $M = He(2^1S)_{aq}, He(2^3S)_{aq}, He(2^3P)_{aq}, He(2^1P)_{aq}, He(3S)_{aq}, He(3P)_{aq}$	1.29×10^{-36} cm^6/s	[1]
$M_{aq} + H_2O_{aq} + H_2O_{aq} \rightarrow He_{aq} + H_{aq} + OH^+_{aq} + e(H_2O)_{aq}$ $M = He(2^1S)_{aq}, He(2^3S)_{aq}, He(2^3P)_{aq}, He(2^1P)_{aq}, He(3S)_{aq}, He(3P)_{aq}$	7.51×10^{-36} cm^6/s	[1]
$M_{aq} + H_2O_{aq} \rightarrow He_{aq} + H_{aq} + OH_{aq}$ $M = He(2^1S)_{aq}, He(2^3S)_{aq}, He(2^3P)_{aq}, He(2^1P)_{aq}, He(3S)_{aq}, He(3P)_{aq}$	1.25×10^{-12}	[1]
$He_2{}^*_{aq} + H_2O_{aq} + H_2O_{aq} \rightarrow H_2O^+_{aq} + He_{aq} + He_{aq} + e(H_2O)_{aq}$	1.98×10^{-34} cm^6/s	[1]
$He_2{}^*_{aq} + H_2O_{aq} + H_2O_{aq} \rightarrow H^+_{aq} + OH_{aq} + He_{aq} + He_{aq} + e(H_2O)_{aq}$	3.91×10^{-36} cm^6/s	[1]
$He_2{}^*_{aq} + H_2O_{aq} + H_2O_{aq} \rightarrow H^+_{aq} + OH(A^2\Sigma)_{aq} + He_{aq} + He_{aq} + e(H_2O)_{aq}$	3.91×10^{-36} cm^6/s	[1]

$He_2^{*}{}_{aq} + H_2O_{aq} + H_2O_{aq} \rightarrow H_{aq} + OH^{+}_{aq} + He_{aq} + He_{aq} + e(H_2O)_{aq}$	4.51×10^{-35} cm^6/s	[1]
$He_2^{*}{}_{aq} + H_2O_{aq} \rightarrow H_{aq} + OH_{aq} + He_{aq} + He_{aq}$	3.0×10^{-12}	[1]
$He^{+}_{aq} + H_2O_{aq} \rightarrow H_2O^{+}_{aq} + He_{aq}$	6.05×10^{-13}	[1]
$He^{+}_{aq} + H_2O_{aq} \rightarrow H_{aq} + OH^{+}_{aq} + He_{aq}$	2.86×10^{-12}	[1]
$He^{+}_{aq} + H_2O_{aq} \rightarrow H^{+}_{aq} + OH_{aq} + He_{aq}$	2.04×10^{-12}	[1]
$He^{+}_{aq} + H_2O_{aq} \rightarrow H^{+}_{aq} + OH(A^2\Sigma)_{aq} + He_{aq}$	5.0×10^{-15}	[1]
$He_2^{+}{}_{aq} + H_2O_{aq} \rightarrow He_{aq} + He_{aq} + H_2O^{+}_{aq}$	6.05×10^{-13}	[1]
$He_2^{+}{}_{aq} + H_2O_{aq} \rightarrow H_{aq} + OH^{+}_{aq} + He_{aq} + He_{aq}$	2.86×10^{-12}	[1]
$He_2^{+}{}_{aq} + H_2O_{aq} \rightarrow H^{+}_{aq} + OH_{aq} + He_{aq} + He_{aq}$	2.10×10^{-12}	[1]
$He_2^{+}{}_{aq} + H_2O_{aq} \rightarrow H_{2aq} + O^{+}_{aq} + He_{aq} + He_{aq}$	2.10×10^{-12}	[1]
$He_2^{+}{}_{aq} + H_2O_{aq} \rightarrow H_2^{+}{}_{aq} + O_{aq} + He_{aq} + He_{aq}$	2.10×10^{-12}	[1]
Argon excited state solvation		
$M_{aq} + H_2O_{aq} + H_2O_{aq} \rightarrow Ar_{aq} + H_2O^{+}_{aq} + e(H_2O)_{aq}$ $M = Ar(1s_1)_{aq}, Ar(1s_2)_{aq}, Ar(1s_3)_{aq}, Ar(1s_4)_{aq}$	3.31×10^{-33} cm^6/s	[1]
$M_{aq} + H_2O_{aq} + H_2O_{aq} \rightarrow Ar_{aq} + H^{+}_{aq} + OH_{aq} + e(H_2O)_{aq}$ $M = Ar(1s_1)_{aq}, Ar(1s_2)_{aq}, Ar(1s_3)_{aq}, Ar(1s_4)_{aq}$	1.29×10^{-34} cm^6/s	[1]
$M_{aq} + H_2O_{aq} + H_2O_{aq} \rightarrow Ar_{aq} + H^{+}_{aq} + OH(A^2\Sigma)_{aq} + e(H_2O)_{aq}$ $M = Ar(1s_1)_{aq}, Ar(1s_2)_{aq}, Ar(1s_3)_{aq}, Ar(1s_4)_{aq}$	1.29×10^{-34} cm^6/s	[1]
$M_{aq} + H_2O_{aq} + H_2O_{aq} \rightarrow Ar_{aq} + H_{aq} + OH^{+}_{aq} + e(H_2O)_{aq}$	7.51×10^{-34} cm^6/s	[1]

$M = Ar(1s_1)_{aq}, Ar(1s_2)_{aq}, Ar(1s_3)_{aq}, Ar(1s_4)_{aq}$		
$M_{aq} + H_2O_{aq} \rightarrow Ar_{aq} + H_{aq} + OH_{aq}$ $M = Ar(1s_1)_{aq}, Ar(1s_2)_{aq}, Ar(1s_3)_{aq}, Ar(1s_4)_{aq}$	1.25×10^{-10}	1
$Ar_2{}^*{}_{aq} + H_2O_{aq} + H_2O_{aq} \rightarrow H_2O^+{}_{aq} + Ar_{aq} + Ar_{aq} + e(H_2O)_{aq}$	$1.98 \times 10^{-32}\ cm^6/s$	1
$Ar_2{}^*{}_{aq} + H_2O_{aq} + H_2O_{aq} \rightarrow H^+{}_{aq} + OH_{aq} + Ar_{aq} + Ar_{aq} + e(H_2O)_{aq}$	$3.91 \times 10^{-34}\ cm^6/s$	1
$Ar_2{}^*{}_{aq} + H_2O_{aq} + H_2O_{aq} \rightarrow H^+{}_{aq} + OH(A^2\Sigma)_{aq} + Ar_{aq} + Ar_{aq} + e(H_2O)_{aq}$	$3.91 \times 10^{-34}\ cm^6/s$	1
$Ar_2{}^*{}_{aq} + H_2O_{aq} + H_2O_{aq} \rightarrow H^+{}_{aq} + OH^+{}_{aq} + Ar_{aq} + Ar_{aq} + e(H_2O)_{aq}$	$4.51 \times 10^{-33}\ cm^6/s$	1
$Ar_2{}^*{}_{aq} + H_2O_{aq} \rightarrow H_{aq} + OH_{aq} + Ar_{aq} + Ar_{aq}$	3.0×10^{-10}	1
$Ar^+{}_{aq} + H_2O_{aq} \rightarrow H_2O^+{}_{aq} + Ar_{aq}$	6.05×10^{-11}	1
$Ar^+{}_{aq} + H_2O_{aq} \rightarrow H_{aq} + OH^+{}_{aq} + Ar_{aq}$	2.86×10^{-10}	1
$Ar^+{}_{aq} + H_2O_{aq} \rightarrow H^+{}_{aq} + OH_{aq} + Ar_{aq}$	2.04×10^{-10}	1
$Ar^+{}_{aq} + H_2O_{aq} \rightarrow H^+{}_{aq} + OH(A^2\Sigma)_{aq} + Ar_{aq}$	5.0×10^{-13}	1
$Ar_2{}^+{}_{aq} + H_2O_{aq} \rightarrow Ar_{aq} + Ar_{aq} + H_2O^+{}_{aq}$	6.05×10^{-11}	1
$Ar_2{}^+{}_{aq} + H_2O_{aq} \rightarrow H_{aq} + OH^+{}_{aq} + Ar_{aq} + Ar_{aq}$	2.86×10^{-10}	1
$Ar_2{}^+{}_{aq} + H_2O_{aq} \rightarrow H^+{}_{aq} + OH_{aq} + Ar_{aq} + Ar_{aq}$	2.10×10^{-10}	1
$Ar_2{}^+{}_{aq} + H_2O_{aq} \rightarrow H_2{}^+{}_{aq} + O_{aq} + Ar_{aq} + Ar_{aq}$	2.10×10^{-10}	1
$Ar_2{}^+{}_{aq} + H_2O_{aq} \rightarrow H_{2aq} + O^+{}_{aq} + Ar_{aq} + Ar_{aq}$	2.10×10^{-10}	1
$M_{aq} + H_2O_{aq} \rightarrow H_{aq} + OH_{aq} + Ar_{aq}$ $M = Ar(1s_1)_{aq}, Ar(1s_2)_{aq}, Ar(1s_3)_{aq}, Ar(1s_4)_{aq}, Ar(4P)_{aq}, Ar(4D)_{aq}$	5.0×10^{-15}	1,3
$Ar_2{}^*{}_{aq} + H_2O_{aq} \rightarrow H_{aq} + OH_{aq} + Ar_{aq} + Ar_{aq}$	5.0×10^{-15}	1,3
$M_{aq} + O_{2aq} \rightarrow O(^1D)_{aq} + O_{aq} + Ar_{aq}$	5.0×10^{-15}	1,3

$M = Ar(1s_1)_{aq}, Ar(1s_2)_{aq}, Ar(1s_3)_{aq}, Ar(1s_4)_{aq}, Ar(4P)_{aq}, Ar(4D)_{aq}$		
$Ar^{*}_{2\,aq} + O_{2aq} \rightarrow O(^{1}D)_{aq} + O_{aq} + Ar_{aq} + Ar_{aq}$	5.0×10^{-15}	[1,3]
$M_{aq} + O_{3aq} \rightarrow O(^{1}D)_{aq} + O_{2aq} + Ar_{aq}$ $M = Ar(1s_1)_{aq}, Ar(1s_2)_{aq}, Ar(1s_3)_{aq}, Ar(1s_4)_{aq}, Ar(4P)_{aq}, Ar(4D)_{aq}$	5.0×10^{-15}	[1,3]
$Ar_2{}^{*}{}_{aq} + O_{3aq} \rightarrow O(^{1}D)_{aq} + O_{2aq} + Ar_{aq} + Ar_{aq}$	5.0×10^{-15}	[1,3]
$M_{aq} + H_2O_{2\,aq} \rightarrow OH_{aq} + OH_{aq} + Ar_{aq}$ $M = Ar(1s_1)_{aq}, Ar(1s_2)_{aq}, Ar(1s_3)_{aq}, Ar(1s_4)_{aq}, Ar(4P)_{aq}, Ar(4D)_{aq}$	5.0×10^{-15}	[1,3]
$Ar_2{}^{*}{}_{aq} + H_2O_{2aq} \rightarrow OH_{aq} + OH_{aq} + Ar_{aq} + Ar_{aq}$	5.0×10^{-15}	[1,3]

[1] Added from Lietz and Kushner [23].

[2] Rate changed from Lietz and Kushner [23].

[3] Rate is estimated.

[4] From NIST chemical kinetics database.

Table 6.3. Henry's law constants [25].

Species	Dimensionless Henry's law constant	Note
Ar, Ar(1s$_1$), Ar(1s$_2$), Ar(1s$_3$), Ar(1s$_4$), Ar(4P), Ar(4D), Ar_2^*	3.47×10^{-2}	1
H, H^*	6.48×10^{3}	1
H_2, H_2(r), H_2(v), H_2^*	1.80×10^{-2}	1
OH, OH($A^2\Sigma$)	6.20×10^{2}	1
HO_2	1.32×10^{5}	
H_2O_2	1.92×10^{6}	
H_2O(v)	1.00	2
O_2, O_2(v), O_2(r), $O_2(^1\Delta)$, $O_2(^1\Sigma)$	3.24×10^{-2}	1
O, $O(^1D)$	1.00	1
O_3, O_3^*	3.00×10^{-1}	1
N_2, N_2(r), N_2(v), $N_2(A^3\Sigma_u)$, $N_2(a'^1\Sigma)$, N, $N(^2D)$	1.60×10^{-2}	1
NO	4.40×10^{-2}	
NO_2	2.80×10^{-1}	
NO_3	4.15×10^{1}	
N_2O, N_2O(v)	5.99×10^{-1}	1
N_2O_3	6.00×10^{2}	
N_2O_4	3.69×10^{1}	
N_2O_5	4.85×10^{1}	
NH	1.47×10^{3}	3
HNO_2, HNO	1.15×10^{3}	1
HNO_3	4.80×10^{6}	
HNO_4	3.47×10^{6}	
CO, CO(v)	2.42×10^{-2}	1
CO_2, CO_2(v)	8.23×10^{-1}	1

He, He(2^3S), He(2^1S), He(2^3P), He(2^1P), He(3P), He(3S), He_2^*	9.42×10^{-3}	[1]
HCOOH, HCOO	1.25×10^{5}	[1]

[1] Value corresponds to the first species in the list, and other species listed were assumed to have the same Henry's law constant.

[2] Approximated. Species reacts quickly in water.

[3] Approximated by analogy to NH_3.

Table 6.4. Initial conditions for various $HCOO^-_{aq}$ concentrations.

Species	Mole Fraction at 0.5 mM	Mole fraction at 1 mM	Mole fraction at 2 mM	Mole fraction at 3.5 mM	Mole fraction at 5 mM	Mole fraction at 7.5 mM	Mole fraction at 10 mM
OH^-_{aq} (10^{-9})	2.00	2.00	2.00	2.00	2.00	2.00	2.00
$H_3O^+_{aq}$ (10^{-9})	2.00	2.00	2.00	2.00	2.00	2.00	2.00
$HCOO^-_{aq}$ (10^{-5})	0.903	1.81	3.61	6.32	9.02	13.5	18.0
Na^+_{aq} (10^{-5})	0.903	1.81	3.61	6.32	9.02	13.5	18.0
$HCOOH_{aq}$ (10^{-10})	0.954	1.86	3.56	5.88	7.96	11.0	13.8
$NaOH_{aq}$ (10^{-19})	1.77	3.63	7.60	14.1	21.3	34.5	49.2
O_{2aq} (10^{-6})	4.98	4.98	4.98	4.98	4.98	4.98	4.98
N_{2aq} (10^{-6})	9.13	9.13	9.13	9.13	9.13	9.13	9.13

Table 6.5. Flow rates and corresponding residence times.

Flow Rate (slm)	Residence Time (ms)	Note
0.75	13.5	Ref. [16]
1.0	10.0	Ref. [16]
1.25	9.2	[a]
1.5	8.3	Ref. [16]
1.75	7.4	[a]
2.0	6.4	Ref. [16]
2.5	5.7	[a]
3.0	4.9	Ref. [16]

[a] Residence time estimated by average.

Table 6.6. Powers for different gas mixtures.

Gas Mixture	Power (W)
He/H_2O = 99.8/0.2	14.3
He/O_2 = 99.8/0.2	14.2
He/Ar/H_2O = 82.8/17.0/0.2	13.4
He	13.6
He/Ar = 83/17	5.3
He/H_2 = 99.8/0.2	13.6

Table 6.7. Comparison between experimental measurements and model results for the base case.

	Measurements[4]	Model Results
Electron density[1]	$(8.0 \pm 1.4) \times 10^{10}$ cm^{-3}	1.8×10^{11} cm^{-3}
Electron temperature[1]	3.8 ± 0.4 eV	2.6 eV
OH density[2]	3×10^{14} cm^{-3}	1.5×10^{14} cm^{-3}
$HCOO^-_{aq}$ concentration[3]	0.76 (± 0.15) mM	0.79 mM

[1] Value for model at 5 ms.

[2] Value for model at 10.1 ms (as the power begins to ramp down).

[3] Value for model at end of simulation.

[4] Data taken from [16].

Table 6.8. Comparison between experimental measurements and model results for different droplet diameters.

Droplet Diameter (μm)	Measured $HCOO^-_{aq}$ concentration (mM)[1]	Modeled $HCOO^-_{aq}$ concentration (mM)
36	0.77 (± 0.29)	0.67
41	0.76 (± 0.15)	0.79
56	1.61 (± 0.11)	1.04

[1] Data taken from [15,16].

Table 6.9. Comparison between experiments and model for different gas mixtures.

Gas Mixture	Measured OH density (cm^{-3})[1]	Modeled OH density (cm^{-3})	Measured $HCOO^-_{aq}$ concentration (mM)[1]	Modeled $HCOO^-_{aq}$ concentration (mM)
He/H_2O = 99.8/0.2	3×10^{14}	1.5×10^{14}	0.76 (± 0.16)	0.79
He/O_2 = 99.8/0.2	--	2.4×10^{12}	0.80 (± 0.15)	0.79
$He/Ar/H_2O$ = 82.8/17.0/0.2	5×10^{14}	4.1×10^{14}	0.74 (± 0.10)	0.79

[1] Data taken from [16].

6.7 Figures

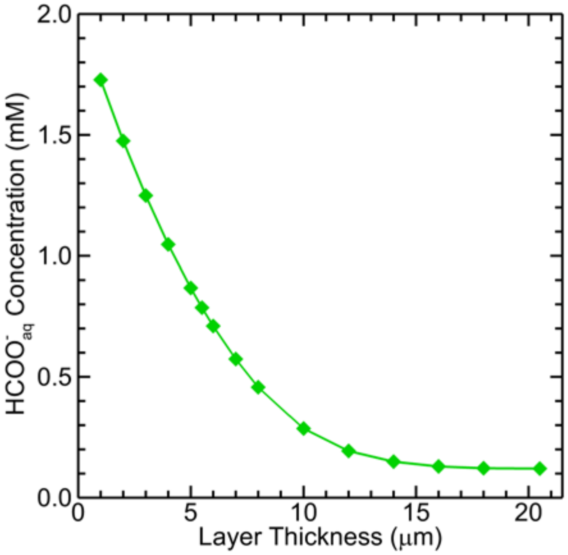

Figure 6.1. $HCOO^-_{aq}$ concentration at simulation end for varying droplet reactive layer thicknesses at 1 slm averaged over the droplet.

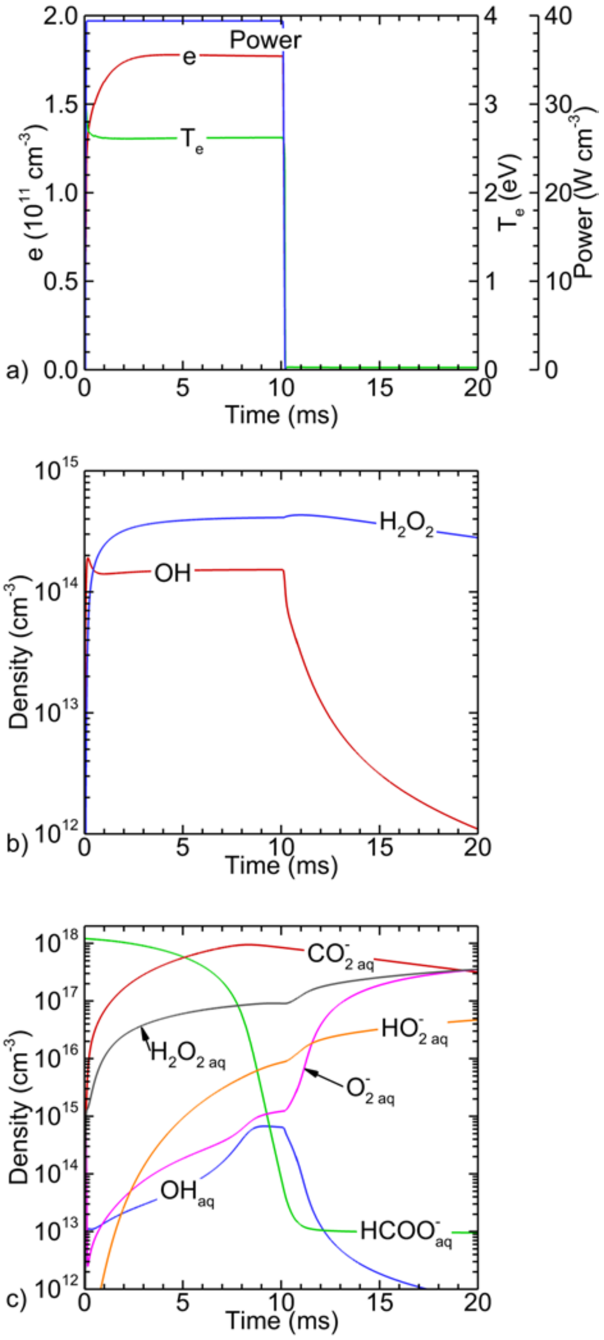

Figure 6.2. Base case results. (a) Plasma properties, (b) gas phase species densities, and (c) liquid phase species densities in the reactive layer of the droplet.

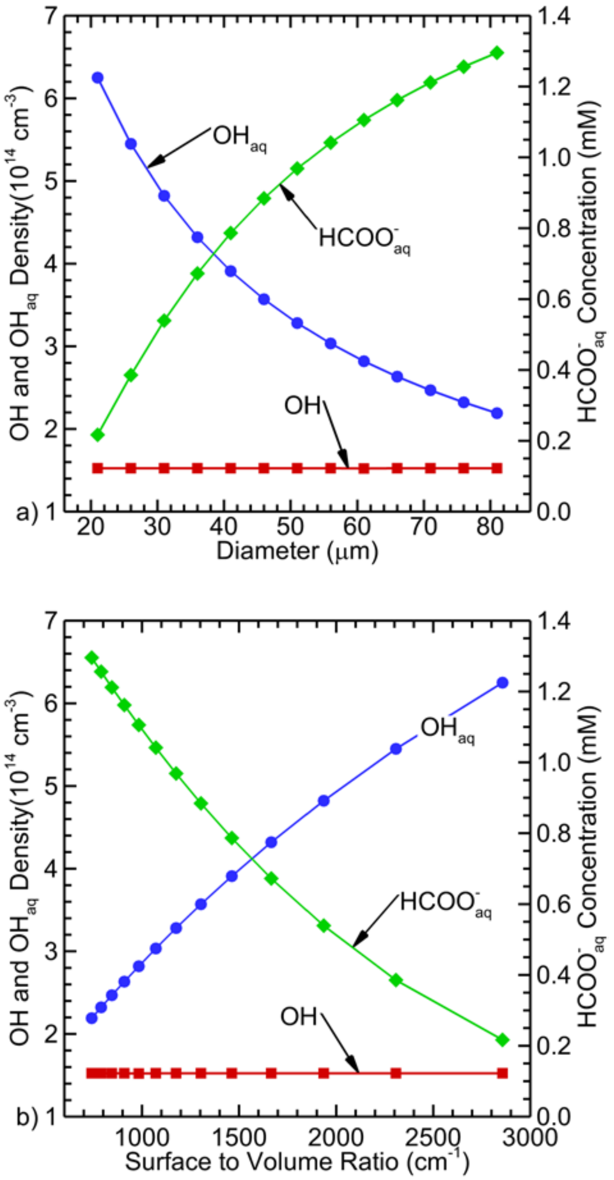

Figure 6.3. OH and OH$_{aq}$ densities as the power begins to ramp down (10.1 ms) and HCOO$^-_{aq}$ concentration at simulation end at 1 slm (a) versus droplet diameter and (b) versus SVR. Aqueous quantities averaged over the droplet.

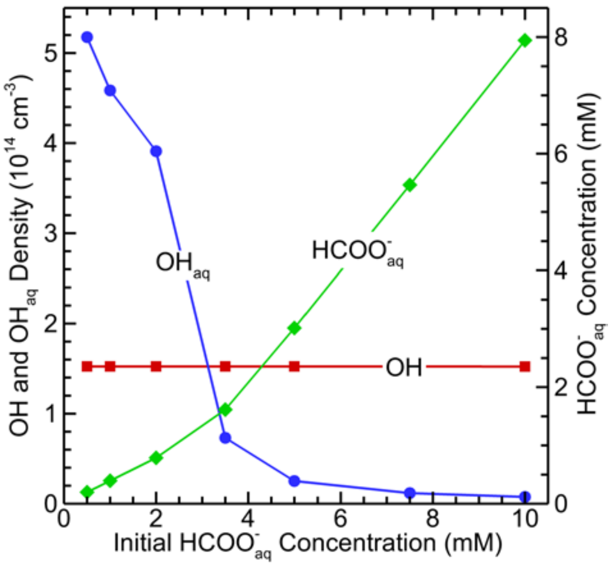

Figure 6.4. OH and OH_{aq} densities as the power begins to ramp down (10.1 ms) and $HCOO^-_{aq}$ concentration at simulation end for varying initial $HCOO^-_{aq}$ concentrations in the droplet at 1 slm. Aqueous quantities averaged over the droplet.

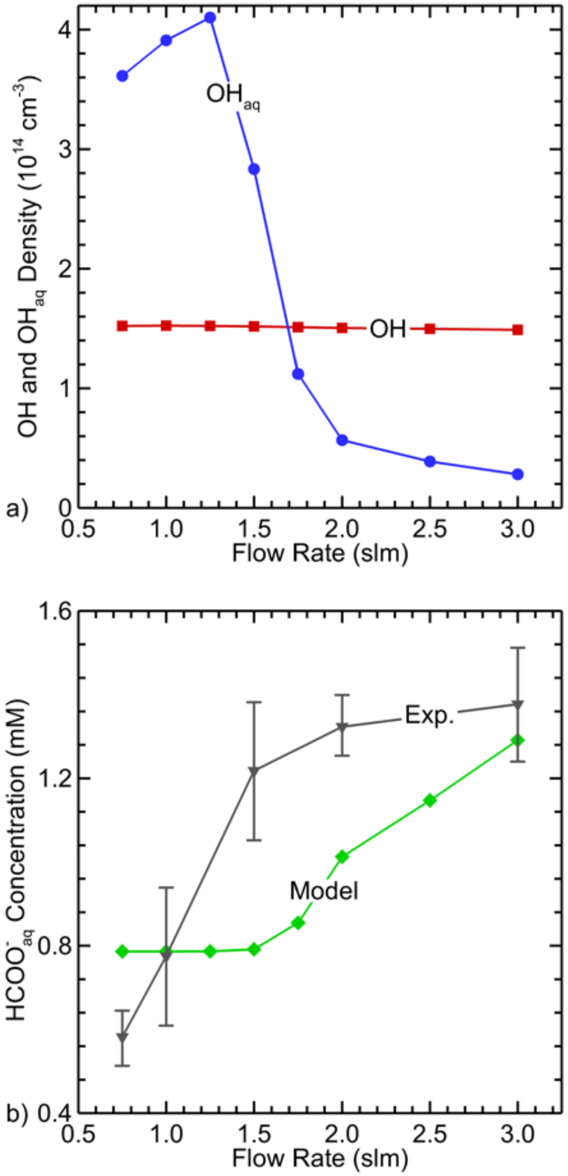

Figure 6.5. Variation in gas flow rates. (a) OH and OH$_{aq}$ densities as the power begins to ramp down and (b) HCOO$^-_{aq}$ concentration at simulation end compared to experimental measurements from Nayak et al. [16]. Aqueous quantities averaged over the droplet.

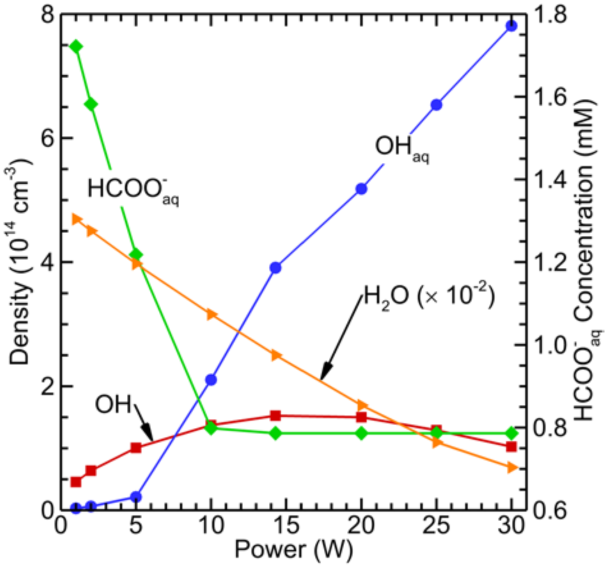

Figure 6.6. OH, H_2O, and OH_{aq} densities as the power begins to ramp down (10.1 ms) and $HCOO^-_{aq}$ concentration at simulation end for varying power deposited at 1 slm. Aqueous quantities averaged over the droplet.

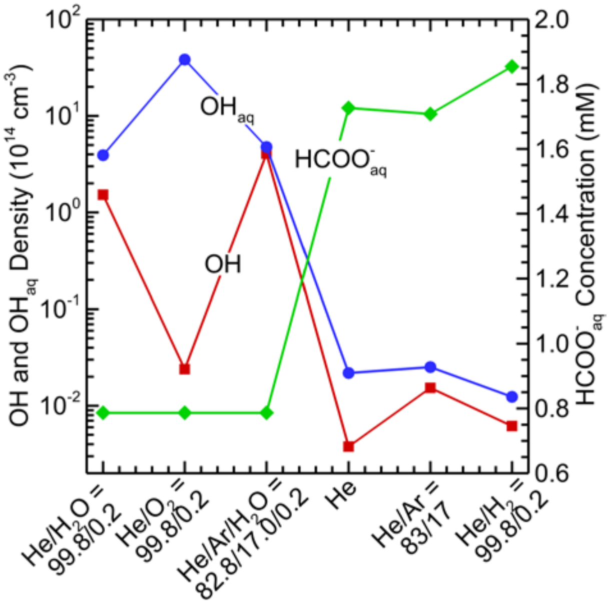

Figure 6.7. OH and OH_{aq} densities as the power begins to ramp down (10.1 ms) and $HCOO^-_{aq}$ concentration at simulation end for varying gas mixtures at 1 slm. Aqueous quantities averaged over the droplet.

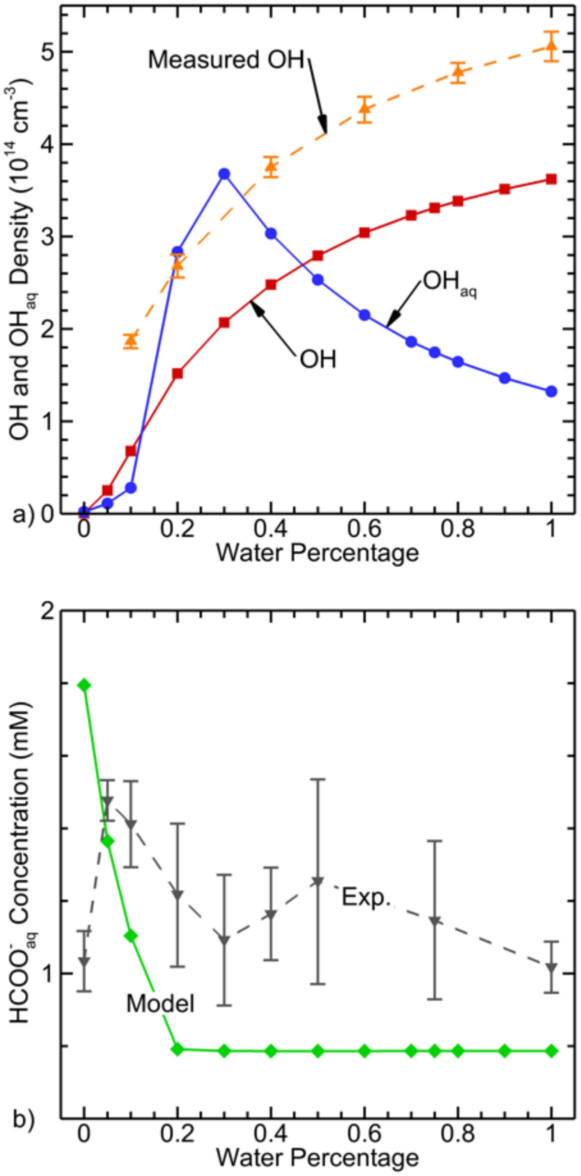

Figure 6.8. Variation with percentage of water in the inlet (He + X% H_2O). (a) OH and OH_{aq} densities as the power begins to ramp down (8.4 ms) at 1.5 slm compared to experimental measurements of OH from Oinuma et al. [15] and (b) $HCOO^-_{aq}$ concentration at simulation end at 1.5 slm compared to experimental measurements from Oinuma et al. [15]. Aqueous quantities averaged over the droplet.

6.8 References

[1] J. E. Foster, Phys. Plasmas **24,** 055501 (2017).

[2] P. J. Bruggeman, M. J. Kushner, B. R. Locke, J. G. E. Gardeniers, W. G. Graham, D. B. Graves, R. C. H. M. Hofman-Caris, D. Maric, J. P. Reid, E. Ceriani, D. Fernandez Rivas, J. E. Foster, S. C. Garrick, Y. Gorbanev, S. Hamaguchi, F. Iza, H. Jablonowski, E. Klimova, J. Kolb, F. Krcma, P. Lukes, Z. MacHala, I. Marinov, D. Mariotti, S. Mededovic Thagard, D. Minakata, E. C. Neyts, J. Pawlat, Z. L. Petrovic, R. Pflieger, S. Reuter, D. C. Schram, S. Schröter, M. Shiraiwa, B. Tarabová, P. A. Tsai, J. R. R. Verlet, T. Von Woedtke, K. R. Wilson, K. Yasui and G. Zvereva, Plasma Sources Sci. Technol. **25,** 053002 (2016).

[3] T. Von Woedtke, D. Weltmann, S. Emmert, H. Metelmann, S. Rupf and K.-D. Weltmann, Phys. Plasmas **27,** 070601 (2020).

[4] A. Stancampiano, T. Gallingani, M. Gherardi, Z. Machala, P. Maguire, V. Colombo, J. Pouvesle and E. Robert, Appl. Sci. **9,** 3861 (2019).

[5] M. E. Hassan, M. Janda and Z. Machala, Water **13,** 182 (2021).

[6] Z. Liu, S. Wang, B. Pang, H. Zhang, Y. Gao, D. Xu and M. G. Kong, J. Phys. D. Appl. Phys. **54,** 215203 (2021).

[7] R. K. Singh, E. Brown, S. Mededovic Thagard and T. M. Holsen, J. Hazard. Mater. **408,** 124452 (2021).

[8] J. Jose and L. Philip, J. Environ. Manage. **286,** 112202 (2021).

[9] S. Jaiswal and E. M. Aguirre, AIP Adv. **11,** 045311 (2021).

[10] E. Casado, M. C. Garcia, D. A. Krawczyk, F. J. Romero-Salguero and A. Rodero, Plasma Process. Polym. **17,** 2000030 (2020).

[11] I. Sremački, G. Bruno, H. Jablonowski, C. Leys, A. Nikiforov and K. Wende, Plasma

Sources Sci. Technol. **30,** 095018 (2021).

[12] T. Xia, A. Kleinheksel, E. M. Lee, Z. Qiao, K. R. Wigginton and H. L. Clack, J. Phys. D. Appl. Phys. **52,** 255201 (2019).

[13] G. Nayak, M. S. Simeni, J. Rosato, N. Sadeghi and P. J. Bruggeman, J. Appl. Phys. **128,** 243302 (2020).

[14] G. Nayak, N. Sadeghi and P. J. Bruggeman, Plasma Sources Sci. Technol. **28,** 125006 (2019).

[15] G. Oinuma, G. Nayak, Y. Du and P. J. Bruggeman, Plasma Sci. Technol. **29,** 095002 (2020).

[16] G. Nayak, G. Oinuma, Y. Yue, J. S. Sousa and P. J. Bruggeman, Plasma Sources Sci. Technol. **30,** 115003 (2021).

[17] W. Van Gaens and A. Bogaerts, J. Phys. D. Appl. Phys. **46,** 275201 (2014).

[18] S. Norberg, "Modeling Atmospheric Pressure Plasma Jets: Plasma Dynamics, Interaction with Dielectric Surfaces, Liquid Layers and Cells," Ph.D. Thesis (University of Michigan, 2015).

[19] F. Emmert, H. H. Angermann, R. Dux and H. Langhoff, J. Phys. D. Appl. Phys. **21,** 667 (1988).

[20] A. M. Lietz, E. V Barnat, J. E. Foster and M. J. Kushner, J. Appl. Phys. **128,** 083301 (2020).

[21] P. Tian and M. J. Kushner, Plasma Sources Sci. Technol. **24,** 34017 (2015).

[22] W. Tian and M. J. Kushner, J. Phys. D. Appl. Phys. **47,** 165201 (2014).

[23] A. M. Lietz and M. J. Kushner, J. Phys. D. Appl. Phys. **49,** 425204 (2016).

[24] W. Tian, K. Tachibana and M. J. Kushner, J. Phys. D. Appl. Phys. **47,** 055202 (2014).

[25] R. Sander, Atmos. Chem. Phys. **15,** 4399 (2015).

[26] G. Imoberdorf and M. Mohseni, Chem. Eng. Sci. **66,** 1159 (2011).

[27] Y. Zheng, L. Wang and P. Bruggeman, J. Vac. Sci. Technol. A **38,** 063005 (2020).

[28] T. Løgager and K. Sehested, J. Phys. Chem. **97,** 10047 (1993).

Chapter 7 Ozone Destruction in Dielectric Barrier Discharges

Atmospheric pressure plasmas formed in pulsed dielectric barrier discharges can be used to synthesize O_3 for use in water purification. The addition of N_2 into an otherwise pure O_2 feed gas has been shown to increase the O_3 production. A working hypothesis for that observation is that N atoms produced by electron-impact dissociation of N_2 occupies surface sites on the bounding dielectrics that otherwise result in O_3 destruction. A pulsed dielectric barrier discharge used for O_3 formation was examined using both *nonPDPSIM* and *GlobalKin* to investigate the consequences of N_2 addition to ozone generators. The results from *nonPDPSIM* show the spatially resolved electron density, as well as O and O_3 density, over one pulse in pure O_2. In *GlobalKin*, one such surface reaction mechanism is implemented to explain the increase in O_3 production. At nonzero N_2 percentages, the surface mostly consists of adsorbed nitrogen atoms, N_s, leading to an increase in O_3 concentration with N_2 addition compared to pure O_2.

7.1 Introduction

Atmospheric pressure plasmas formed in dielectric barrier discharges (DBDs) containing O_2 are used to produce ozone, O_3, for industrial applications. O_3, as an oxidizing agent, can be used to purify water and preserve and decontaminate food [1–4].

O_3 concentrations in a DBD often decrease after several hours of use, in some cases stopping production entirely [5–8]. This phenomenon has been termed the ozone zero phenomenon (OZP). The addition of N_2 to the feed gas suppresses the OZP and increases the concentration of O_3 in the reactor [9,10]. This effect of N_2 addition persists even after the flow of N_2 into the discharge chamber ceases and after many gas residence times, indicating the process by which N_2 increases O_3 concentration occurs on the surface and is not a volumetric process [10,11].

One hypothesis for this surface process is that O_3 is reduced to O_2 on the reactor walls [11,12]. By adding N_2, surface sites that would be otherwise used for O_3 destruction are instead occupied by adsorbed nitrogen atoms, N_s. (The subscript ‘s’ denotes an adsorbed species.) However, the mechanism on the surface for O_3 destruction and N adsorption is not presently known.

The production of O_3 in a pulsed atmospheric pressure DBD was examined using two different models. The results of *nonPDPSIM* show the propagation of the streamer (filament of plasma) over one pulse, as well as the spatially-resolved densities of O and O_3 after the pulse. These results also show the local variation in O and O_3 densities with surface roughness. A surface reaction mechanism was developed and implemented in *GlobalKin* that describes the effect of N_2 addition on O_3 density. Results over many pulses show that O_3 density is maximized at 0.05% N_2 in O_2 and that increasing surface roughness increases O_3 density for a given admixture of N_2.

This chapter is organized as follows. The conditions and geometry modeled in this chapter are described in Section 7.2. The results of *nonPDPSIM* are discussed in Sections 7.3 and 7.4. The discharge in pure O_2 as modeled by *GlobalKin* is analyzed in Section 7.5, and the effects of N_2 addition and surface roughness are discussed in Sections 7.6 and 7.7, respectively. Concluding remarks are given in Section 7.8.

7.2 Geometry and Conditions

The geometry and conditions for *nonPDPSIM* and *GlobalKin* are described in this section. *nonPDPSIM* and *GlobalKin* are described in detail in Sections 2.2 and 2.3, respectively.

7.2.1 *nonPDPSIM*

The DBD modeled in *nonPDPSIM* is shown in Figure 7.1. The plasma was in contact with the grounded electrode on the bottom and the dielectric on the top. The gap the plasma was formed in is 300 µm. The dielectric was 1 mm thick, and the depth of the reactor was 1 cm. A symmetric boundary condition was applied to the left boundary. This geometry was a subset of the reactor being modeled, as the plasma gap extended for 4.4 cm instead of 1.6 cm. The mesh consisted of 10,312 nodes total and 6,899 plasma nodes. The electron Monte Carlo module was used, with meshes extending from 30 µm into the plasma from the top and bottom electrodes.

The voltage pulse applied to the powered electrode was -5 kV. The pulse was 80 ns in length, with an additional 0.5 ns rise and fall times. 150 ns in total was modeled, capturing the pulse and the immediate afterglow.

The DBD operated at atmospheric pressure in pure O_2. The species included in the reaction mechanism are listed in Table 7.1, including O_2, O, and O_3, their ions, and various excited states. The reaction mechanism was based on Van Gaens and Bogaerts [13]. Updates were made to include higher order excited states of O [14–20]. The reaction mechanism included 209 reactions. Photo-emission and photoionization reactions were included:

$$\mathrm{O}\left({}^{3}\mathrm{S}\right) \rightarrow \mathrm{O} + h\nu \left(k = 3.4 \times 10^{8}\,\mathrm{s}^{-1}\right) \tag{7.1}$$

$$\mathrm{O}_2 + h\nu \rightarrow \mathrm{O}_2 \;(\sigma = 10^{-21}\mathrm{cm}^2). \tag{7.2}$$

7.2.2 *GlobalKin*

The full plasma volume is analyzed in *GlobalKin*, measuring 4.4 cm × 4.4 cm × 300 µm. *GlobalKin* has the ability to model multiple pulses, as described in Section 2.3. The pulses had a peak power of 20 W (35 W/cm^3). The pulse length was 80 ns, with an additional 5 ns rise and fall, at a 10 kHz pulse repetition rate. 200 ms, or 2000 pulses, were modeled in total. The flow rate of the feed gas was 2 slm. The feed gas was O_2 with varying admixtures of N_2, ranging from 0% to 5%.

With the addition of N_2, additional species were required in *GlobalKin* when compared with *nonPDPSIM*. The species included in *GlobalKin* are listed in Table 7.2. Ions and excited states of O_2, N_2, O, O_3, and N are included, as well as N_xO_y species. The reaction mechanism for oxygen species is the same as in *nonPDPSIM*, and the reaction mechanism for nitrogen-containing species is based on Van Gaens and Bogaerts [13]. The reaction mechanism included 685 reactions. The photo-emission and photoionization reactions from *nonPDPSIM* were included.

GlobalKin has a surface kinetics module (SKM), as described in Section 2.3.2. The SKM is called every 50 ns and integrated for 50 ms. The surface site density varied from the base case of 10^{15} cm^{-2} to 3×10^{15} cm^{-2} to analyze the effect of surface roughness on O_3 production. The surface in contact with the plasma was assumed to be a dielectric (Pyrex).

The surface reaction mechanism was developed for this application and is shown in Table 7.3. The surface reaction mechanism included the manner of O_3 destruction proposed by Li et al. [12], given by

$$O_3 + W_s \rightarrow O_s + O_2 \tag{7.3}$$

$$O_3 + O_s \rightarrow O_{2s} + O_2, \tag{7.4}$$

where W_s is an unoccupied surface site. The adsorption and desorption of O_2 was included, as well as the adsorption and recombination of O and N. Reactions with N_s include NO formation and NO_x reactions. Reaction probabilities were largely estimated so O_3 was maximized at a nonzero N_2 percentage.

7.3 Streamer Propagation and Spatially-Resolved O and O_3 Densities

The electron density and T_e are shown in Figure 7.2 at various times throughout the duration of the pulse. The electrons were initialized near the dielectric at the top of the discharge gap. As the voltage rises, an ionization wave is formed, propagating away from the powered electrode and towards the grounded electrode. The ionization wave increases the electron density due to electron-impact ionization collisions. T_e increases during propagation of the ionization wave, increasing to over 7 eV during the first 0.5 ns. Once the ionization wave reaches the grounded electrode, another ionization wave, called a restrike, is launched towards the powered electrode. The electron density during the restrike is shown at 0.6 ns – 5 ns in Figure 7.2. T_e is maximized above of the maximum in electron density, enabling propagation of the restrike. After the restrike reaches the grounded electrode, the electron density decreases through the middle of the pulse (30 ns in Figure 7.2). Since the source of electrons decreases as T_e decreases, attachment and recombination become the dominant loss mechanisms for electrons. Shortly after the voltage reaches zero (82 ns in Figure 7.2), another ionization wave is launched from the top dielectric towards the grounded electrode, leading to an increase in electron density. T_e is maximized below the maximum in electron density. The electron density and T_e decrease after the ionization wave reaches the grounded electrode (87 ns and 90 ns in Figure 7.2) as the power deposition goes to zero.

The densities of O and O_3 after 150 ns are shown in Figure 7.3. The primary formation mechanism of O is electron-impact dissociation of O_2 in the feed gas. Therefore, O is found primarily where the electron density is maximized over the pulse. O_3 is formed through $O + O_2 + M \rightarrow O_3 + M$, where M is a third body (primarily O_2 in this pure O_2 discharge). Since O_3 requires

O to form, and the density of O is maximized where the electron density is maximized, O_3 is also maximized where the electron density is maximized over the pulse.

7.4 Spatially-Resolved O and O_3 Production with Rough Surfaces

The roughness of the top dielectric surface is varied in *nonPDPSIM*. The resulting electron density at 5 ns into the pulse is shown in Figure 7.4. Overall, the electron density is similar between the varying roughness considered. However, locally, the electron density is increased near the features. This increase is due to the electric field enhancement near rough features leading to more electron-impact ionizations. This increase in electron density can lead to an increase in O and O_3 density, as shown in Figure 7.5 at 150 ns. While the overall spread of O and O_3 is similar, maxima in O and O_3 are seen near the rough features. These maxima correspond to the electron density maxima over the pulse.

The total inventories of O and O_3 increase slightly with surface roughness, as shown in Table 7.4. The largest increase in O inventory is seen for pattern 1, with an increase in O of 2.9×10^{10} atoms when compared to the flat surface. Similarly, the largest increase in O_3 inventory is seen for pattern 1 (9×10^8 molecules compared to the flat surface). The O_3 production efficiency is of interest and is also shown in Table 7.4. The O_3 production efficiency η is calculated by

$$\eta = \frac{[O]+[O_3]}{E}, \tag{7.5}$$

where [O] is the inventory of O, $[O_3]$ is the inventory of O_3, and E is the energy deposited. η is the highest for pattern 1, followed by the flat surface and pattern 2. Pattern 2 has the lowest η due to the higher energy deposited. However, the variation from the flat surface is less than 10%, indicating that surface roughness does not significantly increase η.

7.5 Reactive Species Densities and Surface Coverages over Many Pulses

The results from *GlobalKin* track the volume-averaged plasma properties and species densities over 2000 pulses, while implementing the proposed surface reaction mechanism shown in Table 7.3. In this section, the plasma formed in pure O_2 is examined.

The plasma properties over the last pulse are shown in Figure 7.6. During the rise of the power pulse, T_e peaks, igniting the plasma and initiating the electron avalanche. As the electron density increases, T_e decreases. The electron density and T_e reach their steady state values of 9×10^8 cm^{-3} and 3.2 eV shortly after the power reaches its constant value of 20 W (35 W cm^{-3}). As the power decreases at the end of the pulse, the electron density and T_e also decrease.

The O and O_3 densities over the last pulse are shown in Figure 7.7. The O density is low (1.3×10^9 cm^{-3}) before the power ramps up. The O density increases continually through the rise of the pulse and through the plateau of the pulse. O is formed primarily through electron-impact dissociation of O_2, and the electron density is high during the pulse. The O density reaches a maximum of 5.2×10^{12} cm^{-3} as the power begins to decrease. As the power decreases, the O density slowly begins decreasing. This decrease occurs because the electron density decreases and consumption of O becomes dominant. The O_3 density remains relatively constant over the pulse. The O_3 density slightly increases as the O density decreases, indicating that O is reacting to form O_3. However, it then slightly decreases as O_3 is lost to the surface.

The occupancy of the surface sites over time is shown in Figure 7.8. Initially, the surface is empty wall sites (W_s). After less than 1 s, the surface is primarily composed of W_s and adsorbed O_{2s}. Note that since the surface sites are integrated for 50 ms while being called every 50 ns, the first pulse is not complete until 100 s. While O_{2s} does not react on the surface (see the surface mechanism in Table 7.3), it does occupy W_s that are required for destruction of O_3. Adsorbed O_s

initially increases to occupy more than 0.1 of surface sites. However, after 10^4 s (100 pulses), O_s decreases to occupy only 0.01 of surface sites, corresponding to an increase in O_{2s} and W_s and a decrease in O_3.

7.6 Effect of N_2 Admixture on O_3 Production

The addition of N_2 has been shown to increase the O_3 concentration. The hypothesis is that N_s occupies empty wall sites W_s that are required for O_3 destruction on the walls. Despite the formation of NO_x species, the reduction of the loss of O_3 on the walls increases the O_3 concentration. To model this process in *GlobalKin*, N_2 was added to the otherwise pure O_2 discharge in admixtures ranging from 0% - 5%.

The surface coverages at the end of the simulation are shown in Figure 7.9 for varying admixtures of N_2. As the admixture of N_2 increases from 0% to 0.05%, O_s decreases from 0.012 of surface sites to less than 0.010 of surface sites. The largest decrease, however, is seen in the O_{2s} and W_s fractional occupancies. At 0% N_2, O_{2s} and W_s each occupied nearly half of the surface sites; at 0.05% N_2, O_{2s} and W_s occupy less than 0.15 of the surface sites. This decrease occurs because N_s occupies over 0.7 of surface sites at 0.05% N_2 despite occupying no surface sites at 0% N_2. The occupancy of N_s is high as the loss mechanisms of N_s (recombination with N to form N_2, reduction of NO_x species) are low.

As the admixture of N_2 increases beyond 0.05% N_2, the occupancy of N_s decreases because the loss mechanisms of N_s increase. These loss mechanisms depend on the flux of N and NO_x to the surface, which in turn depends on their abundance in the gas phase. As discussed in the following paragraph, N, NO, and NO_2 densities increase as the admixture of N_2 increases. As N_s decreases with increasing admixture of N_2, O_{2s} and W_s make up the sites not occupied by N_s. O_s decreases slightly as the admixture of N_2 increases beyond 0.05% N_2.

The reactive species densities at the end of the simulation are shown in Figure 7.10 for varying admixtures of N_2. The O and O_3 densities increase from 0% N_2 to 0.05% N_2. The loss of O_3 on the surface decreases because N_s occupies the otherwise empty W_s that are required for O_3 destruction. Beyond 0.05% N_2, the O and O_3 densities decrease as O (a precursor to O_3) is consumed in reactions forming NO_x species. N increases linearly with N_2 percentage, as N is formed by electron-impact dissociation of N_2. NO increases very rapidly from 0% N_2 to 0.05% N_2 as NO requires O and N to form. NO_2 increases rapidly below 0.5% N_2 as NO_2 requires NO to form. NO_2 continues increasing after 0.5% N_2 but is consumed in reactions forming higher order N_xO_y species.

7.7 Effect of Surface Roughness on O_3 Production

The variation of O_3 density with surface roughness density was modeled in *GlobalKin*. The area in contact with the plasma was kept the same, but the surface site density was increased from 10^{15} to 3×10^{15} cm^{-2}.

The fractional occupancy of N_s is shown in Figure 7.11 for varying surface site densities. The fractional occupancy of N_s increases as surface site density increases. This corresponds to a decrease in O_{2s} and W_s. At all surface site densities, N_s is maximized for 0.05% N_2 and minimized for 5% N_2.

The O_3 density is shown in Figure 7.12. Since N_s occupies W_s that are otherwise available for O_3 destruction on the surface, O_3 follows the same trends as N_s, increasing as surface site density increases. At all surface site densities, O_3 is maximized for 0.05% N_2 and decreases to 5% N_2. When pure O_2 (0% N_2) is used, the O_3 density is the lowest at each given surface site density. The O_3 density does not vary with surface site density at 0% N_2. The O_3 reaching the surface is destroyed at the lowest surface site density, and adding more surface sites does not affect the O_3 destruction.

7.8 Concluding Remarks

The production of O_3 in an atmospheric pressure DBD was examined using *nonPDPSIM* and *GlobalKin*. The results of *nonPDPSIM* showed the propagation of the streamer, as well as that O and O_3 were maximized near where the electrons exhibited maxima. The results of *nonPDPSIM* also showed that surface roughness does not play a large factor in increasing O_3 production efficiency. The surface mechanism implemented in *GlobalKin* showed that without any N_2 in the discharge, the surface is mostly O_{2s} and W_s. When N_2 was added to the discharge, the surface was mostly occupied by N_s. Since O_3 destruction in the surface mechanism requires W_s, the addition of N_2 increased the O_3 density. Increasing the surface roughness increased N_s occupancy and O_3 density. However, increasing the surface roughness did not change the O_3 density when there was not any N_2 in the discharge, indicating the O_3 that reached the surface was sufficiently destroyed at the lowest surface site density.

The surface reaction mechanism proposed here is one possibility of many potential surface reaction mechanisms. The surface reaction mechanism was developed for a generic surface, with a few reaction probabilities obtained for Pyrex glass. However, the surface reaction mechanism will change depending on the surface in question, as different materials were shown to have different characteristic timescales for the OZP [9,11]. Surface reaction probabilities may be very different on metals, where oxidation can change the composition of the surface and catalytic effects may become important. However, the surface reaction mechanism in this chapter shows that the effect of N adsorption can indeed increase the O_3 production by occupying surface sites that could otherwise destroy O_3.

7.9 Tables

Table 7.1. Species included in *nonPDPSIM*.

Charged Species	e, O_2^+, O_2^-, O_4^+, O^+, O^-, O_3^-
Neutral Species	O_2, O, O_3
Excited States	O_2(r), O_2(v), $O_2(^1\Delta_g)$, $O_2(^1\Sigma_u)$, $O(^1D)$, $O(^1S)$, $O(^5S)$, $O(^3S)$, $O(^5P)$, O_3^*

Table 7.2. Species included in *GlobalKin*.

Charged Species	e, O_2^+, O_2^-, O_4^+, O^+, O^-, O_3^-, N_2^+, N_3^+, N_4^+, N^+, NO^+, NO_2^+, NO_2^-, NO_3^-, $NO^+(O_2)$
Neutral Species	O_2, O, O_3, N_2, N, NO, NO_2, NO_3, N_2O, N_2O_3, N_2O_4, N_2O_5
Excited states	O_2(r), O_2(v), $O_2(^1\Delta_g)$, $O_2(^1\Sigma_u)$, $O(^1D)$, $O(^1S)$, $O(^5S)$, $O(^3S)$, $O(^5P)$, O_3^*, N_2(r), N_2(v), $N_2(A^3\Sigma_u)$, $N_2(a'^1\Sigma)$, $N(^2D)$, N_2O(v)

Table 7.3. Surface reaction mechanism implemented in *GlobalKin*.

Surface Reaction	Probability	Reference
$O_3 + W_s \rightarrow O_s + O_2$	0.99	[a]
$O_3 + O_s \rightarrow O_{2s} + O_2$	0.01	[a]
$O + W_s \rightarrow O_s$	0.999	[a]
$O + O_s \rightarrow W_s + O_2$	0.001	[a]
$O_s + O_s \rightarrow W_s + O_2$	1.2×10^{-13} cm^2 s^{-1}	[21]
$O_2 + W_s \rightarrow O_{2s}$	0.01	[a]
$O_2 + O_{2s} \rightarrow W_s + O_2 + O_2$	0.01	[a]
$O_2 + O_s \rightarrow W_s + O_3$	0.0001	[a]
$N + W_s \rightarrow N_s$	0.25	[a]
$N + N_s \rightarrow W_s + N_2$	0.25	[a]
$NO + O_s \rightarrow W_s + NO_2$	10^{-8}	[22]
$O + N_s \rightarrow W_s + NO$	0.25	[a]
$N + O_s \rightarrow W_s + NO$	0.25	[a]
$NO + N_s \rightarrow O_s + N_2$	0.99999	[a]
$NO_2 + N_s \rightarrow O_{2s} + N_2$	0.333	[a]
$NO_2 + N_s \rightarrow W_s + NO + NO$	0.333	[a]
$NO_2 + N_s \rightarrow O_s + N_2O$	0.333	[a]
$NO_3 + N_s \rightarrow W_s + NO + NO_2$	0.999	[a]

[a] Estimated to ensure O_3 maximum at nonzero N_2 admixture.

Table 7.4. Ozone production efficiency for varying surface roughness.

	O Inventory at 150 ns (atoms)	O_3 Inventory at 150 ns (molecules)	Energy deposited in 150 ns (J)	Ozone Production Efficiency (molecules/eV)
Flat	8.53×10^{11}	3.13×10^{10}	8.29×10^{-6}	1.71×10^{-2}
Pattern 1	8.82×10^{11}	3.22×10^{10}	7.91×10^{-6}	1.85×10^{-2}
Pattern 2	8.71×10^{11}	3.20×10^{10}	8.65×10^{-6}	1.67×10^{-2}

7.10 Figures

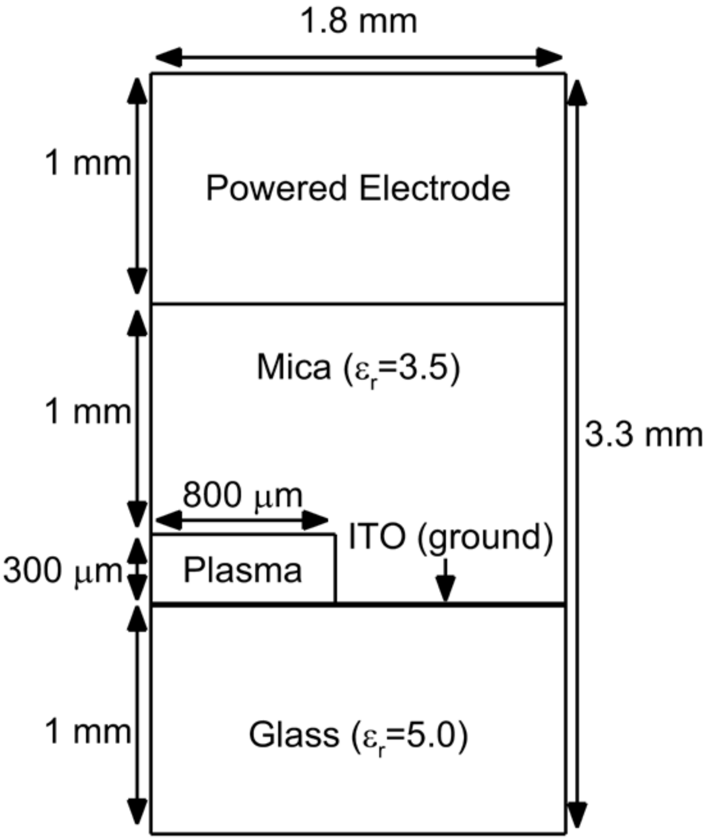

Figure 7.1. Geometry modeled in *nonPDPSIM*.

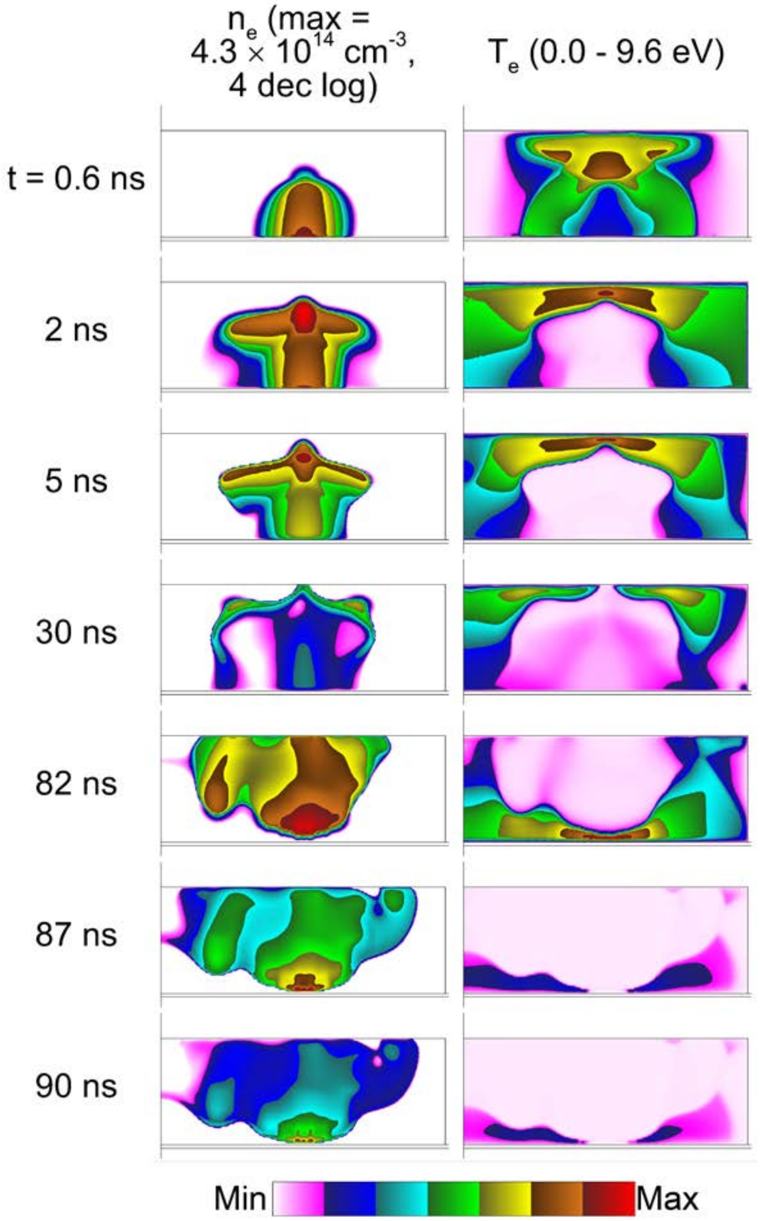

Figure 7.2. Electron density and T_e throughout the pulse.

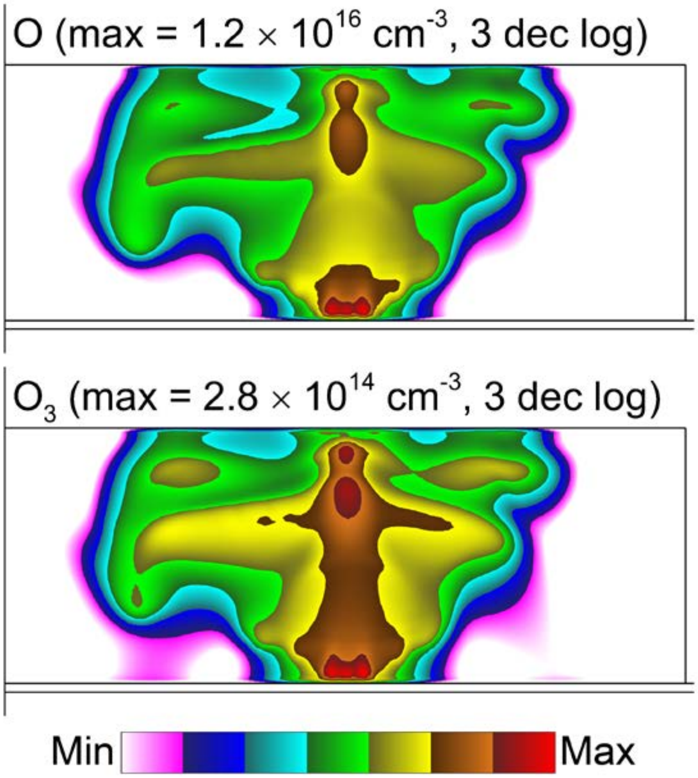

Figure 7.3. O and O_3 densities at 150 ns.

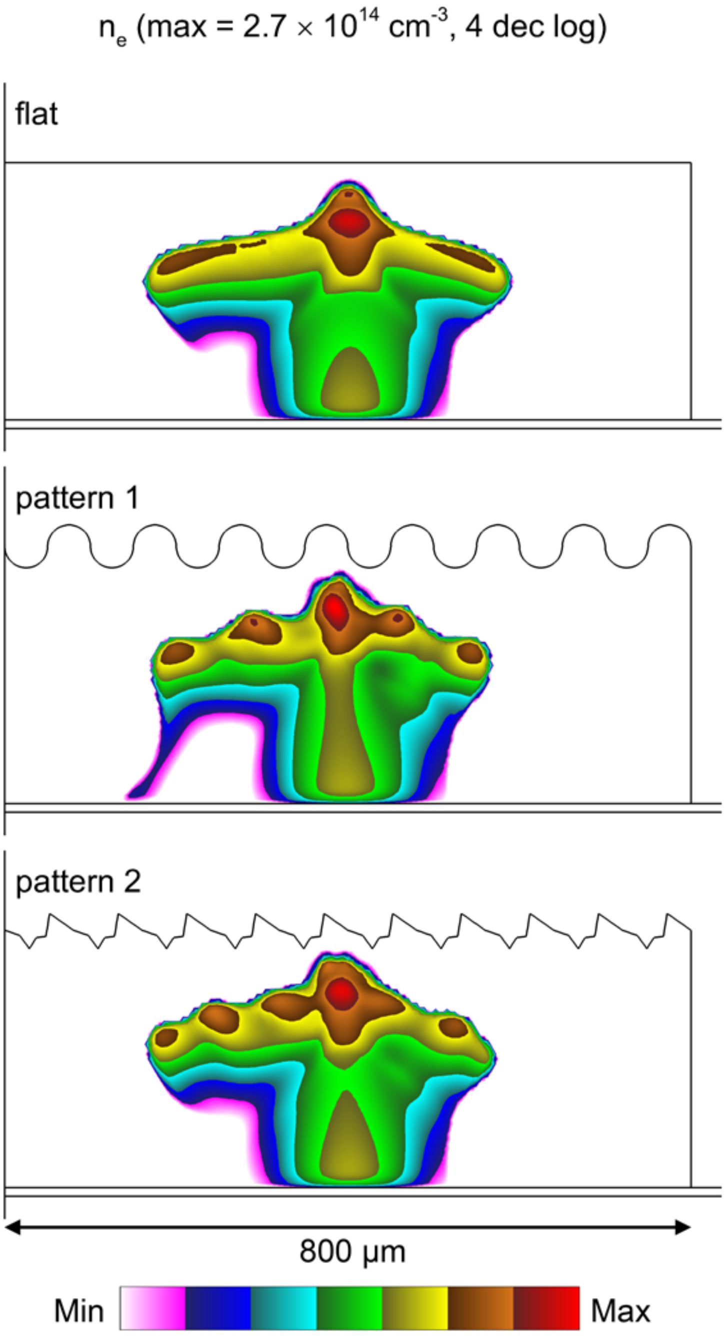

Figure 7.4. Electron density at 5 ns for varying surface roughness.

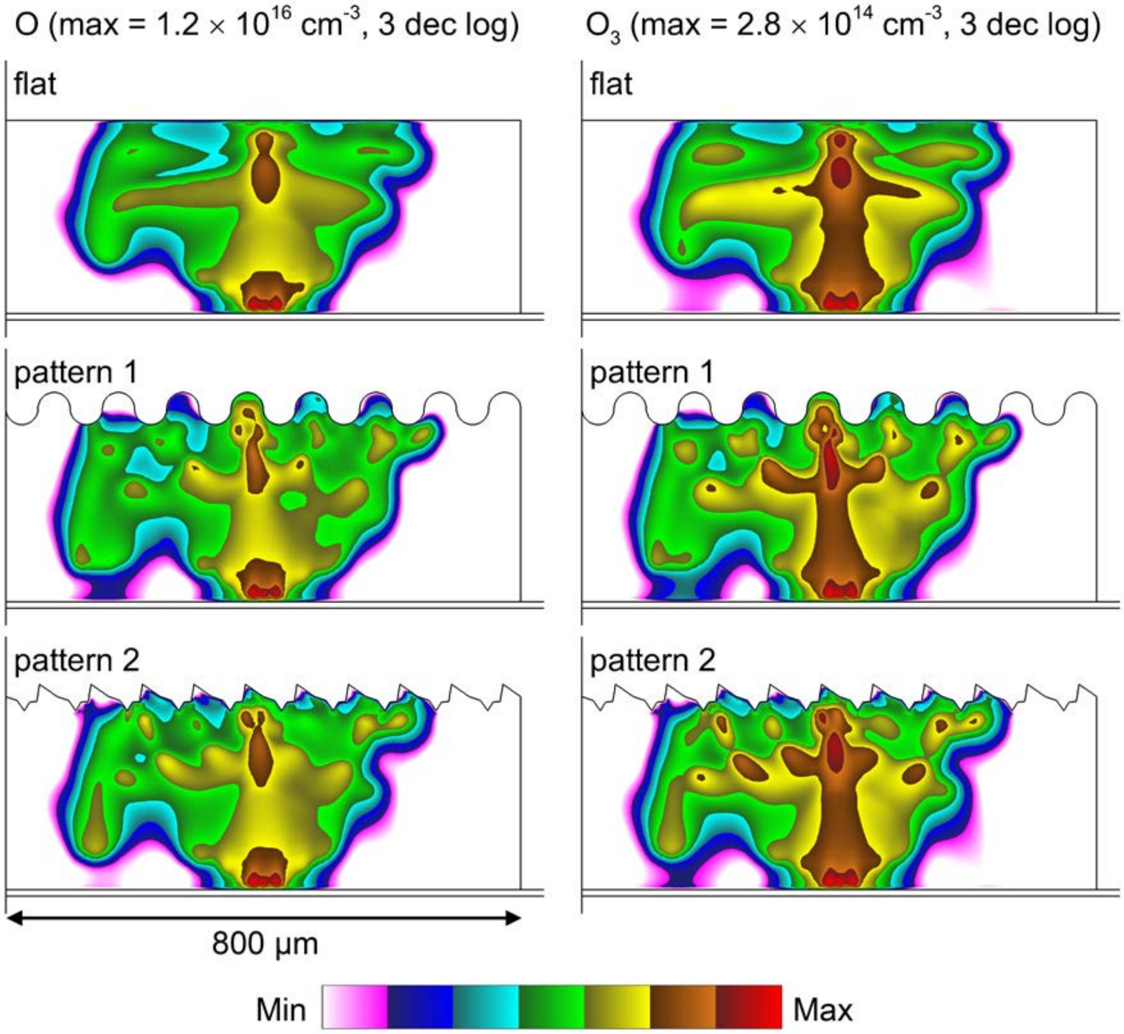

Figure 7.5. O and O_3 densities at 150 ns for varying surface roughness.

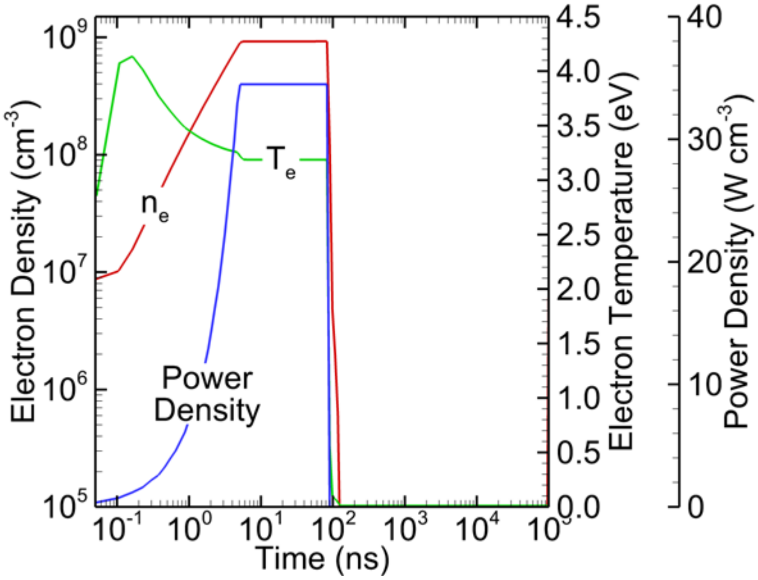

Figure 7.6. Plasma properties over the last pulse in *GlobalKin*.

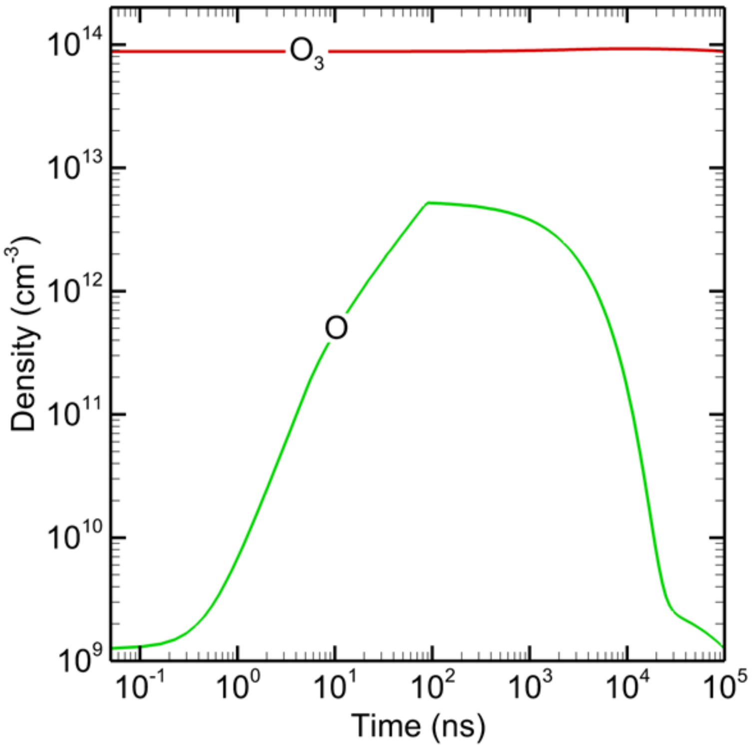

Figure 7.7. O and O_3 densities over the last pulse in *GlobalKin*.

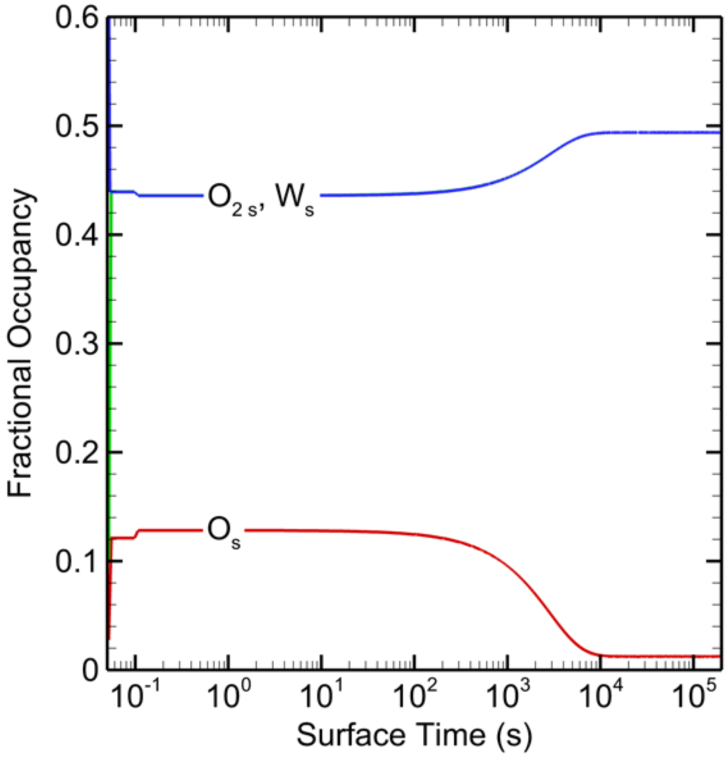

Figure 7.8. Surface coverage over time.

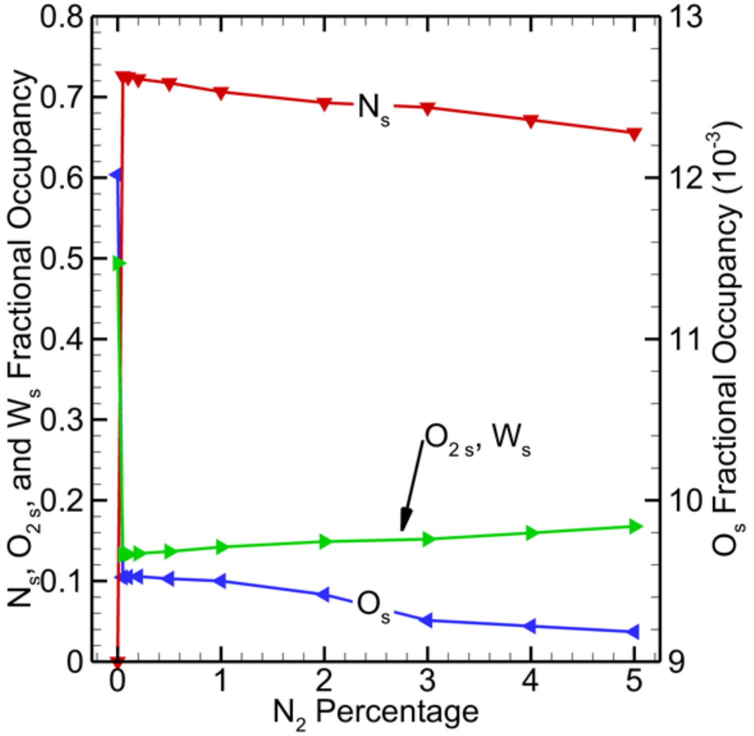

Figure 7.9. Surface coverage variation with N_2 admixture.

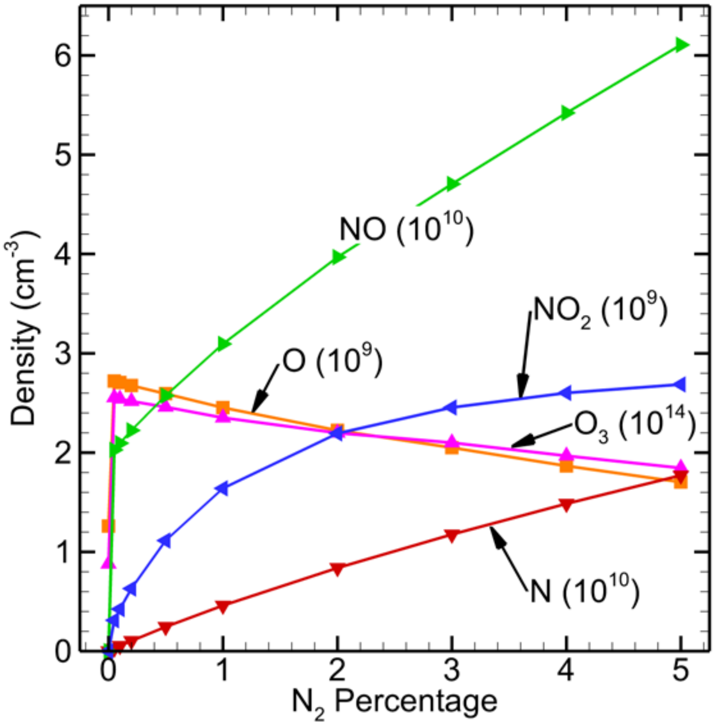

Figure 7.10. Reactive species variation with N_2 admixture.

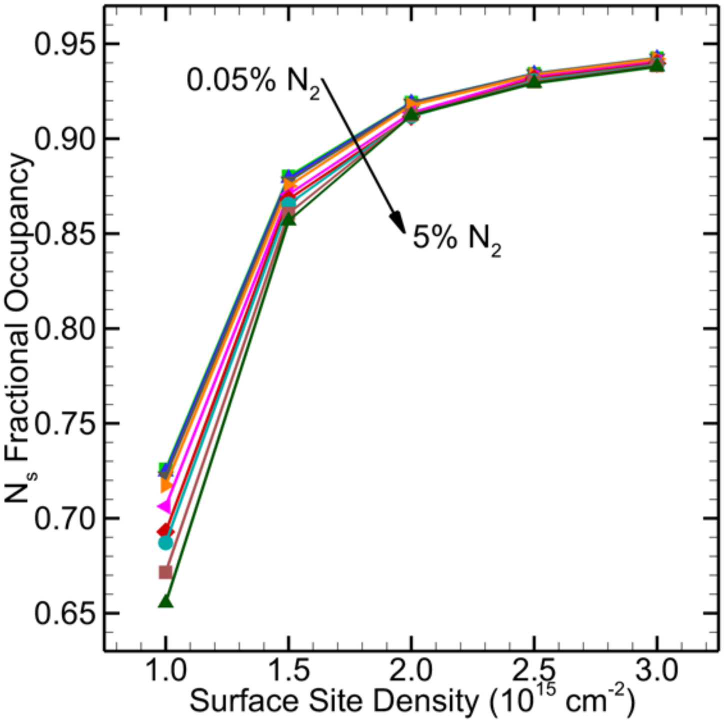

Figure 7.11. Adsorbed N variation with surface site density.

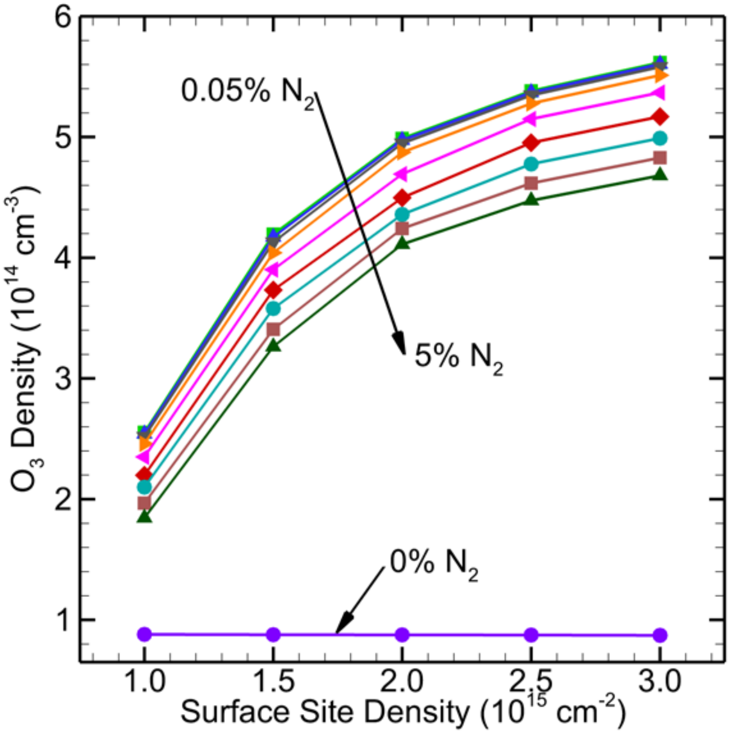

Figure 7.12. O$_3$ variation with surface site density.

7.11 References

[1] J. E. Foster, Phys. Plasmas **24,** 055501 (2017).

[2] H. Karaca and Y. S. Velioglu, Food Rev. Int. **23,** 91 (2007).

[3] A. Niveditha, R. Pandiselvam, V. A. Prasath, S. K. Singh, K. Gul and A. Kothakota, Food Control **130,** 108338 (2021).

[4] J. E. Foster, S. Mujovic, J. Groele and I. M. Blankson, J. Phys. D. Appl. Phys. **51,** 293001 (2018).

[5] M. Taguchi, K. Yamashiro, T. Takano and H. Itoh, Plasma Process. Polym. **4,** 719 (2007).

[6] H. Itoh, T. Nagai, M. Taguchi, K. Teranishi and S. Suzuki, Plasma Res. Express **3,** 035001 (2021).

[7] M. Taguchi, Y. Ochiai, R. Kawagoe, Y. Kato, K. Teranishi, S. Suzuki and H. Itoh, EPJ Appl. Phys. **55,** 13805 (2011).

[8] K. Murayama, N. Matsumura, M. Taguchi, Y. Katoh, K. Teranishi, S. Suzuki and H. Itoh, EPJ Appl. Phys. **47,** 22814 (2009).

[9] S. Seyrling, M. Müller and L. Ramoino, Eur. Phys. J. D **71,** 136 (2017).

[10] S. Seyrling, E. Reisch and L. Ramoino, Ozone Sci. Eng. **40,** 356 (2018).

[11] Y. Qin, S. Qian, C. Wang and W. Xia, Plasma Sci. Technol. **20,** 095501 (2018).

[12] W. Li, G. V. Gibbs and S. T. Oyama, J. Am. Chem. Soc. **120,** 9041 (1998).

[13] W. Van Gaens and A. Bogaerts, J. Phys. D. Appl. Phys. **46,** 275201 (2014).

[14] R. Atkinson, D. L. Baulch, R. A. Cox, R. F. Hampson, J. A. Kerr and J. Troe, J. Phys. Chem. Ref. Data **26,** 521 (1997).

[15] R. Atkinson, D. L. Baulch, R. A. Cox, R. F. Hampson, J. A. Kerr and J. Troe, J. Phys. Chem. Ref. Data **26,** 1329 (1997).

[16] A. Mellouki, G. Poulet and G. Le Bras, J. Geophys. Res. **92,** 4217 (1987).

[17] G. London, R. Gilpin, H. I. Schiff and K. H. Welge, J. Chem. Phys. **54,** 4512 (1971).

[18] B. F. Gordiets, C. M. Ferreira, V. L. Guerra, J. M. A. H. Loureiro, J. Nahorny, D. Pagnon, M. Touzeau and M. Vialle, IEEE Trans. Plasma Sci. **23,** 750 (1995).

[19] R. R. Laher and F. R. Gilmore, J. Phys. Chem. Ref. Data **19,** 277 (1990).

[20] A. Kramida, Y. Ralchenko and J. Reader, NIST Atomic Spectra Database.

[21] G. Cartry, L. Magne and G. Cernogora, J. Phys. D. Appl. Phys. **33,** 1303 (2000).

[22] V. Guerra, D. Marinov, O. Guaitella and A. Rousseau, J. Phys. D. Appl. Phys. **47,** 224012 (2014).

Chapter 8 Maximizing Photon Flux in a Miniaturized Photoionization Detector

Miniaturized photoionization detectors (PIDs) are used to detect volatile compounds in gases by collecting the current from the photoionized analyte gas. One type of photoionization detector forms a plasma in He in a dielectric barrier discharge and uses the VUV photons produced from He to photoionize the analyte gas. To improve performance of the photoionization detector, the photon flux to the analyte should be maximized. To that end, methods to maximize the photon flux from a He plasma in a PID was investigated using *nonPDPSIM*. The results showed that the photon flux from the resonance state of He(3P) responds more quickly to the voltage pulse than the flux from $He(2^1P)$ and that the photon flux from He_2^* increased long after the voltage pulse passed. Increasing the capacitance of the dielectric was found have the largest effect in increasing the photon fluence to the analyte gas. Using an array of pointed electrodes also had a strong effect on increasing the photon fluence.

8.1 Introduction

Photoionization detectors (PIDs) are one type of device used for gas chromatography [1]. In PIDs, photons are produced by a VUV source and ionize the analyte gas if the photon energy is larger than the ionization potential of the gas [2]. The current produced by the ionized gas is collected by biased electrodes. Intrinsically, the PID will ionize all compounds with ionization potentials less than the photon energy. To distinguish the compounds, a separation column can be used, ensuring different compounds enter the ionization chamber at different times so the signal can be attributed to different compounds. PIDs have applications in detecting volatile organic compounds (VOCs) including benzene and toluene as low as a few parts-per-billion (ppb) [3–6], as well as water impurities in oil [7]. Miniaturized PIDs are of special interest, as their portability can lead to measurements at locations of interest, as opposed to transporting samples back to the lab [3].

Miniaturized PIDs can employ a noble gas lamp that is physically separated from the analyte gas by a UV-transparent window as a source of VUV photons [8–12]. However, the lifetime of the detector is determined by the window transparency; solarization of the window material at 11.7 eV (Ar line emission) occurs quickly [1]. Emission from Kr at 10.2 eV does not pose as much of a problem for window degradation but is limited to detection of compounds with ionization potentials below 10.2 eV [1].

VUV photons for miniaturized PIDs can also be formed in a plasma discharge in a noble gas, typically in a dielectric barrier discharge (DBD) configuration [13–18]. In these devices, the plasma is not physically separated from the analyte. Since transparency of the window is not an issue in these discharge devices, gases like He or Ar can be used to produce higher energy VUV photons. He offers the highest energy photons; the first state of He is 19.8 eV above the ground state while the ionization potential of Ar is 15.8 eV. The photon emission from a He plasma occurs from three states. Resonant radiation from He(3P) and He(2^1P) emit photons of 23 and 21.2 eV, respectively. Additional VUV photons are produced by broadband He_2^* dissociation excimer emission, with energies ranging from 11.3 eV to 20.7 eV [1]. The high energy VUV photons produced in a He plasma can photoionize almost all analytes, including most molecular gases (N_2, O_2, H_2, H_2O) and essentially all organic compounds.

To optimize the performance of the miniaturized PID, the photon flux to the analyte must be increased while preventing extensive mixing of the analyte gas with the plasma. However, little research has been done on understanding the plasma itself and maximizing the photon flux to the analyte based on plasma properties. In this chapter, a modeling study using *nonPDPSIM* is performed on a miniaturized PID developed by Li et al. [17] to determine what device parameters have the largest effect on photon flux to the analyte gas. A description of the geometry and the reaction mechanism, including the photoionization reaction mechanism, is given in Section 8.2. Results of the base case are discussed in Section 8.3. Changes in photon fluence due to capacitance of the dielectric and electrode configuration are discussed in Sections 8.4 and 8.5, respectively. Conclusions are drawn in Section 8.6.

8.2 Geometry and Reaction Mechanism

nonPDPSIM was used to model the miniaturized PID. *nonPDPSIM* is described in detail in Section 2.2 and is therefore not described in this chapter.

The miniaturized PID is detailed in Li et al. [17], and the top view is shown schematically in Figure 8.1. The plasma is formed in He that flows into the gap of a double DBD. The electrodes that produced the plasma are on the top and bottom of the dielectric. The plasma produces VUV photons, which photoionize the analyte. The ionized analyte is collected on the biased electrodes. The flow rates of the He and analyte gas were adjusted to minimize the current from the plasma that impacted the collection electrodes, which caused excess noise in the signal. Si separates the dielectric on the top and bottom of the plasma.

A cross-section of the plasma in the miniaturized PID was modeled, and the geometry is shown in Figure 8.2a. The plasma was formed in a 400 µm gap between the dielectric covering the grounded and powered electrodes, and the dielectric thickness was 175 µm. A symmetric boundary condition was applied to the left boundary, and the electrons and positive ions were initialized on that boundary near the top of the plasma gap. The electron Monte Carlo simulation tracked the secondary electron emission, extending 50 µm into the plasma from the top and bottom dielectric in contact with the plasma. The photon flux and fluence to the Si are taken as the photon flux and fluence to the analyte inlet.

Capacitance C of the dielectric can result in a larger electron density and larger photon flux to the Si. C for a parallel plate capacitor is determined from

$$C = \frac{\varepsilon_r \varepsilon_0 A}{d}, \tag{8.1}$$

where ε_r is the relative permittivity of the dielectric, ε_0 is the permittivity of free space, A is the area of the dielectric in contact with the plasma, and d is the thickness of the dielectric. Therefore, increasing ε_r or decreasing d result in an increase in C. Six capacitances were investigated, including three with larger dielectric thicknesses. The geometry for two increased thicknesses (200 µm and 500 µm) is shown in Figures 8.2b and 8.2c.

The electrode configuration also affected the photon flux in the plasma. Different electrode configurations are shown in Figure 8.3. Changing the powered electrode from flat to pointed changed the electric field profile (Figure 8.3a). In this geometry, the gap between the plasma and powered electrode was 225 µm at the widest point, while the gap decreased to 75 µm at the narrowest point. Adding additional powered electrodes allowed for multiple plasma filaments to be sustained at a time (Figures 8.3b-d). With additional powered electrodes, electrons and positive ions were initialized under each powered electrode.

The position of the electrode relative to the Si also affected the photon flux to the Si. To examine the effect of moving the electrodes laterally towards the Si, the full reactor must be modeled, as shown in Figure 8.4a. The geometry was essentially the same as in Figure 8.2a, except a symmetric boundary condition was no longer used. With the full reactor geometry, the electrodes were moved closer to the Si on the right side of the plasma gap, as shown in Figures 8.4b-d.

In all geometries analyzed, a -2 kV voltage pulse was applied to the powered electrode. The voltage pulse was 100 ns in length, with an additional 0.5 ns rise and fall time. The plasma was modeled for 150 ns to ensure the pulse was resolved.

To produce VUV photons, the DBD was operated at atmospheric pressure in He with impurities of 80 ppm of N_2 and 20 ppm O_2. The gas temperature was initialized at 300 K. The species included in the reaction mechanism are listed in Table 8.1, totaling 31 species with 456 reactions. As N_2 and O_2 were present at an impurity level, higher order NO_x and N_xO_y species were not included. The reaction mechanism was based on Van Gaens and Bogaerts [19], updated by Norberg to use He instead of Ar [20]. Further updates included branching ratios of recombination of He^+ and He_2^+ from Emmert et al. [21].

Three photoemission reactions were included:

$$\mathrm{He}(3\mathrm{P}) \rightarrow \mathrm{He}\ \left(9.12 \times 10^{5}\mathrm{s}^{-1}\right) \tag{8.2}$$

$$\mathrm{He}\left(2^{1}\mathrm{P}\right) \rightarrow \mathrm{He}\ \left(2.0 \times 10^{6}\mathrm{s}^{-1}\right) \tag{8.3}$$

$$\mathrm{He}_2^{*} \rightarrow \mathrm{He} + \mathrm{He}\ \left(10^{7}\mathrm{s}^{-1}\right). \tag{8.4}$$

These rates were adjusted for radiation trapping factors, as in Lietz et al. [22]. The photons from each of these three photoemission reactions ionized N_2 with a cross-section of 2.5×10^{-17} cm^2. The flux and fluence of all species, including the photons, was collected on the Si.

8.3 Streamer Propagation and Photon Fluxes

The propagation of the filament of plasma, termed a streamer, over the pulse is shown in Figure 8.5 for the geometry of the base case (Figure 8.2a with $\varepsilon_r = 10$). The ionization wave initially propagates away the powered electrode due to the -2 kV applied to the powered electrode (1 ns), causing the electron density to move towards the bottom of the gap and increase in magnitude. Once the electrons reach the bottom of the plasma gap, a second ionization wave, or restrike, is launched (7 ns). T_e is maximized in front of the electron density, initiating further ionization to continue propagation of the ionization wave. At 17 ns, the electron density begins spreading on both the top and bottom dielectric surfaces as charge accumulates on the dielectric surfaces. This charge produces an electric field component parallel to the surface of the dielectric and allows the propagation of a surface ionization wave. T_e is increased in front of the electron density to continue further spreading of the electrons.

During the pulse (27 ns and 77 ns), the electron density remains high. While electrons recombine with positive ions during the pulse, electrons are also produced during the pulse. One mechanism of production is photoionization of N_2 from He_2^*, $He(2^1P)$, and He(3P). Penning ionization processes, where an excited He ionizes N_2 or O_2 (i.e., $He^* + N_2 \rightarrow He + N_2^+ + e$), also play a large role in sustaining the electron density during the pulse. Just after the voltage pulse falls (103 ns), the electron density again increases. The electron density remains high after the pulse (150 ns) due to photoionization and Penning ionization processes balancing the losses of electrons to recombination.

The photon flux from each of the three photoemission reactions is shown in Figure 8.6 throughout the pulse. The photon flux from He(3P) → He increases quickly, in response to increasing electron density and T_e, reaching a maximum at 17 ns. After 17 ns, the photon flux decreases substantially, indicating He(3P) has a short lifetime compared to the pulse length. At 103 ns, the photon flux again increases just after the voltage falls, corresponding to the increase in electron density at this time. At 150 ns, the photon flux decreases due to the short lifetime of He(3P).

The photon flux from $He(2^1P) \rightarrow He$ follows similar trends as the photon flux from He(3P) → He. However, $He(2^1P)$ has a longer lifetime than He(3P), as shown by less decrease in the photon flux during and after the pulse. While He(3P) and $He(2^1P)$ are both consumed in Penning ionization processes and formation of He_2^* with the same reaction rates, He(3P) also decays by the following reactions:

$$\mathrm{He}\left(3\mathrm{P}\right) \rightarrow \mathrm{He}\left(2^3\mathrm{S}\right)\ \left(9.47\times 10^6\mathrm{s}^{-1}\right) \tag{8.5}$$

$$\mathrm{He}\left(3\mathrm{P}\right) \rightarrow \mathrm{He}\left(2^1\mathrm{S}\right)\ \left(1.34\times 10^7\mathrm{s}^{-1}\right). \tag{8.6}$$

These two reactions result in a more rapid decrease in the density of He(3P) compared to $He(2^1P)$, leading to less decrease in photon flux during and after the pulse from $He(2^1P)$ compared to He(3P). The photon flux from $He(2^1P)$ reaches its maximum at 147 ns and decreases after 147 ns.

The photon flux from $He_2^* \rightarrow He + He$ does not follow the trends of He(3P) and $He(2^1P)$; rather, it continually increases throughout the 150 ns in spite of He_2^* having the largest rate of emission. He_2^* takes longer to form than He(3P) and $He(2^1P)$. Formation of He_2^* occurs by $He^* + He^* + M \rightarrow He_2^* + M$, where He^* is any excited He state, and M is a third body. Therefore, He_2^* increases only after there are appreciable densities of excited He, and the source of He_2^* persists after T_e decreases. Over 3 μs was simulated in the base case to determine when the photon flux from He_2^* decreases. The photon flux from He_2^* reaches a maximum near 200 ns, after the voltage pulse has passed.

The total photon flux (sum of the three photon fluxes) during the pulse to the Si is shown in Figure 8.7, as well as the photon fluence over the 150 ns to the Si. The photon flux increases over the pulse. While the photon flux from He(3P) is strongly modulated during the pulse, the photon fluxes from $He(2^1P)$ and He_2^* remain high during and after the pulse. The photon flux through 27 ns is relatively uniform across the Si. At 77 ns and 103 ns, the photon flux has a maximum on the bottom of the Si, corresponding to the increased photon flux seen in the reactor. The fluence of photons therefore also exhibits a slight maximum near the bottom of the Si but varies by less than 20% over the Si.

8.4 Capacitance of Dielectric

Capacitance is modulated by ε_r and d, as shown in Equation (8.1), with C increasing as ε_r increases or d decreases. The electron density and total photon flux are shown in Figure 8.8 for six different values of C at 150 ns. As C increases, the electron density and total photon flux both increase in magnitude. The increase in electron density and total photon flux occurs because as C increases, less voltage is dropped across the dielectric and more voltage is dropped across the plasma gap. This increased voltage leads to increased electric field, which produces more electrons. The additional electrons excite more He, producing a higher photon flux.

In addition to the increased magnitude of the electron density, the electron density also spreads further along the top and bottom dielectrics as C increases. An increase in C leads to an increase in the charge on the dielectric. The increased charge increases the parallel component of the electric field, leading to more spreading of the surface ionization wave. The additional spreading of the electrons also allows more excited states of He to be generated closer to the Si, increasing the flux to the Si. The maximum in the photon fluence to the Si at 150 ns is shown in Figure 8.9 at the different values of C. The maximum in the photon fluence increases nearly linearly as C increases.

8.5 Electrode Configuration

The configuration of the electrodes also affects the photon flux. The electron density and photon flux for different electrode configurations shown in Figure 8.3 is shown in Figure 8.10 at

150 ns. One pointed electrode shows increased electron density and total photon flux compared to one flat electrode, as the pointed electrode enhances the electric field. The enhanced electric field in turn increases the electron density and therefore total photon flux. Adding two or four flat electrodes also increases the electron density and photon flux when compared to one flat electrode. This is primarily because a more uniform electron density can be achieved, as each electrode can sustain a streamer. The photon flux to the Si also increases with two or four flat electrodes, as one streamer is now closer to the Si. The maximum photon flux occurs for two pointed electrodes, as the electric field is enhanced by the pointed electrodes and two streamers are sustained. The maximum fluence to the Si at 150 ns is shown in Figure 8.11 for these varying electrode configurations, representing well the maximum photon flux as seen in Figure 8.10.

The geometry of the system can also be changed by laterally moving the electrodes towards the Si, as shown in Figure 8.4. In this configuration, the electron density and total photon flux do not significantly vary between different electrode positions, aside from their maximum being shifted to under the electrodes. The maximum fluence to the Si at 150 ns is shown in Figure 8.12 versus the distance from the center of the electrode to the Si. As the distance to the Si decreases, the photon fluence linearly increases.

8.6 Concluding Remarks

The VUV photon flux and fluence in a miniaturized PID was examined over one 100 ns pulse using *nonPDPSIM*. The electron density did not decrease substantially during the pulse, due to sources of electrons from Penning ionization reactions and photoionization of N_2. The photon flux from He(3P) was significantly modulated during the pulse, increasing as the pulse rose and fell. The photon flux from He(2^1P) was less modulated during the pulse, as He(2^1P) has a longer lifetime than He(3P). The photon flux from He_2^* increased until 200 ns, as He_2^* requires other excited He states to form. The total photon flux and fluence to the analyte inlet varied by less than 20% across the height of the analyte inlet.

The electrode configuration and capacitance of the dielectric were varied to maximize the photon fluence to the analyte, as additional photon flux will improve performance of the miniaturized PID. Adding a point to the electrode, as well as using an array of electrodes, increased the photon fluence to the analyte. Moving the electrodes closer to the analyte inlet also increased the photon fluence relative to a centered electrode. However, the largest increase in the photon fluence was seen for the largest capacitance examined (ε_r = 300, d = 175 μm). The electrode configuration effects and capacitance effects were examined independently. However, using a high capacitance dielectric combined with an array of pointed electrodes would likely result in a higher photon fluence than either technique individually.

8.7 Tables

Table 8.1. Species included in *nonPDPSIM*.

Charged Species	e, O_2^+, O_2^-, O^+, O^-, N_2^+, N^+, He^+, He_2^+
Neutral Species	O_2, O, N_2, N, He
Excited States	$O_2(v)$, $O_2(r)$, $O_2(^1\Delta)$, $O_2(^1\Sigma)$, $O(^1D)$, $N_2(r)$, $N_2(v)$, $N_2(A^3\Sigma_u)$, $N_2(a'^1\Sigma)$, $N(^2D)$, $He(2^3S)$, $He(2^1S)$, $He(2^3P)$, $He(2^1P)$, He(3P), He(3S), He_2^*

8.8 Figures

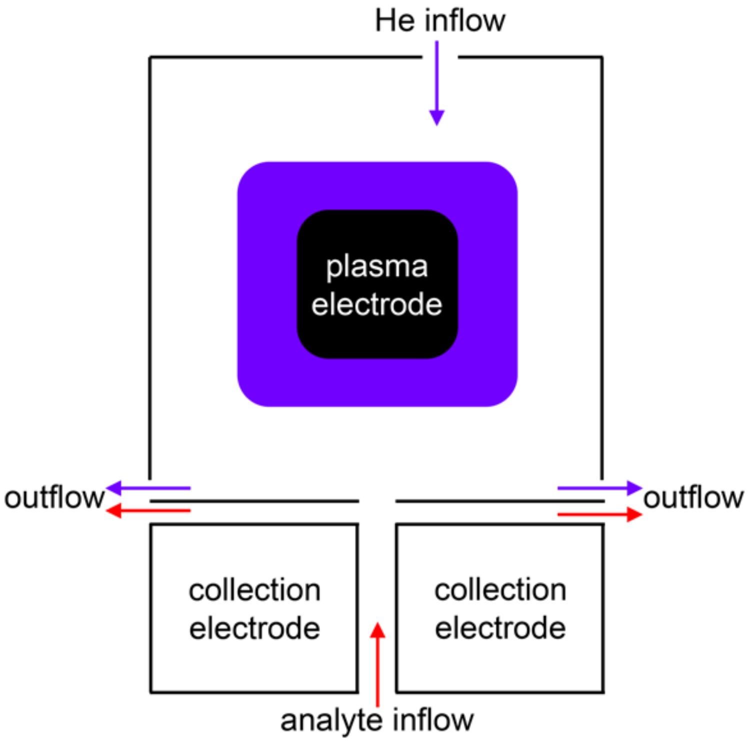

Figure 8.1. Miniaturized PID schematic (top view).

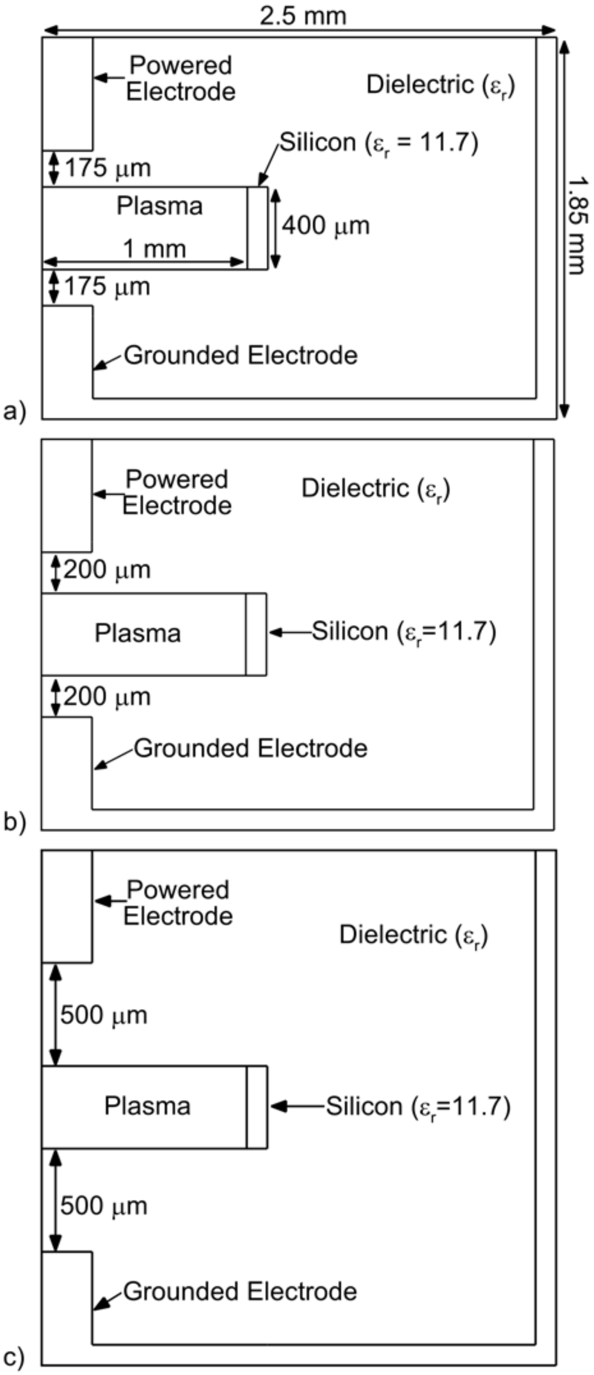

Figure 8.2. Miniaturized PID geometry modeled in *nonPDPSIM*. This geometry is a cross-section of the PID. (a) 175 µm thick dielectric, (b) 200 µm thick dielectric, and (c) 500 µm thick dielectric.

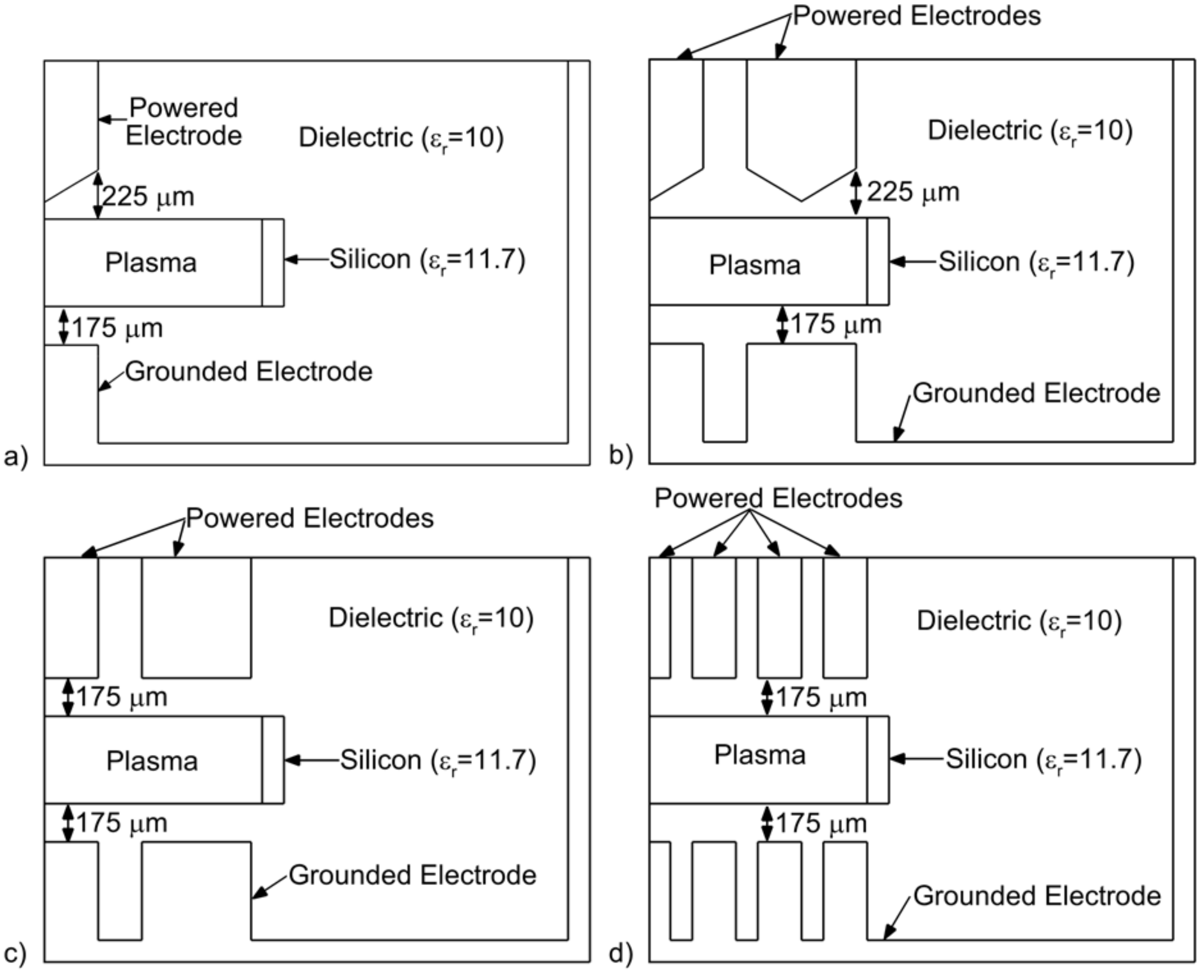

Figure 8.3. Geometry for differing electrode configurations. (a) One pointed electrode, (b) two pointed electrodes, (c) two flat electrodes, and (d) four flat electrodes.

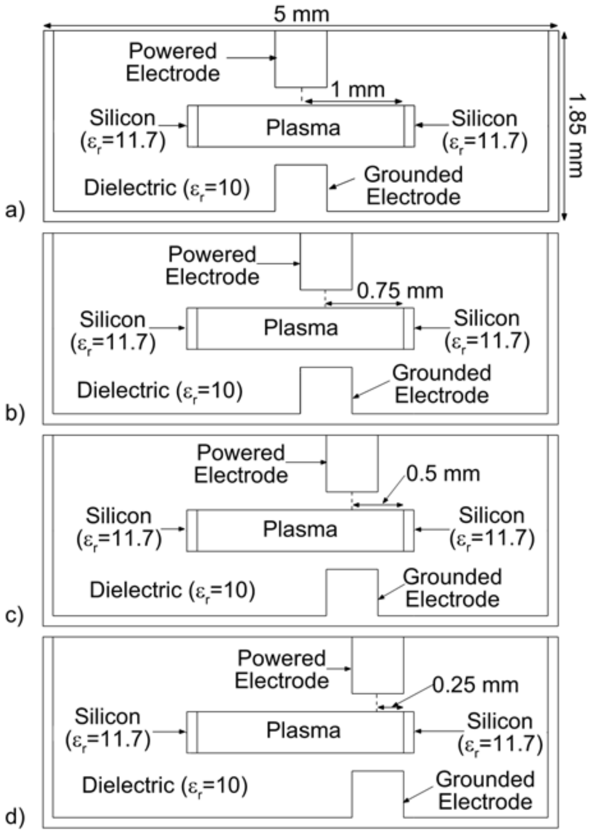

Figure 8.4. Full reactor geometry. (a) 1 mm, (b) 0.75 mm, (c) 0.5 mm, and (d) 0.25 mm distance from the center of the electrode to the Si.

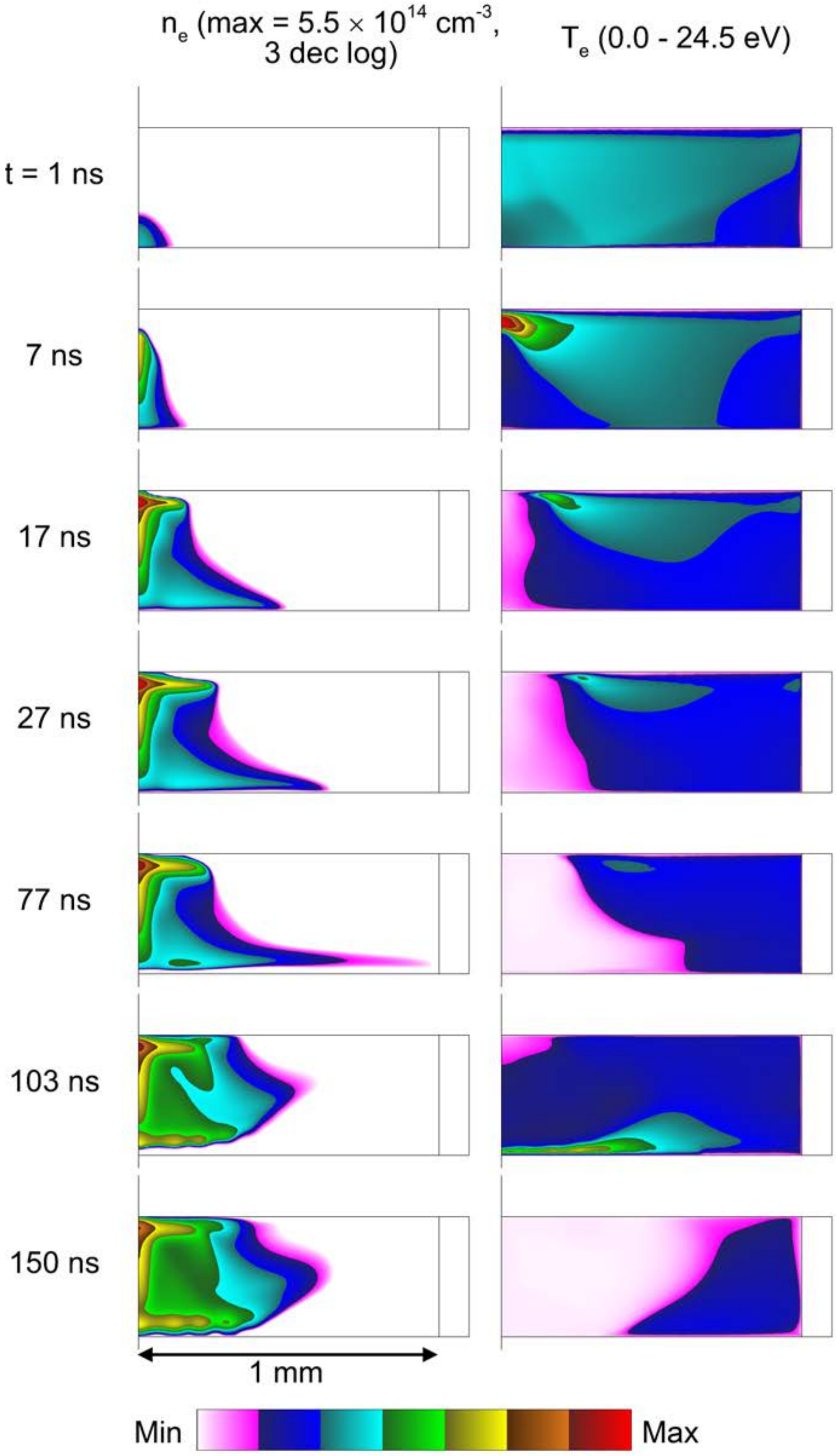

Figure 8.5. Electron density and T_e over the pulse.

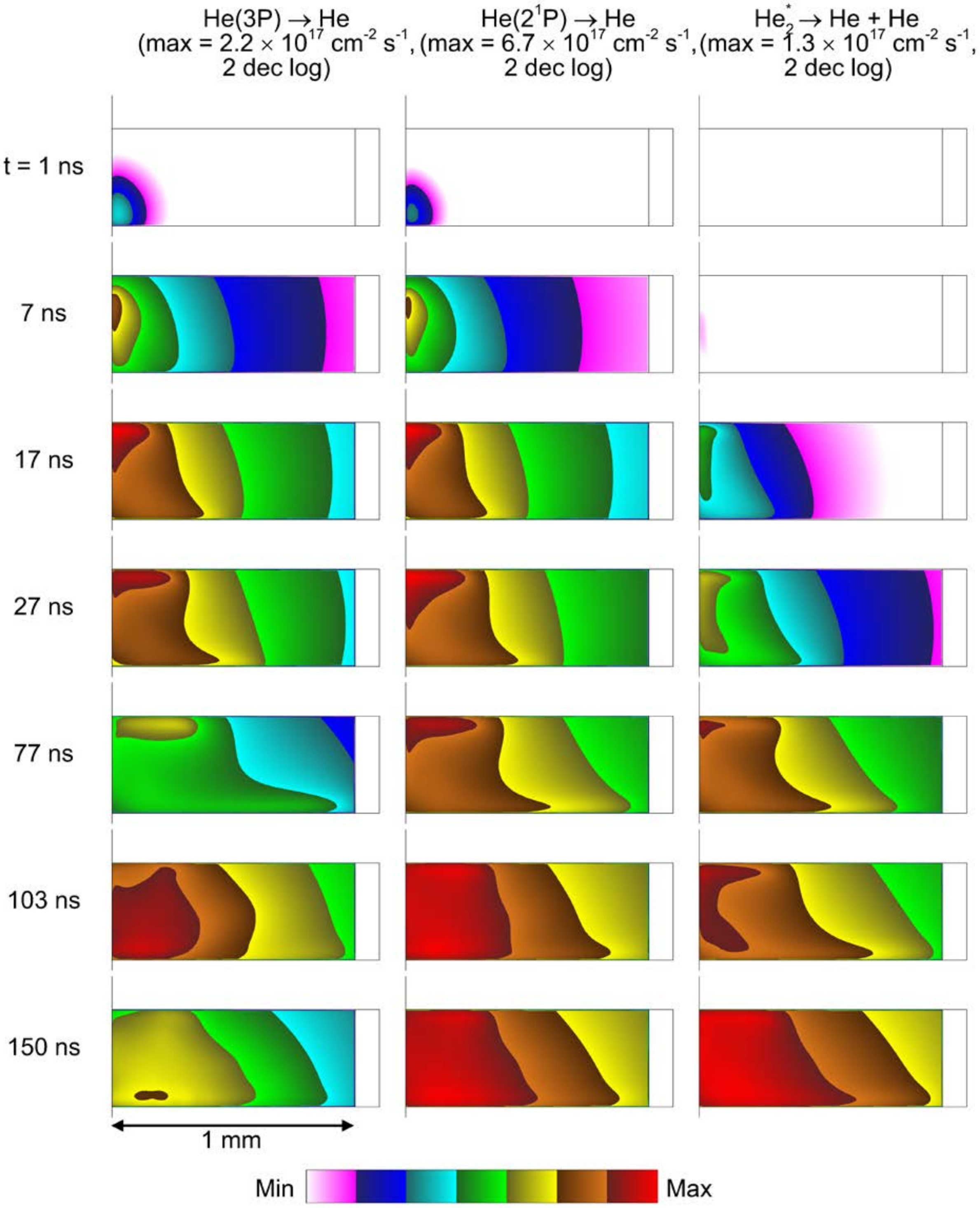

Figure 8.6. Photon flux from He(3P), He(2^1P), and He_2^* over the pulse.

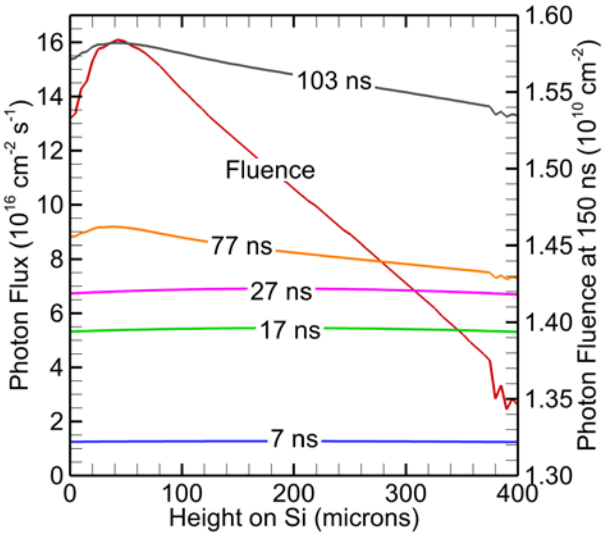

Figure 8.7. Photon flux at different times during the pulse and photon fluence to the Si at 150 ns.

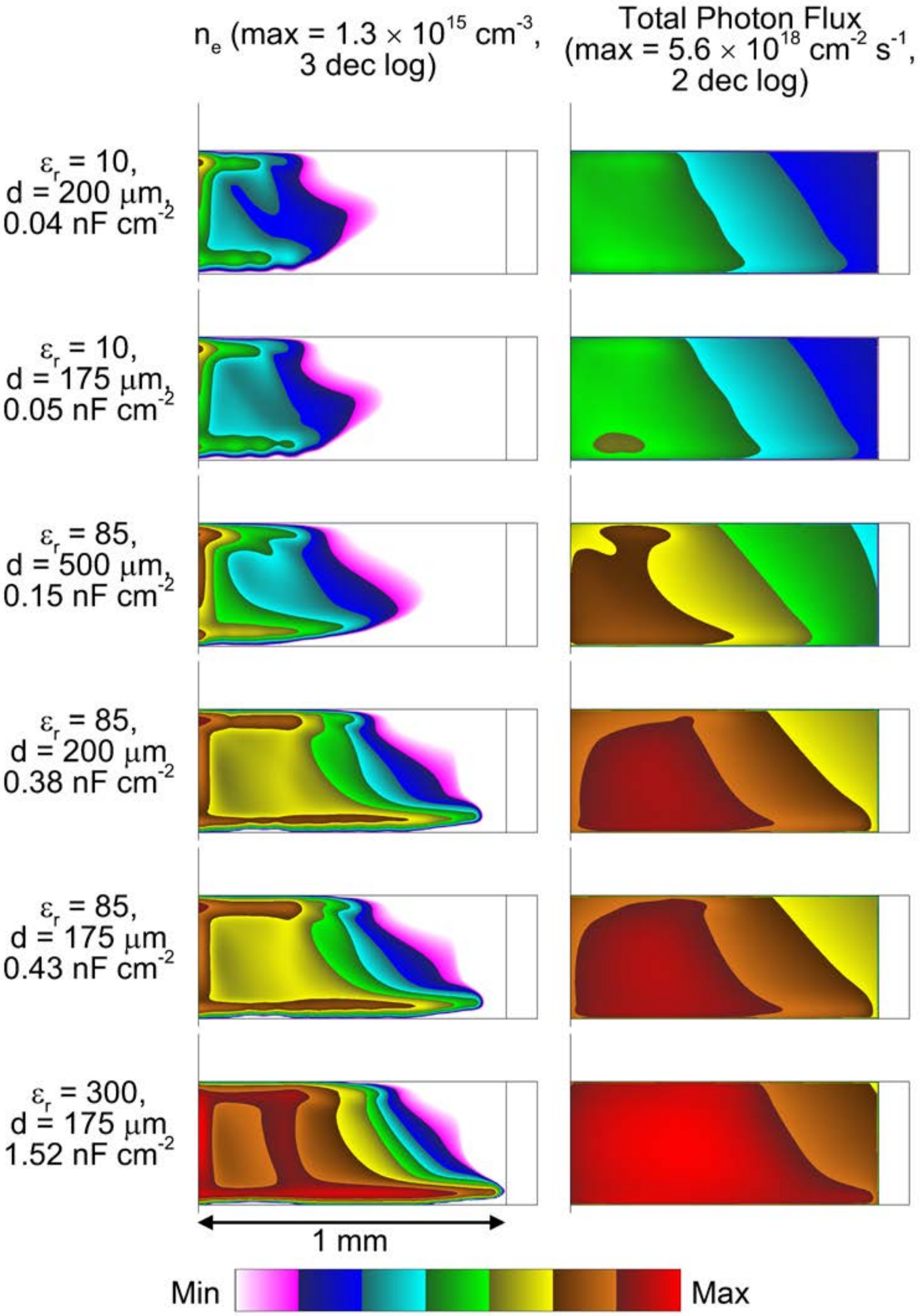

Figure 8.8. Electron density and total photon flux at different capacitances.

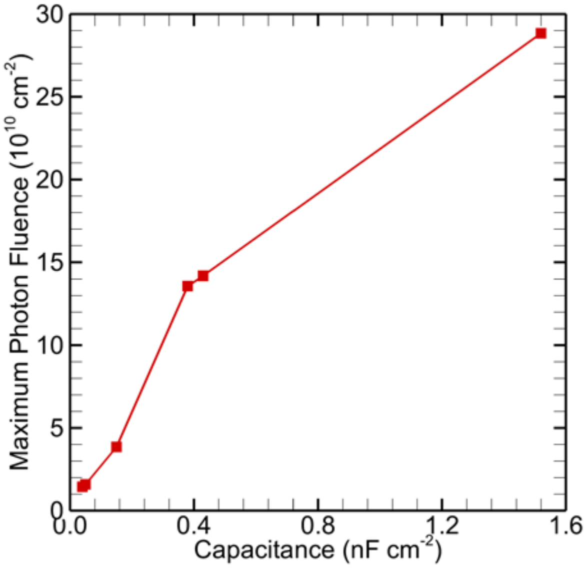

Figure 8.9. Maximum fluence to the Si at 150 ns for different capacitances.

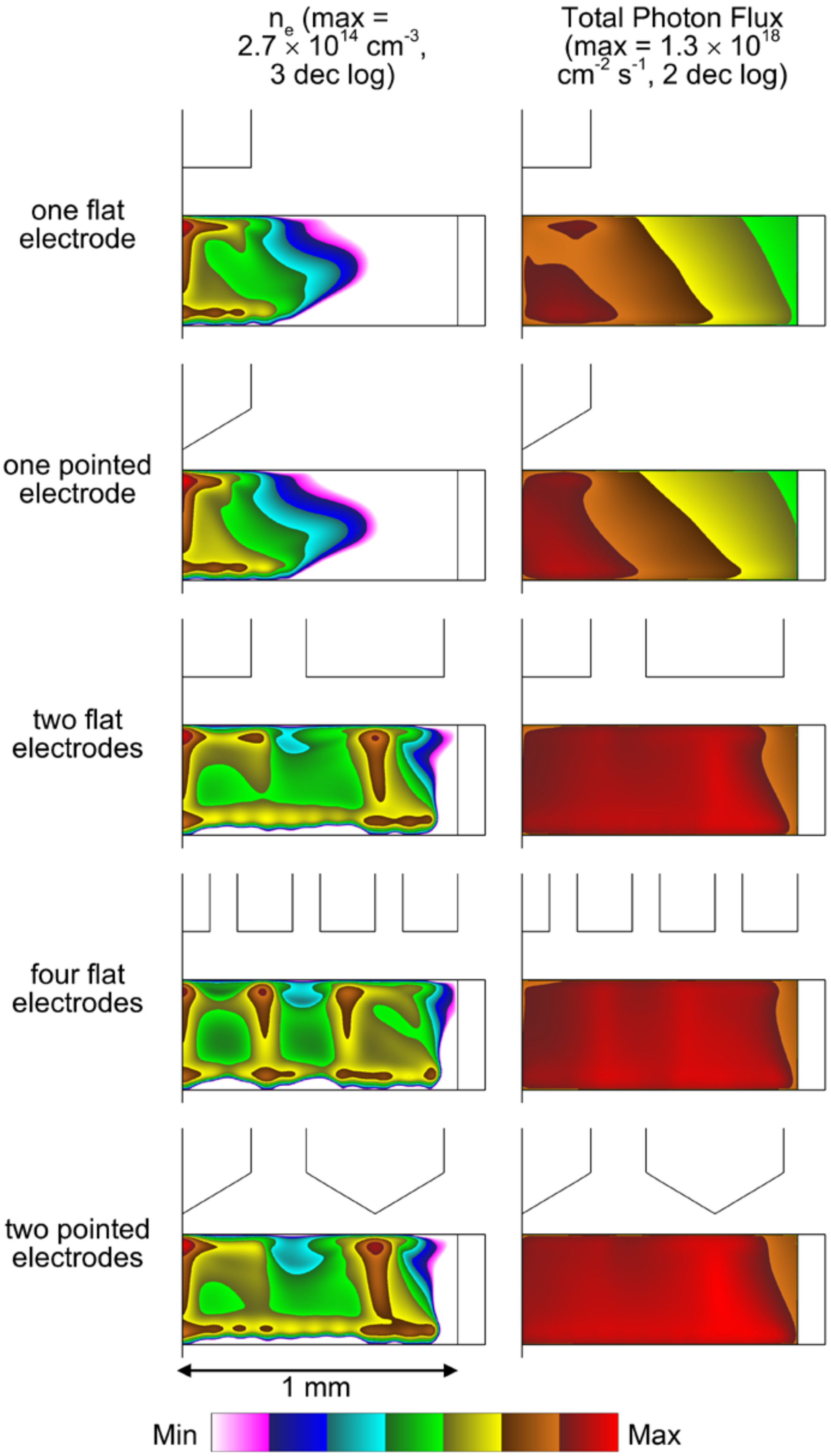

Figure 8.10. Electron density and total photon flux for different electrode configurations.

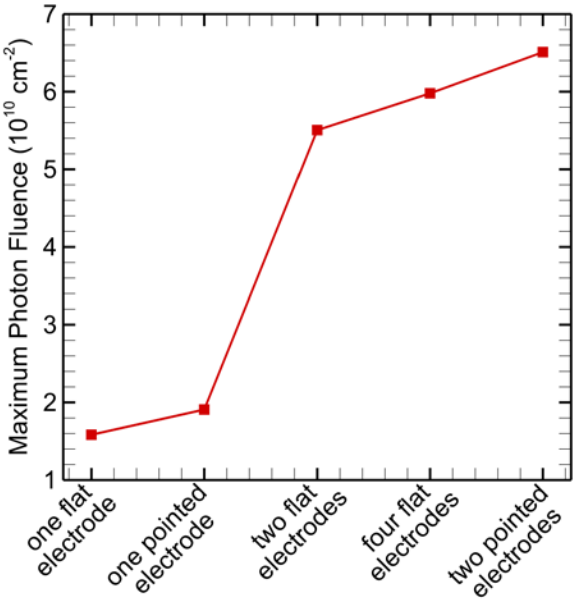

Figure 8.11. Maximum photon fluence to Si at 150 ns for different electrode configurations.

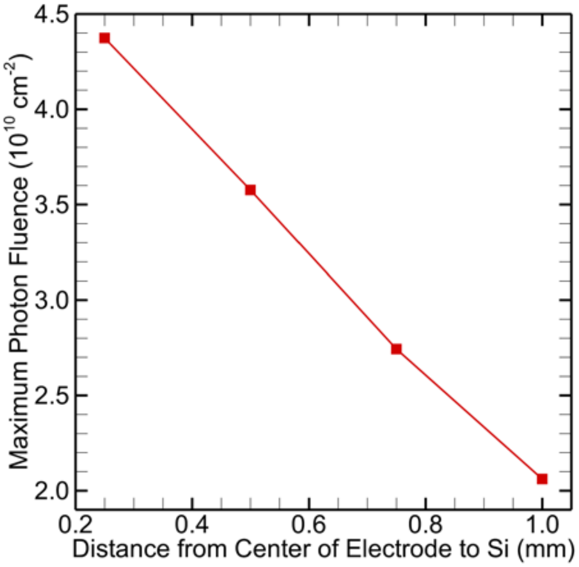

Figure 8.12. Maximum photon fluence to Si at 150 ns for different distances from the center of the electrode to the Si in the full reactor geometry.

8.9 References

[1] C. F. Poole, J. Chromatogr. A **1421,** 137 (2015).

[2] G. C. Rezende, S. Le Calvé, J. J. Brandner and D. Newport, Sensors Actuators B Chem. **287,** 86 (2019).

[3] R. Nasreddine, V. Person, C. A. Serra and S. Le Calvé, Sensors Actuators B Chem. **224,** 159 (2016).

[4] J. C. Soo, E. G. Lee, R. F. LeBouf, M. L. Kashon, W. Chisholm and M. Harper, J. Occup. Environ. Hyg. **15,** 351 (2018).

[5] S. Narayanan, G. Rice and M. Agah, Sensors Actuators B Chem. **206,** 190 (2015).

[6] D. W. You, Y. S. Seon, Y. Jang, J. Bang, J. S. Oh and K. W. Jung, J. Chromatogr. A **1625,** 461267 (2020).

[7] C. D. Mowry, A. S. Pimentel, E. S. Sparks, M. W. Moorman, K. E. Achyuthan and R. P. Manginell, Anal. Sci. **32,** 177 (2016).

[8] H. Zhu, R. Nidetz, M. Zhou, J. Lee, S. Buggaveeti, K. Kurabayashi and X. Fan, Lab Chip **15,** 3021 (2015).

[9] J. Sun, F. Guan, D. Cui, X. Chen, L. Zhang and J. Chen, Sensors Actuators B Chem. **188,** 513 (2013).

[10] G. C. Rezende, S. Le Calvé, J. J. Brandner and D. Newport, Sensors Actuators B. Chem. **324,** 128667 (2020).

[11] M. W. Li, A. Ghosh, A. Venkatasubramanian, R. Sharma, X. Huang and X. Fan, ACS Sensors **6,** 2348 (2021).

[12] H. Zhu, J. She, M. Zhou and X. Fan, Sensors Actuators B. Chem. **283,** 182 (2019).

[13] S. Narayanan, M. Agah and G. Rice, Proc. IEEE Sensors 51 (2013).

[14] M. Akbar, M. Restaino and M. Agah, Microsystems Nanoeng. **1,** 15039 (2015).

[15] M. Akbar, H. Shakeel and M. Agah, Lab Chip **15,** 1748 (2015).

[16] H. Zhu, M. Zhou, J. Lee, R. Nidetz, K. Kurabayashi and X. Fan, Anal. Chem. **88,** 8780 (2016).

[17] M. W. Li, A. Ghosh, R. Sharma, H. Zhu and X. Fan, Sensors Actuators B Chem. **332,** 129504 (2021).

[18] H. Cai and S. D. Stearns, J. Chromatogr. A **1284,** 163 (2013).

[19] W. Van Gaens and A. Bogaerts, J. Phys. D. Appl. Phys. **46,** 275201 (2014).

[20] S. Norberg, "Modeling Atmospheric Pressure Plasma Jets: Plasma Dynamics, Interaction with Dielectric Surfaces, Liquid Layers and Cells," Ph.D. Thesis (University of Michigan, 2015).

[21] F. Emmert, H. H. Angermann, R. Dux and H. Langhoff, J. Phys. D. Appl. Phys. **21,** 667 (1988).

[22] A. M. Lietz, E. V Barnat, J. E. Foster and M. J. Kushner, J. Appl. Phys. **128,** 083301 (2020).

Chapter 9 Summary and Future Work

In this dissertation, various plasma interactions with multiphase surfaces have been investigated through computational models. The results of the computational models inform ways to optimize real-world systems, including where to best place components in the plume of a Hall thruster to minimize erosion with margins of error and how to increase O_3 production in O_3 generators and photon flux to the analyte gas in PIDs. The results also inform fundamental studies of plasma-liquid interactions, including how sheaths form around droplets and how a model organic compound degradation varies with different properties of the liquid and plasma.

9.1 Summary

In Chapter 1, LTPs were discussed, including the importance of collisions and sheaths. Common uses of LTPs were presented, including both at low pressure and atmospheric pressure. These uses include electric propulsion, plasma-liquid interactions, ozone production, and photoionization detectors.

In Chapter 2, the three models used in this dissertation were described in detail. The first was *MEOWS*, developed by the author, that calculates the erosion of a wire when exposed to the plume of a Hall thruster. *MEOWS* requires the ion current density and ion energy distribution at the location of the wire, as well as semi-empirical models for the sputtering yield. *MEOWS* was developed with the application of determining the erosion of a meshed reflector composed of small molybdenum wires coated with gold by discretizing the wire surface and tracking the erosion of flat surfaces over time. The second model described was *nonPDPSIM*, a 2D plasma dynamics model. Poisson’s equation, the continuity equations for charged species and charge accumulated in materials, the electron energy equation, and neutral gas continuity equations are solved. *nonPDPSIM* also includes time-slicing modules, such as the electron Monte Carlo simulation, to solve for dynamics that occur on longer time scales than the plasma propagation. The final model discussed in Chapter 2 was *GlobalKin*, a 0D plasma chemistry model that solves for species densities, electron temperature, and gas temperature as a function of time. *GlobalKin* can also calculate liquid species densities, and the volume of the liquid region can be adjusted by using the droplet module. Surface site densities can be tracked using the time-slicing surface kinetics module.

In Chapter 3, *MEOWS* was validated against experimental measurements of erosion. The plasma properties of the plume of a Hall thruster were taken from experiments and a simulation called *MONACO-PIC*. The normal incidence sputtering yield model from Eckstein and Preuss and the angular incidence model from Wei et al. were found to best predict the measured wire profiles when the measured plume properties were used. The average of the four different combinations of sputtering yield models predicted the measured profiles to within 35% of a wire radius.

In Chapter 4, *MEOWS* was used to quantify the uncertainty in the erosion predictions due to underlying uncertainty in the sputtering yield, as estimates of the uncertainty are required to determine lifetime of spacecraft components. The joint probability distributions of the model parameters of the sputtering yield were calculated using a Bayesian approach, and the joint probability distribution was sampled to obtain 10,000 unique eroded wire profiles. The over-erosion uncertainty in the maximum predicted erosion, a useful metric for spacecraft design, was shown to be up to 190% of the median maximum predicted erosion.

In Chapter 5, the sheath that forms around a dielectric droplet in an RF glow discharge was examined using *nonPDPSIM*. The sheath was asymmetric around the droplet. The droplet was polarized by the electric field in the bulk plasma – an effect that decreased as permittivity of the droplet or diameter of the droplet decreases. Along the equator of the droplet, the bulk and sheath electric fields constructively added to maximize E/N on one side of the droplet and destructively interfered to minimize E/N on the opposite side. T_e, however, was maximized 45° above and below the equator of the droplet, matching the maximum in the power deposited per electron. The nonconductive droplet was charged positively on the poles and negatively on the equator while maintaining an overall negative charge. As conductivity increased, the positive charge on the droplet disappeared, and the negative charge began to oscillate over the RF cycle.

In Chapter 6, the long timescale chemistry in a droplet containing $HCOO^-_{aq}$ was examined using *GlobalKin*. *GlobalKin* was shown to accurately predict experimental measurements with a reactive layer thickness of 5.5 µm. The primary consumption mechanism of OH_{aq} was shown to be the reaction with $HCOO^-_{aq}$. When $HCOO^-_{aq}$ was consumed in the reactive layer, the density of OH_{aq} was generally high. However, if the depletion of $HCOO^-_{aq}$ occurred well before the power turned off, reactions of OH_{aq} with $HO_2{}^-_{aq}$ and OH^-_{aq}, formed from the products of $HCOO^-_{aq}$ and OH_{aq}, decreased the OH_{aq} density. The liquid phase chemistry is affected by both droplet and plasma properties, but only the power, gas mixtures, and water percentage affected the gas phase OH density.

In Chapter 7, the streamer formation in an O_3 generator was examined using *nonPDPSIM*. The ionization wave development led to a maximum in O and O_3 where the electron density was maximized over the pulse. Roughness on the surface of the dielectric lead to a local increase in electrons, as well as O and O_3 densities. However, the O_3 production efficiency was not significantly affected by increased roughness. *GlobalKin* was used to develop a surface reaction mechanism that included the destruction of O_3 on the surface. The results of *GlobalKin* showed O_3 production reached a maximum at 0.05% N_2, due to the maximum in adsorbed N that blocked otherwise empty wall sites that could be used for O_3 destruction. At any given N_2 percentage, increasing the surface roughness increased N_s and O_3 density. However, with 0% N_2, O_3 did not change with increasing surface roughness because the destruction of O_3 was already saturated. The surface mechanism proposed is a general mechanism and would benefit from specific reaction probabilities for specific surfaces.

In Chapter 8, strategies to maximize the photon flux to the analyte gas in a miniaturized PID were identified using *nonPDPSIM*. The base case was first analyzed. The photon flux from the He(3P) state was modulated more quickly than the flux from He(2^1P) as He(3P) can also decay to He(2^3S) and He(2^1S). The photon flux from He_2^* increased through the 150 ns simulated because He_2^* requires other excited He states to form. Increasing the capacitance of the dielectric by increasing permittivity or decreasing thickness increased the photon flux to the analyte gas, as well as increasing spreading of the surface ionization wave along the dielectric. Adding points to electrodes or using an array of electrodes also increased the photon flux. It is possible the increased capacitance coupled with electrode configurations would result in an even further increased photon flux.

9.2 Implications of Results

Throughout this dissertation, the effect of plasmas on multiphase surfaces in contact with the plasma has been modeled. The plasma can have a destructive effect by ion-impact sputtering of spacecraft components (Chapters 3 and 4), can interact both electrically and chemically with embedded liquid droplets (Chapters 5 and 6), can enhance O_3 production by decreasing O_3

destruction on the surfaces (Chapter 7), or can increase photon flux to the analyte gas (Chapter 8). Studying these various interactions between plasmas and multiphase surfaces will lead to a better understanding of these interactions. Potential avenues for improvement of real-world systems are also suggested by these studies.

This dissertation showed that erosion of a wire due to ion-impact sputtering varies drastically at different locations in the plume of a Hall thruster. Generally, the erosion of the wire decreased as angle from thruster centerline increased. However, it is necessary to properly account for margin of error in the erosion estimates, as the uncertainty can be up to twice as large as the maximum predicted erosion itself. The large uncertainty should be accounted for in lifetime estimates and may impact placement of spacecraft components.

In many applications involving plasmas in contact with liquids, improving the transfer of RONS to the liquid will improve the purification or medicinal effects of the plasma. However, many fundamental questions remain unanswered about the interface of the plasma and liquid. One aspect of this interface is the sheath that forms around an embedded droplet. In particular, the dynamics of the sheath and the nonuniform charging of the droplet can influence the flux of species to the droplet. Another aspect of the interface is the reactive species chemistry. Strategies to increase the OH_{aq} concentration and decrease the $HCOO^-_{aq}$ concentration were identified. These included decreasing the diameter of the droplet, increasing the residence time of the droplet in the plasma, using gas mixtures that produce large amounts of O and OH, and increasing the admixture of H_2O in the inlet gas.

Pulsed DBD systems for two different applications were also examined. Adding a small admixture of N_2 to the gas will increase O_3 production, as adsorbed N occupies surface sites otherwise contributing to O_3 destruction. Another way to increase O_3 production includes using surfaces in contact with the plasma with a high probability of adsorption of N. The photon flux to the analyte gas in a miniaturized PID was found to be most increased with a high capacitance dielectric. Adding more electrodes also improves photon flux. Both increasing the capacitance and adding more electrodes is expected to result in an even further increased photon flux. The increased photon flux will enhance the performance of the miniaturized PID.

9.3 Future Work

This section describes potential improvements to models and follow-on studies that could build upon the work described in this dissertation.

The limitations of *MEOWS* are discussed in Section 4.6.4. *MEOWS* relies on many assumptions, including that the ions are singly-charged and impact the wire from one direction. Multiply-charged ions would have a higher energy than singly-charged ions, increasing the erosion of the wire. This would be particularly important for analyzing EP plumes with a large degree of multiply-charged ions. The assumption that the ions impact the wire from one direction is not necessarily correct, particularly at locations where ions formed by charge-exchange collisions dominate. Incorporating the ion velocity distribution would allow ions to impact the wire from any direction and better capture the erosion.

nonPDPSIM could be improved. In particular, the runtime of *nonPDPSIM* could be improved. To reach a quasi-steady state as described in Chapter 5, a runtime of over 2 weeks was required. Much of the computational load involves the Newton-Raphson iteration to solve charge dynamics and Poisson's equation. Decreasing the runtime of the current solver or developing a solver with improved runtime will increase the runtime of the simulation as a whole. This is particularly true when the liquid chemistry is included in *nonPDPSIM*. Another improvement could include collection of the flux of each photon species separately, as the current scheme collects the total photon flux, or the sum of the photon flux from all the photoionization reactions.

Improvements to *GlobalKin* could also be made. As shown in Chapter 6, specifying a reactive layer thickness on a droplet immersed in the plasma can accurately predict the $HCOO^-_{aq}$ concentration observed under some conditions but not others. Adding a source of replenishment of $HCOO^-_{aq}$ by diffusion between the reactive layer and nonreactive core could improve the agreement and more accurately simulate the physical droplet.

Many further studies can expand upon the studies presented in this dissertation. One study to improve the estimates of erosion in the plume of a Hall thruster would be to sample the ion current density and ion energy. This sampling could be performed in the same way as the sampling from the joint probability distributions for the sputtering yield model parameters was done. Including this sampling would more accurately calculate the erosion of the wire and the uncertainty in that erosion. Further quantification of the sputtering yield of gold and molybdenum, particularly the angular incidence sputtering yield, would also improve the erosion estimates. Finally, better understanding of how the plume properties on orbit relate to those in ground tests could improve the estimates of erosion on orbit.

Uncertainty in the results for atmospheric pressure plasmas (Chapters 5 - 8) could be estimated using the sampling methods presented in Chapter 4. The uncertainty in the sheath dynamics could stem from the secondary electron emission coefficient, and the uncertainty in reactive species densities could stem primarily from uncertainty in reaction rates. Sampling from a distribution 10,000 times could be performed in *GlobalKin* but would likely be too computationally expensive to perform in *nonPDPSIM*. Varying the relevant parameters (i.e., reaction rate) in *nonPDPSIM* could show the range of potential results.

Several studies could improve the understanding of the plasma-liquid interactions discussed in Chapters 5 and 6. While the results in Chapter 5 examined the sheath in 2D using *nonPDPSIM*, the results in Chapter 6 looked at the reactive chemistry in the droplet. Modeling the liquid phase chemistry in the geometry described in Chapter 5 would improve the understanding of how charged species fluxes change around the droplet and over the RF cycle, as well as spatial variation of $HCOO^-_{aq}$ degradation. In particular, using the averaged electron-impact rate coefficients described in Section 2.4 could allow *nonPDPSIM* to reach the long timescales required for this study. Photoionization was also neglected in these plasma-liquid interaction studies but may be important due to the abundance of He excited states.

Another study to improve understanding of plasma-liquid interactions could be to include accommodation coefficients of the charged species when encountering the liquid. At present, in both *nonPDPSIM* and *GlobalKin*, charged species are assumed to solvate with unity probability. Different accommodation coefficients for charged species will lead to differences in solvated electron concentrations, which form other reactive species. Estimates of these accommodation coefficients from experiments would be necessary.

Experimental studies could be helpful for confirming the modeling results for the two pulsed DBD systems. For the O_3 reactor, the proposed surface reaction mechanism was estimated. Measurements of the surface reaction probabilities on the materials relevant to the reactors in use would improve the results of the model. A direct comparison between the simulated results and experimental measurements would also be informative for both the O_3 reactor and the miniaturized PID.

Appendix A Post-Processing Scripts

This appendix shows the source code for the post-processing scripts described in Chapter 2 for *nonPDPSIM* and *GlobalKin*. These post-processing scripts are written in Python. Many of them leverage the PyTecplot library to import the 1D and 2D Tecplot files produced by *nonPDPSIM* and *GlobalKin*.

A.1 average_over_time

The script average_over_time reads in the 2D Tecplot file from *nonPDPSIM* and averages over the time in the file. The output is another 2D Tecplot file.

```
import tecplot as tp
import numpy as np

# input base filenames below
fnames = ['Pow_5W_NoDroplet_ResPlt']

# iterate over the base filenames
for i in range(len(fnames)):

    # form the filename
    fname = fnames[i]+'.plt'

    # read in the tecplot file
    dataset = tp.data.load_tecplot(fname,
    read_data_option=tp.constant.ReadDataOption(2))

    # duplicate the first zone
    # forms the basis for the averaged zone
    avg_zone = dataset.zone(0).copy()
    avg_zone.name = "Averaged Zone"
    avg_zone.strand = 0
    avg_zone.solution_time = -1.0

    # generate matrix for each variable and zones by points
    variables = list(dataset.variables())[2:] # skip x and y variables
    zones = list(dataset.zones())[1:-2] # skip the last (averaged) zone,
    # second to last (0.5 ns after cycle ends), and first (t=0) zone

    # iterate over variables
    for var in variables:
```

```
        a = np.empty([len(zones), avg_zone.num_points])

        # iterate through the zones (time)
        for j in range(len(zones)):

            # form the matrix
            z = zones[j]
            values= z.values(var).as_numpy_array()
            a[j,:] = values

        # average over all zones
        avg = np.average(a, axis=0)
        avg_zone.values(var)[:] = avg

    # save the file with only the averaged zone
    tp.data.save_tecplot_ascii(fnames[i]+'_time_average.plt',
    zones=len(list(dataset.zones()))-1, include_geom=True)
```

A.2 calculate_phase

This script reads in the 2D Tecplot file from *nonPDPSIM* and determines the phase of oscillation of the electron density relative to the sinusoidal voltage oscillation. The script also calculates the phase as predicted by the analysis in Chapter 5. The output is a text file containing the simulated and calculated phases of oscillation for each file read in.

```
import tecplot as tp
import numpy as np

# input values in the following block

# input base filenames below
fnames = ['Cond_1e-1_5W_v02_ResPlt', 'Cond_1e-3_5W_v02_ResPlt',
'Cond_1e-5_5W_v02_ResPlt', 'Cond_1e-7_5W_v02_ResPlt', 'Pow_5W_ResPlt']
# relative permittivity
epsr = [80.0, 80.0, 80.0, 80.0, 80.0]
# droplet diameter, cm
diameter = [80.0e-4, 80.0e-4, 80.0e-4, 80.0e-4, 80.0e-4]
# frequency of plasma, MHz
freq = [10.0, 10.0, 10.0, 10.0, 10.0]
# maximum of time-averaged electron density, cm^-3
ne = [7.7e11, 7.7e11, 7.7e11, 7.7e11, 7.7e11]
# radius of the sheath, cm
sheathrad = [0.032, 0.032, 0.032, 0.032, 0.032]
# electron temperature, eV
Te = [3.74, 3.74, 3.74, 3.74, 3.74]

# set up the arrays
sim_phase = []
calc_phase = []
```

```
# iterate over the base filenames
for i in range(len(fnames)):

    # first, determine the phase from nonPDPSIM

    # form the filename
    fname = fnames[i]+'_extract_over_cycle.plt'

    # read in the tecplot file
    dataset = tp.data.load_tecplot(fname,
    read_data_option=tp.constant.ReadDataOption(2))

    # look at the left side of the droplet
    # 1 radius away from the surface
    zones = list(dataset.zones())
    variables = list(dataset.variables())
    zone = ''
    zonename = fnames[i] + ", Left, 0.5 Diameters Away"

    # find the correct zone
    for j in range(len(zones)):
        if dataset.zone(j).name == zonename:
            zone = zones[j]
            break

    # find the electron density and fraction of RF cycle
    for var in variables:
        if var == dataset.variable('E'):
            ne_var = var
        elif var == dataset.variable('Fraction of RF Cycle'):
            t_var = var
    ne_vals = zone.values(ne_var).as_numpy_array()
    t_vals = zone.values(t_var).as_numpy_array()
    ne_max_index = np.argmax(ne_vals)

    # calculate the phase difference between the
    # electron density maximum and maximum of the sinusoidal
    # voltage (25% of RF cycle)
    delta_t = 0.25 - t_vals[ne_max_index]
    phase_i = 360.0*delta_t
    sim_phase.append(phase_i)

    # now, calculate the phase analytically

    # set initial parameters
    # gap between electrodes
    L = 0.3 # cm
    # cross-sectional area of droplet seen by plasma
    A = np.pi*diameter[i]**2/4.0 # cm^2
    # frequency from MHz to rad/s
    omega = 2*np.pi*freq[i]*1e6 # rad/s

    # capacitance of the droplet
    cap_drop = 4.0*np.pi*epsr[i]*8.854e-14*(diameter[i]/2.0)

    # capacitance of sheath around the droplet
```

```
    denom = (2.0/diameter[i]) - (1.0/sheathrad[i])
    cap_sheath = 4.0*np.pi*8.854e-14/denom # in F

    # electrode sheath capacitance of sheath around the electrodes
    debye = np.sqrt((1/1.6e-19)*(8.854e-14*Te[i]/(ne[i]))) # in cm
    cap_elec = 1.226*8.854e-14/(debye)
    cap_elec = cap_elec*A # in F

    # calculate the series capacitance
    denom = 1/cap_drop + 1/cap_sheath + 2/cap_elec
    cap = 1/denom

    # calculate the resistance
    colf = 3.5e11 # collision frequency 1/s, estimate
    cond = 1e4*(1.6e-19)**2*ne[i]/(9.1e-31*colf) # conductivity,
    # 1/(ohm cm)
    res = L/(cond*A) # resistance of plasma, ohms

    # calculate the phase
    arg = res/np.sqrt(res**2 + (1/(omega*cap))**2)
    phase_i = np.arccos(arg)*180.0/np.pi # in degrees
    calc_phase.append(phase_i)

# write the results to a file
with open('calculate_phase_updated.txt', 'w') as f:
    f.write('Case Name: Phase of Oscillation in nonPDPSIM Results
    (Degrees), Calculated Phase of Oscillation (Degrees)\n')
    for i in range(len(fnames)):
        f.write(fnames[i] + ': '+str(np.round(sim_phase[i], decimals=2))
        + ', ' + str(np.round(calc_phase[i], decimals=2)) + '\n')
    f.write('\n')
```

A.3 compare_emissivities

This script calculates the emissivity of the plasma from the extracted 1D line (see Section A.5). The emissivity is calculated by averaging the emissivity produced from the results of *nonPDPSIM* both spatially and temporally. The output is a 1D Tecplot file of emissivity versus wavelength. The result is compared to experimental measurements in Chapter 5.

```
import numpy as np
import scipy.integrate as scipyintegrate
import tecplot as tp

def maxwellian(engy, Te): # Te in eV
    # function gives a Maxwell-Boltzmann energy distribution
    # engy is the energy as an array
    # Te is the electron temperature in eV
    # returns f in eV^-3/2

    f = (2.0/(np.sqrt(np.pi)*(Te)**(1.5)))*np.multiply(np.sqrt(engy),
```

```
    np.exp(-engy/Te))

    return f

def emissivity_integral_max(engy, xsn, wave, Te):
    # function integrates to get the emissivity
    # assumes a Maxwell-Boltzmann energy distribution
    # engy is the energy as an array
    # xsn is the cross-section values for engy
    # wave is the wavelength of the photon for the lowest bound (900 nm)
    # Te is the electron temperature in eV
    # returns the integral in the emissivity equation

    # determine the energy and cross-section to integrate
    # remove values below the energy of the photon
    hc = 4.13e-15*3e8 # (eV s)*(m/s) = eV m
    lbound = hc/wave
    engy_int = []
    xsn_int = []
    for j in range(len(engy)):
        if engy[j] >= lbound:
            engy_int.append(engy[j])
            xsn_int.append(xsn[j])
    engy_int = np.asarray(engy_int)
    xsn_int = np.asarray(xsn_int)

    # integrate to find the emissivity eps_int
    integrand1 = np.multiply(xsn_int, (engy_int)**(3/2))
    l_e = wave*engy_int
    paran = 1 - ((hc/2.0)*np.divide(np.ones(len(l_e)), l_e))
    integrand2 = np.multiply(integrand1, paran)
    sq = np.sqrt(1 - (hc*np.divide(np.ones(len(l_e)), l_e)))
    integrand3 = np.multiply(integrand2, sq)
    fe = maxwellian(engy_int, Te)
    integrand = np.multiply(integrand3, fe)
    eps_int = scipyintegrate.trapz(integrand, engy_int)

    return eps_int

def formLine(array, sigfigs, lenPlt):
    # function forms lines to be written to the output Tecplot file
    # each line contains 10 values
    # array is the array to be written
    # sigfigs is the number of significant digits to write out
    # lenPlt is the length of the file

    line = '  '
    lineFlag = False
    for j in range(lenPlt):
        line = line + str(np.around(array[j],decimals=sigfigs)) + "  "
        lineFlag = False
        if (j+1) % 10 == 0:
            line = line + '\n  '
            lineFlag = True
    if lineFlag is False:
        line = line + '\n'
```

```
    return line

def writePltFile(title, wavelength, emissivity, out_name):
    # function writes the plot file
    # title is an array of titles of the zones
    # wavelength is an array of wavelengths
    # emissivity is an array of emissivities
    # out_name is the output file name

    # form the header
    varheader = '     VARIABLES="Wavelength (nm)",\n'
    varheader = varheader + '        "Emissivity (<greek>m</greek>W
    cm<sup>-3</sup> nm<sup>-1</sup>)"\n'
    lenPlt = len(wavelength)
    sigfigs = 3

    # write the output file
    with open(out_name, 'w') as f:
        f.write(' TITLE = "Comparison to MN Experiments"\n')
        f.write(varheader)
        for j in range(len(emissivity[0])):
            f.write('     ZONE I = '+ str(lenPlt) + ', F=BLOCK,\n
            T="'+titles[j]+'"\n')

            line = formLine(wavelength, sigfigs, lenPlt)
            f.write(line)

            line = formLine(emissivity[:,j], sigfigs, lenPlt)
            f.write(line)

    return

def main():

    # import the cross-section from file
    sigma_ea_elastic = [] # cross-section, m^2
    e_elastic = [] # energy, eV
    with open('phelps_database_he_elastic.txt', 'r') as f:
        d = f.readlines()
        for i in range(2, len(d)):
            splt = d[i].split('\t')
            e_elastic.append(float(splt[0]))
            sigma_ea_elastic.append(float(splt[1]))
    sigma_ea_elastic = np.asarray(sigma_ea_elastic)
    e_elastic = np.asarray(e_elastic)

    # interpolate the cross-section for better energy resolution
    interp = 1
    if interp == 1:
        engy_temp = []
        sigma_temp = []
        stepsize = 0.1
        for i in range(15):
            engy_temp.append(e_elastic[i])
            sigma_temp.append(sigma_ea_elastic[i])
```

```
            step = 0.0
            while e_elastic[i] + step < e_elastic[i+1]:
                engy_temp.append(e_elastic[i] + step)
                interp_val = np.interp(e_elastic[i] + step,
                e_elastic[i:i+2], sigma_ea_elastic[i:i+2])
                sigma_temp.append(interp_val)
                step = step + stepsize
        e_elastic = np.copy(np.asarray(engy_temp))
        sigma_ea_elastic = np.copy(np.asarray(sigma_temp))

    # input the filenames
    fnames = ['MNCase_NoDrop_expairimp_v02_ResPlt_extract_1d_horizontal']

    # input the titles
    titles = ['Scan Over Gap (No Average, Lower Bound Te)']

    # set values
    na = 2.45e19 # 1/cm^3, gas density at 760 Torr and 300 K
    C_ea = 1.77 # W m^2 J^-3/2 sr^-1

    # set up arrays
    wavelength_nm = np.linspace(300, 900, num=1000)
    wavelength = wavelength_nm*1e-9 # in m
    lower_bound_te_val = (4.13e-15*3e17)/wavelength_nm[-1] #(eV s *
    # nm/s)/nm = eV
    lower_bound_te = [lower_bound_te_val]
    lenemis = len(fnames)
    emissivity = np.zeros((len(wavelength), lenemis))

    # iterate over filenames
    for ff in range(len(fnames)):

        # form the filename
        fname = fnames[ff] + '.plt'
        emis_idex = ff

        # read in the tecplot file
        dataset = tp.data.load_tecplot(fname,
        read_data_option=tp.constant.ReadDataOption(2))

        # list the variables and zones
        variables = list(dataset.variables())
        zones = list(dataset.zones())

        # save the relevant variables
        for var in variables:
            if var == dataset.variable('E'):
                ne_var = var
            if var == dataset.variable('TE'):
                te_var = var
            if var == dataset.variable('X'):
                x_var = var

        # calculate the emissivity
        emissivity_zones = np.zeros((len(wavelength), len(zones)))
        zone_names = []
```

```
# iterate through zones (time)
for jj in range(len(zones)):

    # get the relevant values
    z = zones[jj]
    zone_names.append(dataset.zone(z).name)
    ne_vals = z.values(ne_var).as_numpy_array()
    te_vals = z.values(te_var).as_numpy_array()
    x_vals = z.values(x_var).as_numpy_array()

    # store the number of points used
    ne_len_used = 0

    # iterate over number of points
    for k in range(len(ne_vals)):

        # ensure x values are between the electrodes (not within
        # the electrodes)
        if x_vals[k] > 1.15 and x_vals[k] < 1.35:

            # only calculate the emissivity if the electron
            # temperature is higher than the lower bound
            if te_vals[k] > lower_bound_te[ff]:

                ne_len_used = ne_len_used + 1

                # iterate over wavelengths
                for i in range(len(wavelength)):

                    # calculate integral in emissivity
                    emiss = emissivity_integral_max(e_elastic,
                    sigma_ea_elastic, wavelength[i], te_vals[k])

                    # add to running sum
                    emissivity_zones[i,jj] =
                    emissivity_zones[i,jj] +
                    (C_ea*ne_vals[k]*na*emiss/wavelength[i]**2)

    # average by dividing by the number of points used (spatial)
    emissivity_zones[:,jj] = emissivity_zones[:,jj]/ne_len_used

# iterate over wavelengths to average over zones (time)
for i in range(len(wavelength)):

    emiss_sum = 0

    # iterate over zones
    for jj in range(len(zones)):

        # add to running sum
        emiss_sum = emiss_sum + emissivity_zones[i,jj]

    # average by dividing by number of zones (time)
    emissivity[i, emis_idex] = emiss_sum/len(zones)
```

```
    # convert units to muW cm^-3 nm^-1 sr^-1
    emissivity = emissivity*(1e3*(1.6e-19)**(1.5))

    # convert to muW cm^-3 nm^-1
    emissivity = emissivity*4.0*np.pi

    # write the file
    writePltFile(titles, wavelength_nm, emissivity,
    'MNCase_NoDrop_expairimp_v02_ResPlt_emissivity_estimates_v02.plt')

    return

if __name__ == "__main__":
    main()
```

A.4 displacement_current

This script reads in the 2D Tecplot file from *nonPDPSIM* and calculates the displacement and conduction currents. The output is another 2D Tecplot file containing the displacement, conduction, and total currents.

```
import tecplot as tp
import numpy as np

# input base filenames below
fnames = ['Pow_5W_ResPlt', 'Cond_1e-5_5W_v02_ResPlt',
'Cond_1e-3_5W_v02_ResPlt', 'Cond_1e-1_5W_v02_ResPlt',
'Cond_1e-7_5W_v02_ResPlt']

# iterate over the base filenames
for i in range(len(fnames)):

    # form the filename
    fname = fnames[i]+'.plt'

    # read in the tecplot file
    dataset = tp.data.load_tecplot(fname,
    read_data_option=tp.constant.ReadDataOption(2))

    # create new variables
    dataset.add_variable('EPS')
    dataset.add_variable('dEx/dt')
    dataset.add_variable('dEy/dt')
    dataset.add_variable('Jx')
    dataset.add_variable('Jy')
    dataset.add_variable('Ix (A/cm^2)')
    dataset.add_variable('Iy (A/cm^2)')

    # determine which variables to save
    variables = list(dataset.variables())
```

```
zones = list(dataset.zones())[1:] # skip the first (t=0) zone
vars_to_save = []
for var in variables:
    if var == dataset.variable('EX'):
        ex_var = var
        vars_to_save.append(var)
    if var == dataset.variable('EY'):
        ey_var = var
        vars_to_save.append(var)
    if var == dataset.variable('dEx/dt'):
        dex_var = var
        vars_to_save.append(var)
    if var == dataset.variable('dEy/dt'):
        dey_var = var
        vars_to_save.append(var)
    if var == dataset.variable('TOTCH'):
        vars_to_save.append(var)
    if var == dataset.variable('E'):
        vars_to_save.append(var)
    if var == dataset.variable('E/N'):
        vars_to_save.append(var)
    if var == dataset.variable('TE'):
        vars_to_save.append(var)
    if var == dataset.variable('Y'):
        vars_to_save.append(var)
    if var == dataset.variable('X'):
        vars_to_save.append(var)
    if var == dataset.variable('IMAT_NAME'):
        mat_var = var
        vars_to_save.append(var)
    if var == dataset.variable('COND'):
        sigma_var = var
        vars_to_save.append(var)
    if var == dataset.variable('Jx'):
        jx_var = var
        vars_to_save.append(var)
    if var == dataset.variable('Jy'):
        jy_var = var
        vars_to_save.append(var)
    if var == dataset.variable('Ix (A/cm^2)'):
        ix_var = var
        vars_to_save.append(var)
    if var == dataset.variable('Iy (A/cm^2)'):
        iy_var = var
        vars_to_save.append(var)
    if var == dataset.variable('TIME'):
        time_var = var
        vars_to_save.append(var)
    if var == dataset.variable('EPS'):
        eps_var = var
        vars_to_save.append(var)

# form matrices for relevant variables over time
ex = np.zeros((len(zones), zones[0].num_points))
ey = np.zeros((len(zones), zones[0].num_points))
sigma = np.zeros((len(zones), zones[0].num_points))
```

```
eps = np.zeros((len(zones), zones[0].num_points))
mat = np.zeros((len(zones), zones[0].num_points))
time = np.zeros(len(zones))

# get the values over time
for j in range(len(zones)):
    z = zones[j]
    ex[j,:] = z.values(ex_var).as_numpy_array()
    ey[j,:] = z.values(ey_var).as_numpy_array()
    time[j] = z.values(time_var).as_numpy_array()[0]
    sigma[j,:] = z.values(sigma_var).as_numpy_array()
    mat[j,:] = z.values(mat_var).as_numpy_array()

    # determine the permittivity based on the material number
    for k in range(len(eps[j])):
        if mat[j,k] == 2:
            eps[j,k] = 80
        elif mat[j,k] == 0:
            eps[j,k] = 1

# calculate values over time
for j in range(len(zones)):
    z = zones[j]
    dex = np.zeros(z.num_points)
    dey = np.zeros(z.num_points)

    # first, calculate dEx/dt and dEy/dt
    # use a forward difference for all except the last point
    if j < len(zones) - 1:
        dt = time[j+1] - time[j]
        dex[:] = (ex[j+1,:] - ex[j,:])/dt
        dey[:] = (ey[j+1,:] - ey[j,:])/dt
    # use a backward difference for the last point
    elif j == len(zones) - 1:
        dt = time[j] - time[j-1]
        dex[:] = (ex[j,:] - ex[j-1,:])/dt
        dey[:] = (ey[j,:] - ey[j-1,:])/dt

    # assign the variables
    z.values(dex_var)[:] = dex
    z.values(dey_var)[:] = dey

    # calculate J = sigma E and assign the variables
    jx = np.multiply(ex[j,:], sigma[j,:])
    jy = np.multiply(ey[j,:], sigma[j,:])
    z.values(jx_var)[:] = jx
    z.values(jy_var)[:] = jy

    # calculate the total current and assign the variables
    z.values(ix_var)[:] = jx[:] + 8.854e-14*np.multiply(eps[j,:],
    dex[:])
    z.values(iy_var)[:] = jy[:] + 8.854e-14*np.multiply(eps[j,:],
    dey[:])
    z.values(eps_var)[:] = eps[j,:]
    z.name = fnames[i] + ', ' + z.name
```

```
    # save the file with the relevant variables
    tp.data.save_tecplot_plt(fnames[i]+'_displacement_current_total.plt',
    variables=vars_to_save, zones=zones, include_geom=True)
```

A.5 extract_1d_lines

This script reads in the 2D Tecplot file produced by *nonPDPSIM* and extracts values across the plasma gap through the center of the droplet. The output is a 1D Tecplot file containing the extracted values across the plasma gap, with different zones corresponding to different times.

```
import tecplot as tp
import numpy as np

# input base filenames below
fnames = ['MNCase_NoDrop_expairimp_v02_ResPlt']

# iterate over the base filenames
for i in range(len(fnames)):

    # form the filename
    fname = fnames[i] + '.plt'

    # read in the tecplot file
    dataset = tp.data.load_tecplot(fname,
    read_data_option=tp.constant.ReadDataOption(2))

    # set the coordinates to extract values
    # these coordinates are across the plasma gap
    # and through the center of the droplet
    len_extract_pts = 1000
    extract_pts = np.zeros((len_extract_pts, 2))
    extract_pts[:,0] = np.linspace(1.14, 1.36, len_extract_pts)
    extract_pts[:,1] = np.ones(len_extract_pts)*.975

    # list the zones
    zones = list(dataset.zones())
    counter = len(zones)
    frame = tp.active_frame()
    zones_to_save = []

    # iterate over zones (time)
    for z in zones:

        # extract the points across the plasma gap
        frame.active_zones(z)
        extract_line = tp.data.extract.extract_line(extract_pts)
        zones_to_save.append(counter)
        dataset.zone(counter).name = dataset.zone(z).name
        counter = counter + 1
```

```
    # save the file
    tp.data.save_tecplot_plt(fnames[i]+'_extract_1d_horizontal.plt',
    zones=zones_to_save, include_geom=False)
```

A.6 extract_over_cycle

This script reads in the 2D Tecplot file from *nonPDPSIM* and extracts values at locations near the droplet (i.e., on the surface, 1 diameter away) from the equators and poles. This script produces a 1D Tecplot file containing values versus time.

```
import tecplot as tp
import numpy as np

# input values in the following block

# input base filenames below
fnames = ['Cond_1e-7_5W_v02_ResPlt']
# droplet diameter, cm
diameters = np.array([80.0])*1e-4
# RF period of plasma, s
period = [1e-7]

# iterate over the base filenames
for i in range(len(fnames)):

    # form the filename
    fname = fnames[i]+'.plt'

    # read in the tecplot file
    dataset = tp.data.load_tecplot(fname,
    read_data_option=tp.constant.ReadDataOption(2))

    # form the points to extract at
    extract_pts =[]
    names = []

    # input the factors to multiply the diameters by to get the locations
    diameter_factors = [0.5, 0.75, 1.0, 1.25, 1.5, 2.0, 2.5] # factors to
    # multiply diameter by - from center of droplet
    diameter_factor_names = ['On Droplet', '0.25 Diameters Away',
    '0.5 Diameters Away', '0.75 Diameters Away', '1 Diameter Away',
    '1.5 Diameters Away', '2 Diameters Away']

    # iterate through diameter multiplicative factors
    for j in range(len(diameter_factors)):

        # determine the distance away from the center of the droplet
        away = diameter_factors[j]*diameters[i]

        # calculate the point to the left of the center of the droplet
        extract_pts.append([0.3-away, 0.975])
        names.append(fnames[i] + ', Left, '+diameter_factor_names[j])
```

```
    # calculate the point to the right of the center of the droplet
    extract_pts.append([0.3+away, 0.975])
    names.append(fnames[i] + ', Right, '+diameter_factor_names[j])

    # calculate the point below the center of the droplet
    extract_pts.append([0.3, 0.975-away])
    names.append(fnames[i] + ', Bottom, '+diameter_factor_names[j])

    # calculate the point above the center of the droplet
    extract_pts.append([0.3, 0.975+away])
    names.append(fnames[i] + ', Top, '+diameter_factor_names[j])

# calculate a point in the powered electrode
extract_pts.append([0.5, 1])
names.append(fnames[i] + ', Powered Electrode')

extract_pts = np.asarray(extract_pts)

# list the zones and variables
zones = list(dataset.zones())[1:] # skip the first (t=0) zone
variables = list(dataset.variables())
counter = len(zones)+1 # + 1 because the first zone has been skipped
frame = tp.active_frame()
zones_to_save = []
extracted_zones = []

# iterate over zones (time)
for z in zones:

    # extract the points
    frame.active_zones(z)
    extract_line = tp.data.extract.extract_line(extract_pts)
    extracted_zones.append(counter)
    dataset.zone(counter).name = dataset.zone(z).name
    counter = counter + 1

extracted_zones = list(dataset.zones())[len(zones)+1:] # + 1 because
# the first zone has been skipped

# format the data to be versus time
initTime = zones[0].values('TIME').as_numpy_array()[0]

# iterate over extracted points
for j in range(len(extract_pts)):

    # add a new zone
    jzone = dataset.add_zone(tp.constant.ZoneType.Ordered, names[j],
    len(extracted_zones))
    zones_to_save.append(counter)
    counter = counter + 1

    # iterate over variables
    for var in variables:

        # form the matrix
        a = np.zeros(len(extracted_zones))
```

```
            # iterate over time
            for z1 in extracted_zones:

                # reformat the data
                a[extracted_zones.index(z1)] =
                z1.values(var).as_numpy_array()[j]

                # calculate fraction of the RF cycle and replace time
                if var == dataset.variable('TIME'):
                    a[extracted_zones.index(z1)] =
                    (a[extracted_zones.index(z1)] - initTime)/period[i]

            # apply the values to the new zone
            jzone.values(var)[:] = a

    # iterate through the variables to rename "TIME" as "Fraction of RF
    # Cycle"
    for var in variables:
        if var == dataset.variable('TIME'):
            dataset.variable(var).name = 'Fraction of RF Cycle'
            break

    # save the file with the extracted zones
    tp.data.save_tecplot_ascii(fnames[i]+'_extract_over_cycle.plt',
    zones=zones_to_save, include_geom=False)
```

A.7 extract_over_cycle_flux1d

This script reads in the 1D Tecplot file produced by *nonPDPSIM* containing the fluxes of species to the droplet surface and extracts the values at the equators and poles of the droplet. The output is a 1D Tecplot file containing fluxes versus time.

```
import tecplot as tp
import numpy as np

# input values in the following block

# input base filenames below
fnames = ['Pow_5W_ResPlt', 'Cond_1e-1_5W_v02_ResPlt',
'Cond_1e-3_5W_v02_ResPlt', 'Cond_1e-5_5W_v02_ResPlt',
'Cond_1e-7_5W_v02_ResPlt', 'Diameter_40_5W_ResPlt', 'Diameter_60_5W_ResPlt',
'Eps_01_5W_v02_ResPlt', 'Eps_04_5W_v02_ResPlt', 'Eps_20_5W_v02_ResPlt',
'Freq_50MHz_5W_ResPlt', 'Pow_1W_ResPlt', 'Pow_10W_ResPlt2',
'Pow_15W_ResPlt2']
# droplet diameter, cm
diameters = np.array([80.0, 80.0, 80.0, 80.0, 80.0, 40.0, 60.0, 80.0, 80.0,
80.0, 80.0, 80.0, 80.0, 80.0])*1e-4
# RF period of plasma, s
period = [1e-7, 1e-7, 1e-7, 1e-7, 1e-7, 1e-7, 1e-7, 1e-7, 1e-7, 1e-7,
2e-8, 1e-7, 1e-7, 1e-7]

# iterate over the base filenames
```

```
for i in range(len(fnames)):

    # form the filename
    fname = fnames[i]+'_flux1d.plt'

    # read in the tecplot file
    dataset = tp.data.load_tecplot(fname,
    read_data_option=tp.constant.ReadDataOption(2))

    # form the points to extract at
    names = [fnames[i] + ', Bottom', fnames[i] + ', Left', fnames[i] +
    ', Top', fnames[i] + ', Right']

    # determine the xmat coordinate to extract at based on diameter
    if diameters[i] == 80.0e-4:
        extract_xmat = [0.0, 0.006276, 0.01255, 0.01883]
    elif diameters[i] == 60.0e-4:
        extract_xmat = [0.0, 0.004707, 0.009414, 0.01412]
    elif diameters[i] == 40.0e-4:
        extract_xmat = [0.0, 0.003138, 0.006276, 0.009414]

    # form the arrays
    extract_indices = []
    extract_xmat = np.asarray(extract_xmat)
    zones = list(dataset.zones())

    # add fraction of RF cycle as a variable
    dataset.add_variable('Fraction of RF Cycle')
    tvar = dataset.variable('Fraction of RF Cycle')

    # get the initial time in the file
    initTime = float((dataset.zone(zones[0]).name).split('=')[1][:-1])

    # calculate the fraction of RF cycle values
    for z in zones:
        time = float((dataset.zone(z).name).split('=')[1][:-1])
        z.values(tvar)[:] = ((time –
        initTime)/period[i])*np.ones(len(z.values(tvar)))
    variables = list(dataset.variables())
    counter = len(zones)

    # find indices that correspond to each xmat
    all_xmats = zones[0].values(dataset.variable('x-mat
    (cm)')).as_numpy_array()

    # iterate over xmats
    for j in range(len(extract_xmat)):

        # get the indices that correspond to above and below the xmat
        # desired
        above = all_xmats[all_xmats >= extract_xmat[j]].min()
        above_index = np.where(all_xmats == above)[0]
        below = all_xmats[all_xmats <= extract_xmat[j]].max()
        below_index = np.where(all_xmats == below)[0]

        # use the exact value if xmat is exactly in the file
```

```
        # otherwise, interpolate between the two closest points
        if above_index == below_index:
            extract_indices.append(above_index)
        else:
            extract_indices.append([below_index, above_index])

    zones_to_save = []

    # iterate over xmats
    for j in range(len(extract_xmat)):

        # add a new zone
        jzone = dataset.add_zone(tp.constant.ZoneType.Ordered, names[j],
        len(zones))
        zones_to_save.append(counter)
        counter = counter + 1

        # iterate over variables
        for var in variables:

            vindex = variables.index(var)
            vals = np.zeros(len(zones))

            # iterate over zones (time)
            for z in zones:

                zindex = zones.index(z)
                values = z.values(var).as_numpy_array()

                # either use the exact value or interpolate
                if len(extract_indices[j]) == 1:
                    vals[zindex] = values[extract_indices[j]]
                else:
                    vals[zindex] = np.interp(extract_xmat[j], all_xmats,
                    values)

            # store the values
            jzone.values(var)[:] = vals

    # save the file
    tp.data.save_tecplot_ascii(fnames[i]+
    '_extract_over_cycle_flux1d.plt', zones=zones_to_save,
    include_geom=False)
```

A.8 he_metastable_calculation

This script reads in the extracted 1D line (see Section A.5) of the time-averaged (see Section A.1) 2D Tecplot file. It normalizes the He_2^* density by the ratio of $He(2^3S)$ over by the total He excited state density, as well as smooths the excited state densities from *nonPDPSIM* to facilitate comparison with the experimental results.

```
import tecplot as tp
import numpy as np

# input base filename below
fname = 'MNCase_NoDrop_expairimp_v02_ResPlt_time_average_perpendicular_to_
electrodes_he_star.plt'

# read in the tecplot file
dataset = tp.data.load_tecplot(fname,
read_data_option=tp.constant.ReadDataOption(2))

# create new variables
dataset.add_variable('HE2* Lower Bound')
dataset.add_variable('HE2* Smoothed')
dataset.add_variable('HE2* Lower Bound Smoothed')
dataset.add_variable('HE23S Smoothed')

# list variables and zones
# note there is only one zone as this is a time averaged file
variables = list(dataset.variables())
zones = list(dataset.zones())
vars_to_save = []

# determine which variables to save
for var in variables:
    if var == dataset.variable('X'):
        x_var = var
        vars_to_save.append(var)
    if var == dataset.variable('Y'):
        y_var = var
        vars_to_save.append(var)
    if var == dataset.variable('HE23S'):
        he23s_var = var
        vars_to_save.append(var)
    if var == dataset.variable('HE21S'):
        he21s_var = var
        vars_to_save.append(var)
    if var == dataset.variable('HE23P'):
        he23p_var = var
        vars_to_save.append(var)
    if var == dataset.variable('HE21P'):
        he21p_var = var
        vars_to_save.append(var)
    if var == dataset.variable('HE3P'):
        he3p_var = var
        vars_to_save.append(var)
    if var == dataset.variable('HE3S'):
        he3s_var = var
        vars_to_save.append(var)
    if var == dataset.variable('HE2STAR'):
        he2_var = var
        vars_to_save.append(var)
    if var == dataset.variable('HE2* Lower Bound'):
        he2_lower_var = var
        vars_to_save.append(var)
    if var == dataset.variable('HE2* Lower Bound Smoothed'):
```

```
        he2_lower_smooth_var = var
        vars_to_save.append(var)
    if var == dataset.variable('HE2* Smoothed'):
        he2_smooth_var = var
        vars_to_save.append(var)
    if var == dataset.variable('HE23S Smoothed'):
        he23s_smooth_var = var
        vars_to_save.append(var)

# get the excited state He densities
he23s_vals = zones[0].values(he23s_var).as_numpy_array()
he21s_vals = zones[0].values(he21s_var).as_numpy_array()
he23p_vals = zones[0].values(he23p_var).as_numpy_array()
he21p_vals = zones[0].values(he21p_var).as_numpy_array()
he3s_vals = zones[0].values(he3s_var).as_numpy_array()
he3p_vals = zones[0].values(he3p_var).as_numpy_array()
he2_vals = zones[0].values(he2_var).as_numpy_array()
he2_lower_vals = np.zeros(len(he2_vals))

# iterate over points to calculate lower bound on He2*
for i in range(len(he2_vals)):

    # calculate the total He excited state densities
    he_sum = he23s_vals[i] + he21s_vals[i] + he23p_vals[i] +
    he21p_vals[i] + he3s_vals[i] + he3p_vals[i]

    # calculate the lower bound on He2* by normalizing
    if he2_vals[i] > 0.0:
        he2_lower_vals[i] = he2_vals[i]*he23s_vals[i]/he_sum

# assign the values
zones[0].values(he2_lower_var)[:] = he2_lower_vals

# form matrices to average by spatial resolution
x_vals = zones[0].values(x_var).as_numpy_array()
he2_vals_smooth = np.zeros(len(he2_vals))
he2_lower_vals_smooth = np.zeros(len(he2_lower_vals))
he23s_vals_smooth = np.zeros(len(he23s_vals))

# resolution to average over
resolution = 0.02 # cm, 0.2 mm

# iterate over points
for i in range(len(he2_vals)):

    num_points = 0
    run_avg_he2 = 0.0
    run_avg_he2_lower = 0.0
    run_avg_he23s = 0.0

    # average over spatial resolution by adding to running sums
    # iterate over points again
    for j in range(len(he2_vals)):

        # find values within the resolution
        if x_vals[j] >= x_vals[i] - resolution/2.0 and x_vals[j] <=
```

```
        x_vals[i] + resolution/2.0:

            # add to running sum
            run_avg_he2 = run_avg_he2 + he2_vals[j]
            run_avg_he2_lower = run_avg_he2_lower + he2_lower_vals[j]
            run_avg_he23s = run_avg_he23s + he23s_vals[j]
            num_points = num_points + 1

    # average by dividing by number of points
    he2_vals_smooth[i] = run_avg_he2/num_points
    he2_lower_vals_smooth[i] = run_avg_he2_lower/num_points
    he23s_vals_smooth[i] = run_avg_he23s/num_points

# assign the values
zones[0].values(he2_smooth_var)[:] = he2_vals_smooth
zones[0].values(he2_lower_smooth_var)[:] = he2_lower_vals_smooth
zones[0].values(he23s_smooth_var)[:] = he23s_vals_smooth

# save the file
tp.data.save_tecplot_plt('MNCase_NoDrop_expairimp_v02_ResPlt_time_average_per
pendicular_to_electrodes_smoothed_he_200micronres_v02.plt',
variables=vars_to_save, zones=zones, include_geom=False)
```

A.9 parameter_sweep

This script reads in the 1D Tecplot files produced by *GlobalKin* for a parameter sweep (i.e., droplet diameter). The script extracts specified values at specified times, as well as the final value or the maximum value, and outputs a 1D Tecplot file with those values versus the swept value like droplet diameter.

```
import numpy as np

def importTecplot(fname):
    # function outputs a list of variable names and an array of variable
    # values
    # fname is the .plt filename to be read in

    # form arrays
    var = []
    val_array = []

    # open the file
    with open(fname, 'r') as f:

        # generate a list of lines in the file
        d = f.readlines()

        # set flags and counters
        var_flag = 0
        val_flag = 0
        var_counter = 0
```

```
val_counter = 0

# iterate over the lines in the file
for i in range(len(d)):

    # set flags to import the variables
    if (d[i].strip()).startswith('VARIABLES='):
        var_flag = 1
        val_flag = 0

    # set flags and counters to import the values
    if (d[i].strip()).startswith('ZONE'):
        var_flag = 0
        var_counter = 0
        val_counter = 0

        # form arrays
        val_len = int((d[i].split('=')[1]).split(',')[0])
        val_array = np.zeros((len(var), val_len))

    # import the variable names
    if var_flag == 1:
        var_name = (d[i].split('"'))[1]
        var.append(var_name.strip())

    # import the values
    if val_flag == 1:

        # split the line about the spaces to get the values
        splt = d[i].split(' ')
        splt = [value for value in splt if value != '' and value
        != '\n']

        # iterate over the values in the line
        for j in range(len(splt)):

            # if values are < 1e-100, the "e" will be omitted
            # add the "e" back in to ensure proper importing
            if "E" not in splt[j]:
                splt2 = splt[j].split('-')
                splt[j] = splt2[0] + 'E-' + splt2[1]

            # add to the array
            val_array[var_counter, val_counter] = float(splt[j])
            val_counter = val_counter + 1

        # one line will only contain values for one variable
        # set flags to go to the next variable
        if val_counter >= val_len:
            val_counter = 0
            var_counter = var_counter + 1

    # set the value flag based on the blank line
    if d[i] == '\n':
        val_flag = 1
```

```
    return var, val_array

def importNam(fname):
    # function outputs initial liquid phase mole fractions
    # fname is the .nam file for the cases

    # set up the arrays
    init_mole_frac_spec = []
    init_mole_frac = []

    # open the file
    with open(fname, 'r') as f:

        # generate a list of lines in the file
        d = f.readlines()

        # iterate over the lines
        spec_flag = 0
        for i in range(len(d)):

            # begin importing the species
            if (d[i].strip()).startswith('$END'):
                spec_flag = 1

            # end importing the species and break the for loop
            if (d[i].strip()).startswith('*'):
                spec_flag = 0
                break

            # import the initial species and their mole fractions
            if spec_flag == 1:

                # split the line about the spaces to get the values
                splt = d[i].split(' ')
                splt = [value for value in splt if value != '' and value
                != '\n']

                # only store the initial mole fraction for the liquid
                # species
                if len(splt) == 2 and splt[0].endswith('_L'):
                    splt[1] = splt[1].replace('D','E')
                    init_mole_frac_spec.append(splt[0])
                    init_mole_frac.append(float(splt[1]))

    return init_mole_frac_spec, init_mole_frac

def extractFromPlt(var, val_array, extract_time, varName, maxBool):
    # function extracts a value at a given time from the .plt file
    # var is the list of variables
    # val_array is the array of values
    # extract_time is the time to get the value at
    # the final value is extracted if extract_time < 0
    # varName is the variable to extract
    # maxBool = True extracts the maximum value
    # maxBool = False extracts the value at extract_time
    # returns the value of varName at extract_time or the maximum value
```

```
    # of varName

    # get the index of the variable varName
    var_index = var.index(varName)

    # get the maximum value
    if maxBool is True
        extract_val = np.max(val_array[var_index])

    # get the value at the given time
    elif maxBool is False:

        # get the value at the last time
        if extract_time < 0.0:
            val_len = np.shape(val_array)[1]
            extract_val = val_array[var_index, val_len - 1]

        # get the value at extract_time by interpolation
        else:
            time_index = var.index('T (s)')
            extract_val = np.interp(extract_time,
            val_array[time_index, :], val_array[var_index, :])

    return extract_val

def formLine(array, sigfigs):
    # function forms lines to be written to the output Tecplot file
    # each line contains 10 values
    # array is the array to be written
    # sigfigs is the number of significant digits to write out

    line = '    '
    lineFlag = False
    for i in range(len(array)):
        line = line + str(np.around(array[i],decimals=sigfigs)) + "    "
        lineFlag = False
        if (i+1) % 10 == 0:
            line = line + '\n    '
            lineFlag = True
    if lineFlag is False:
        line = line + '\n'

    return line

def writePltFile(out_var, extract_vals, out_fname, title, sigfigs):
    # function writes the plot file
    # out_var is the output variable
    # extract_vals is the extracted values
    # out_fname is the output filename
    # title is the title of the zone
    # sigfigs is the number of significant digits to be written

    # form the header
    varheader = '     VARIABLES="' + out_var[0] + '",\n'
    for i in range(1, len(out_var)):
        varheader = varheader + '              "' + out_var[i] + '",\n'
```

```
    # write the output file
    with open(out_fname, 'w') as f:
        f.write(' TITLE = "'+title+'"\n')
        f.write(varheader)
        f.write('     ZONE I = '+ str(len(extract_vals[:,0])) +
        ', F=BLOCK,\n           T="1-D DATA"\n')

        for i in range(len(out_var)):
            line = formLine(extract_vals[:,i], sigfigs)
            f.write(line)

    return

def calcVals(fnames, first_var, sweepVal, svr, vin, vtot, vlay,
initial_formate_concentration, end_pulse_time):
    # function calculates the variables desired
    # fnames is the list of filenames
    # first_var is the first variable for the output Tecplot file
    # sweepVal is the values for first_var
    # svr is the surface to volume ratio
    # vin is the volume of the nonreactive core of the droplet
    # vtot is the total volume of the droplet
    # vlay is the volume of the reactive layer of the droplet
    # initial_formate_concentration is the initial formate concentration
    # end_pulse_time is the time the power ends at in s
    # outputs a list of the variables extracted and an array of their
    # values

    # input the variables to be extracted
    out_var = [first_var, 'OH<sub>aq</sub> at Power Off (10<sup>14</sup>
    cm<sup>-3</sup>)', 'HCOO<sup>-</sup><sub>aq</sub> Concentration at
    Simulation End (mM)', 'HCOO<sup>-</sup><sub>aq</sub> at Simulation
    End (cm<sup>-3</sup>)', 'Initial HCOO<sup>-</sup><sub>aq</sub>
    (cm<sup>-3</sup>)', 'Percent HCOO<sup>-</sup><sub>aq</sub>
    Remaining', 'Surface to Volume Ratio (1/cm)', 'Max Electron Density
    (cm<sup>-3</sup>)', 'Max Te (eV)', 'OH at Power Off (10<sup>14</sup>
    cm<sup>-3</sup>)', 'Maximum OH (10<sup>14</sup> cm<sup>-3</sup>)',
    'H<sub>2</sub>O at Power Off (10<sup>16</sup> cm<sup>-3</sup>)',
    'H<sub>2</sub>O<sub>2</sub> at Power Off (10<sup>14</sup> cm<sup>-
    3</sup>)', 'H<sub>2</sub>O<sub>2 aq</sub> at Power Off
    (10<sup>16</sup> cm<sup>-3</sup>)', 'HO<sub>2</sub> at Power Off
    (10<sup>13</sup> cm<sup>-3</sup>)', 'HO<sub>2 aq</sub> at Power Off
    (10<sup>12</sup> cm<sup>-3</sup>)', 'pH at Power Off', 'pH at
    Simulation End', 'HCOOH<sub>aq</sub> at Power Off (10<sup>10</sup>
    cm<sup>-3</sup>)', 'HCOOH<sub>aq</sub> at Simulation End
    (10<sup>9</sup> cm<sup>-3</sup>)', 'Simulation End (s)',
    'Power Off Time (s)','T<sub>gas</sub> at Power Off (K)']
    extract_vals = np.zeros((len(fnames), len(out_var)))

    # iterate over the files
    for i in range(len(fnames)):

        # import the .plt and .nam files
        var, val_array = importTecplot(fnames[i]+'.plt')
        init_mole_frac_spec, init_mole_frac = importNam(fnames[i]+'.nam')
```

```
# the first value is the sweepVal
extract_vals[i,0] = sweepVal[i]

# extract aqueous OH density at the power off time
extract_vals[i,1] = extractFromPlt(var, val_array,
end_pulse_time[i], 'OH_L', False)
# calculate aqueous OH density throughout the droplet
if vin[i] != 0.0:
    extract_vals[i,1] = extract_vals[i,1]*vlay[i]/vtot[i]
extract_vals[i,1] = extract_vals[i,1]/1.0e14

# extract aqueous formate density at the end of the simulation
formateEnd = extractFromPlt(var, val_array, -1.0, 'HCOOL-_L',
False)
# calculate aqueous formate density throughout the droplet
if vin[i] != 0.0:
    ind = init_mole_frac_spec.index('HCOOL-_L')
    formateEnd = ((init_mole_frac[ind]*3.347e22*vin[i]) +
    (formateEnd*vlay[i]))/vtot[i]
# concentration of aqueous formate
extract_vals[i,2] = formateEnd*1e3/(1e-3*6.02e23)
# density of aqueous formate
extract_vals[i,3] = formateEnd

# calculate initial formate density
extract_vals[i,4] = initial_formate_concentration[i]
*1e-3*6.02e23/1e3

# calculate percent of formate remaining
extract_vals[i,5] =
100.0*extract_vals[i,2]/initial_formate_concentration[i]

# surface to volume ratio
extract_vals[i,6] = svr[i]

# extract maximum electron density
extract_vals[i,7] = extractFromPlt(var, val_array, 0.0, 'E',
True)

# extract maximum electron temperature
extract_vals[i,8] = extractFromPlt(var, val_array, 0.0, 'TE',
True)

# extract OH density at the power off time
extract_vals[i,9] = extractFromPlt(var, val_array,
end_pulse_time[i], 'OH', False)
extract_vals[i,9] = extract_vals[i,9]/1.0e14

# extract maximum OH density
extract_vals[i,10] = extractFromPlt(var, val_array, 0.0, 'OH',
True)
extract_vals[i,10] = extract_vals[i,10]/1.0e14

# extract H2O density at the power off time
extract_vals[i,11] = extractFromPlt(var, val_array,
```

```
end_pulse_time[i], 'H2O', False)
extract_vals[i,11] = extract_vals[i,11]/1.0e16

# extract H2O2 density at the power off time
extract_vals[i,12] = extractFromPlt(var, val_array,
end_pulse_time[i], 'H2O2', False)
extract_vals[i,12] = extract_vals[i,12]/1.0e14

# extract aqueous H2O2 density at the power off time
extract_vals[i,13] = extractFromPlt(var, val_array,
end_pulse_time[i], 'H2O2_L', False)
# calculate aqueous H2O2 density throughout the droplet
if vin[i] != 0.0:
    extract_vals[i,13] = extract_vals[i,13]*vlay[i]/vtot[i]
extract_vals[i,13] = extract_vals[i,13]/1.0e16

# extract HO2 density at power off time
extract_vals[i,14] = extractFromPlt(var, val_array,
end_pulse_time[i], 'HO2', False)
extract_vals[i,14] = extract_vals[i,14]/1.0e13

# extract aqueous HO2 density at power off time
extract_vals[i,15] = extractFromPlt(var, val_array,
end_pulse_time[i], 'HO2_L', False)
# calculate aqueous HO2 density throughout the droplet
if vin[i] != 0.0:
    extract_vals[i,15] = extract_vals[i,15]*vlay[i]/vtot[i]
extract_vals[i,15] = extract_vals[i,15]/1.0e12

# extract aqueous H3O+ density at power off time
extract_vals[i,16] = extractFromPlt(var, val_array,
end_pulse_time[i], 'H3O+_L', False)
# calculate aqueous H3O+ density throughout the droplet
if vin[i] != 0.0:
    ind = init_mole_frac_spec.index('H3O^_L')
    extract_vals[i,16] = ((init_mole_frac[ind]*3.347e22*vin[i]) +
    (extract_vals[i,16]*vlay[i]))/vtot[i]
# calculate pH from aqueous H3O+ density
extract_vals[i,16] = -np.log10(extract_vals[i,16]*1000.0/6.02e23)

# extract aqueous H3O+ density at end of simulation
extract_vals[i,17] = extractFromPlt(var, val_array, -1.0,
'H3O+_L', False)
# calculate aqueous H3O+ density throughout the droplet
if vin[i] != 0.0:
    ind = init_mole_frac_spec.index('H3O^_L')
    extract_vals[i,17] = ((init_mole_frac[ind]*3.347e22*vin[i]) +
    (extract_vals[i,17]*vlay[i]))/vtot[i]
# calculate pH from aqueous H3O+ density
extract_vals[i,17] = -np.log10(extract_vals[i,17]*1000.0/6.02e23)

# extract aqueous formic acid density at power off time
extract_vals[i,18] = extractFromPlt(var, val_array,
end_pulse_time[i], 'HCOOH_L', False)
# calculate aqueous formic acid density throughout the droplet
if vin[i] != 0.0:
```

```
            ind = init_mole_frac_spec.index('HCOOH_L')
            extract_vals[i,18] = ((init_mole_frac[ind]*3.347e22*vin[i]) +
            (extract_vals[i,18]*vlay[i]))/vtot[i]
        extract_vals[i,18] = extract_vals[i,18]/1.0e10

        # extract aqueous formic acid density at end of simulation
        extract_vals[i,19] = extractFromPlt(var, val_array, -1.0,
        'HCOOH_L', False)
        # calculate aqueous formic acid density throughout the droplet
        if vin[i] != 0.0:
            ind = init_mole_frac_spec.index('HCOOH_L')
            extract_vals[i,19] = ((init_mole_frac[ind]*3.347e22*vin[i]) +
            (extract_vals[i,19]*vlay[i]))/vtot[i]
        extract_vals[i,19] = extract_vals[i,19]/1.0e9

        # extract the last time in the file
        extract_vals[i,20] = extractFromPlt(var, val_array, -1.0,
        'T (s)', False)

        # extract the residence time (amount of time the power is on)
        extract_vals[i,21] = end_pulse_time[i] - 0.1e-3

        # extract the gas temperature at power off time
        extract_vals[i,22] = extractFromPlt(var, val_array,
        end_pulse_time[i], 'TGAS', False)

    return out_var, extract_vals

def volCalc(radius, lay_thick):
    # function calculates the volume of the droplet, nonreactive core,
    # and reactive layer
    # function also calculates the surface to volume ratio
    # radius is an array of droplet radii
    # lay_thick is an array of layer thicknesses
    # returns the surface to volume ratio, volume of the nonreactive
    # core, volume of the droplet, and volume of the reactive layer

    # form the arrays
    svr = np.zeros(len(radius))
    vin = np.zeros(len(radius))
    vlay = np.zeros(len(radius))
    vtot = np.zeros(len(radius))

    # iterate over the radii
    for i in range(len(radius)):

        # calculate the surface to volume ratio
        svr[i] =
        (4.0*np.pi*(radius[i]**2.0))/((4.0/3.0)*np.pi*(radius[i]**3.0))

        # calculate the volumes
        if radius[i] != lay_thick[i]:
            vin[i] = (4.0/3.0)*np.pi*((radius[i] - lay_thick[i])**3.0)
            vtot[i] = (4.0/3.0)*np.pi*(radius[i]**3.0)
            vlay[i] = vtot[i] - vin[i]
        elif radius[i] == lay_thick[i]:
```

```
            vtot[i] = (4.0/3.0)*np.pi*(radius[i]**3.0)
            vlay[i] = vtot[i]
            vin[i] = 0.0

    return svr, vin, vtot, vlay

def main():

    # set which parameter sweeps to output files for
    iLaySweep = 0
    iPowSweep = 0
    iFlowRateSweep = 1
    iFormateConSweep = 1
    iDiameterSweep = 0
    iMixtureSweep = 0
    iWaterSweep = 0

    # layer thickness sweep
    if iLaySweep == 1:

        # set the filenames and values swept
        fnames = ['layer_sweep/he_h2o_1slm_1micronlayer',
        'layer_sweep/he_h2o_1slm_2micronlayer',
        'layer_sweep/he_h2o_1slm_3micronlayer',
        'layer_sweep/he_h2o_1slm_4micronlayer',
        'layer_sweep/he_h2o_1slm_5micronlayer',
        'base_cases/he_h2o_1slm',
        'layer_sweep/he_h2o_1slm_6micronlayer',
        'layer_sweep/he_h2o_1slm_7micronlayer',
        'layer_sweep/he_h2o_1slm_8micronlayer',
        'layer_sweep/he_h2o_1slm_10micronlayer',
        'layer_sweep/he_h2o_1slm_12micronlayer',
        'layer_sweep/he_h2o_1slm_14micronlayer',
        'layer_sweep/he_h2o_1slm_16micronlayer',
        'layer_sweep/he_h2o_1slm_18micronlayer',
        'layer_sweep/he_h2o_1slm_nolayer']
        sweepVal = np.array([1.0, 2.0, 3.0, 4.0, 5.0, 5.5, 6.0, 7.0, 8.0,
        10.0, 12.0, 14.0, 16.0, 18.0, 20.5])

        # set initial concentrations and power off time
        initial_formate_concentration = np.array([2.0, 2.0, 2.0, 2.0,
        2.0, 2.0, 2.0, 2.0, 2.0, 2.0, 2.0, 2.0, 2.0, 2.0, 2.0]) # mM
        end_pulse_time = np.array([10.1, 10.1, 10.1, 10.1, 10.1, 10.1,
        10.1, 10.1, 10.1, 10.1, 10.1, 10.1, 10.1, 10.1, 10.1])*1e-3
        # seconds

        # set radii and layer thicknesses
        radius = np.array([41.0, 41.0, 41.0, 41.0, 41.0, 41.0, 41.0,
        41.0, 41.0, 41.0, 41.0, 41.0, 41.0, 41.0, 41.0])*1e-4/2.0 # cm
        lay_thick = np.copy(sweepVal)*1e-4 # cm
        # calculate surface to volume ratio and volumes
        svr, vin, vtot, vlay = volCalc(radius, lay_thick)

        # extract the values
        out_var, extract_vals = calcVals(fnames,
        'Layer Thickness (<greek>m</greek>m)', sweepVal, svr, vin, vtot,
```

```
    vlay, initial_formate_concentration, end_pulse_time)

    # write the .plt file
    writePltFile(out_var, extract_vals,
    'layer_sweep_he_h2o_1slm_v5.plt',
    'Layer Thickness Sweep (0.2% H2O, 1 slm)', 10)

# power deposition sweep
if iPowSweep == 1:

    # set the filenames and values swept
    fnames = ['power_sweep/power_01_he_h2o_1slm',
    'power_sweep/power_02_he_h2o_1slm',
    'power_sweep/power_05_he_h2o_1slm',
    'power_sweep/power_10_he_h2o_1slm',
    'base_cases/he_h2o_1slm',
    'power_sweep/power_20_he_h2o_1slm',
    'power_sweep/power_25_he_h2o_1slm',
    'power_sweep/power_30_he_h2o_1slm']
    sweepVal = np.array([1.0, 2.0, 5.0, 10.0, 14.3, 20.0, 25.0,
    30.0])

    # set initial concentrations and power off time
    initial_formate_concentration = np.array([2.0, 2.0, 2.0, 2.0,
    2.0, 2.0, 2.0, 2.0]) # mM
    end_pulse_time = np.array([10.1, 10.1, 10.1, 10.1, 10.1, 10.1,
    10.1, 10.1])*1e-3 # seconds

    # set radii and layer thicknesses
    radius = np.array([41.0, 41.0, 41.0, 41.0, 41.0, 41.0, 41.0,
    41.0])*1e-4/2.0 # cm
    lay_thick = np.array([5.5, 5.5, 5.5, 5.5, 5.5, 5.5, 5.5,
    5.5])*1e-4
    # calculate surface to volume ratio and volumes
    svr, vin, vtot, vlay = volCalc(radius, lay_thick)

    # extract the values
    out_var, extract_vals = calcVals(fnames, 'Power (W)', sweepVal,
    svr, vin, vtot, vlay, initial_formate_concentration,
    end_pulse_time)

    # write the .plt file
    writePltFile(out_var, extract_vals,
    'power_sweep_he_h2o_1slm_v5.plt',
    'Power Sweep (0.2% H2O, 1 slm)', 10)

# flow rate sweep
if iFlowRateSweep == 1:

    # set the filenames and values swept
    fnames = ['flow_rate_sweep/he_h2o_pt75slm',
    'base_cases/he_h2o_1slm',
    'flow_rate_sweep/he_h2o_1pt25slm',
    'base_cases/he_h2o_1pt5slm',
    'flow_rate_sweep/he_h2o_1pt75slm',
    'flow_rate_sweep/he_h2o_2slm',
```

```
    'flow_rate_sweep/he_h2o_2pt5slm',
    'flow_rate_sweep/he_h2o_3slm']
    sweepVal = np.array([0.75, 1.0, 1.25, 1.5, 1.75, 2.0, 2.5, 3.0])

    # set initial concentrations and power off time
    initial_formate_concentration = np.array([2.0, 2.0, 2.0, 2.0,
    2.0, 2.0, 2.0, 2.0]) # mM
    end_pulse_time = np.array([13.6, 10.1, 9.3, 8.4, 7.5, 6.5, 5.8,
    5.0])*1e-3 # seconds

    # set radii and layer thicknesses
    radius = np.array([41.0, 41.0, 41.0, 41.0, 41.0, 41.0, 41.0,
    41.0])*1e-4/2.0 # cm
    lay_thick = np.array([5.5, 5.5, 5.5, 5.5, 5.5, 5.5, 5.5,
    5.5])*1e-4
    # calculate surface to volume ratio and volumes
    svr, vin, vtot, vlay = volCalc(radius, lay_thick)

    # extract the values
    out_var, extract_vals = calcVals(fnames, 'Flow Rate (slm)',
    sweepVal, svr, vin, vtot, vlay, initial_formate_concentration,
    end_pulse_time)

    # write the .plt file
    writePltFile(out_var, extract_vals,
    'flow_rate_sweep_he_h2o_v6.plt', 'Flow Rate Sweep (0.2% H2O)',
    10)

# initial formate concentration sweep
if iFormateConSweep == 1:

    # set the filenames and values swept
    fnames = ['formate_sweep/formate_pt5mM_he_h2o_1slm',
    'formate_sweep/formate_1mM_he_h2o_1slm',
    'base_cases/he_h2o_1slm',
    'formate_sweep/formate_3pt5mM_he_h2o_1slm',
    'formate_sweep/formate_5mM_he_h2o_1slm',
    'formate_sweep/formate_7pt5mM_he_h2o_1slm',
    'formate_sweep/formate_10mM_he_h2o_1slm']
    sweepVal = np.array([0.5, 1.0, 2.0, 3.5, 5.0, 7.5, 10.0])

    # set initial concentrations and power off time
    initial_formate_concentration = np.array([0.5, 1.0, 2.0, 3.5,
    5.0, 7.5, 10.0]) # mM
    end_pulse_time = np.array([10.1, 10.1, 10.1, 10.1, 10.1, 10.1,
    10.1])*1e-3 # seconds

    # set radii and layer thicknesses
    radius = np.array([41.0, 41.0, 41.0, 41.0, 41.0, 41.0, 41.0])
    *1e-4/2.0 # cm
    lay_thick = np.array([5.5, 5.5, 5.5, 5.5, 5.5, 5.5, 5.5])*1e-4
    # calculate surface to volume ratio and volumes
    svr, vin, vtot, vlay = volCalc(radius, lay_thick)

    # extract the values
    out_var, extract_vals = calcVals(fnames,
```

```
    'Formate Concentration (mM)', sweepVal, svr, vin, vtot, vlay,
    initial_formate_concentration, end_pulse_time)

    # write the .plt file
    writePltFile(out_var, extract_vals,
    'formate_sweep_he_h2o_1slm_v6.plt',
    'Formate Concentration Sweep (0.2% H2O, 1 slm)', 10)

# droplet diameter sweep
if iDiameterSweep == 1:

    # set the filenames and values swept
    fnames = ['diameter_sweep/diameter_21_he_h2o_1slm',
    'diameter_sweep/diameter_26_he_h2o_1slm',
    'diameter_sweep/diameter_31_he_h2o_1slm',
    'diameter_sweep/diameter_36_he_h2o_1slm',
    'base_cases/he_h2o_1slm',
    'diameter_sweep/diameter_46_he_h2o_1slm',
    'diameter_sweep/diameter_51_he_h2o_1slm',
    'diameter_sweep/diameter_56_he_h2o_1slm',
    'diameter_sweep/diameter_61_he_h2o_1slm',
    'diameter_sweep/diameter_66_he_h2o_1slm',
    'diameter_sweep/diameter_71_he_h2o_1slm',
    'diameter_sweep/diameter_76_he_h2o_1slm',
    'diameter_sweep/diameter_81_he_h2o_1slm']
    sweepVal = np.array([21.0, 26.0, 31.0, 36.0, 41.0, 46.0, 51.0,
    56.0, 61.0, 66.0, 71.0, 76.0, 81.0])

    # set initial concentrations and power off time
    initial_formate_concentration = np.array([2.0, 2.0, 2.0, 2.0,
    2.0, 2.0, 2.0, 2.0, 2.0, 2.0, 2.0, 2.0, 2.0]) # mM
    end_pulse_time = np.array([10.1, 10.1, 10.1, 10.1, 10.1, 10.1,
    10.1, 10.1, 10.1, 10.1, 10.1, 10.1, 10.1])*1e-3 # seconds

    # set radii and layer thicknesses
    radius = np.copy(sweepVal)*1e-4/2.0 # cm
    lay_thick = np.array([5.5, 5.5, 5.5, 5.5, 5.5, 5.5, 5.5, 5.5,
    5.5, 5.5, 5.5, 5.5, 5.5])*1e-4
    # calculate surface to volume ratio and volumes
    svr, vin, vtot, vlay = volCalc(radius, lay_thick)

    # extract the values
    out_var, extract_vals = calcVals(fnames,
    'Diameter (<greek>m</greek>m)', sweepVal, svr, vin, vtot, vlay,
    initial_formate_concentration, end_pulse_time)

    # write the .plt file
    writePltFile(out_var, extract_vals,
    'diameter_sweep_he_h2o_1slm_v5.plt',
    'Diameter Sweep (0.2% H2O, 1 slm)', 10)

# gas mixture sweep
if iMixtureSweep == 1:

    # set the filenames and values swept
    fnames = ['base_cases/he_h2o_1slm',
```

```
        'gas_mixture_sweep/he_o2_1slm',
        'gas_mixture_sweep/he_ar_h2o_1slm', 'gas_mixture_sweep/he_1slm',
        'gas_mixture_sweep/he_ar_1slm', 'gas_mixture_sweep/he_h2_1slm']
        sweepVal = np.array([1.0, 2.0, 3.0, 4.0, 5.0, 6.0])

        # set initial concentrations and power off time
        initial_formate_concentration = np.array([2.0, 2.0, 2.0, 2.0,
        2.0, 2.0]) # mM
        end_pulse_time = np.array([10.1, 10.1, 10.1, 10.1, 10.1,
        10.1])*1e-3 # seconds

        # set radii and layer thicknesses
        radius = np.array([41.0, 41.0, 41.0, 41.0, 41.0, 41.0])*1e-4/2.0
        # cm
        lay_thick = np.array([5.5, 5.5, 5.5, 5.5, 5.5, 5.5])*1e-4
        # calculate surface to volume ratio and volumes
        svr, vin, vtot, vlay = volCalc(radius, lay_thick)

        # extract the values
        out_var, extract_vals = calcVals(fnames, 'Gas Mixture', sweepVal,
        svr, vin, vtot, vlay, initial_formate_concentration,
        end_pulse_time)

        # write the .plt file
        writePltFile(out_var, extract_vals,
        'gas_mixture_sweep_1slm_v5.plt', 'Gas Mixture Sweep (1 slm)', 10)

    # water concentration sweep
    if iWaterSweep == 1:

        # set the filenames and values swept
        fnames = ['water_sweep/he_1pt5slm',
        'water_sweep/he_pt05h2o_1pt5slm',
        'water_sweep/he_pt1h2o_1pt5slm', 'base_cases/he_h2o_1pt5slm',
        'water_sweep/he_pt3h2o_1pt5slm', 'water_sweep/he_pt4h2o_1pt5slm',
        'water_sweep/he_pt5h2o_1pt5slm', 'water_sweep/he_pt6h2o_1pt5slm',
        'water_sweep/he_pt7h2o_1pt5slm',
        'water_sweep/he_pt75h2o_1pt5slm','water_sweep/he_pt8h2o_1pt5slm',
        'water_sweep/he_pt9h2o_1pt5slm', 'water_sweep/he_1h2o_1pt5slm']
        sweepVal = np.array([0.0, 0.05, 0.1, 0.2, 0.3, 0.4, 0.5, 0.6,
        0.7, 0.75, 0.8, 0.9, 1.0])

        # set initial concentrations and power off time
        initial_formate_concentration = np.array([2.0, 2.0, 2.0, 2.0,
        2.0, 2.0, 2.0, 2.0, 2.0, 2.0, 2.0, 2.0, 2.0]) # mM
        end_pulse_time = np.array([8.4, 8.4, 8.4, 8.4, 8.4, 8.4, 8.4,
        8.4, 8.4, 8.4, 8.4, 8.4, 8.4])*1e-3 # seconds

        # set radii and layer thicknesses
        radius = np.array([41.0, 41.0, 41.0, 41.0, 41.0, 41.0, 41.0,
        41.0, 41.0, 41.0, 41.0, 41.0, 41.0])*1e-4/2.0 # cm
        lay_thick = np.array([5.5, 5.5, 5.5, 5.5, 5.5, 5.5, 5.5, 5.5,
        5.5, 5.5, 5.5, 5.5, 5.5])*1e-4
        # calculate surface to volume ratio and volumes
        svr, vin, vtot, vlay = volCalc(radius, lay_thick)
```

```
        # extract the values
        out_var, extract_vals = calcVals(fnames, 'Water Percentage',
        sweepVal, svr, vin, vtot, vlay, initial_formate_concentration,
        end_pulse_time)

        # write the .plt file
        writePltFile(out_var, extract_vals,
        'water_sweep_he_h2o_1pt5slm_v5.plt', 'Water Sweep (1.5 slm)', 10)

    return

if __name__ == "__main__":
    main()
```